NASA Technical Memorandum 103250

Aerodynamics of a Linear Oscillating Cascade

Daniel H. Buffum
Lewis Research Center
Cleveland, Ohio

and

Sanford Fleeter
Purdue University
West Lafayette, Indiana

August 1990

NASA

AERODYNAMICS OF A LINEAR OSCILLATING CASCADE

Daniel H. Buffum
NASA Lewis Research Center
Cleveland, Ohio

Sanford Fleeter
School of Mechanical Engineering
Purdue University
West Lafayette, Indiana

ABSTRACT

The steady and unsteady aerodynamics of a linear oscillating cascade are investigated using experimental and computational methods. Experiments are performed to quantify the torsion mode oscillating cascade aerodynamics of the NASA Lewis Transonic Oscillating Cascade for subsonic inlet flow fields using two methods: (1) simultaneous oscillation of all the cascaded airfoils at various values of interblade phase angle, and (2) the unsteady aerodynamic influence coefficient technique. Analysis of these data and correlation with classical linearized unsteady aerodynamic analysis predictions indicate that the wind tunnel walls enclosing the cascade have, in some cases, a detrimental effect on the cascade unsteady aerodynamics. An Euler code for oscillating cascade aerodynamics is modified to incorporate improved upstream and downstream boundary conditions and also the unsteady aerodynamic influence coefficient technique. The new boundary conditions are shown to improve the unsteady aerodynamic predictions of the code, and the computational unsteady aerodynamic influence coefficient technique is shown to be a viable alternative for calculation of oscillating cascade aerodynamics.

E-5677

TABLE OF CONTENTS

LIST OF SYMBOLS

a	speed of sound
C	airfoil chord
C_m	unsteady aerodynamic moment coefficient
$\hat{C}_m^n$	unsteady aerodynamic moment influence coefficient for airfoil n
C_p	unsteady pressure coeffcient, $p_1/\left(\frac{1}{2}\rho V^2 \alpha_1\right)$
$\overline{C}_p$	steady pressure coefficient, $(\overline{p}_{in} - p_0)/\left(\frac{1}{2}\rho V^2\right)$
$\hat{C}_p^n$	unsteady pressure influence coefficient for n^{th} airfoil
k	reduced frequency, $\omega C/(2V)$
l	axial wavenumber
M	cascade inlet Mach number
N	limit of summation
m	tangential wavenumber
$\overline{p}_{in}$	mean inlet static pressure
$\overline{p}_{ex}$	mean exit static pressure
p_t	inlet total pressure
p_j	j^{th} harmonic of airfoil surface static pressure
S	airfoil spacing
t	time
V	inlet velocity

x	chordwise coordinate
x^*	nondimensional chordwise coordinate, x/C
y	coordinate normal to chordwise direction
α_j	j^{th} harmonic of incidence angle
β	interblade phase angle (positive when airfoil n+1 leads airfoil n)
γ	stagger angle
ΔC_p	unsteady pressure difference coefficient
δC_p	dynamic periodicity magnitude difference
$\delta\phi$	dynamic periodicity phase difference
θ	direction of disturbance pressure wave propagation
ρ	density
ϕ	phase of first harmonic unsteady pressure
ω	airfoil oscillation frequency

CHAPTER 1

INTRODUCTION

Blade vibration problems continue to hinder the development of advanced turbomachines and propellers. Blade flutter, a self-excited oscillation in which the unsteady aerodynamic forces depend upon the blade motion, typically results in failure of the blading. Costly re-design of the blading is then required, with aerodynamic performance often compromised in the process.

Traditional design methodology, in which flutter boundaries based upon testing of previous designs are applied to new designs, has been found to be inadequate even for conventional turbofan engines [1]. When new propulsion concepts are investigated, the use of past experience to avoid flutter is even more dubious. For example, highly efficient advanced propellers currently under development are characterized by thin, highly-swept blades of relatively high solidity operating with supersonic tip relative Mach numbers. The novel design features of the advanced propeller place it well outside the realm of previous experience: the solidity is too large for it to be analyzed as an isolated airfoil but much smaller than a conventional turbomachine, and it also has much greater aerodynamic sweep. Flutter of an advanced propeller model [2] indicated that cascade effects had a destabilizing effect on the flutter boundary. In addition, flutter was not encountered in tests of similar propellers with less sweep, implying that sweep is a destabilizing influence. Thus the features largely responsible for placing advanced propeller designs outside the realm of previous experience had significant influences on the occurrence of flutter.

To improve the ability to predict flutter in turbomachines and propellers, advanced analyses to predict oscillating cascade aerodynamics must be developed. Classical unsteady aerodynamic models are based on fully linearized aerodynamic theory in which the unsteady flow is assumed to be a small perturbation to a uniform steady flow. The problem is thus reduced to analyzing the unsteady aerodynamics of a cascade of flat plates operating at zero mean incidence. Efficient semi-analytical techniques have been developed for rapid computer-generated solutions to the fully linearized problem for subsonic flow [3-5]. However, the unsteady aerodynamic effects due to interactions between the steady and unsteady flow fields, i.e., the effects of blade geometry and nonzero incidence angle (steady loading), are not considered in these models. To overcome these limitations, linearized models are being developed which take into account the effects of a nonuniform mean flow field on the unsteady flow, which is assumed to be a small perturbation to the steady flow field, references 6-12, for example. While these linearized models should be computationally efficient, nonlinear analyses which solve the time-dependent full potential and Euler equations are also being used to predict oscillating cascade aerodynamics [13-15], although they require relatively large computing times.

1.1 Oscillating Cascade Experiments

To direct the development of advanced unsteady aerodynamic models and to evaluate these as well as existing analyses, data obtained from oscillating cascade experiments are needed. Appropriate experimental data will quantify the airfoil surface steady and unsteady pressure distributions over a range of oscillating cascade operating conditions. The steady flow field, as a function of inlet Mach number, solidity, stagger angle and airfoil geometry, should be in the appropriate regime of compressible flow, i.e., subsonic, transonic or supersonic, be of either compressor or turbine geometry as required, and data should be obtained for several steady flow

conditions so that the effect of steady loading on the cascade unsteady aerodynamics may be investigated. Unsteady data are needed over a range of interblade phase angles at values of reduced frequency which are realistic for the application.

With these experimental objectives in mind, a review of previous oscillating cascade investigations reveals there is, in general, little data available for cascaded airfoils driven to oscillate simultaneously. Focusing on subsonic and transonic flows for compressor geometries, there are several noteworthy publications. Davies and Whitehead [16] performed experiments in an annular oscillating cascade in subsonic through supersonic flow regimes, but there is significant scatter in the data and the measurements were limited to unsteady aerodynamic moment data from strain gages. Of particular interest herein, unsteady pressure measurements have been made at the NASA Lewis Research Center in a transonic oscillating cascade [17]. Unfortunately, there were some discrepancies in the analysis of the unsteady data as well as the steady airfoil surface pressure data. As a part of the current investigation, these discrepancies in the steady and unsteady data are corrected. Kobayashi [18] has made detailed blade surface pressure measurements in an annular oscillating cascade at high subsonic and supersonic inlet conditions. Large pressure fluctuations occurred due to shock wave motion and cascade instability was noted over a wide range of conditions.

The lack of oscillating cascade data is due to the inherent complexity of the experiments. First, oscillating cascades are expensive to build, requiring a drive system capable of oscillating the airfoils simultaneously at realistic reduced frequency values. Second, because the measurements must be obtained not only for each steady flow condition and reduced frequency, but also over a range of interblade phase angles, these experiments are quite time consuming. As a result, data are typically obtained for only several interblade phase angles.

To avoid these problems, oscillating cascade data might be obtained through simpler experiments. In particular, when the unsteady disturbances are small, as in a typical flutter stability problem, an unsteady aerodynamic influence coefficient technique might be utilized. In this technique, only one airfoil in the cascade is oscillated, with the resulting airfoil surface unsteady pressure distributions measured on the oscillating airfoil and its stationary neighbors. The unsteady aerodynamics of an equivalent cascade with all airfoils oscillating at any specified interblade phase angle is then determined through a vector summation of these influence coefficient data.

Figure 1.1 depicts a two-dimensional finite cascade representation of a blade row. For a given mean flow field and reduced frequency of oscillation, and assuming small unsteady disturbances, the cascade unsteady aerodynamics may be expressed as linearly combined influence coefficients which can be determined experimentally or analytically. Consider a finite airfoil cascade with 2N + 1 airfoils executing constant amplitude harmonic oscillations with a constant interblade phase angle β. The airfoil surface unsteady pressure, expressed as a pressure coefficient $C_p(x,\beta)$ acting at a point on the reference airfoil (airfoil 0 in Figure 1.1), can be expressed as a Fourier series

$$C_p(x,\beta) = \sum_{n=-N}^{N} \hat{C}_p^n(x) e^{in\beta} \qquad (1.1)$$

where $\hat{C}_p^n$ is the complex-valued unsteady aerodynamic influence coefficient. Thus this influence coefficient defines the unsteady pressure coefficient developed on the reference airfoil due to the motion of airfoil n.

Mathematical models for an infinite cascade of airfoils oscillating with a specified interblade phase angle can also be used to determine these unsteady

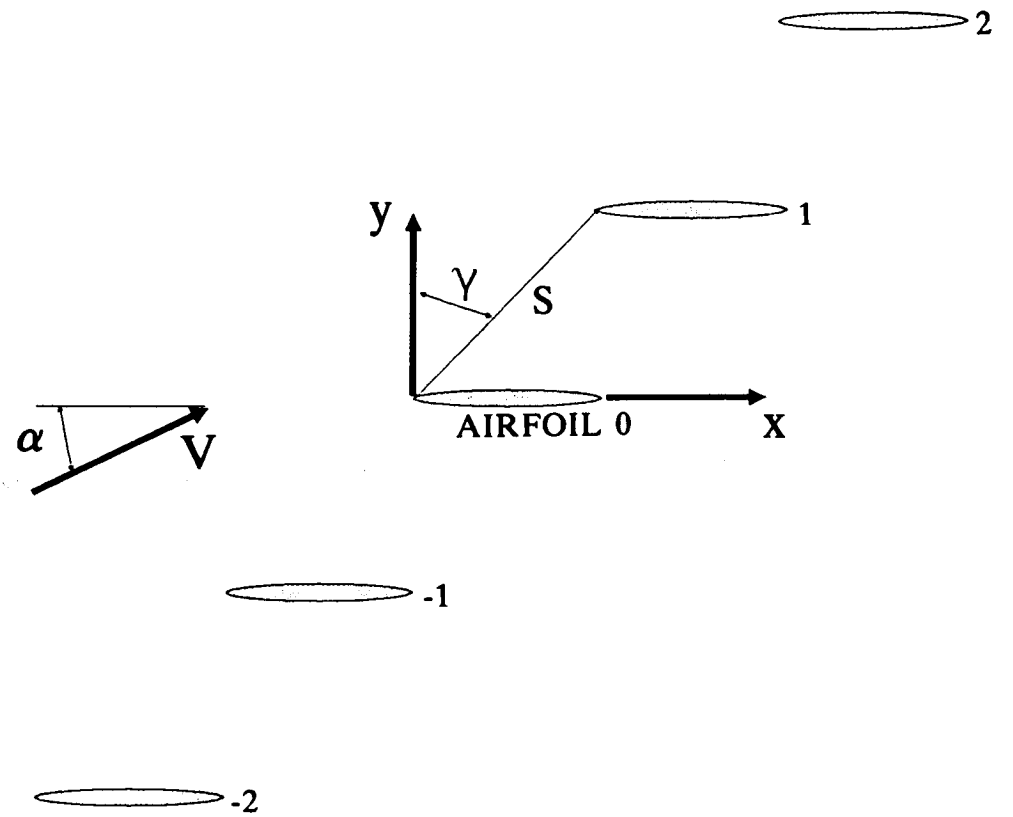

Figure 1.1 Two-dimensional finite cascade model of a blade row

aerodynamic influence coefficients. For this case, the influence coefficients are determined by inversion of Equation 1.1.

$$\hat{C}_p^n(x) = \frac{1}{2\pi}\int_{-\pi}^{\pi} C_p(x,\beta)e^{-in\beta}d\beta \qquad (1.2)$$

Analytically determined unsteady aerodynamic influence coefficients can thus be determined from oscillating cascade mathematical models by integrating over the complete interblade phase angle interval, Equation 1.2. Utilizing these influence coefficients in Equation 1.1 then enables analytical results for a finite number of airfoils oscillating in an infinite cascade to be determined.

Several experimental investigations have been directed at validation of this technique through correlation of unsteady aerodynamic influence coefficient results with corresponding data acquired with all airfoils oscillating at specified interblade phase angles. Hanamura et al. [19] found good results for flow in a water channel and subsequently applied this technique, without further validation, to subsonic and transonic flows [20,21]. Davies and Whitehead [16] performed such experiments at high subsonic inlet conditions and reduced frequencies based on semichord up to 0.1, but the validity of the influence coefficient technique cannot be assessed due to scatter in the data. In supersonic inlet Mach number experiments at ONERA [22], the summation of influence coefficients has been compared to data for a linear cascade with two airfoils oscillating, but the scope of the experiments was very limited. Recently, Bolcs et al. [23] reported very good results for this technique in an annular turbine cascade.

1.2 Calculation of Oscillating Cascade Aerodynamics

Time-marching solutions of the nonlinear equations of fluid dynamics for the oscillating cascade problem are similar to the experiments in that they tend to be

very time-consuming. To remedy this problem, the unsteady aerodynamic influence coefficient technique may also be applied to the computational aerodynamics of oscillating, cascaded airfoils. Gerolymos [24] has used this technique to predict the aerodynamics of a supersonic oscillating cascade with some success.

As with the experimental unsteady aerodynamic influence coefficient technique, only one airfoil in the cascade is oscillated, and the influences of these oscillations are determined for the oscillating airfoil and its stationary neighbors. The unsteady aerodynamics of an equivalent cascade with all airfoils oscillating at any specified interblade phase angle is then determined through a vector summation of the influence coefficients. The unsteady solution is obtained for oscillations relative to the previously-computed steady flow, thus the effects of a nonuniform steady flow field are included in the unsteady solution.

1.3 Objective

The objective of the experimental research reported herein is twofold: (1) the aerodynamics of a cascade of airfoils oscillating simultaneously is quantified for two cascade solidities, several mean flow conditions and a number of interblade phase angle/reduced frequency combinations; and (2) a detailed experimental study is made of the unsteady aerodynamic influence coefficient technique. In particular, the steady and unsteady aerodynamics of a cascade of biconvex airfoils executing torsion mode oscillations are investigated for subsonic inlet Mach numbers. This is accomplished by obtaining fundamental aerodynamic data in the NASA Lewis Transonic Oscillating Cascade Facility. Detailed steady airfoil surface pressure distributions quantify the mean flow field. Unsteady airfoil surface pressure distributions are measured both with all airfoils oscillating at specified interblade phase angles and with only one

airfoil oscillating. The experimentally-determined influence coefficient data are summed for correlation with the data obtained with all airfoils oscillating and also with the predictions of a linearized subsonic oscillating cascade analysis.

In addition, an Euler code for oscillating, cascaded airfoils is modified for implementation of the unsteady aerodynamic influence coefficient technique. The Euler code is first improved by modification of the upstream and downstream boundary conditions. The unsteady aerodynamic influence coefficient technique is then implemented by further modification of the code. The resulting predictions are correlated with the experimental data and also with the linearized analysis predictions.

CHAPTER 2

FACILITY AND INSTRUMENTATION

The NASA Lewis Transonic Oscillating Cascade Facility combines a linear, transonic cascade wind tunnel capable of inlet flow approaching Mach one with a high-speed airfoil drive system which imparts torsion-mode oscillations to the cascaded airfoils at specified interblade phase angles and realistic high reduced frequency values. Appropriate steady-state instrumentation is used to determine the cascade inlet Mach number, verify the cascade passage-to-passage periodicity and quantify the steady airfoil surface pressure distribution for each steady flow field. Miniature dynamic pressure transducers are used to quantify the unsteady airfoil surface pressures on the oscillating cascaded airfoils.

2.1 Oscillating Cascade Facility

The NASA Lewis Transonic Oscillating Cascade Facility is shown in Figure 2.1. Air drawn from the atmosphere passes through a smooth contraction inlet section into a constant area test section of 9.78 cm span which measures 58.6 cm along the stagger line. Up to nine airfoils may be accommodated, spaced by 5.86 cm. Upstream of the test section, suction is applied through perforated walls to reduce the boundary layer thickness. Adjustable tailboards are used to adjust the cascade exit region static pressure and also form bleed scoops which further reduce upper and lower wall boundary layer effects. Downstream of the test section, the air is expanded through a diffuser into an exhaust header. The flow rate is controlled by two valves located in the header which operate in parallel, the smaller of the two providing fine

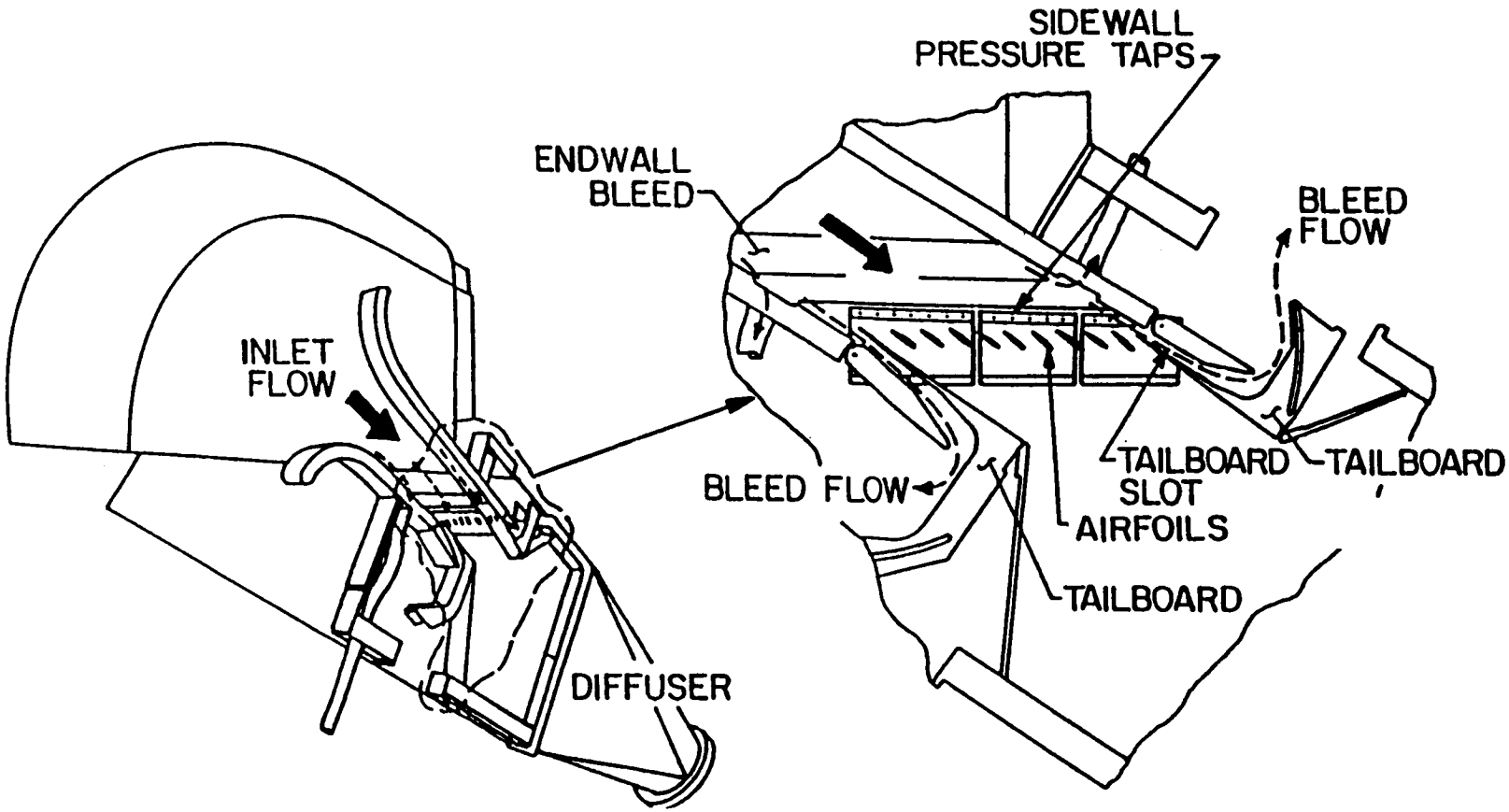

Figure 2.1 NASA Lewis Transonic Oscillating Cascade Facility

adjustment to the flow rate. The exhaust system, part of a central air facility at Lewis, maintains a 30 kPa pressure downstream of the flow control valves. The inlet and airfoil angles are adjustable, allowing a wide range of incidence and stagger angle combinations.

A boundary layer bleed system is provided to minimize tunnel wall boundary layer effects. Perforated end walls having an open area ratio of 0.225 with 0.15 cm perforation hole diameters are located upstream of the airfoils. These bleeds are partitioned into five segments on each wall, with each segment having an individual flow control valve for localized control. Adjustable tailboards form scoops with the top and bottom side walls, and also have individual flow control valves. Headers route the bleed flow into the exhaust system.

Uncambered, zero-twist biconvex airfoils fabricated out of titanium alloy are used for these experiments. The radius of curvature of each airfoil surface is 27.4 cm, and the leading and trailing edges are rounded to 0.025 cm radii of curvature. With a chord length of 7.62 cm and a maximum thickness of 0.577 ± 0.004 cm, the thickness-to-chord ratio is 0.076. The span is 9.60 cm, making the aspect ratio 1.26. Trunnions which support the airfoil and allow coupling to the drive system are located at the mid-chord, resulting in a mid-chord elastic axis.

Tests were conducted to ensure that the airfoils would not deform when oscillated at high frequency [25]. The first torsion mode was determined by interferometry to occur at 932 Hz, and negligible airfoil deflections were found to occur during torsional oscillation at 600 Hz.

To obtain realistically high values of the reduced frequency, the mechanical drive system must provide high frequency controlled oscillations of the airfoils. Figure 2.2 illustrates the main components of the drive system. Nine stainless steel barrel cams, each with a six cycle sinusoidal groove machined into its periphery, are mounted

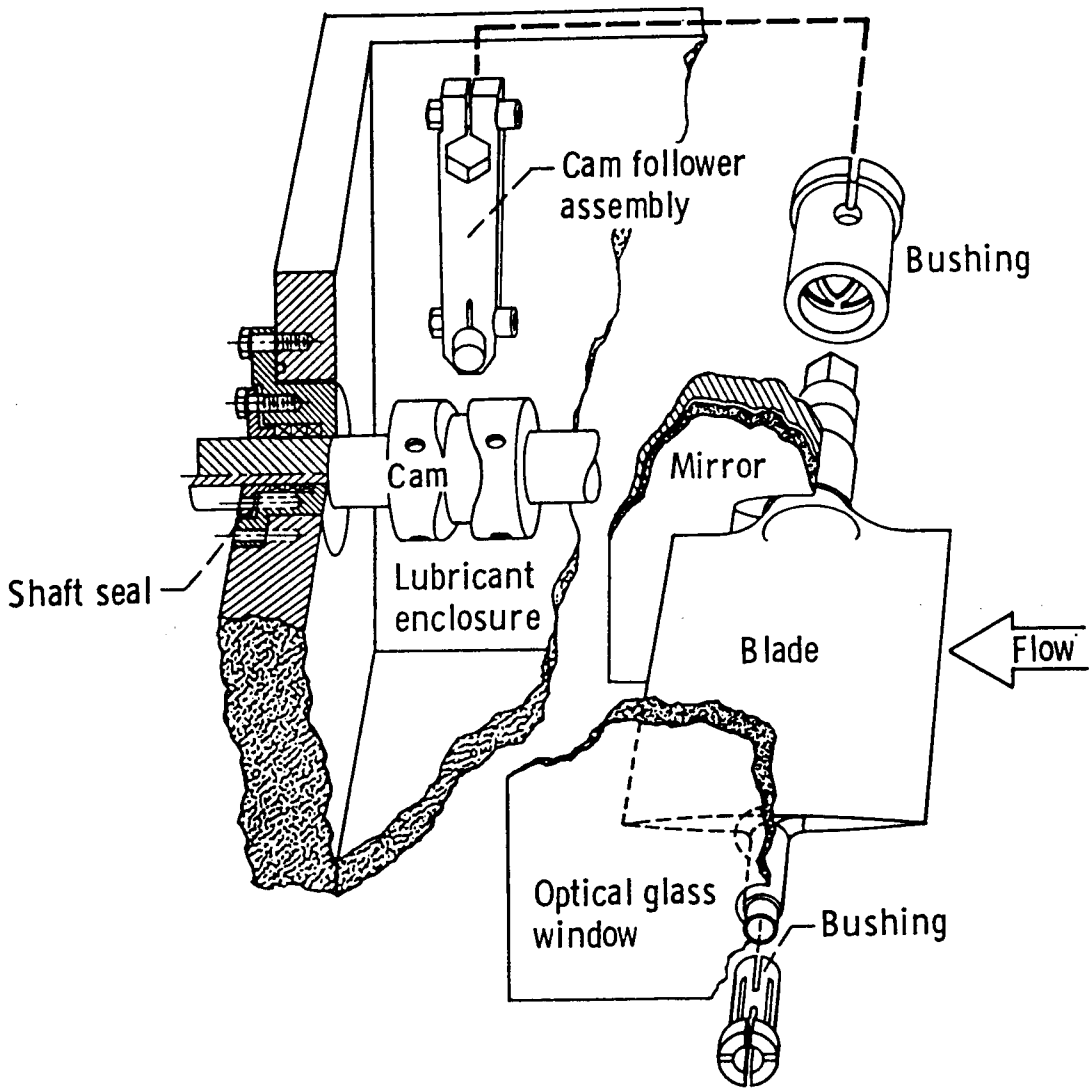

Figure 2.2 High speed airfoil oscillation mechanism

on a common rotating shaft driven by a 74.6 kW electric motor. A cam follower assembly, consisting of a titanium alloy connecting arm with a stainless steel button on one end, is joined on the other end to an airfoil trunnion. The button fits into the cam groove, thus coupling the airfoil to the camshaft. Lubrication for the cam/follower assembly is provided by an oil bath. The amplitude of the torsional airfoil motion is 1.2 degrees as dictated by the cam and follower geometry. The drive system is configured for oscillations at a chosen fixed interblade phase angle by fixing the cams at the required relative positions on the shaft.

2.2 Instrumentation for Steady-State Measurements

A row of 22 wall static pressure taps, located upstream of the cascaded airfoils, is used to determine the inlet static pressure distribution. A similar row of static taps, located downstream of the cascade, determines the cascade exit region static pressure.

Two airfoils are instrumented with static pressure taps so that airfoil upper and lower surface pressures may be determined simultaneously. There are sixteen chordwise measurement locations with a higher density in the leading edge region to capture the higher gradients there, Figure 2.3. Four additional taps, numbers 17 through 20 in the figure, are used to indicate the spanwise pressure distribution. Two airfoils are instrumented so that data for the two airfoil surfaces defining one cascade passage may be obtained simultaneously.

2.3 Instrumentation for Unsteady Measurements

The primary unsteady data are the magnitude and phase of the unsteady airfoil surface pressures relative to the airfoil motion. The elements crucial to these measurements are the dynamic pressure transducers and the airfoil motion detection system.

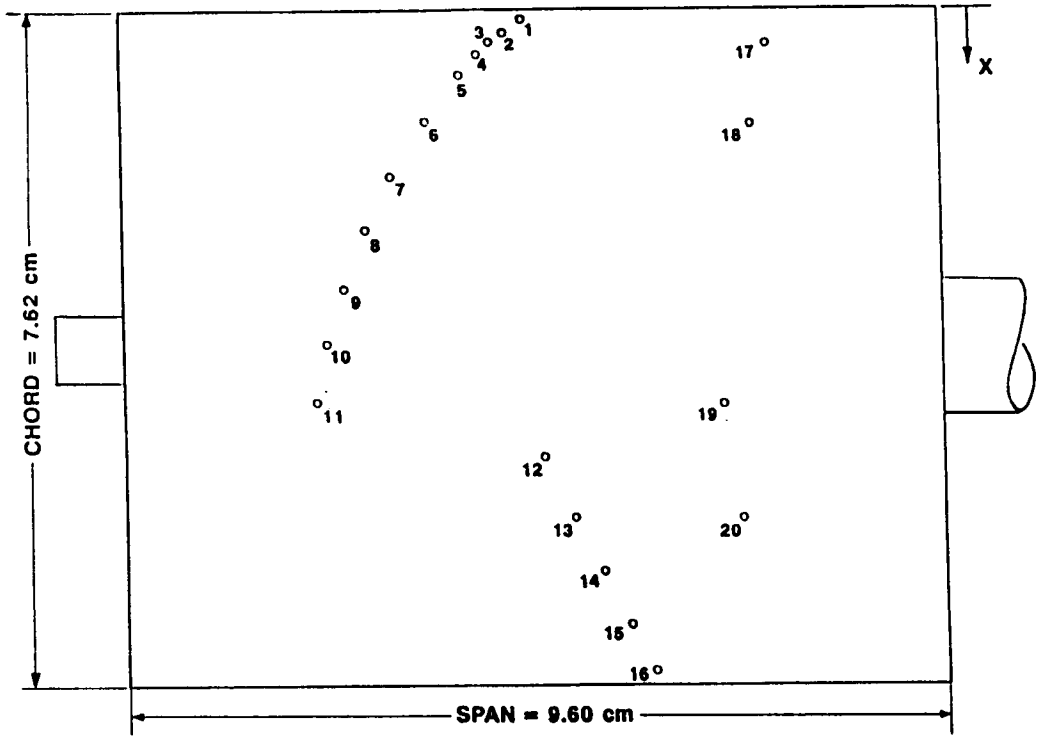

Tap no.	% Chord
1	1.5
2	3.1
3	4.7
4	6.4
5	9.7
6	16.3
7	24.7
8	33.1
9	41.4
10	49.8
11	58.2
12	66.5
13	75.0
14	83.3
15	91.5
16	98.2
17	4.7
18	16.3
19	58.2
20	75.0

Figure 2.3 Airfoil surface static pressure tap locations

2.3.1 Pressure Transducers

Miniature semiconductor pressure transducers are used to measure the airfoil surface unsteady pressures. Consisting of a silicon diaphragm containing a four arm strain gage bridge mounted over a cylindrical cavity, the transducer has several desirable characteristics: (1) frequency response sufficient to measure at least several harmonics of the oscillation frequency; (2) small dimensions for good spatial resolution and minimal flow disturbance; (3) insensitivity of output to transducer acceleration; and (4) invariance of the transducer dynamic response with change in temperature. In addition, a mounting technique which effectively isolates the transducer from airfoil strain is necessary.

Six Kulite Semiconductor Products dynamic pressure transducers are flush mounted symmetrically about the midchord of one surface of the airfoil, Figure 2.4. These transducers, having active sensor diameters of 0.097 cm (1.3% of the airfoil chord), are epoxied into milled slots and potted in room temperature vulcanizing rubber (RTV) for isolation from airfoil strain. A thin coating of room-temperature-vulcanizing rubber is used to fair the transducer surface into the surface contour of the airfoil and also protect the transducer.

Static calibration consists of measuring the transducer output over a range of applied pressures. The transducers were calibrated before the oscillating cascade experiments and then recalibrated periodically. In all cases, the output voltage was a highly linear function of the applied pressure differential, and the typical transducer had a negligible change in its calibration over the course of the experiments.

Frequency Response

Due to the high stiffness-to-mass ratio of the diaphragm, the transducers have a high natural frequency, reported to be 230 kHz. Since the transducers are expected to have unity gain and negligible phase shift up to 20% of the natural frequency, the

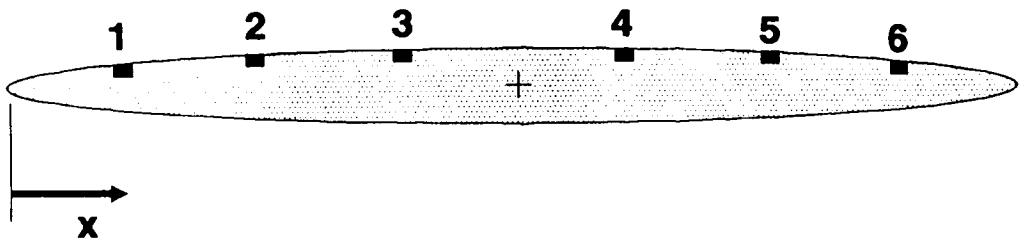

Transducer no.	% Chord
1	12
2	25
3	40
4	60
5	75
6	88

Figure 2.4 Airfoil surface dynamic pressure transducer locations

frequency response is more than adequate for these experiments, which require harmonic information to about 1 kHz. However, RTV coating applied to the transducer diaphragm will reduce its natural frequency. To be certain that this has no detrimental effect on the transducer response at the frequencies of interest, frequency-response verification tests were undertaken.

A resonant tube assembly similar to that of Capece and Fleeter [26] is used to generate plane acoustic waves to excite the pressure transducers at discrete frequencies. The assembly consists of an 20.3 cm diameter, 4.6 m long plastic tube with a speaker mounted at one end. An instrumented airfoil is inserted in the opposite end of the tube, which is open to the atmosphere, and an Endevco pressure transducer positioned adjacent to the instrumented airfoil serves as the reference. Amplified sine waves are used to drive the speaker which in turn creates acoustic waves in the tube for excitation of the transducers. The resulting pressure transducer responses are flat to frequencies in excess of 1000 Hz within ±2% in magnitude and ±2 degrees in phase.

Strain Isolation

Airfoil strain may induce transducer strain, thus resulting in an apparent pressure signal. To achieve effective strain isolation, Kulite was commissioned by NASA Lewis to conduct a transducer mounting study, reference 27. Potting the transducer in rubber was found to be effective: in tests conducted using one of the biconvex airfoils, blade tip deflections of ± 0.05 cm were found to have no measurable effect on the transducer output to 0.01 millivolt, which corresponds to about 0.07 kPa (0.01 psi).

As described in reference 25, one of the biconvex airfoils was oscillated at high frequencies to verify its structural integrity. Specifically, based on the test data, a

conservative estimate of the maximum airfoil tip deflection at 600 Hz oscillation frequency is 0.003 cm. Combining this with the results of the strain isolation study, the response to airfoil strain will be negligible.

Acceleration Effects

During the oscillating cascade experiments, the pressure transducers are subject to accelerations which may produce apparent pressure signals. Although uncoated transducers are highly insensitive to acceleration effects [28], the RTV-coated transducers require calibration. To quantify this effect, the instrumented airfoil was oscillated at several frequencies under no-flow or zero mean velocity conditions. Figure 2.5 shows the amplitude response of six coated transducers as a function of the acceleration magnitude. The response is a linear function of the acceleration, implying that the acoustic response, which will vary with the airfoil velocity magnitude, is dominated by the acceleration response. Significant amplitude variation is apparent among the transducers, and is probably due to differences in rubber coating thicknesses. The phase angle variation with frequency was linear and small for all the transducers.

Temperature Drift

Since only the fluctuating pressure will be measured by the transducers, only the slope of the transducer calibration curve is required. This is determined by static calibration at the ambient temperature, but the test section air static temperature may be as much as 60 degrees C less than the ambient. Because the rated maximum change in sensitivity with temperature is ± 4.5% per 100 degrees C [28], the temperature drift effect is believed to be negligible.

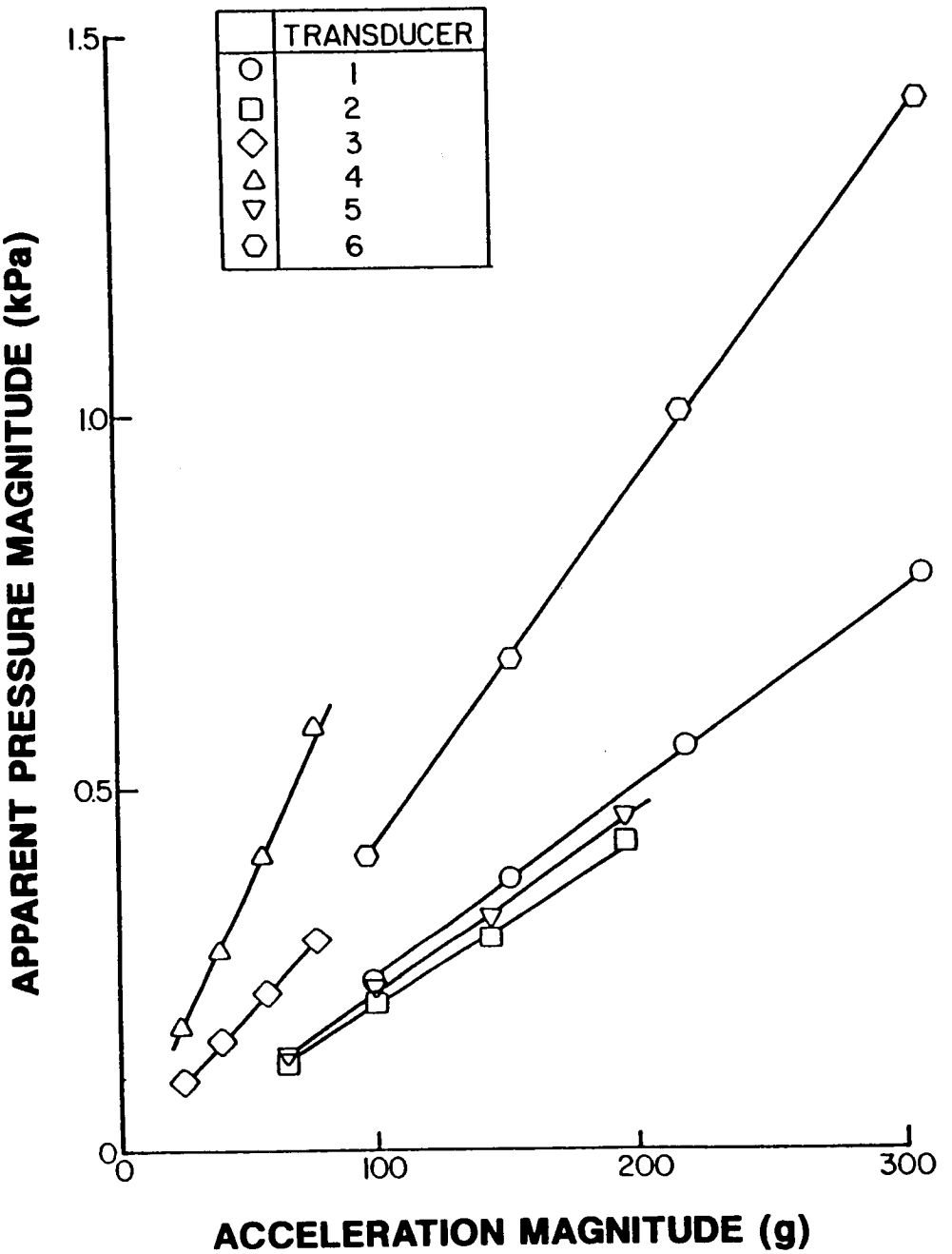

Figure 2.5 Dynamic pressure transducer acceleration response

2.3.2 Airfoil Motion Measurement

The time-variant position of the reference oscillating airfoil is determined by a capacitance-type proximity sensor which produces a voltage proportional to the air gap between the sensor and an adjacent object. This sensor is positioned to face a six cycle sinusoidally-shaped cam which is mounted on the airfoil drive camshaft When the camshaft rotates, the proximity sensor produces a sinusoidal output voltage which is in phase with the reference airfoil motion. In addition, an electro-optical displacement meter is available to directly track the motion of the reference airfoil by focusing on the edge of the airfoil. These two measurement systems were found to agree within ± 3 degrees in phase. This indicates that deformations in the drive system, which would cause phase errors in the measurement of the reference airfoil motion, are negligible, and verifies the displacement meter alignment relative to the cam.

CHAPTER 3

DATA ACQUISITION AND ANALYSIS

The steady-state data of interest are the cascade inlet Mach number, inlet static pressure, exit static pressure and the airfoil surface pressure distribution. A conventional pressure measurement system using Scanivalves and computerized data acquisition and reduction is used to quantify these data. Signals which quantify the pertinent unsteady data, the airfoil motion and the airfoil surface unsteady pressure distribution, are recorded on FM tape and analyzed using a computer-based digitization and Fourier analysis system.

3.1 Acquisition and Analysis of Steady-State Data

A computer-based data acquisition and analysis system is used to monitor the cascade operating conditions and acquire and reduce the steady-state data. Microprocessors control the digitization of the data and feed the data to a remotely-located minicomputer which stores data for later analysis and also calculates various quantities pertintent to operation of the wind tunnel. Post-processing of steady-state data is done on a VAX computer.

Steady-state pressures are determined using three 48 port Scanivalve units which operate in parallel. Time-average static pressures are determined from the average of at least 30 readings. The mean inlet static pressure, $\overline{p}_{in}$, is the spatial average of the time-average wall static pressures as determined from the taps located upstream

of the airfoils. The inlet total pressure, p_t, is determined by a remotely-located barometer. The inlet Mach number is then calculated from the isentropic relation

$$M = \sqrt{\frac{2}{\gamma - 1}\left(\left(\frac{p_t}{\overline{p}_{in}}\right)^{\frac{\gamma-1}{\gamma}} - 1\right)}. \qquad (3.1)$$

The airfoil surface steady pressure coefficient is defined as

$$\overline{C}_p(x) = \frac{\overline{p}_{in} - p_0(x)}{\frac{1}{2}\rho V^2} \qquad (3.2)$$

where p_0 is the time-average airfoil surface static pressure at the chordwise coordinate x, and ρ and V are the inlet values of density and velocity. The mean exit static pressure, $\overline{p}_{ex}$, is the spatial average of the time-average wall static pressures as determined from the taps located downstream of the airfoils.

3.2 Acquisition and Analysis of Unsteady Data

Figure 3.1 is a schematic of the unsteady data acquisition and analysis system. Within the test cell, the dynamic pressure transducers are connected to strain gage bridge amplifiers. The amplifier gains are set to 200 to boost the signals, initially in the millivolt range, to levels on the order of 1 volt, thus minimizing the effects of low-level noise acquired during transmission of the signals. The airfoil motion signal is of a sufficiently high amplitude, on the order of 1 volt, that it does not require amplification before transmission. High-pass filters remove d.c. components in the signals and instrumentation amplifiers are used to adjust the signal levels to be compatible with the recording equipment. To determine the frequency of oscillation, the airfoil motion signal passes through a frequency counter. Monitor oscilloscopes are used to observe the unsteady signals during the experiments. A fourteen channel FM tape recorder is used for permanent analog recording of the data.

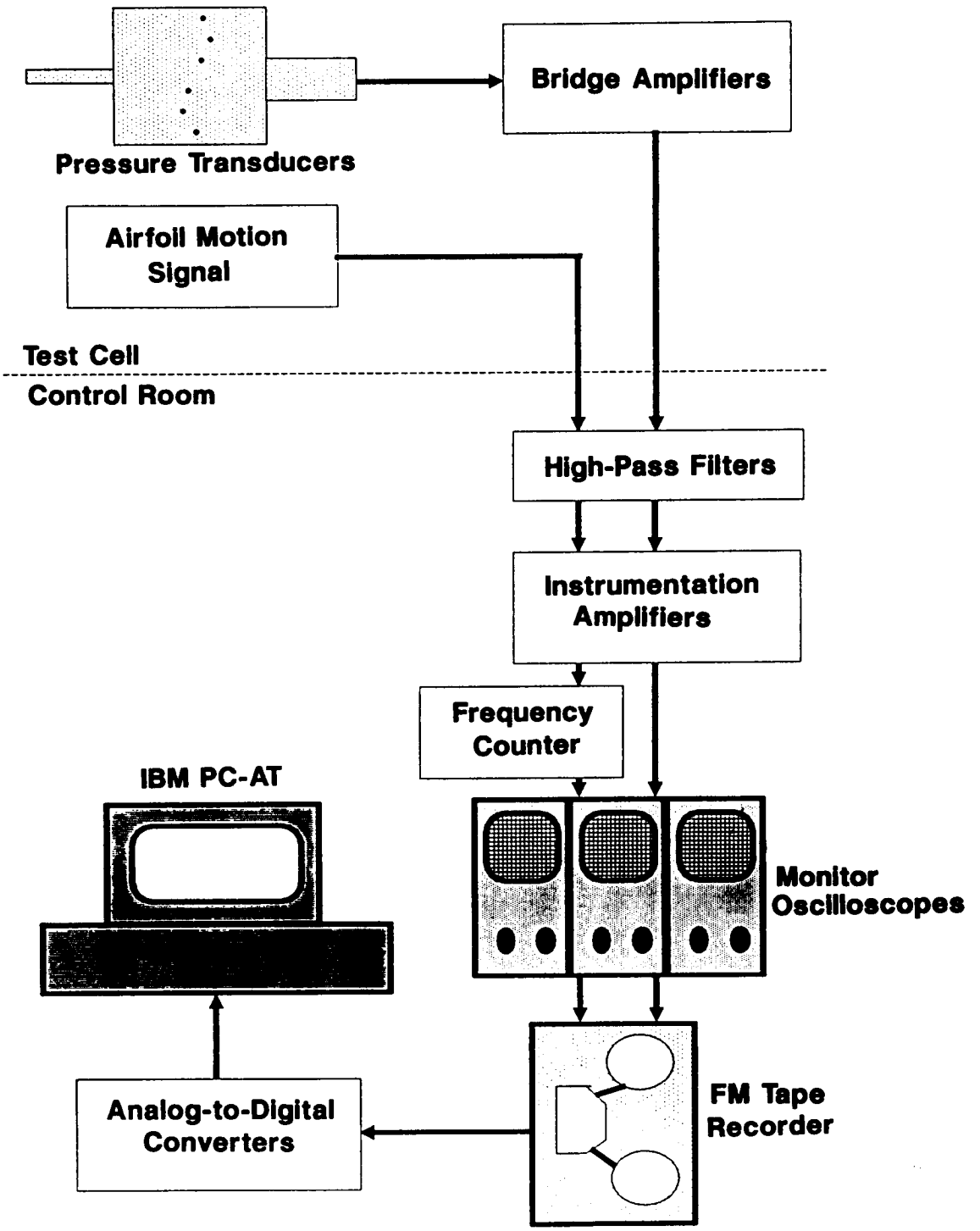

Figure 3.1 System for acquisition and analysis of unsteady data

Analysis of the unsteady data centers around an IBM PC-AT computer-based system which controls digitization of the recorded signals, executes the data analysis software and drives the post-processing plotting devices. Two Gould 8 channel waveform recorders are used to digitize the signals. Each channel has its own 8 bit A/D converter and 32 kilobyte memory buffer, thus enabling simultaneous digitization and storage of 16 channels of unsteady data. Gould software controls transfer of the data from the waveform recorders to the computer through an IEEE-488 interface and provides graphics for viewing the digitized signals.

The unsteady data acquisition system is calibrated using sinusoidal signals input to all the channels simultaneously starting at the high pass filters. These signals are recorded on tape and then digitized and reduced using the computerized data reduction system. It was found that small phase shifts of several degrees may occur depending upon the tape recorder track, and these calibration results are incorporated into the data reduction system. In addition, the accuracy of the 8 bit A/D converters was compared to a 12 bit FFT analyzer using unsteady pressure signals. Negligible differences between the two systems were found in the calculated first harmonic components of the signals.

The unsteady pressure signals are digitized at rates sufficient to capture at least three harmonics of the oscillation frequency, with 32,768 (32k) samples taken per channel. An averaging technique, Bartlett's procedure [29], is then applied to the data. This procedure is shown in Figure 3.2 for one channel of data: the data are divided into contiguous blocks, each block typically with 2048 samples, and then Fourier decomposed (using an algorithm of Bergland and Dolan [30]). To minimize errors due to spectral leakage, an interpolation scheme, as described in Appendix A, is used to determine the first harmonic pressure of each block of data. Each block's first harmonic pressure is referenced to the airfoil motion by subtracting the phase

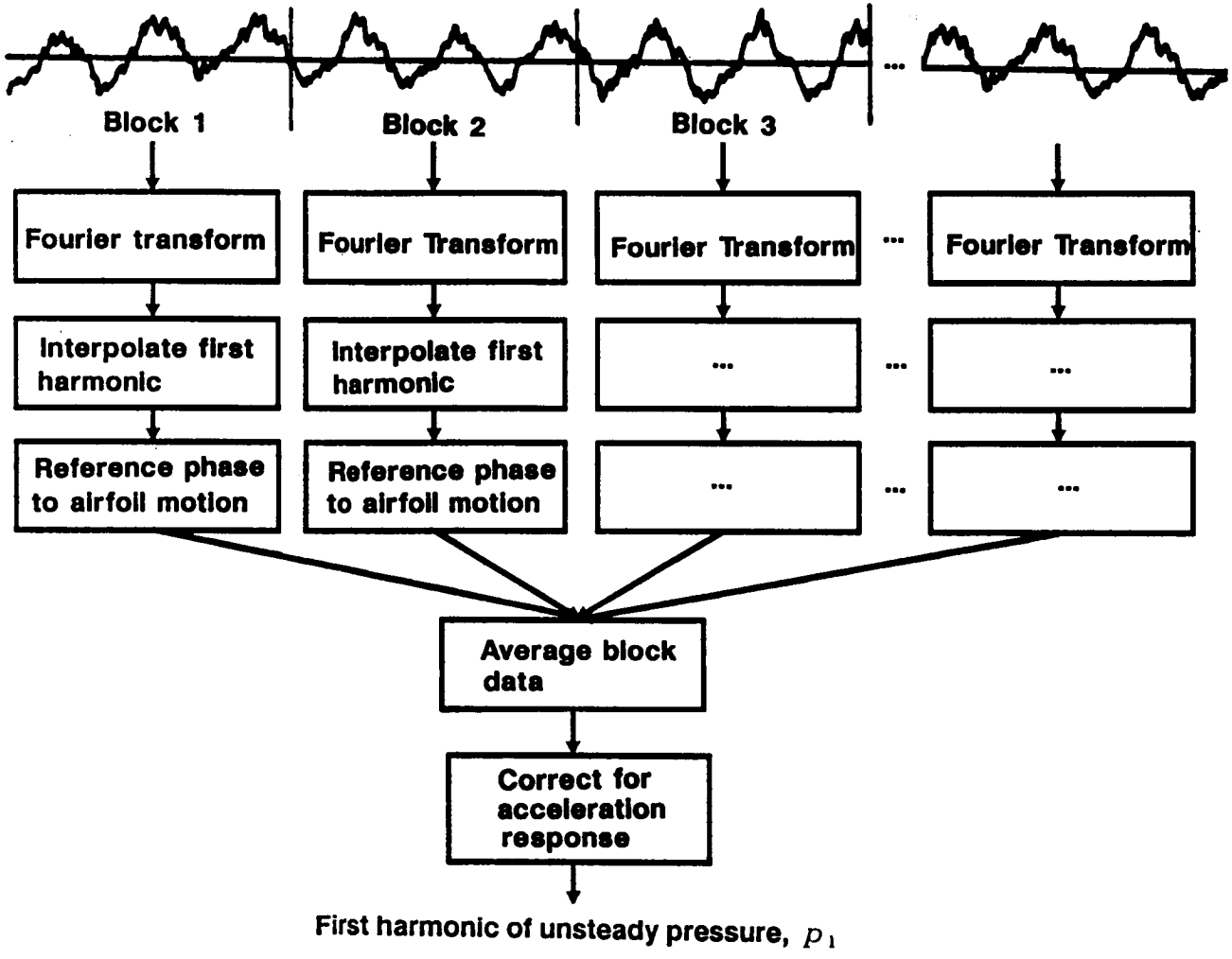

Figure 3.2 Processing of unsteady pressure data

of the first harmonic motion signal of the corresponding block from it. Once all of the blocks from a channel are decomposed in this manner, the block results are averaged and the complex-valued acceleration response is subtracted vectorally.

To demonstrate this data analysis technique, the time-dependent pressure transducer signals shown in Figure 3.3 and the corresponding airfoil motion signal are considered. The pressure signals are seen to be sinusoidal in nature with superimposed noise. The resulting averaged pressure spectra are characterized by a large spike at the oscillation frequency, 200 Hz, some small spikes at higher harmonics of the oscillation frequency, and other small spikes near 55 and 110 Hz caused by wind tunnel tones.

In these experiments, the airfoil motion is defined by the change in the incidence angle with time:

$$\alpha(t) = \alpha_0 + \alpha_1 Re\{e^{i\omega t}\} \tag{3.3}$$

where α_0 is the mean incidence angle, α_1 is the oscillatory amplitude of 1.2 degrees and ω is the frequency. The final unsteady pressure data are presented in the form of the complex-valued dynamic pressure coefficient

$$C_p(x) = \frac{p_1(x)}{\frac{1}{2}\rho V^2 \alpha_1} \tag{3.4}$$

where p_1 is the first harmonic of the airfoil surface static pressure, ρ and V are the inlet values of density and velocity, and α_1 is the torsional oscillation amplitude. The dynamic pressure difference coefficient is defined by

$$\Delta C_p = C_{pl} - C_{pu}. \tag{3.5}$$

The subscripts l and u refer to the airfoil lower and upper surfaces, respectively. These coefficients are referenced to the airfoil motion, with a positive phase corresponding to the unsteady pressure leading the airfoil motion.

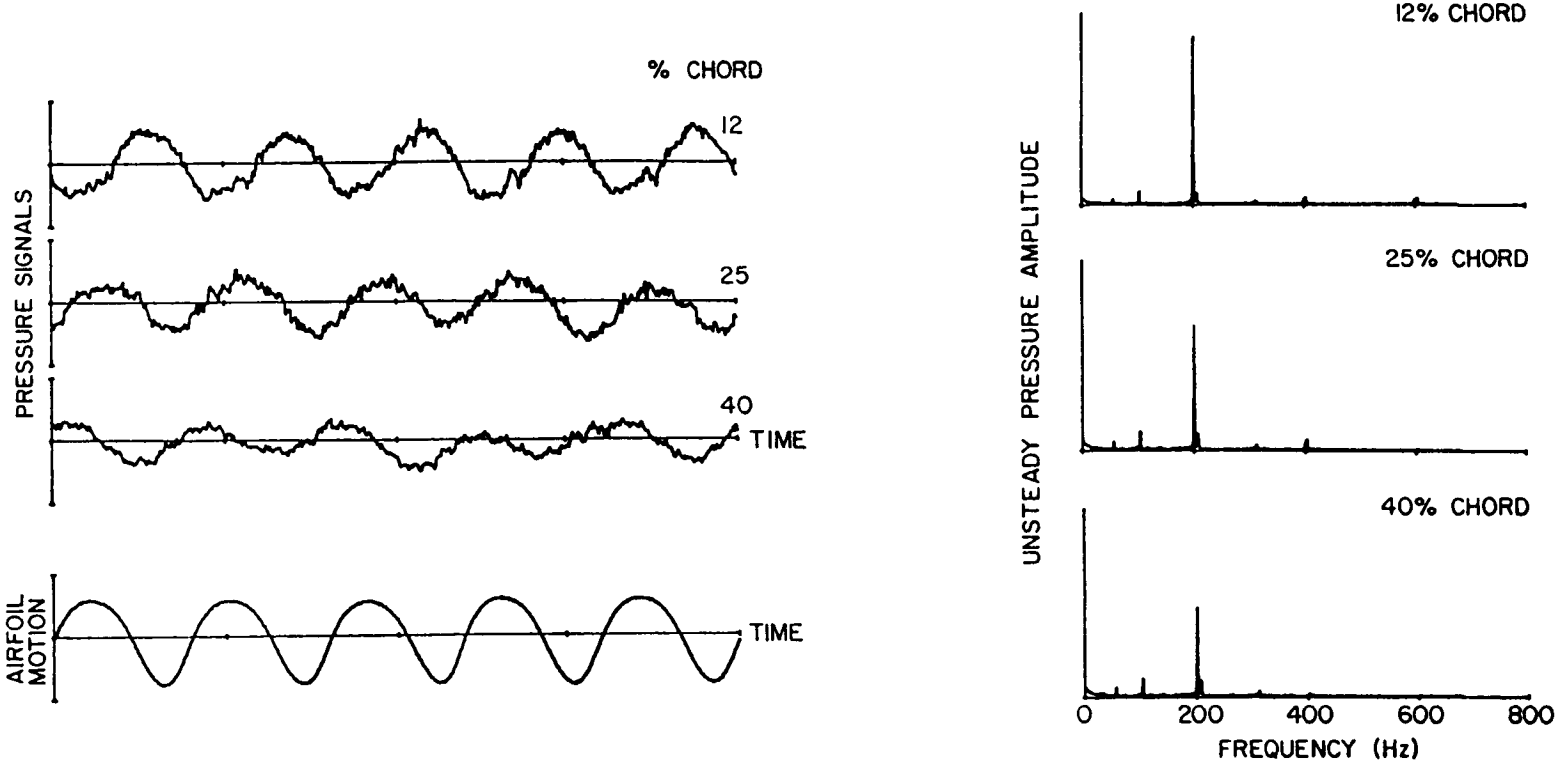

Figure 3.3 Time-variant signals and averaged pressure spectra

CHAPTER 4

EXPERIMENT RESULTS

The torsion mode oscillating cascade aerodynamics are experimentally investigated in both low and high solidity configurations which are summarized in Table 4.1. As the oscillating cascade aerodynamics are a function of the underlying mean flow field, several mean flow conditions are investigated for each cascade configuration.

For the low solidity cascade, there are two steady flow conditions, defined by inlet Mach numbers of 0.55 and 0.80 at 2 degrees incidence. With the instrumented (reference) airfoil in relative position 0 as defined in Figure 1.1, influence coefficient data are acquired on this airfoil with the airfoils in positions -2, -1, 0, 1 and 2 individually oscillating at reduced frequencies of 0.2 and 0.32 for the two inlet Mach numbers plus $k=0.45$ for $M=0.55$. Corresponding data are obtained from baseline experiments in which the airfoils are oscillating simultaneously at fixed interblade phase angle values of 0, 45, -45, 90, -90 and 180 degrees.

The high solidity configuration is investigated for incidence angles of 0 and 7 degrees at an inlet Mach number of 0.65 and at 7 degrees with an inlet Mach number of 0.80. Influence coefficient data are obtained for reduced frequencies of 0.185 and 0.32 at $M=0.8$, and 0.22 and 0.39 at $M=0.65$. Corresponding baseline data are obtained for all the airfoils oscillating simultaneously at fixed interblade phase angles of 0, 90 and -90 degrees.

Table 4.1 Airfoil and cascade geometry

AIRFOIL	
Type	biconvex, no camber
Surface radius of curvature	27.4 cm
Leading and trailing edge radii of curvature	0.025 cm
Chord, C	7.62 cm
Maximum airfoil thickness / chord	0.076
Elastic axis	midchord
Dynamic pressure transducer locations, % chord	12,25,40,60,75,88
LOW SOLIDITY CASCADE	
Number of airfoils	4
Airfoil spacing, S	11.72 cm
Solidity, C/S	0.65
Stagger angle, γ	45 degrees
Amplitude of torsional oscillation	1.2 degrees
HIGH SOLIDITY CASCADE	
Number of airfoils	9
Airfoil spacing, S	5.86 cm
Solidity, C/S	1.3
Stagger angle, γ	53 degrees
Amplitude of torsional oscillation	1.2 degrees

The steady airfoil surface pressure distributions are presented first followed by a detailed study of the cascade unsteady aerodynamics. The dynamic periodicity of the cascade with all airfoils oscillating is investigated, then unsteady pressure influence coefficients are presented. These influence coefficient data are then summed to predict the unsteady aerodynamics of an equivalent cascade with all airfoils oscillating at a fixed interblade phase angle. The resulting unsteady pressure distributions are correlated with the data for all airfoils oscillating and the predictions from the linearized unsteady cascade analysis of reference 3. To aid the interpretation of these results, the limitations of conducting oscillating cascade experiments in a finite, linear cascade are considered.

4.1 Steady State Aerodynamics

4.1.1 Low Solidity Cascade

To demonstrate periodicity at the steady state conditions, airfoil surface pressure distributions are obtained for multiple passages in the low solidity cascade. For example, Figure 4.1 presents data at an inlet Mach number of 0.55 for the center cascade passage and the two adjacent passages. Good cascade periodicity is readily apparent, with the only significant differences found at the leading edge of the airfoil upper surface. Using the methods of reference 31, a 95% confidence interval of ± 0.01 is calculated for the airfoil surface steady pressure coefficients.

Figure 4.2 presents the $M = 0.80$ steady flow airfoil surface pressure coefficient distributions for the cascade center passage. For both inlet Mach numbers, the upper surface distribution peaks near the leading edge and the pressure difference tends toward zero near the trailing edge. There is negligible loading beyond 50% of chord. Darkened symbols in Figure 4.2 indicate multiple spanwise data used to indicate spanwise uniformity of the steady flow (see Figure 2.3 for the pressure tap locations).

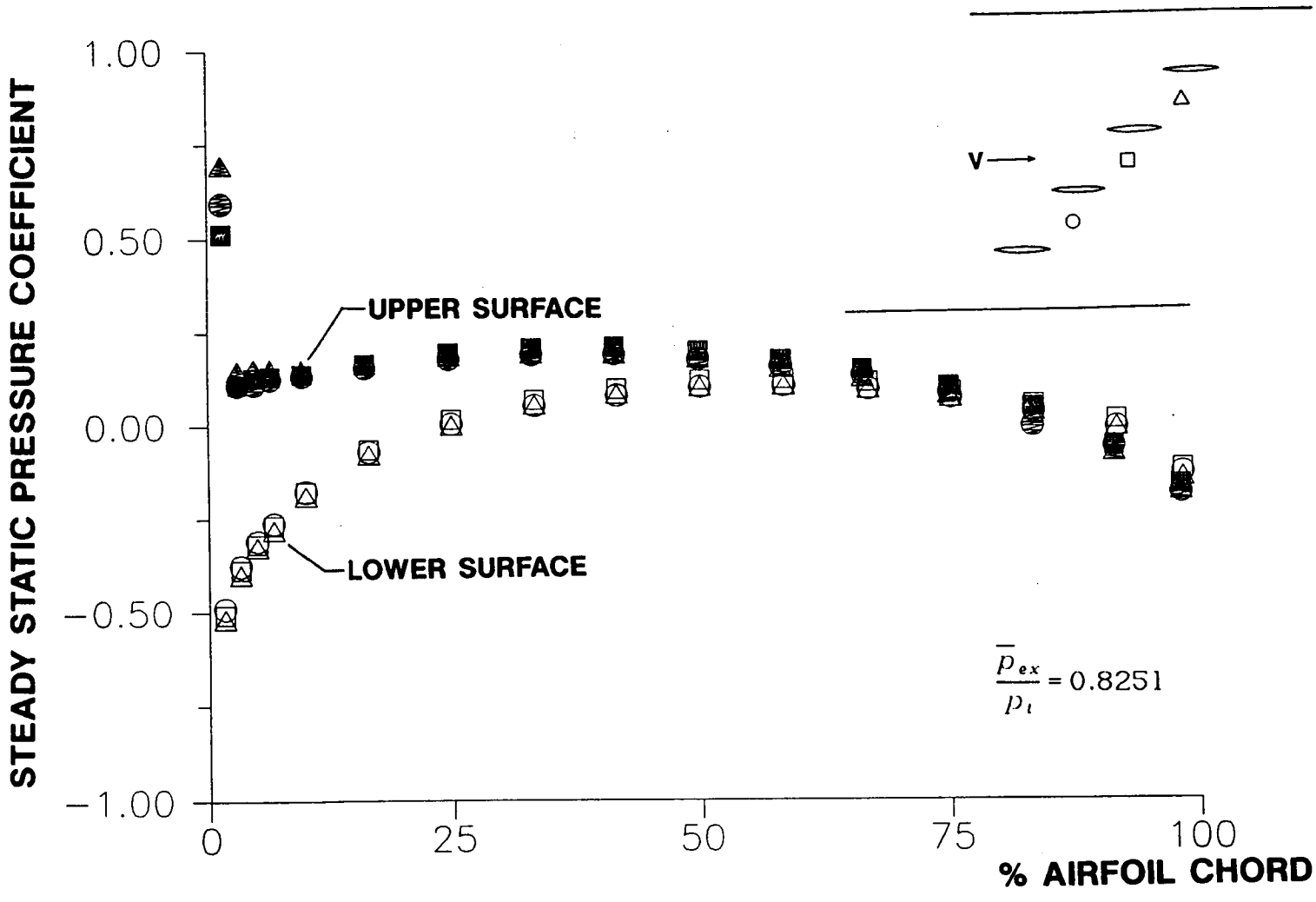

Figure 4.1 Periodicity of airfoil surface steady pressure coefficient distributions, low solidity cascade, M = 0.55

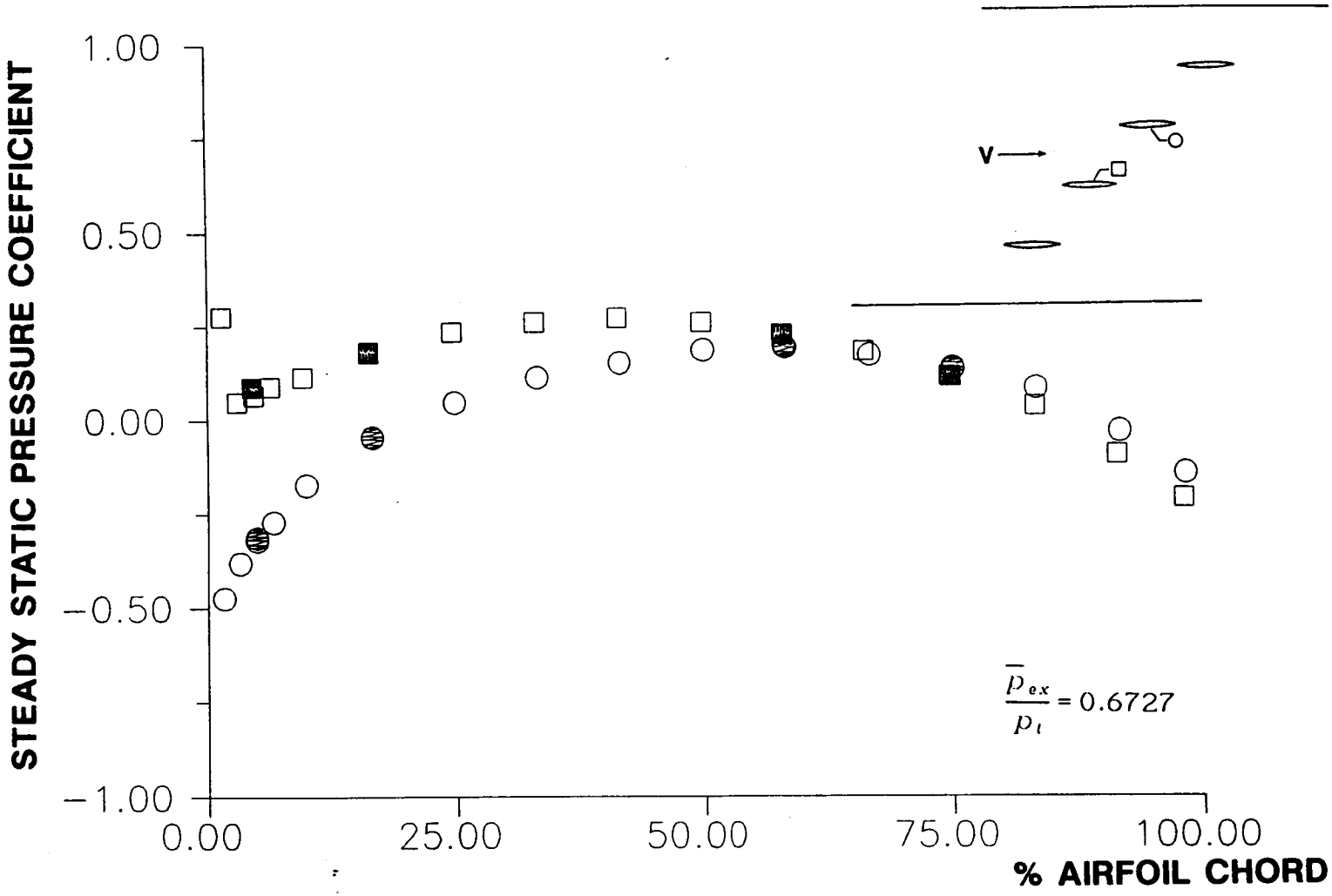

Figure 4.2 Airfoil surface steady pressure coefficient distribution, low solidity cascade, M=0.80

As shown, departure from two-dimensionality is negligible except for small differences near the leading edge on the upper surface. Since $\overline{C}_p = 0.435$ for sonic flow with an inlet Mach number of 0.8, the flow field is entirely subsonic for both inlet Mach numbers.

4.1.2 High Solidity Cascade

The steady flow airfoil surface pressure coefficient distributions for the center airfoil of the high solidity cascade are shown in Figure 4.3 for 0.65 inlet Mach number and zero incidence, and Figure 4.4 for inlet Mach numbers of 0.65 and 0.8 at 7 degrees incidence. The zero incidence condition exhibits airfoil loading due to cascade effects. At 7 degrees incidence, the pressure coefficient distributions are nearly identical for the two Mach numbers, with loading only on the airfoil forward half. At an inlet Mach number of 0.8, the sonic value of $\overline{C}_p$ is 0.435. Thus there is a small region of supersonic flow on the upper surface near the leading edge. This supersonic region is terminated by a small shock, as determined from schlieren images. At an inlet Mach number of 0.65, the sonic value of $\overline{C}_p$, 1.01, is slightly exceeded on the upper surface at the leading edge. In this case, no shock was detected.

4.2 Unsteady Aerodynamics

4.2.1 Data for All Airfoils Oscillating

In this section, summaries of the unsteady data obtained for the low and high solidity cascade configurations are presented. In addition, for the low solidity cascade, the cascade dynamic periodicity is investigated for a range of experiment parameters. First, however, the theoretical modes of oscillating cascade wave propagation as predicted by linearized unsteady aerodynamic theory are considered.

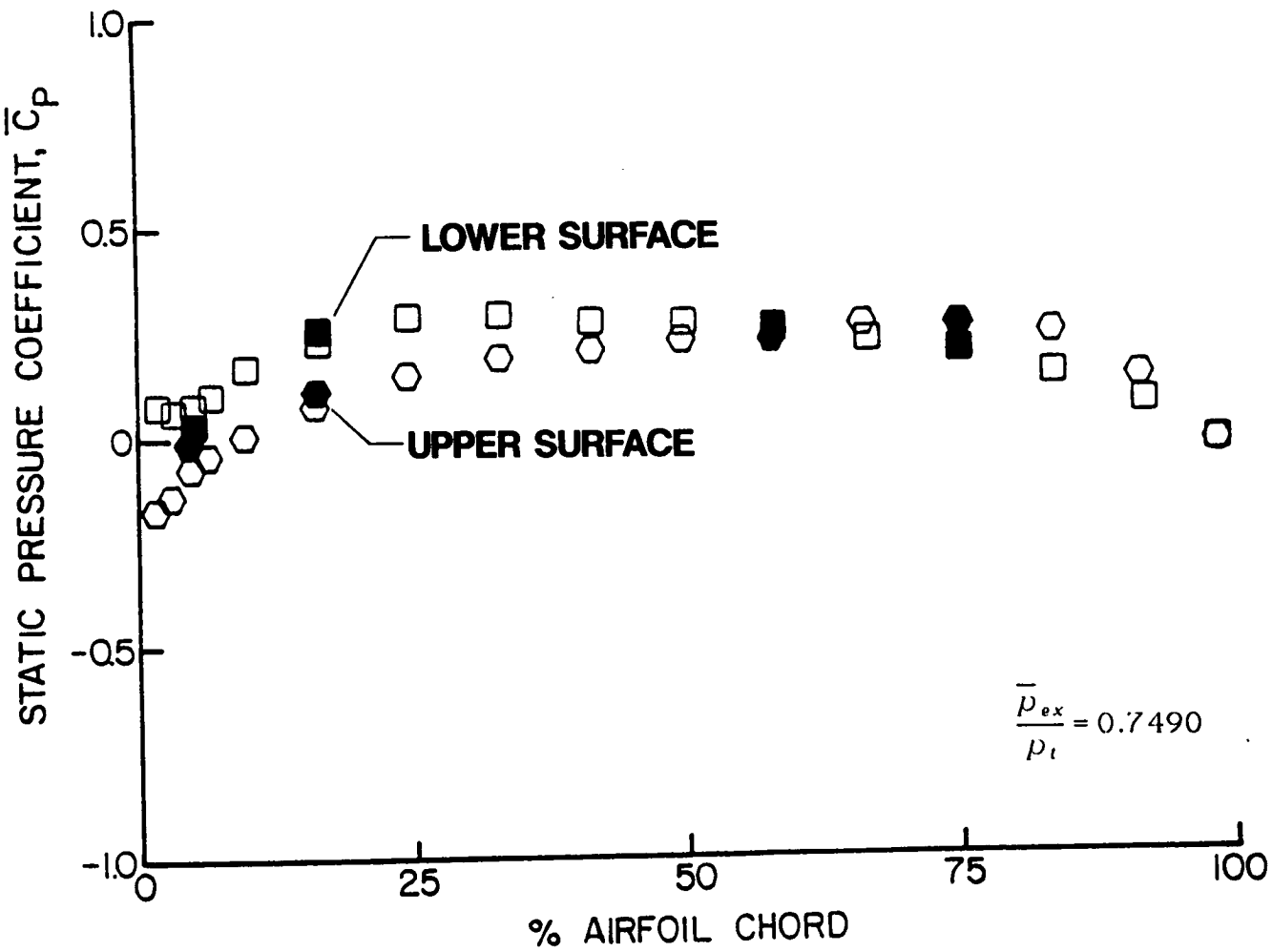

Figure 4.3 Airfoil surface steady pressure coefficient distribution, high solidity cascade, M = 0.65, 0 degrees incidence

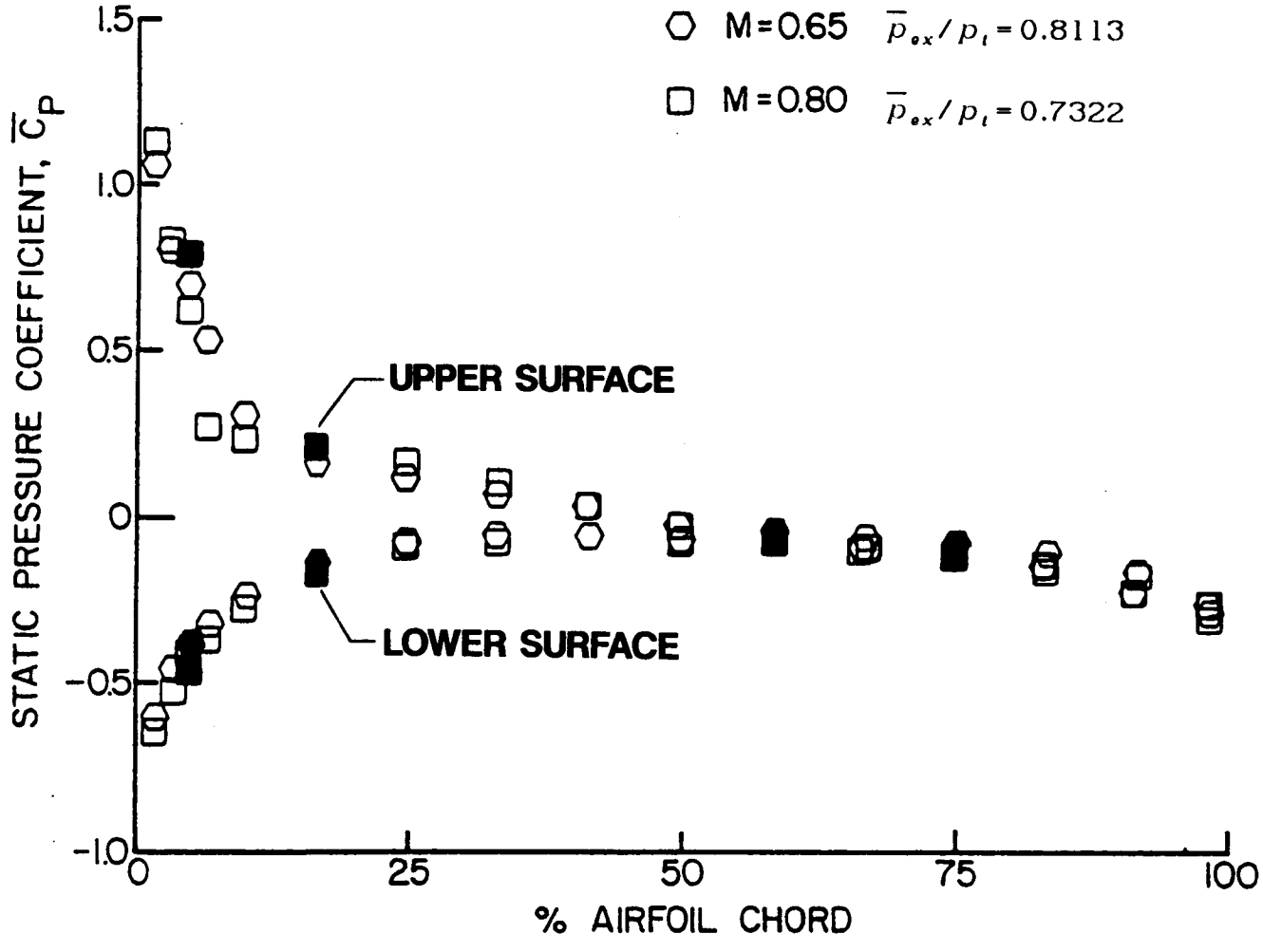

Figure 4.4 Airfoil surface steady pressure coefficient distributions, high solidity cascade, M = 0.65 and M = 0.80, 7 degrees incidence

The unsteady aerodynamic conditions investigated herein may result in the oscillating cascade operating at several modes of wave propagation as predicted by linearized unsteady aerodynamic theory. An oscillating cascade in subsonic flow is said to be superresonant when pressure disturbances are produced which propagate away from the cascade unattenuated. When the pressure disturbances decay exponentially with distance from the cascade, the behavior is called subresonant. A point where subresonant and superresonant regions meet is called an acoustic resonance. At an acoustic resonance, the pressure disturbances propagate energy along the blade row. An expression for the resonant interblade phase angle, Equation 4.1, is derived in Appendix C.

$$\beta_r^* = \frac{2kMS}{c(1-M^2)}\left(M\sin(\alpha_0+\gamma) \pm \sqrt{1-M^2\cos^2(\alpha_0+\gamma)}\right) \qquad (4.1)$$

Figure 4.5 illustrates typical subsonic cascade behavior in terms of these wave propagation modes. Acoustic resonances at positive and negative interblade phase angle values, β_r^*, bracket the wave-propagating superresonant region which always includes $\beta=0$ when $0<M<1$ and $k>0$. When $\beta>\beta_r^+$ or $\beta<\beta_r^-$, the cascade is subresonant and the waves decay. Table 4.2 lists the resonant interblade phase angle values for the both cascade configurations.

Low Solidity Cascade

Airfoil surface unsteady pressure distributions were obtained in the low solidity configuration (C/S=0.65) for interblade phase angle values of 0, 45, -45, 90, -90 and 180 degrees at reduced frequencies of 0.2 and 0.32 for M=0.80, and those reduced frequencies and also 0.45 for M=0.55.

For a linear cascade to be a valid model of an axial-flow turbomachine blade row, the cascade must exhibit good passage-to-passage periodicity for both steady and unsteady flow. Low solidity cascade data for all airfoils oscillating simultaneously were obtained by instrumenting the two airfoil surfaces defining the center passage

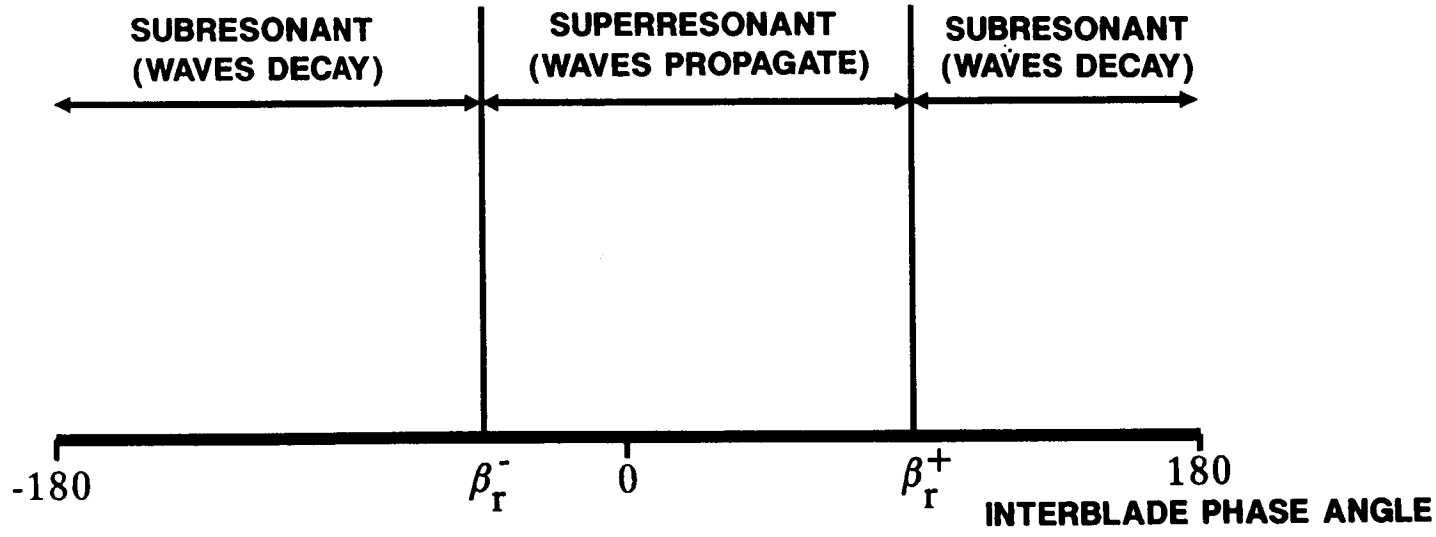

Figure 4.5 Modes of subsonic oscillating cascade wave propagation

Table 4.2 Resonant values of interblade phase angle

(a) Low solidity cascade

M	k		
	0.20	0.32	0.45
0.55	-14.6, 37.0	-23.3, 59.1	-32.8, 83.2
0.80	-19.8, 111.5	-31.7, 178.4	

(b) High solidity cascade, M=0.65

M	α_0	k=0.22	k=0.39
0.65	0°	-8.8, 31.4	-15.5, 55.7
	7°	-8.4, 32.9	-14.8, 58.4

(c) High solidity cascade, M=0.80

M	α_0	k=0.185	k=0.32
0.80	7°	-8.1, 58.3	-14.0, 100.8

of the cascade. The unsteady periodicity of the low solidity cascade was determined by subsequently positioning the instrumented airfoils to measure the opposite surfaces of the two center airfoil positions, thus giving dynamic pressure measurements for both surfaces of the two most centrally located airfoils.

First harmonic unsteady pressure coefficient periodicity data are presented in Figure 4.6 for M = 0.55, k = 0.2 and β = -45 degrees. To simplify the discussion of these results, the two instrumented airfoils will be referred to as A and B as labeled in the figure. The data indicate that the dynamic periodicity is excellent in both magnitude and phase for the airfoil upper surface. Although the lower surface periodicity is good, the magnitudes tend to be larger on airfoil A, particularly over the forward half of the airfoil. There are also small but noticeable phase differences in the midchord region on the lower surface.

To aid the presentation of the periodicity data, new quantities are defined. The dynamic periodicity magnitude and phase differences, δC_p and $\delta\phi$, are defined in Equations 4.2 and 4.3.

$$\delta C_p = \frac{|C_p^A| - |C_p^B|}{\frac{1}{2}(|C_p^A| + |C_p^B|)_{x/C=0.12}} \tag{4.2}$$

$$\delta\phi = \phi_p^A - \phi_p^B \tag{4.3}$$

Figure 4.7 presents the dynamic periodicity data determined from the data presented in Figure 4.6. Both the excellent upper surface periodicity and defects in the lower surface periodicity are now clearly revealed.

The oscillating cascade periodicity is now investigated as a function of the interblade phase angle using the quantities δC_p and $\delta\phi$. Reduced frequency crossplots of the periodicity data for M = 0.55, k = 0.2 and 0.45 are presented in Figures 4.8 through 4.13 for the various interblade phase angle values. Beginning with $\beta = 0°$, Figure 4.8, the dynamic periodicity is generally poor, regardless of reduced frequency,

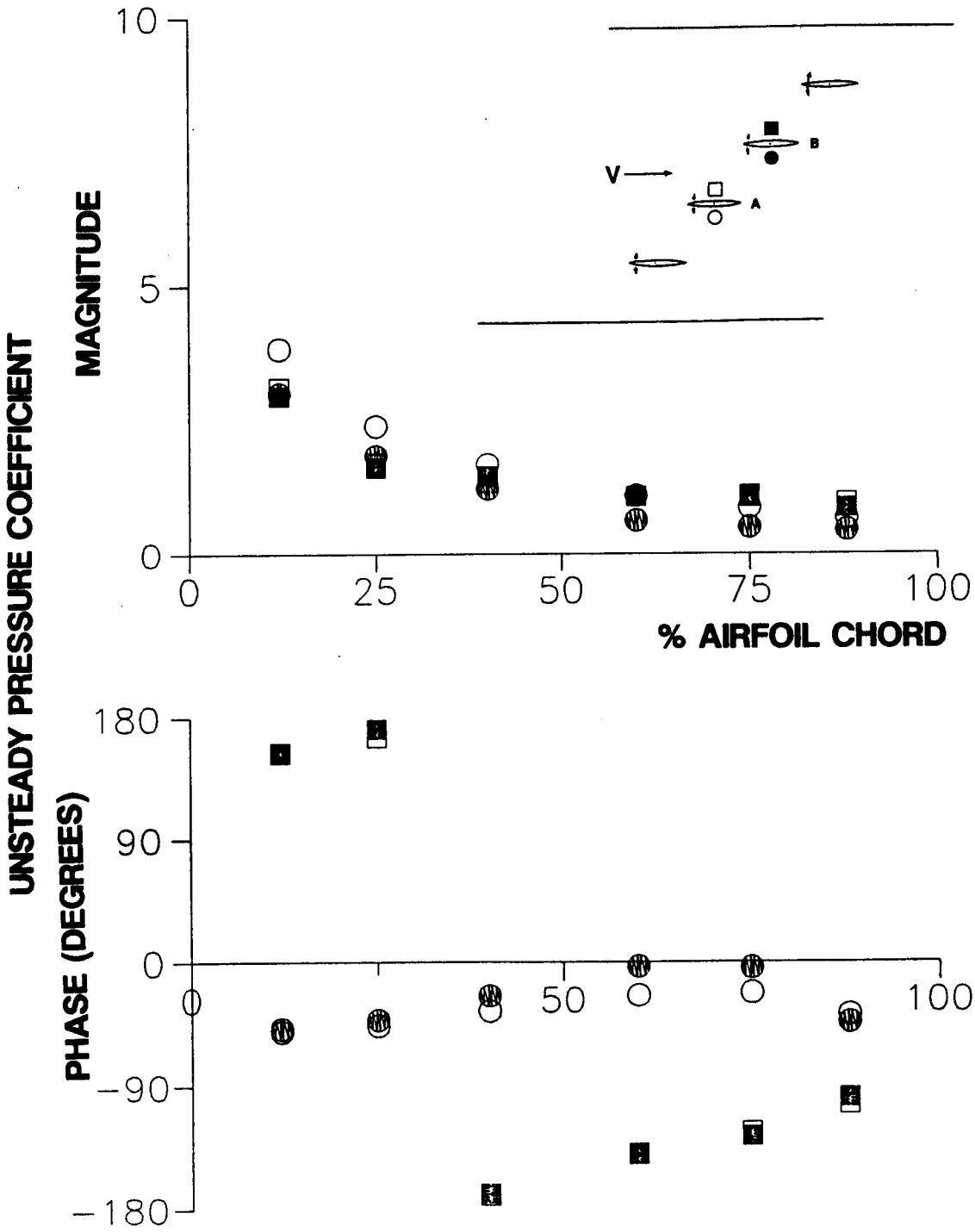

Figure 4.6 Dynamic periodicity of the low solidity cascade, M=0.55, k=0.20, β=-45 degrees

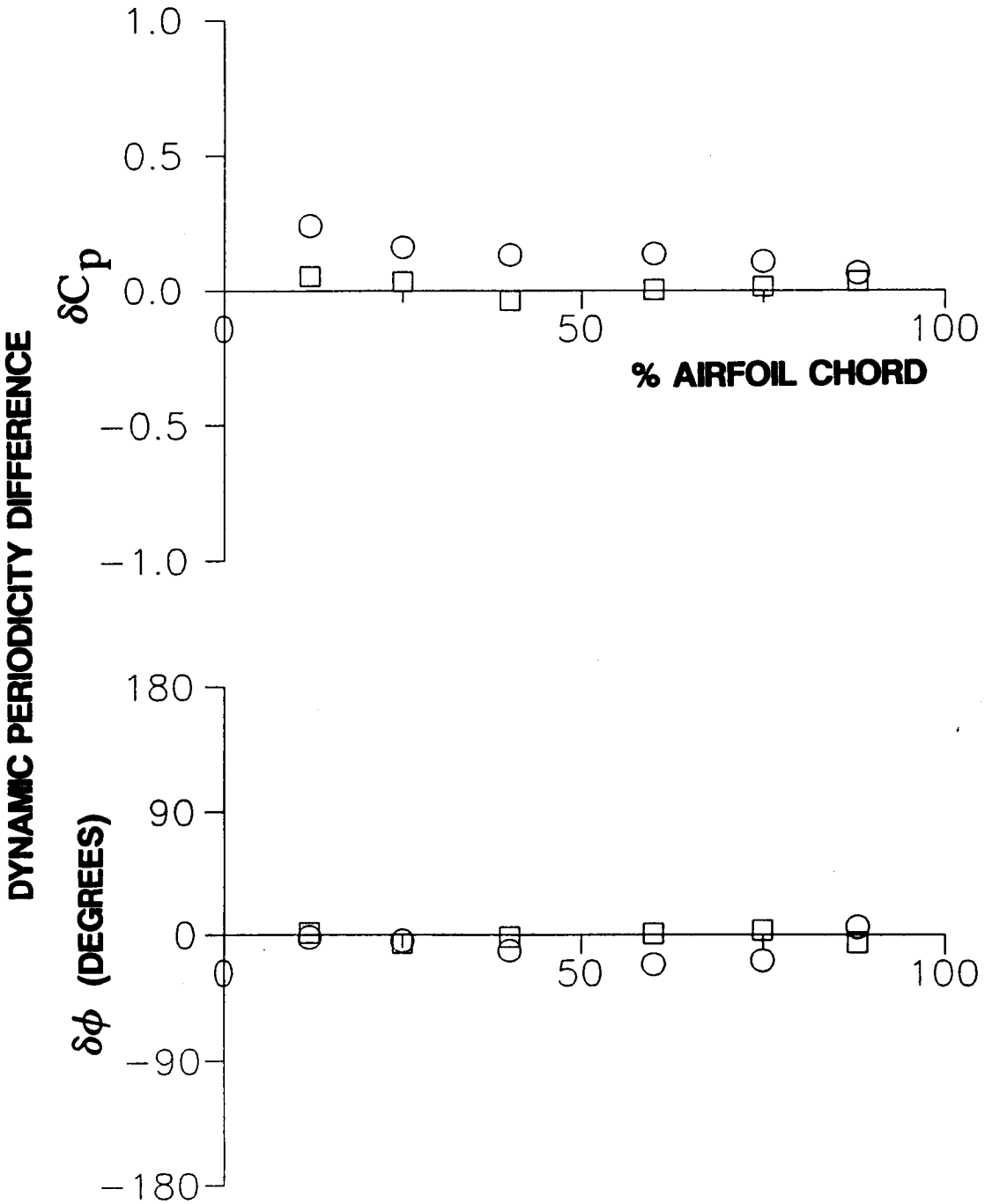

Figure 4.7 Dynamic periodicity difference, low solidity cascade, M=0.55, k=0.20, β=-45 degrees

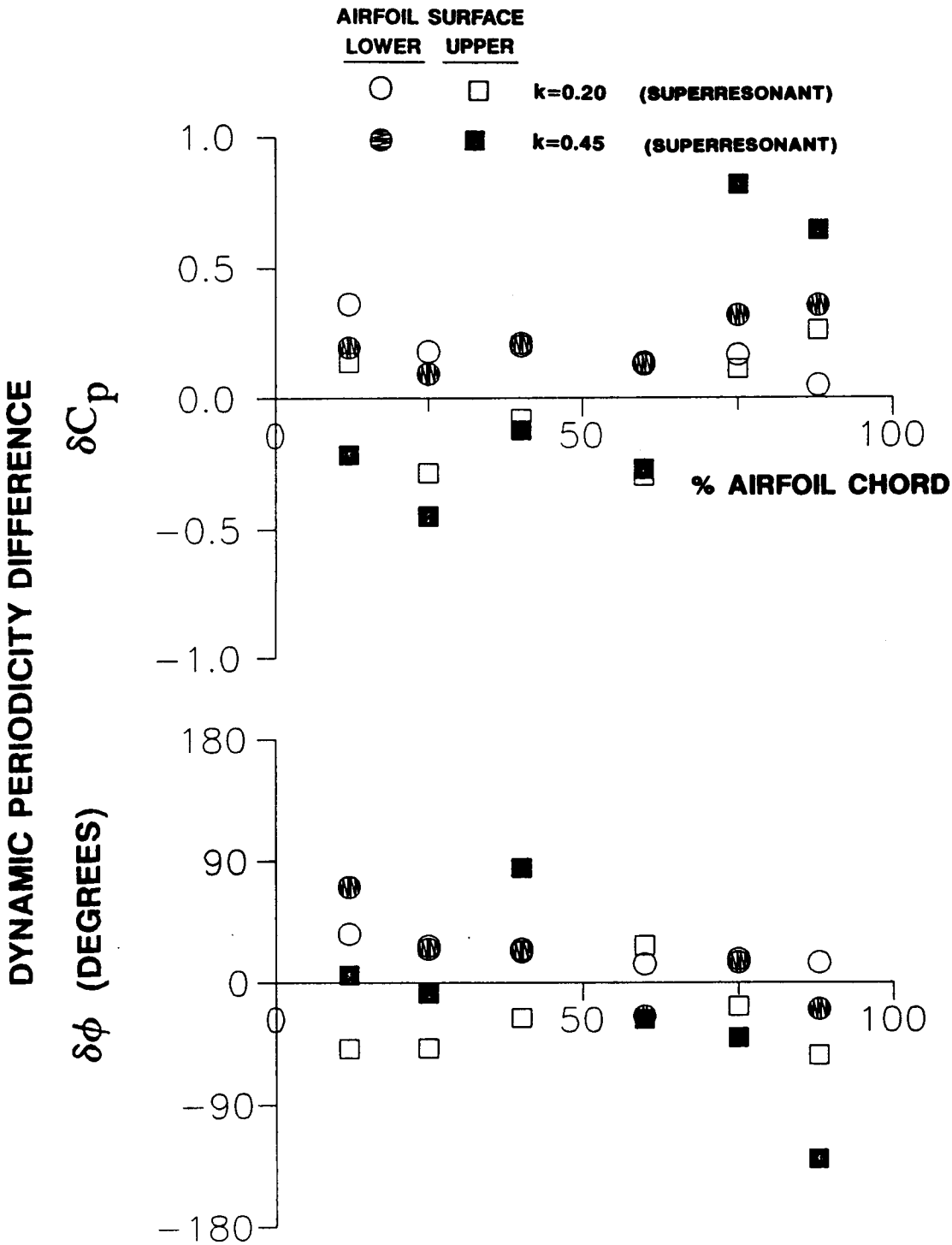

Figure 4.8 Reduced frequency crossplot of dynamic periodicity difference, low solidity cascade, M = 0.55, β = 0 degrees, k = 0.20 and 0.45

in both magnitude and phase for these superresonant conditions. Reduced frequency affects the dynamic periodicity when $\beta = 45°$, Figure 4.9: the periodicity is fairly good for the subresonant oscillations of k = 0.2, except for some large phase differences at 60 and 75% of chord, but poor for k = 0.45 (superresonant), which has large magnitude differences on both airfoil surfaces. In contrast, the periodicity is much better for $\beta = -45°$ for the two values of k, both of which are subresonant, Figure 4.10. When $\beta = 90°$, the periodicity is poor for both subresonant conditions, Figure 4.11. In this case, only the lower surface periodicity for k = 0.45 is respectable. When $\beta = -90°$, Figure 4.12, dynamic periodicity is generally good for the subresonant lower reduced frequency except for the upper surface magnitude at 12% of chord. Increasing k to 0.45 (also subresonant) results in reasonably good periodicity except at 60% of chord. Finally, for out-of-phase oscillations (subresonant), Figure 4.13, the magnitude differences are fairly small, especially for k = 0.2, but the phase differences are not small for that value of reduced frequency. In contrast, the phase differences are usually small for k = 0.45.

To summarize these dynamic periodicity data, the periodicity is largely a function of the predicted cascade wave propagation mode: cascade dynamic periodicity is relatively good for subresonant oscillations but poor for superresonant oscillations. However, subresonance does not guarantee good dynamic periodicity: dynamic periodicity is poor for $\beta = 90°$, a subresonant interblade phase angle for both values of reduced frequency shown in Figure 4.11.

Similar trends are found for M = 0.80 and reduced frequencies of 0.2 and 0.32, Figures 4.14 through 4.19. Periodicity is relatively good for subresonant oscillations, interblade phase angles of -45, -90 and 180 degrees, but poor for superresonant oscillations, interblade phase angle values of 0, 45 and 90 degrees. An exception is $\beta = -45°$ and k = 0.32, a subresonant condition with poor dynamic periodicity.

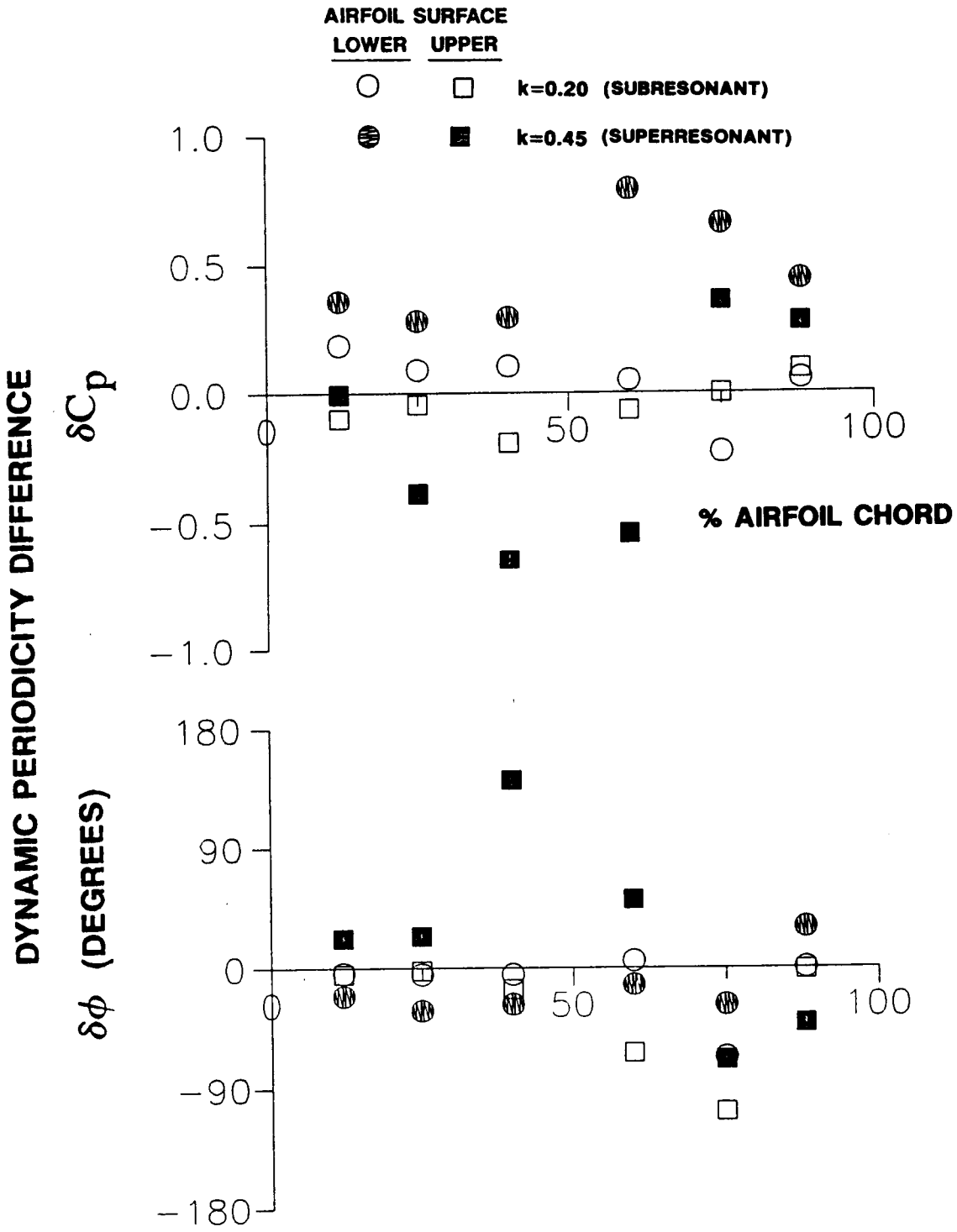

Figure 4.9 Reduced frequency crossplot of dynamic periodicity difference, low solidity cascade, M=0.55, β=45 degrees, k=0.20 and 0.45

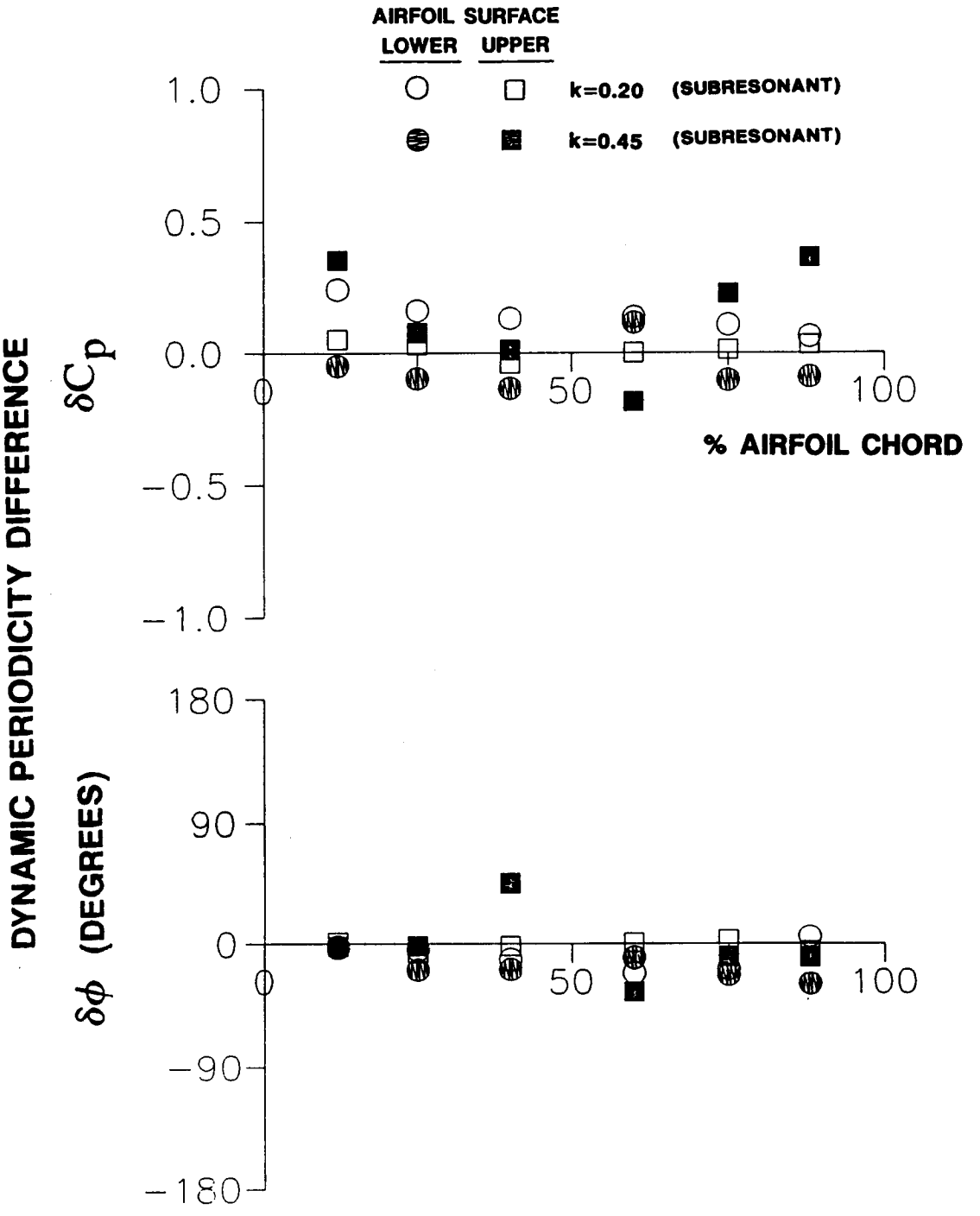

Figure 4.10 Reduced frequency crossplot of dynamic periodicity difference, low solidity cascade, M = 0.55, β = -45 degrees, k = 0.20 and 0.45

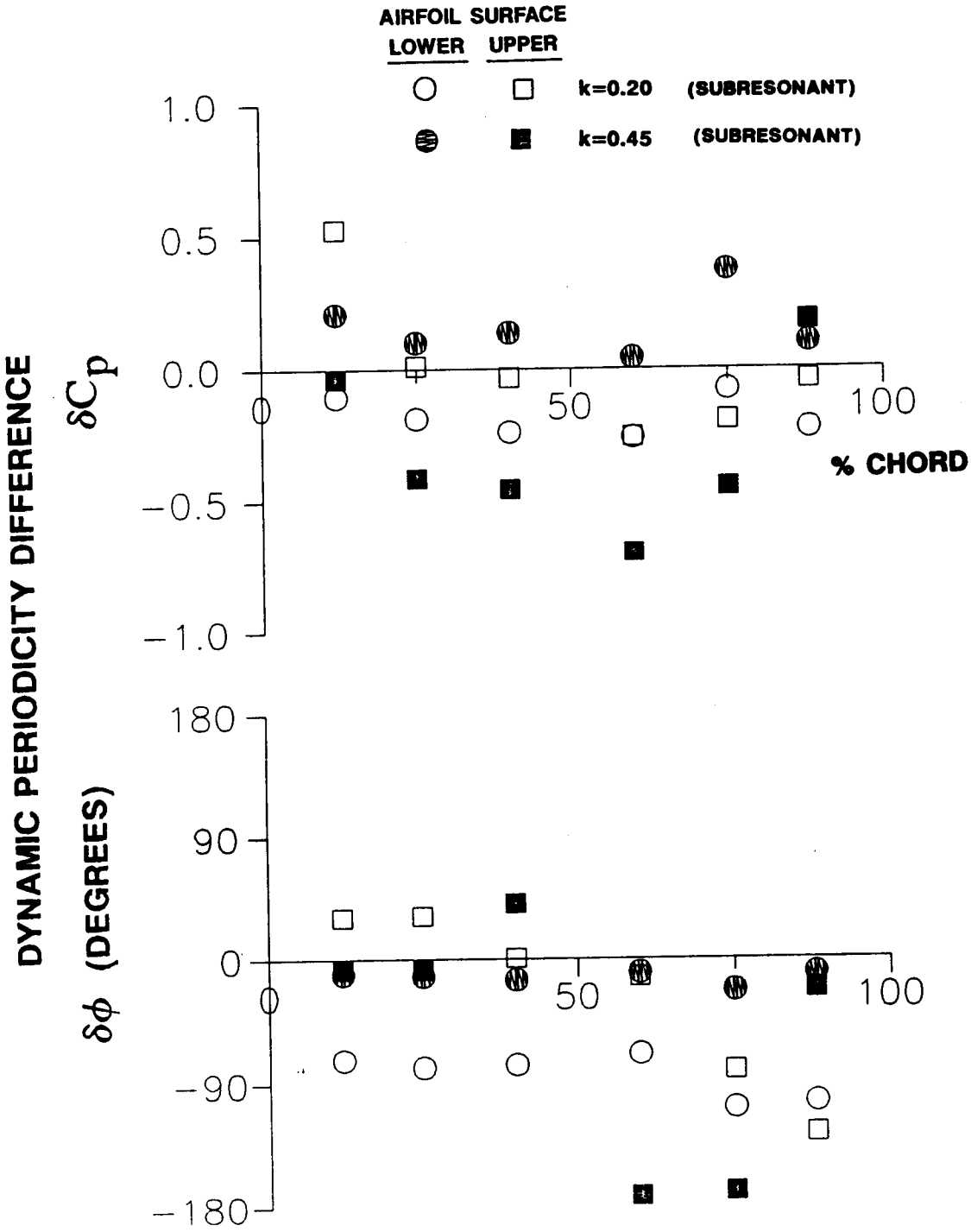

Figure 4.11 Reduced frequency crossplot of dynamic periodicity difference, low solidity cascade, M=0.55, β=90 degrees, k=0.20 and 0.45

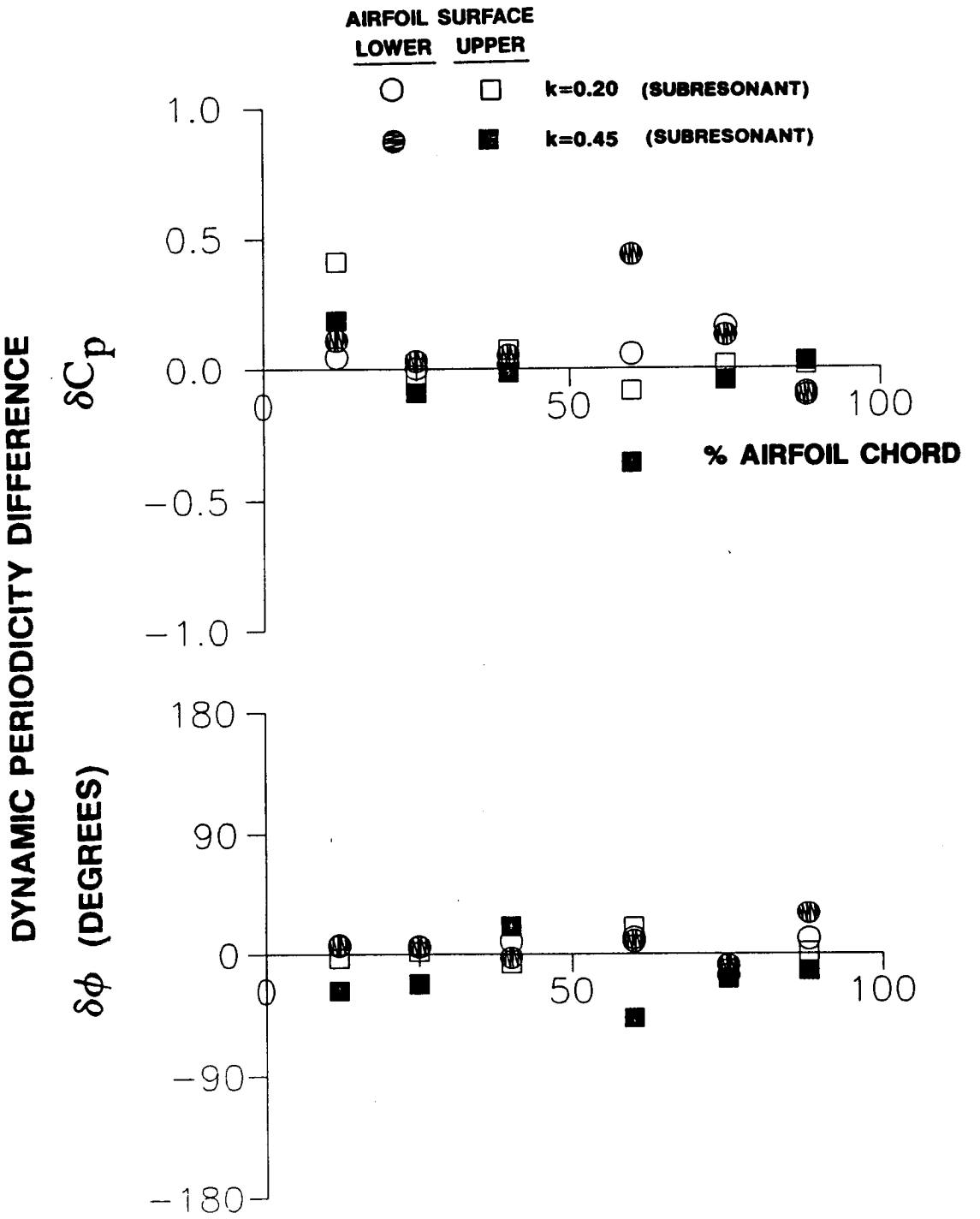

Figure 4.12 Reduced frequency crossplot of dynamic periodicity difference, low solidity cascade, M = 0.55, β = -90 degrees, k = 0.20 and 0.45

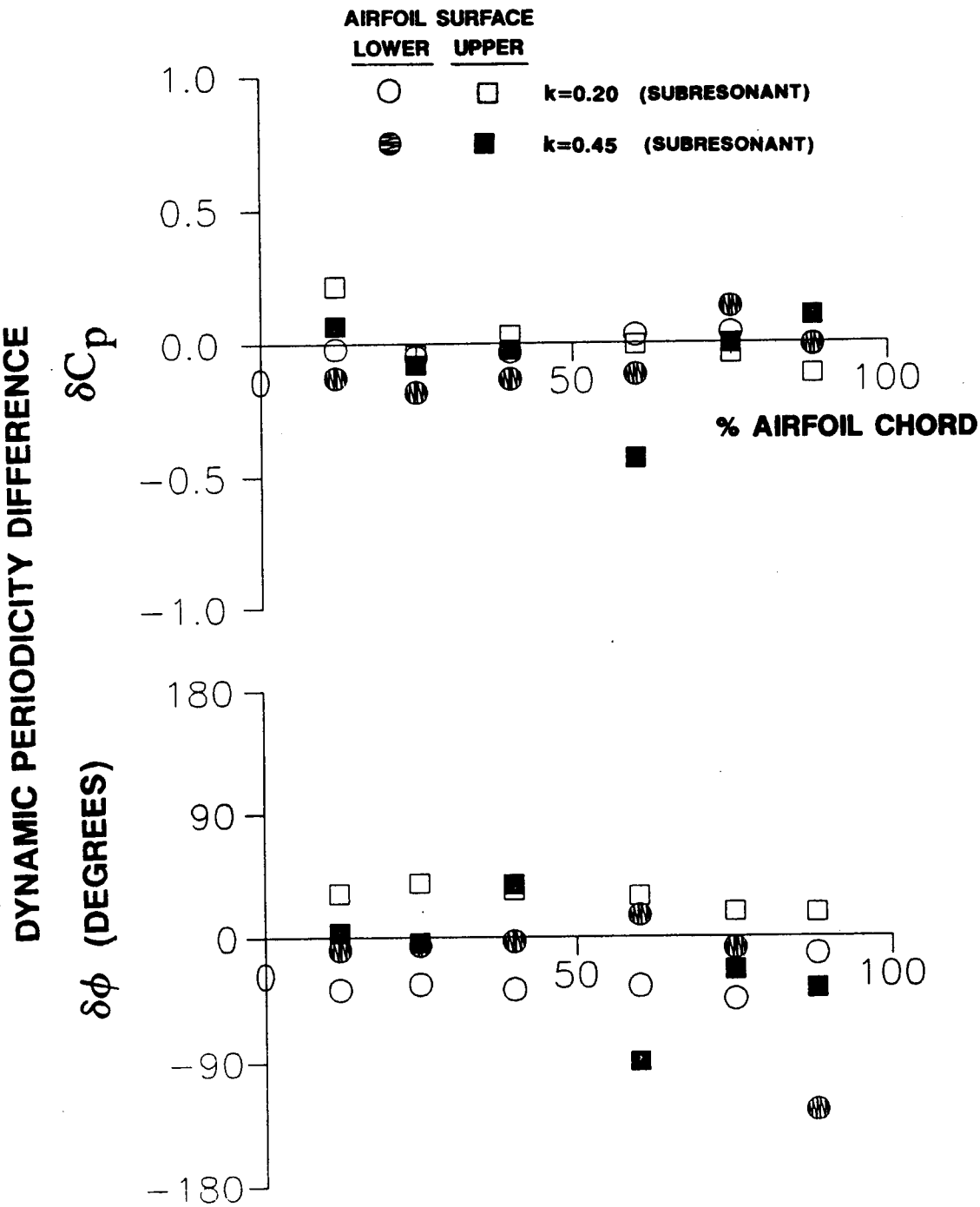

Figure 4.13 Reduced frequency crossplot of dynamic periodicity difference, low solidity cascade, M = 0.55, β = 180 degrees, k = 0.20 and 0.45

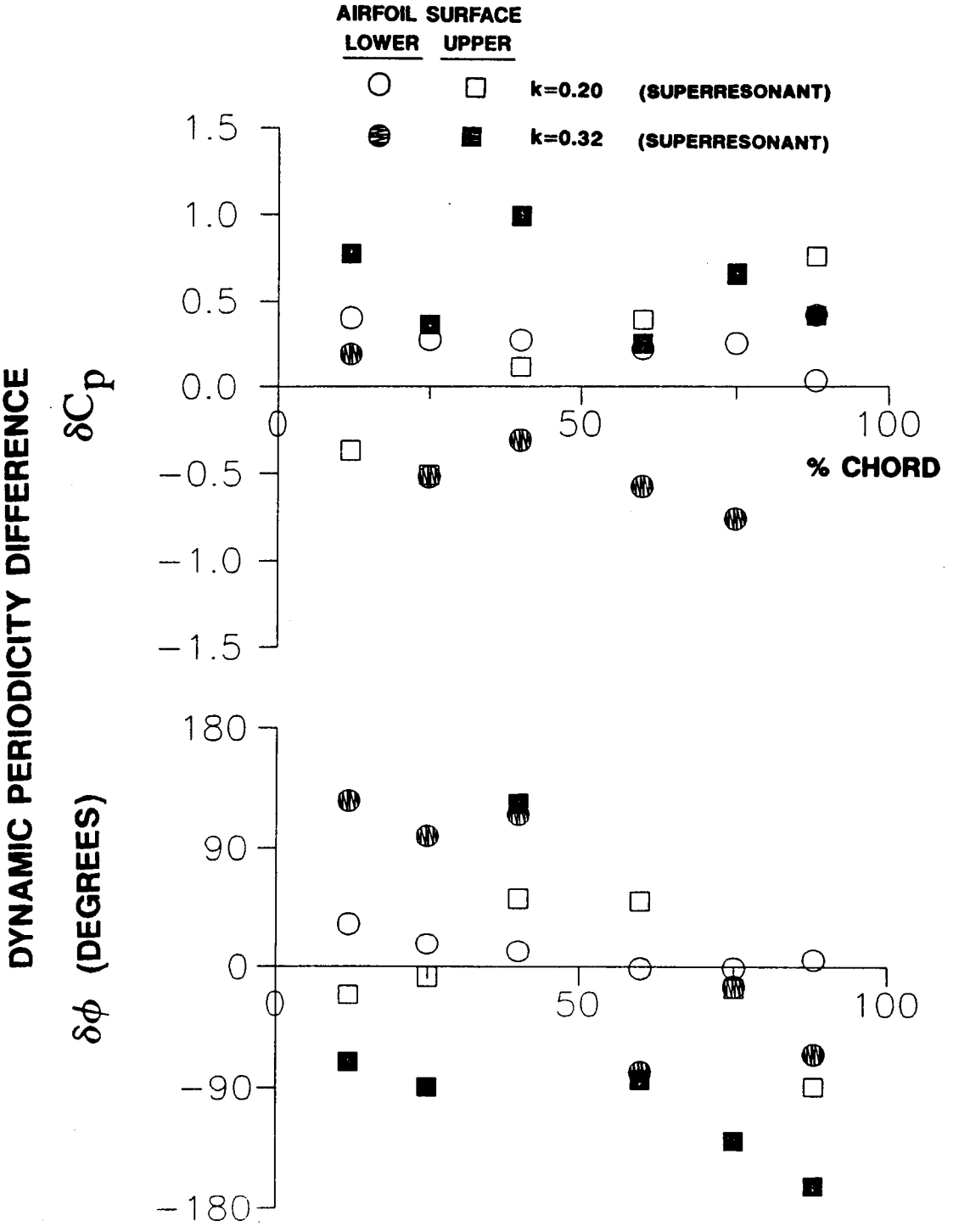

Figure 4.14 Reduced frequency crossplot of dynamic periodicity difference, low solidity cascade, M = 0.80, β = 0 degrees, k = 0.20 and 0.32

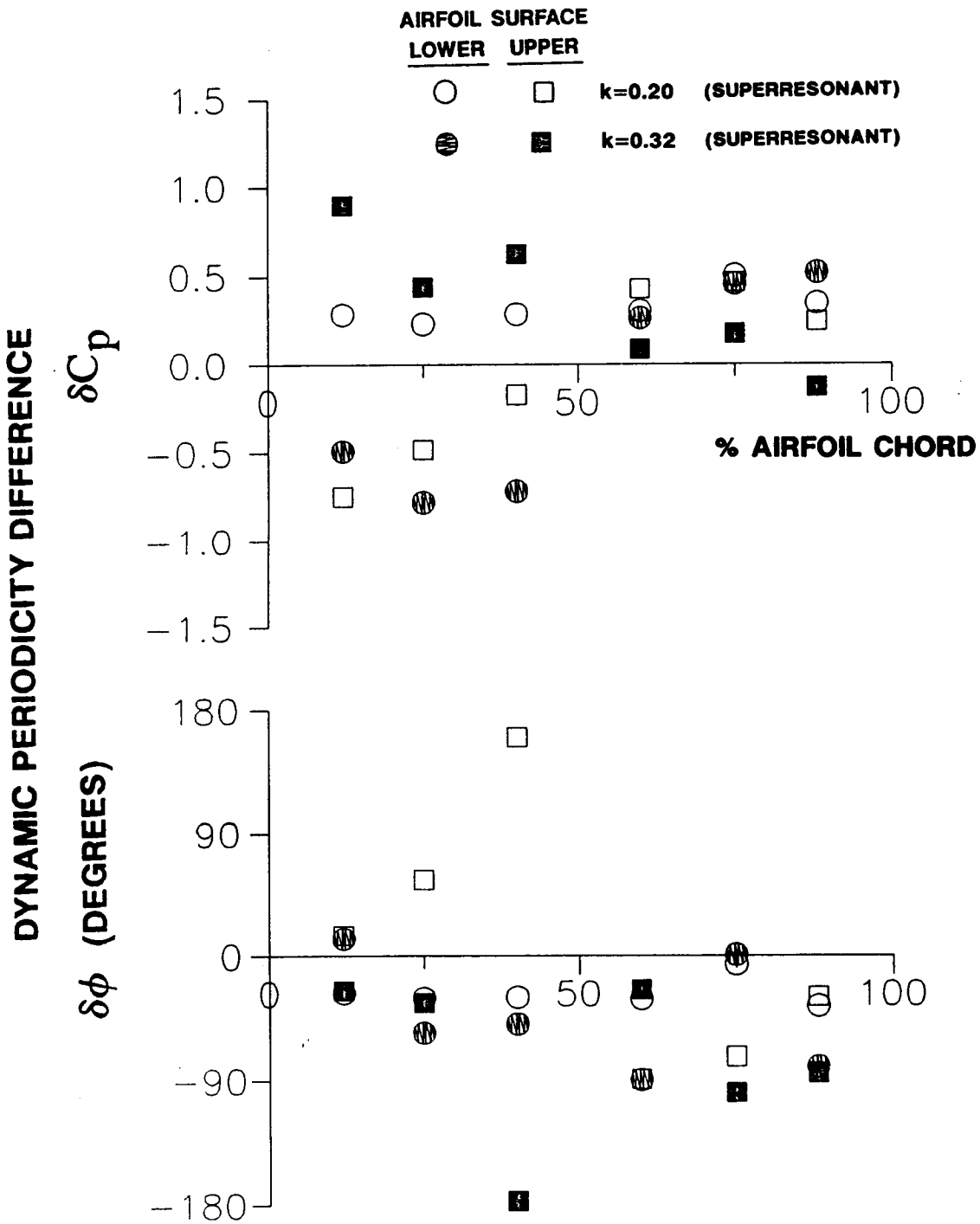

Figure 4.15 Reduced frequency crossplot of dynamic periodicity difference, low solidity cascade, M=0.80, β=45 degrees, k=0.20 and 0.32

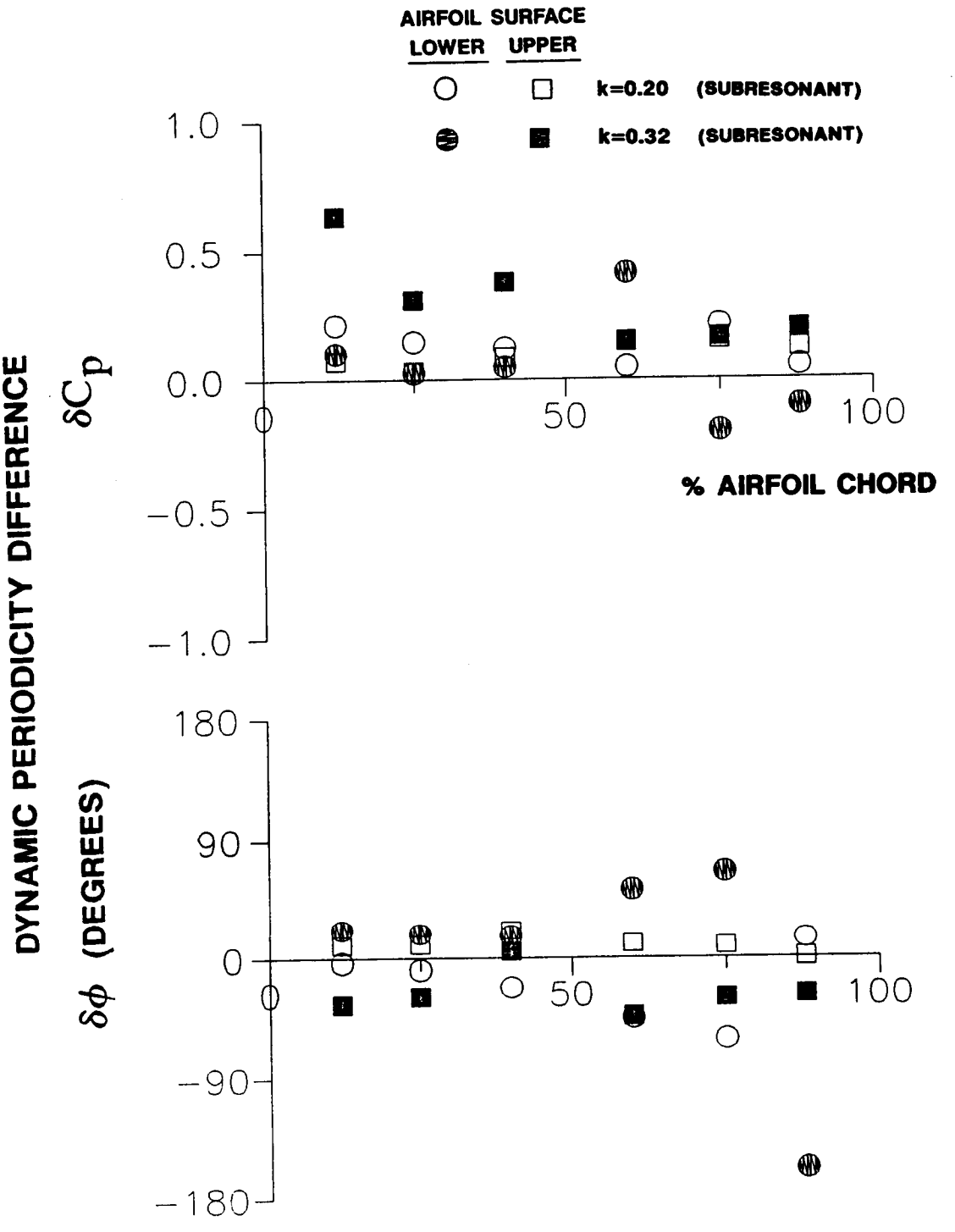

Figure 4.16 Reduced frequency crossplot of dynamic periodicity difference, low solidity cascade, M = 0.80, β = -45 degrees, k = 0.20 and 0.32

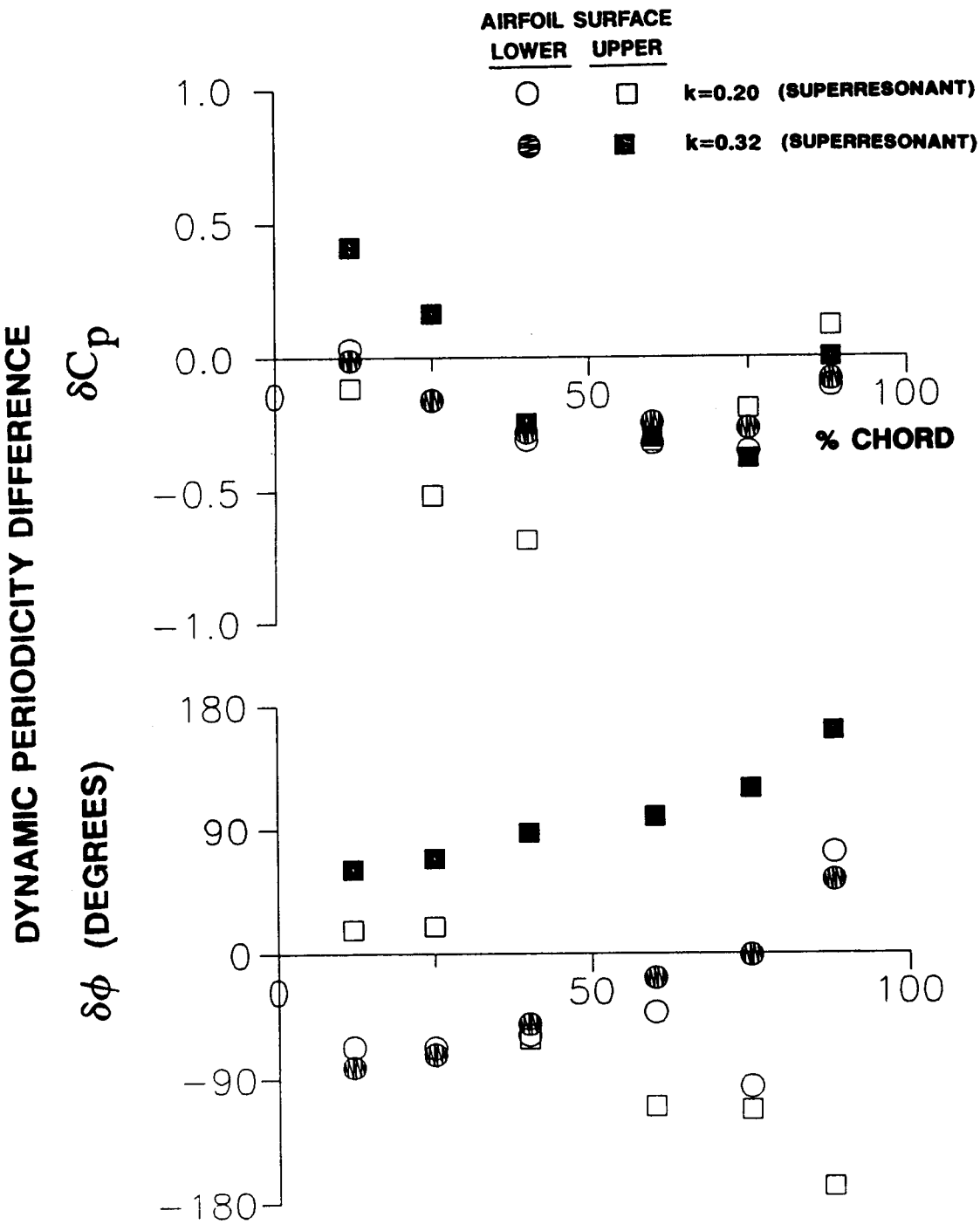

Figure 4.17 Reduced frequency crossplot of dynamic periodicity difference, low solidity cascade, M=0.80, β=90 degrees, k=0.20 and 0.32

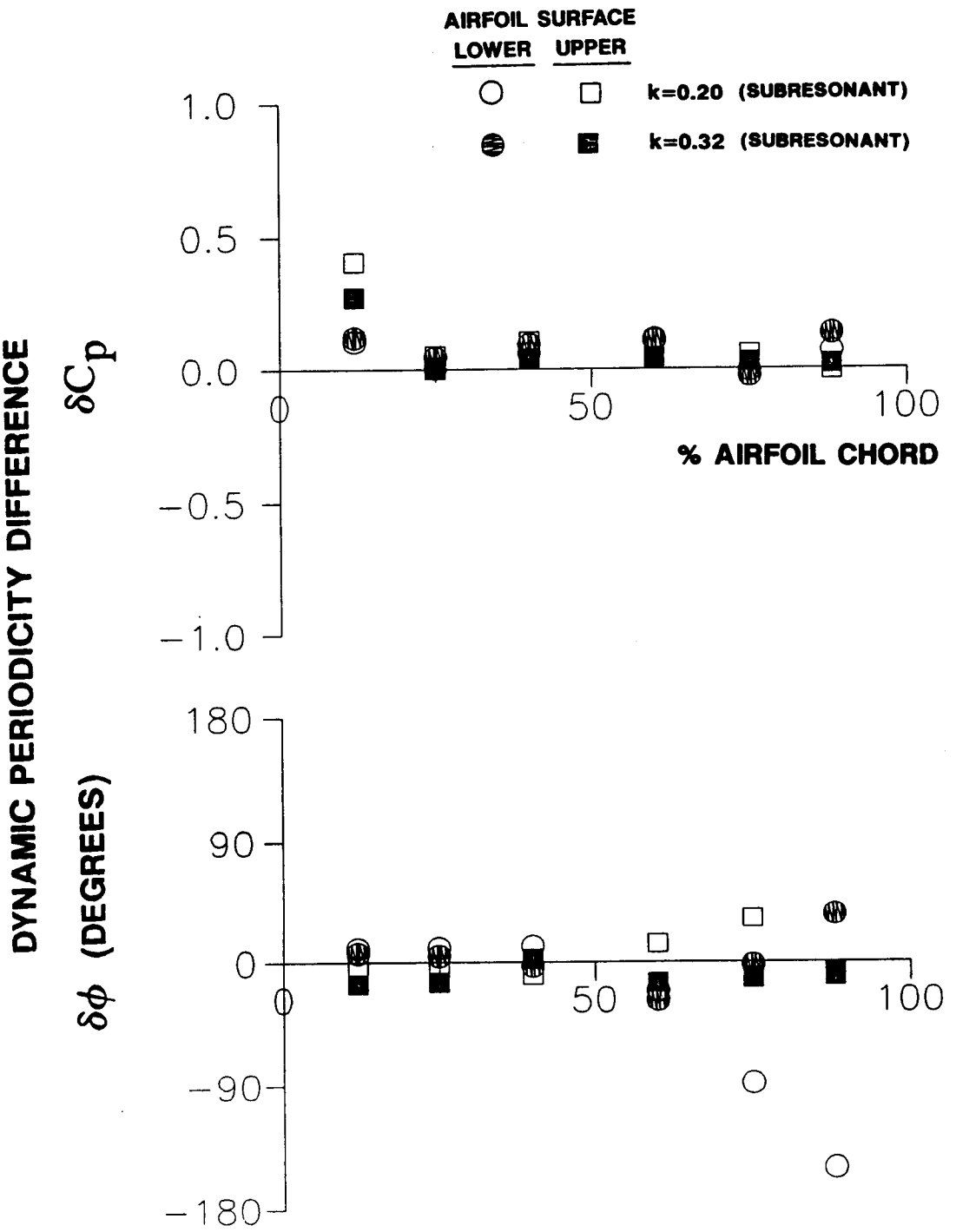

Figure 4.18 Reduced frequency crossplot of dynamic periodicity difference, low solidity cascade, M=0.80, β=-90 degrees, k=0.20 and 0.32

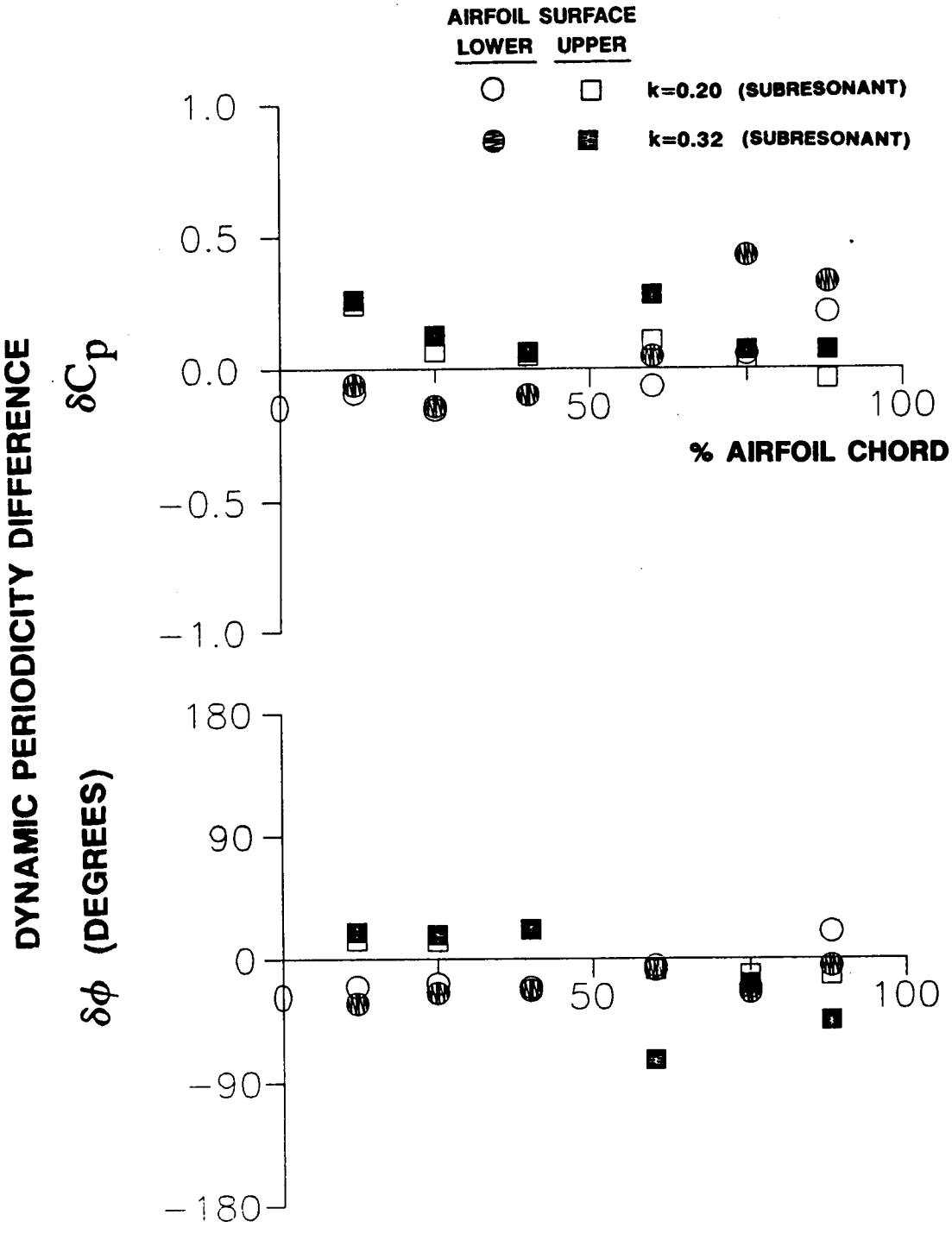

Figure 4.19 Reduced frequency crossplot of dynamic periodicity difference, low solidity cascade, M = 0.80, β = 180 degrees, k = 0.20 and 0.32

High Solidity Cascade

The airfoil surface unsteady pressure distributions were obtained in the high solidity configuration (C/S = 1.3) for interblade phase angle values of 0, 90, and -90 degrees at reduced frequencies of 0.22 and 0.39 for M = 0.65, and reduced frequencies of 0.185 and 0.32 for M = 0.80. A portion of these data were presented in Reference 17, but anomalies were found to exist in the data due to an unreliable airfoil motion signal. As a part of the current investigation, these signals were re-analyzed using the backup airfoil motion signal.

The results presented in Reference 17 were derived using an electro-optical displacement meter to track the motion of the instrumented airfoil. A second measure of the airfoil motion was provided by a proximity sensor as described in Section 2.3.2. Samples of these two signals, Figure 4.20, illustrate the main difference between the output of the two devices: while the proximity probe signal is virtually noise-free, the optical sensor produces a relatively noisy signal. The two signals generally agreed to within ± 4 degrees in phase, so either signal could often be used as a reference for the unsteady pressure measurements. In some cases, however, there were large phase differences between the two measurements, most likely caused by the excessive noise in the optical signal or dropout of that signal altogether. Thus the proximity sensor was used as the measure of the airfoil motion for the re-analysis of these data.

Note that due to limitations in the time available for these high solidity cascade experiments with all airfoils oscillating, dynamic periodicity data were not obtained.

4.2.2 Influence Coefficient Data

Chordwise distributions of the first harmonic dynamic pressure influence coefficients on the individual surfaces of the position 0 reference instrumented airfoil are presented for the oscillating airfoil in the five relative positions defined by -2 through 2.

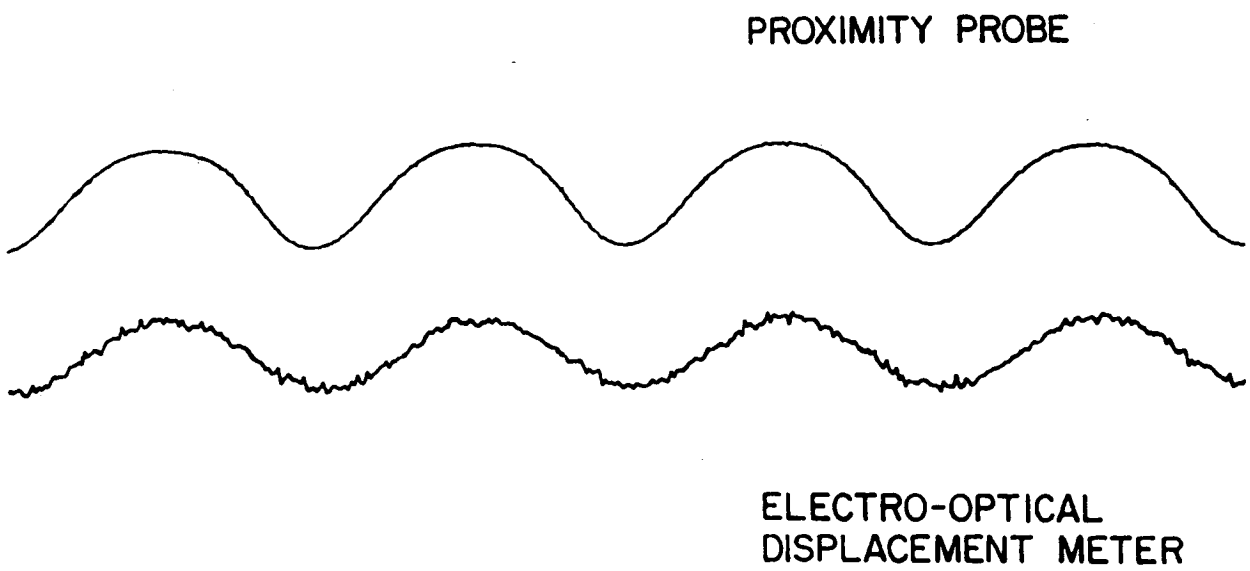

Figure 4.20 Sample airfoil motion signals

Dynamic Periodicity

To investigate the dynamic periodicity of the low solidity cascade, self-induced unsteady pressure data were obtained for the two airfoil locations which define the cascade center passage. Results are presented in the format of dynamic periodicity difference quantities as defined in Equations 4.2 and 4.3 for M=0.55, k=0.2 and 0.45, and M=0.80, k=0.2 and 0.32, Figures 4.21 and 4.22. For M=0.55, the periodicity is generally good except for δC_p for k=0.45 on the upper surface at 12% of chord. Except for several large phase differences, the M=0.8, k=0.2 data are periodic. However, the k=0.32 δC_p values are relatively large at 25 and 40% of chord. For the remainder of this study, the $\hat{C}_p^0$ data used for the low solidity cascade are those obtained from the airfoil surfaces defining the center cascade passage. For the high solidity cascade, the $\hat{C}_p^0$ data were obtained from the center airfoil in the cascade.

Effect of Relative Position of Oscillating Airfoil

To investigate the effect of the relative position of the oscillating airfoil, first harmonic dynamic pressure influence coefficient data are presented for the five relative positions of the oscillating airfoil in the low solidity cascade. For 0.55 inlet Mach number and 0.20 reduced frequency, the first harmonic dynamic pressure influence coefficients $\hat{C}_p^n$ are presented for the airfoil lower surface in Figure 4.23. In the accompanying schematic, each symbol corresponds to the effect of oscillation of the indicated airfoil on the reference instrumented airfoil.

For the lower surface data, self-induced unsteady pressures, $|\hat{C}_p^0|$, are dominant, attaining a maximum near the leading edge then tending toward zero at the trailing edge. The unsteady pressure magnitude distribution due to airfoil -1 oscillations, the airfoil adjacent to the reference airfoil lower surface, also peaks near the leading edge. Airfoil 1 oscillations cause smaller amplitudes along the forward

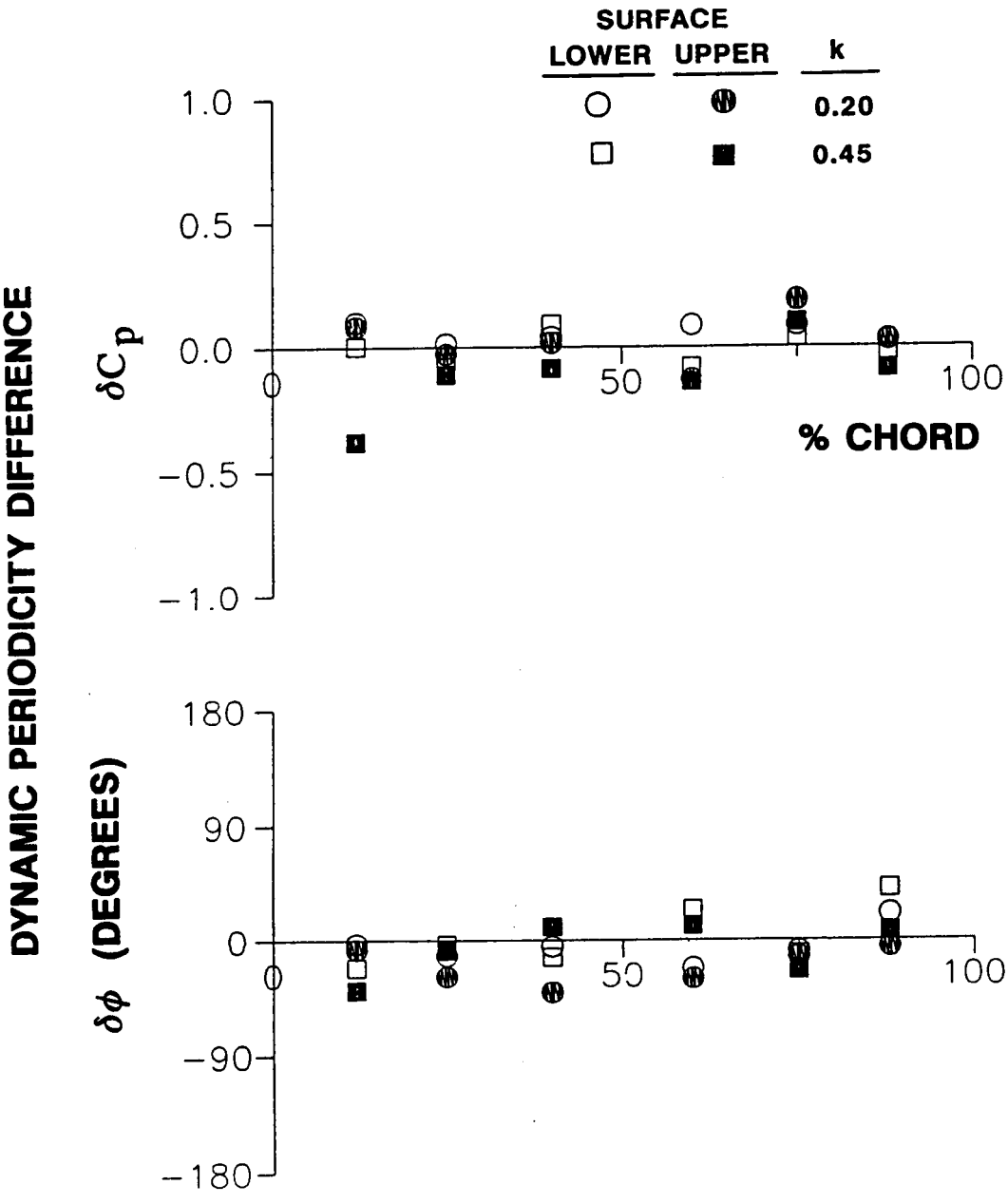

Figure 4.21 Effect of reduced frequency on dynamic periodicity difference, oscillating airfoil in relative position 0, low solidity cascade, M = 0.55

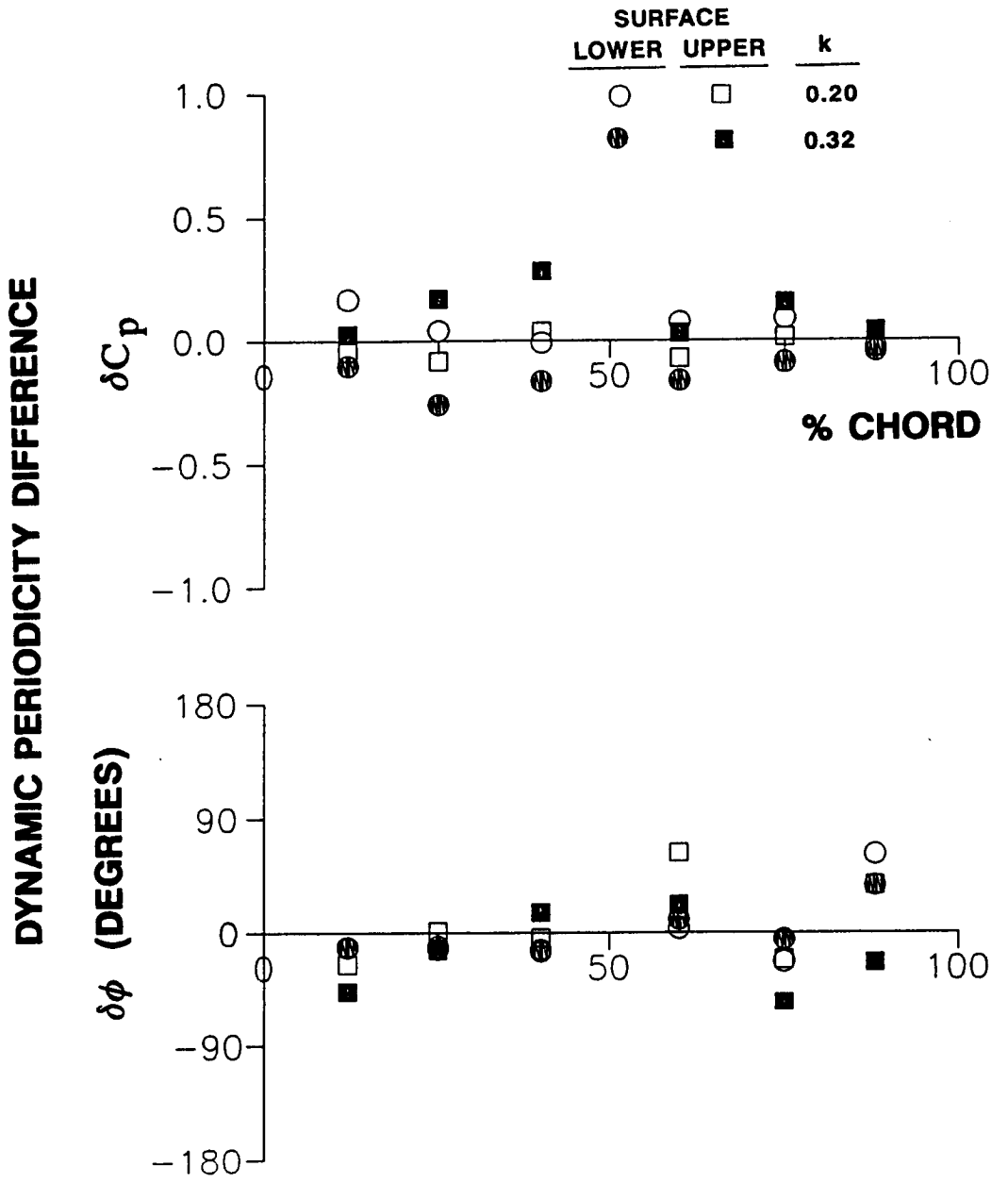

Figure 4.22 Effect of reduced frequency on dynamic periodicity difference, oscillating airfoil in relative position 0, low solidity cascade, M = 0.80

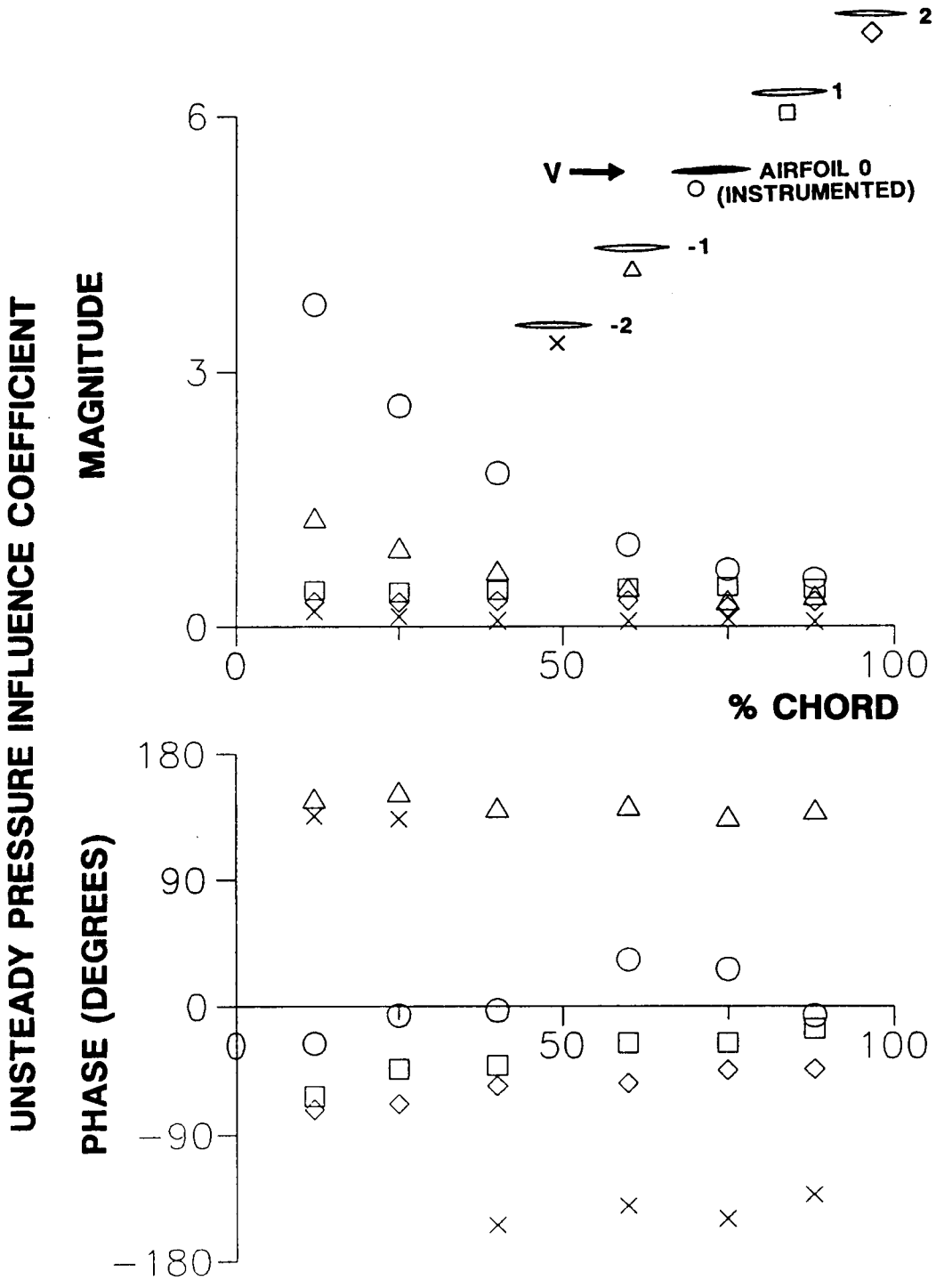

Figure 4.23 Airfoil lower surface unsteady pressure influence coefficient distribution as a function of the oscillating airfoil relative position, low solidity cascade, M=0.55, k=0.20

half of the reference airfoil lower surface, but $|\hat{C}_p^1|$ is slightly larger than $|\hat{C}_p^{-1}|$ along the aft half. The n=2 and n=-2 magnitudes are quite small, illustrating the decrease in unsteady pressure magnitude with distance from the oscillating airfoil.

Lower surface phase angle data are strong functions of the oscillating airfoil position but, for any one value of n, change little with chordwise position. The n=0 phase changes linearly from a phase lag over the forward half of the airfoil to a phase lead over the aft half. For n=-1 and -2, the phase data are roughly out-of-phase with respect to the oscillating airfoil motion but the n=1 and n=2 phases lag the airfoil motion.

For the airfoil upper surface, the self-induced unsteady pressures and those due to oscillations of the airfoil adjacent to the instrumented airfoil surface are most significant, Figure 4.24, analogous to the lower surface results. Decreasing values of $|\hat{C}_p^n|$ with distance from the oscillating airfoil are apparent when n=1 and n=2, but when the airfoils upstream of the instrumented airfoil, n=-1 and n=-2, are oscillating, values of $|\hat{C}_p^{-2}|$, although small, are larger than $|\hat{C}_p^{-1}|$ except at the leading and trailing edges. The n=0 unsteady pressure fluctuations are approximately out-of-phase relative to the airfoil motion while airfoil 1 oscillations result in in-phase unsteady pressures. The rest of the unsteady pressures tend to lag the motion by varying amounts.

Increasing the reduced frequency to 0.45 while maintaining a 0.55 inlet Mach number dramatically increases the effects of oscillating airfoils in relative positions 1 and 2, the airfoils downstream of the instrumented airfoil. This is shown in Figures 4.25 and 4.26 for the lower and upper surfaces, respectively. Unexpectedly, $|\hat{C}_p^1|$ and $|\hat{C}_p^2|$ are equal to each other and almost constant with chordwise position on both surfaces. $|\hat{C}_p^{-1}|$ And $|\hat{C}_p^{-2}|$ are relatively small on the lower surface except at

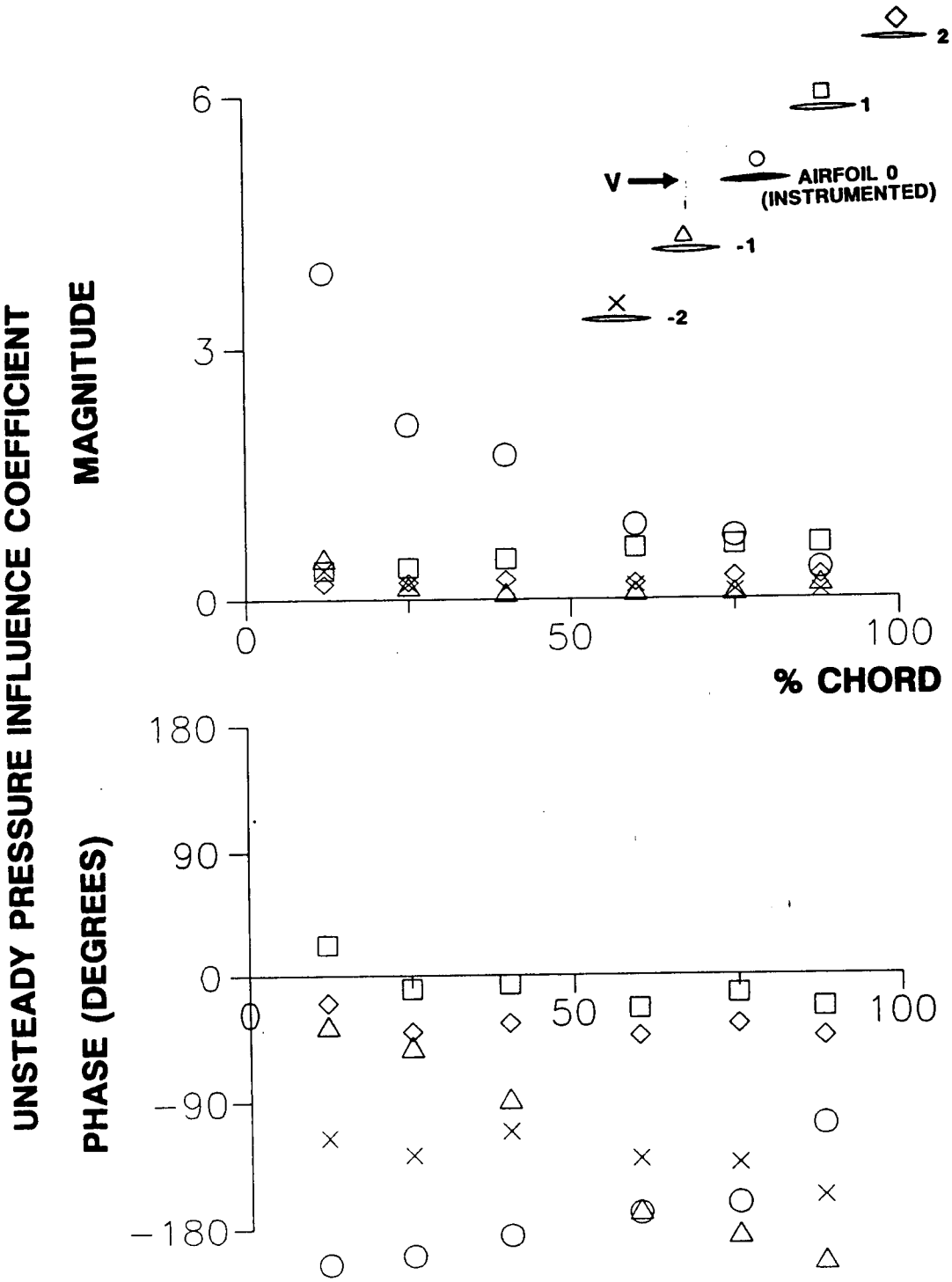

Figure 4.24 Airfoil upper surface unsteady pressure influence coefficient distribution as a function of the oscillating airfoil relative position, low solidity cascade, M = 0.55, k = 0.20

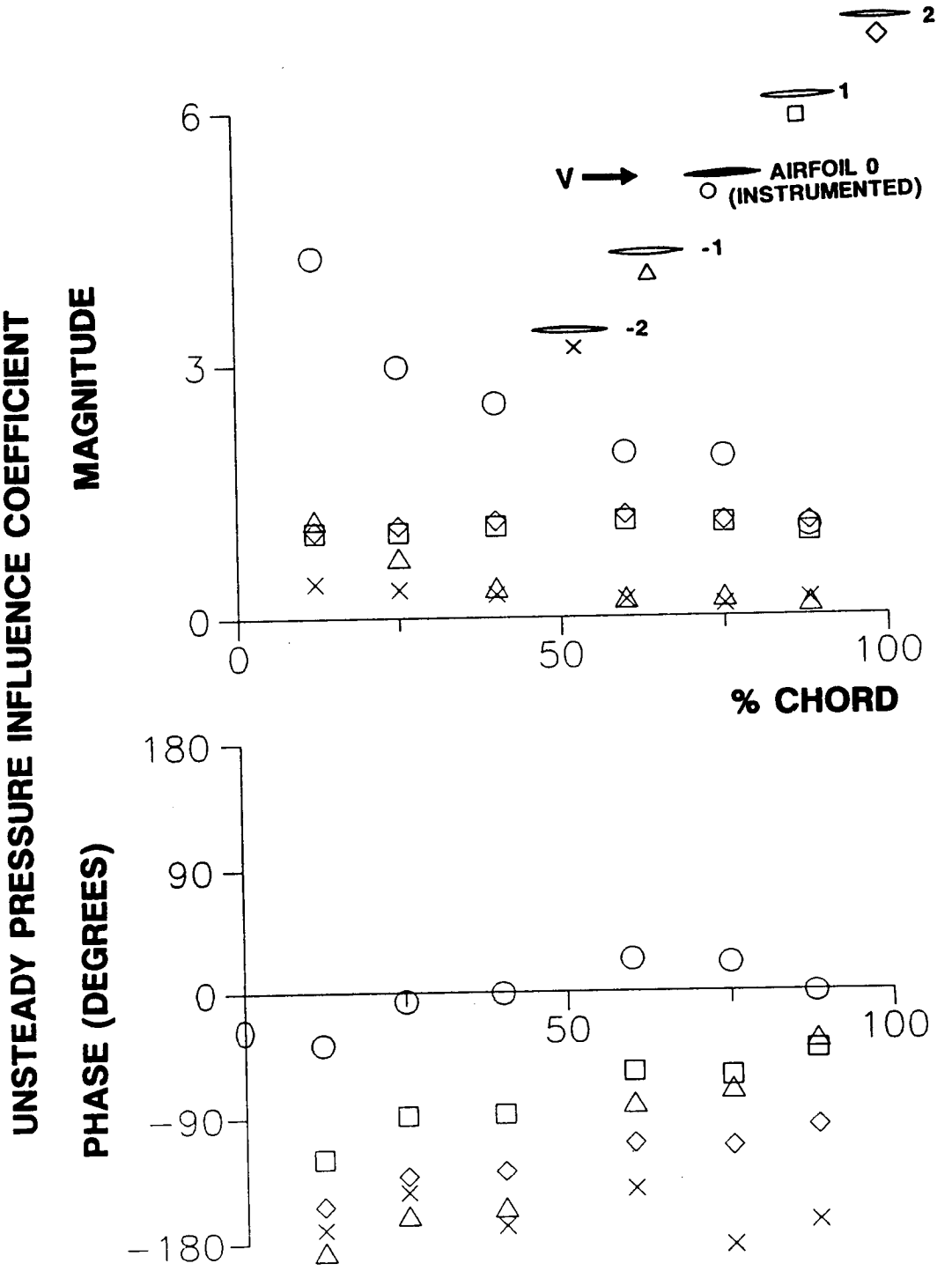

Figure 4.25 Airfoil lower surface unsteady pressure influence coefficient distribution as a function of the oscillating airfoil relative position, low solidity cascade, M=0.55, k=0.45

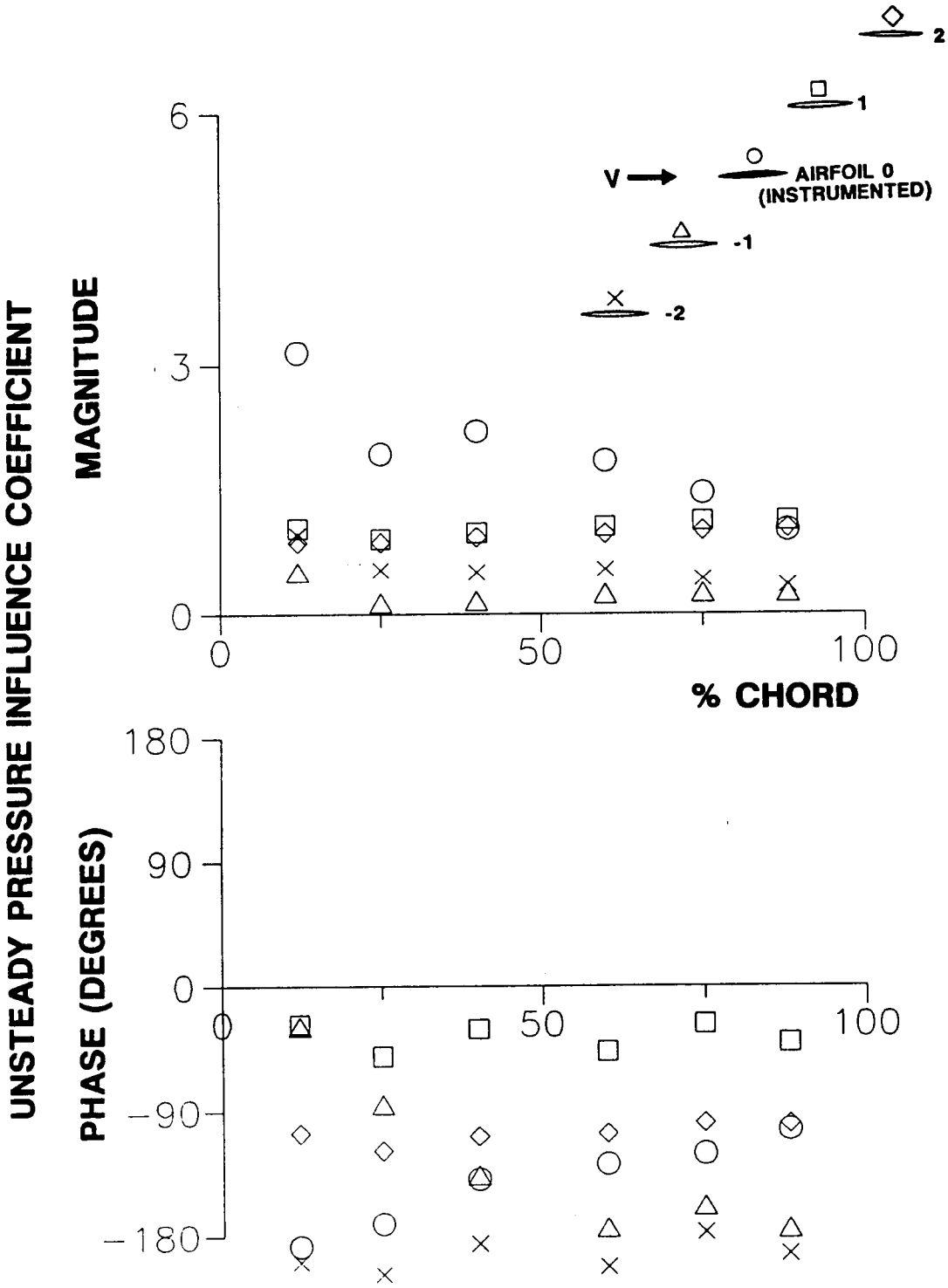

Figure 4.26 Airfoil upper surface unsteady pressure influence coefficient distribution as a function of the oscillating airfoil relative position, low solidity cascade, M=0.55, k=0.45

12% of chord. On the upper surface, $|\hat{C}_p^{-1}|$ and $|\hat{C}_p^{-2}|$ are still smaller than $|\hat{C}_p^{1}|$ and $|\hat{C}_p^{2}|$, and $|\hat{C}_p^{-1}|$ is smaller than $|\hat{C}_p^{-2}|$ - this is similar to the data for k=0.20 in Figure 4.24.

Figures 4.27 and 4.28 show lower and upper surface influence coefficient data for the higher Mach number, M=0.8, and k=0.2. As expected, the self-induced unsteady pressures $|\hat{C}_p^{o}|$ are still the largest, but similar to the M=0.55, k=0.45 data, relatively large unsteady pressures are found due to airfoil 1 and airfoil 2 oscillations. On the lower surface, $|\hat{C}_p^{1}| \approx |\hat{C}_p^{2}|$ while $|\hat{C}_p^{1}| > |\hat{C}_p^{2}|$ on the upper surface. Values of $|\hat{C}_p^{-2}|$ tend to be slightly larger than $|\hat{C}_p^{-1}|$ on the upper surface.

The following briefly summarizes the effect of the relative position of the oscillating airfoil, as presented in Figures 4.23 through 4.28.

(1) The airfoil surface first harmonic pressure influence coefficients are a strong function of the relative position of the oscillating airfoil, with the self-induced pressure fluctuations having the largest magnitudes.

(2) Phase angle data for the self-induced unsteady pressures tend to be in-phase with the airfoil motion for the lower surface and out-of-phase for the upper surface.

(3) The expected decrease in unsteady pressure magnitude with distance between the oscillating and instrumented airfoils does not necessarily occur.

   (a) On the reference airfoil upper surface, $|\hat{C}_p^{-2}|$ is generally greater than $|\hat{C}_p^{-1}|$.

   (b) The influences of the airfoils downstream of the instrumented airfoil, $\hat{C}_p^{1}$ and $\hat{C}_p^{2}$, are unexpectedly large except at the lowest Mach number/reduced frequency combination, M=0.55 and k=0.20.

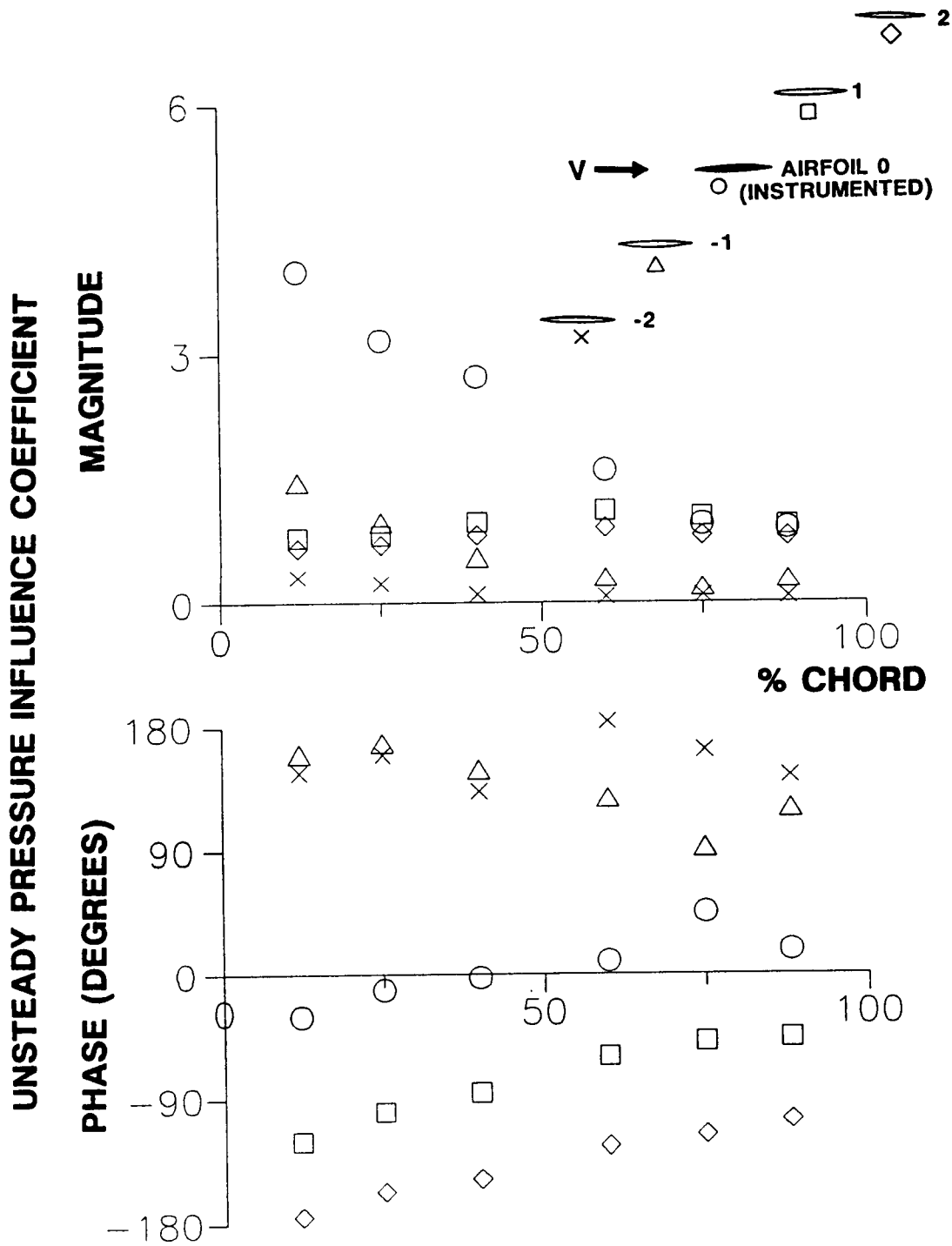

Figure 4.27 Airfoil lower surface unsteady pressure influence coefficient distribution as a function of the oscillating airfoil relative position, low solidity cascade, M=0.80, k=0.20

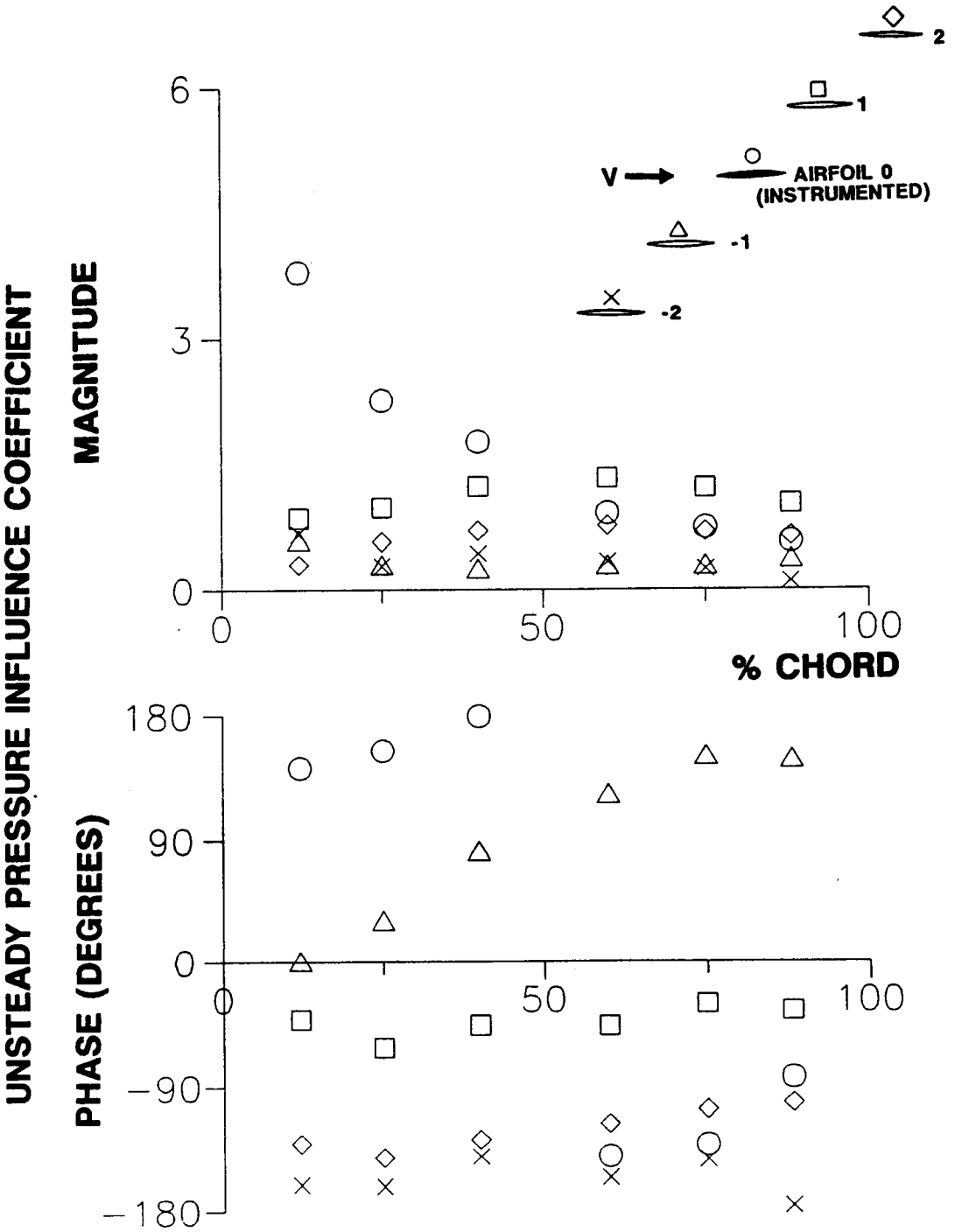

Figure 4.28 Airfoil upper surface unsteady pressure influence coefficient distribution as a function of the oscillating airfoil relative position, low solidity cascade, M = 0.80, k = 0.20

Effect of Reduced Frequency

From the previous results, it is apparent that the reduced frequency has significant effects on the influence coefficients. To clarify these effects, a series of dynamic pressure influence coefficient plots having data for $k=0.20$ and $k=0.45$ are presented for $M=0.55$. Each figure corresponds to a different oscillating airfoil relative position and includes data for both airfoil surfaces, thus also allowing the upper and lower surface unsteady pressure distributions to be compared.

The effect of reduced frequency on the self-induced oscillating airfoil unsteady pressure distribution is shown in Figure 4.29. The larger amplitudes are generally associated with the higher value of k, except near the leading edge on the upper surface. For $k=0.45$, the lower surface amplitudes are typically larger than the upper surface amplitudes. For $k=0.20$, the amplitudes for the two surfaces are about equal. Reduced frequency affects the phase of the unsteady pressure distribution to some extent on the upper surface but not on the lower surface.

Unsteady pressures resulting from oscillations of the airfoil in relative position 1 are shown in Figure 4.30. A schematic of the cascade configuration used to obtain the data is also shown. In the schematic, the solid lines above and below the cascaded airfoils designate the wind tunnel walls. The unsteady pressure magnitudes at either reduced frequency are nearly constant with chordwise position and equal for each of the two surfaces. The magnitude increases with reduced frequency, $k=0.45$ having nearly twice the magnitude as $k=0.2$. For either value of reduced frequency, the phases of the upper and lower surface unsteady pressures are about the same along the aft half of the airfoil. Forward of there, the phase distributions diverge with the lower surface lagging the upper surface. The lower surface phases vary in a fairly linear fashion, while the upper surface phases are nearly constant.

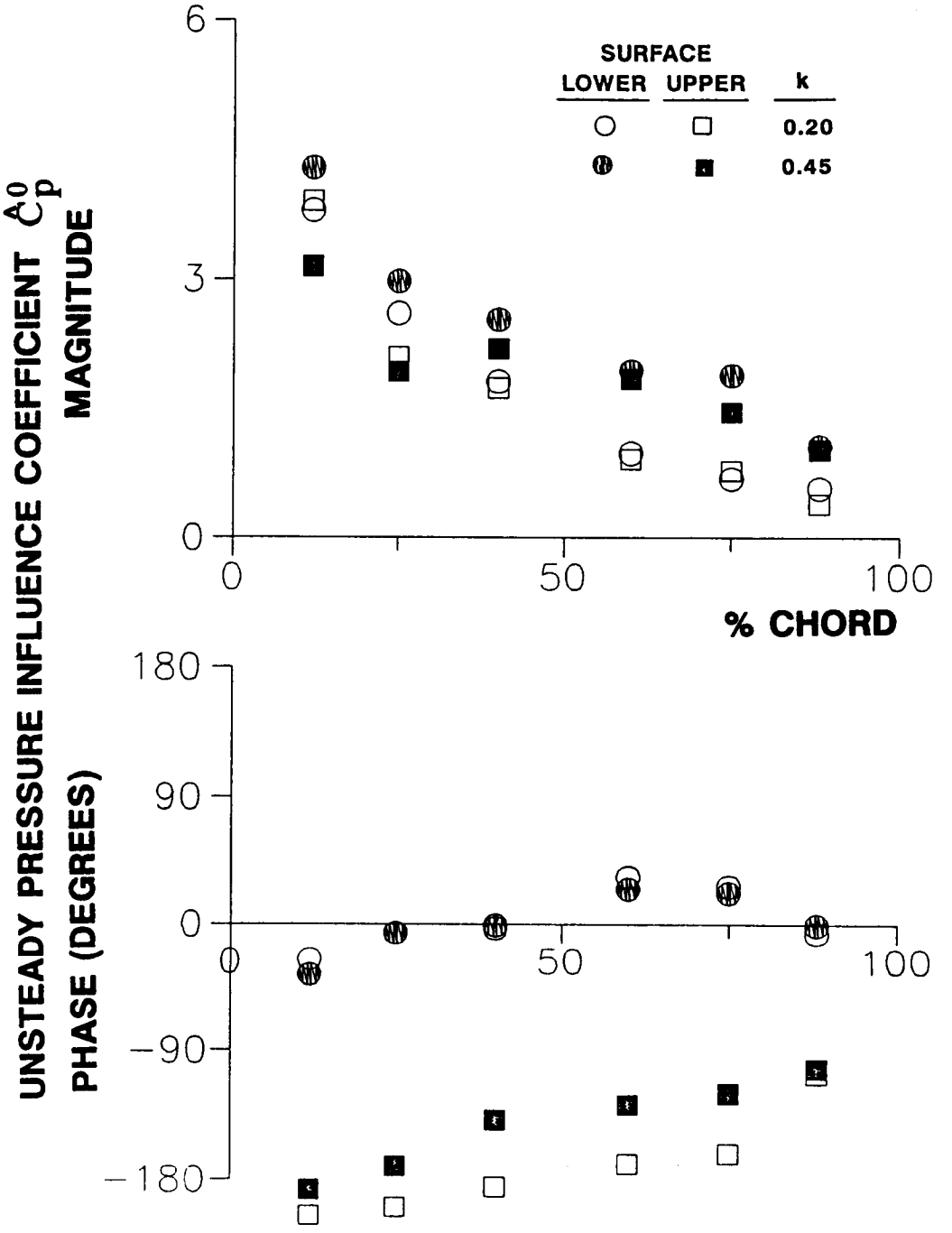

Figure 4.29 Effect of reduced frequency on unsteady pressure influence coefficient, oscillating airfoil in relative position 0, low solidity cascade, M = 0.55

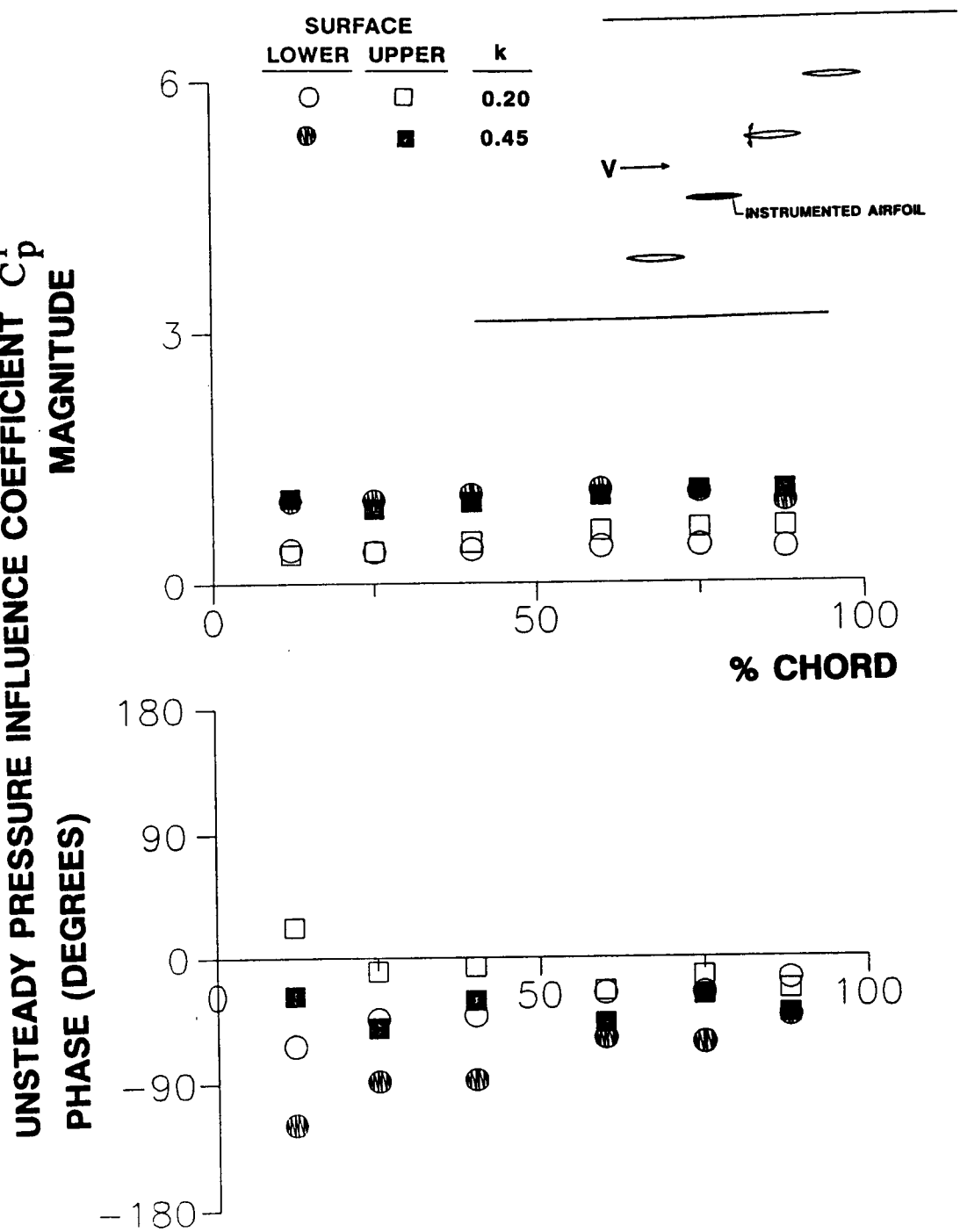

Figure 4.30 Effect of reduced frequency on unsteady pressure influence coefficient, oscillating airfoil in relative position 1, low solidity cascade, M=0.55

That the magnitudes of $\hat{C}_p^1$ in Figure 4.30 are constant and equal for the two airfoil surfaces suggest that these unsteady pressure distributions are due to plane traveling waves. Such waves would ideally also have a linear phase variation with chordwise position, the rate of variation depending upon the direction the wave is propagating and the mean flow conditions. The lower surface phase data approximate this condition, having a fairly linear phase change with chord. The upper surface phase data also approximate this condition, with the phase changing little with chord - indicative of a wave traveling normal to the airfoil chord.

The rate-of-change with chord of the phase data may be used to calculate a wave propagation velocity in the chordwise direction. Based on least squares fits of the lower surface data of Figure 4.30, the waves propagate in the upstream direction at velocities divided by the speed of sound of 0.23 and 0.31 for k=0.20 and 0.45, respectively. Assuming that the steady flow field is uniform, a wave traveling upstream in the chordwise direction would have a velocity of propagation divided by the speed of sound of $(V_p/a) = 1 - M_\infty = 1 - 0.55 = 0.45$. The differences between the theoretical and calculated values indicate the waves are actually propagating in a direction oblique to the airfoil chordwise direction.

Similar trends occur for $\hat{C}_p^2$, Figure 4.31, further supporting the upstream-traveling wave concept. Again, for either k, the unsteady pressure magnitude distributions vary little with chordwise position and are nearly equal for the two surfaces. The higher reduced frequency data have significantly larger magnitudes. The phase distribution for the k=0.45 data is nearly the same for both airfoil surfaces except at 12% of chord. The k=0.2 phase distributions for the two airfoil surfaces are equal at 88% of chord then gradually diverge forward of there.

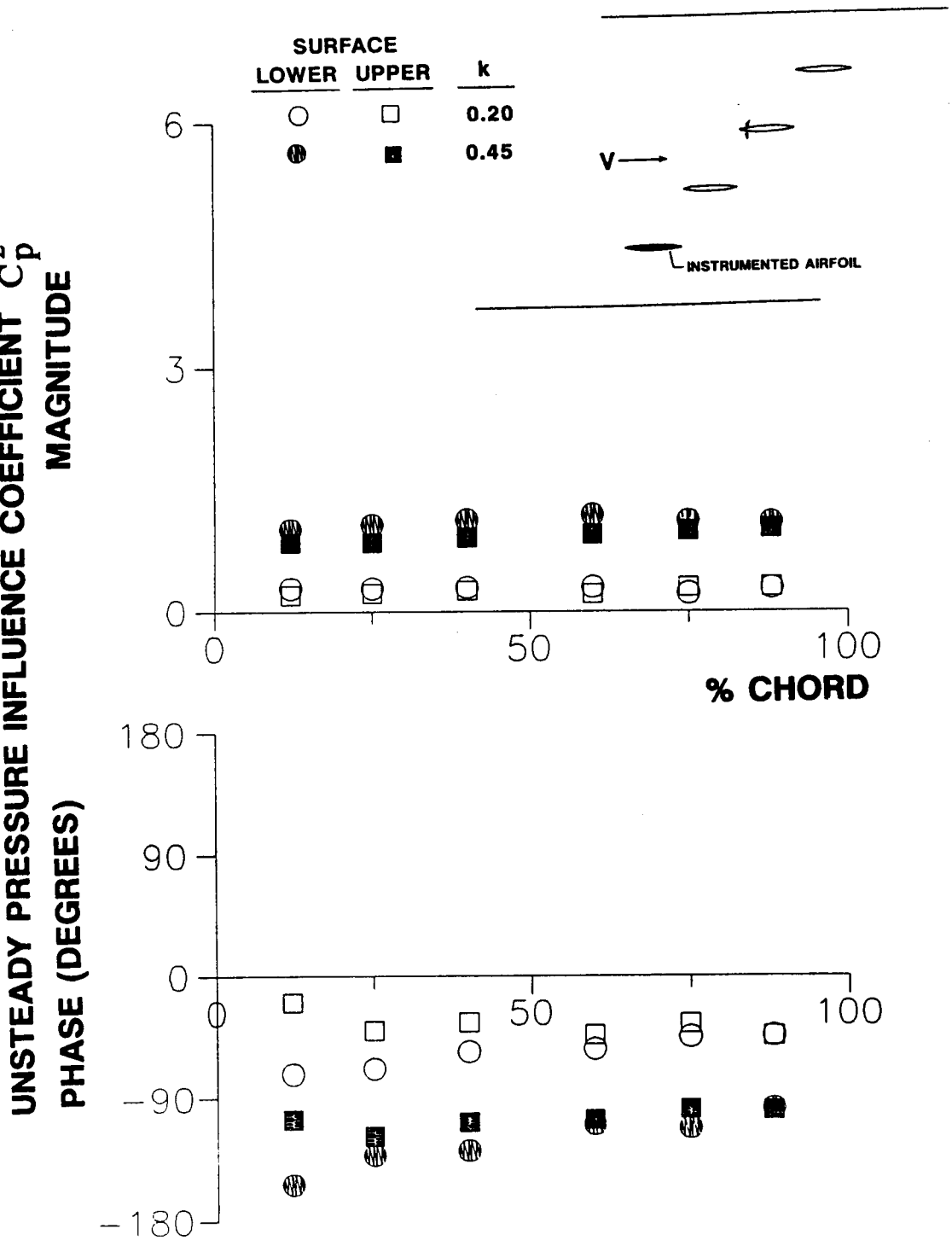

Figure 4.31 Effect of reduced frequency on unsteady pressure influence coefficient, oscillating airfoil in relative position 2, low solidity cascade, M = 0.55

Experimental values of V_p/α are 0.33 for k=0.20 and 0.44 for k=0.45. The experimental value for k=0.45 is approximately equal to the theoretical value, 0.45, indicating that this wave is propagating in the chordwise direction.

The main effect of oscillating the airfoil in relative position -1 is a peak in the unsteady pressure magnitude near the leading edge on the adjacent, lower surface of the instrumented airfoil, Figure 4.32. Upper surface magnitudes are very small except near the leading edge. Contrary to the trend for n>0 of larger magnitudes for higher reduced frequencies, the magnitudes on the lower surface are larger for the lower reduced frequency. Phase distributions for the upper surface are very similar for the two reduced frequencies, both with the phase at 12% of chord leading the phase at 88% of chord by about 150 degrees and having reasonably linear variation with chordwise position. There are large differences due to reduced frequency in the phase distributions on the lower surface: the k=0.2 data remain constant with chord while the k=0.45 data vary greatly with position.

Figure 4.33 presents $\hat{C}_p^{-2}$. The larger magnitude data are associated with the higher reduced frequency. A more significant finding is that the unsteady pressure magnitudes are larger on the airfoil upper surface. Referring to the accompanying cascade schematic, it is seen that the instrumented airfoil upper surface is adjacent to a wind tunnel wall. The relatively large unsteady pressures found in the data are likely due to reflection of pressure waves off the wind tunnel wall toward the instrumented airfoil upper surface. The phase distributions change little with position and are approximately out-of-phase.

In summary, Figures 4.29 through 4.33 illustrate the effect of reduced frequency on the unsteady pressure influence coefficient distribution and the differences in $\hat{C}_p^n$ for the two airfoil surfaces. Important trends found in these plots are as follows.

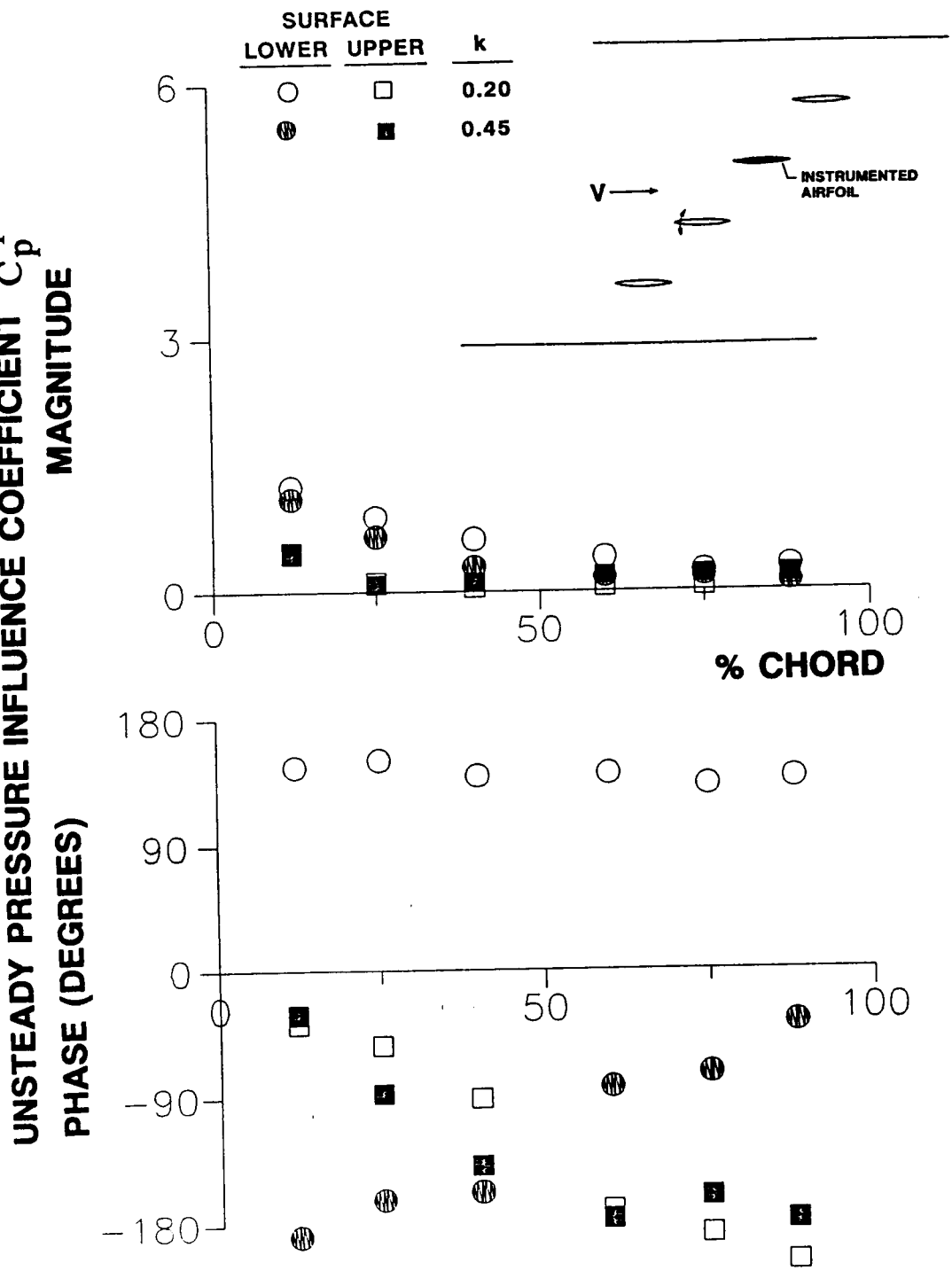

Figure 4.32 Effect of reduced frequency on unsteady pressure influence coefficient, oscillating airfoil in relative position -1, low solidity cascade, M=0.55

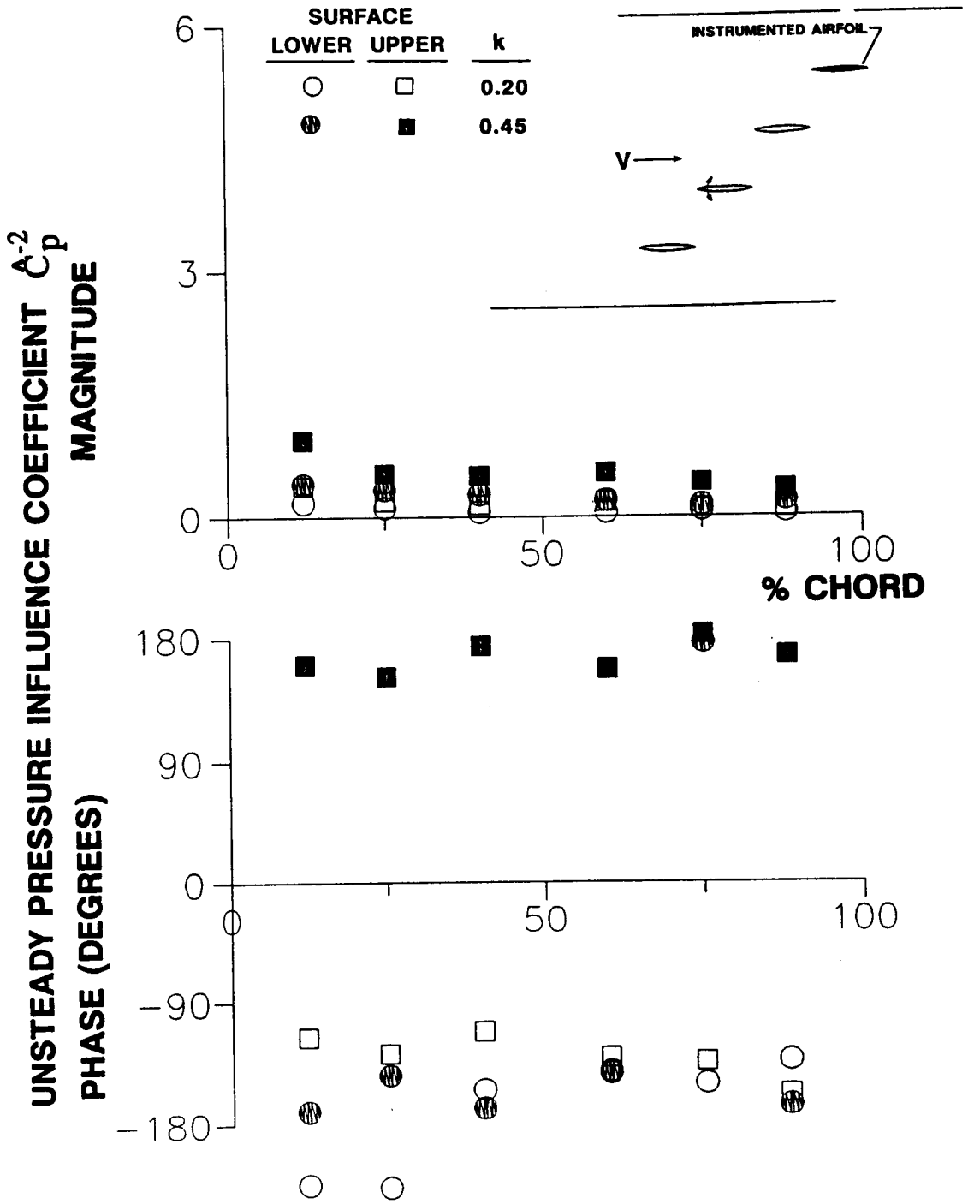

Figure 4.33 Effect of reduced frequency on unsteady pressure influence coefficient, oscillating airfoil in relative position -2, low solidity cascade, M=0.55

(1) Larger unsteady pressure coefficients generally result at the higher reduced frequency. An exception is $\hat{C}_p^{-1}$ for the lower surface.

(2) For either value of reduced frequency, oscillation of airfoil 1 or airfoil 2 causes unsteady pressure fluctuation magnitudes on the reference airfoil surface which are nearly constant along the airfoil and nearly equal for the two airfoil surfaces. This behavior appears to be a consequence of a plane traveling wave.

(3) For either value of reduced frequency, oscillation of airfoil -1 causes unsteady pressure fluctuations on the nearest reference airfoil surface, the lower surface, which are larger than those on the opposite surface.

(4) When airfoil -2 is oscillating, the reference airfoil upper surface unsteady pressures are larger than those on the lower surface, most likely due to waves being reflected off the adjacent wind tunnel wall.

Plots analogous to those just presented but for an inlet Mach number of 0.80 and reduced frequencies of 0.20 and 0.32, Figures 4.34 through 4.38, reveal many similar trends concerning the effect of reduced frequency and differences in $\hat{C}_p^n$ for the two airfoil surfaces. These results are summarized in the following.

(1) Larger unsteady pressures generally result at the higher reduced frequency.

(2) For either value of reduced frequency, oscillation of airfoil 1 causes unsteady pressure fluctuations on the reference airfoil surface which are nearly equal in magnitude on both airfoil surfaces. However, the magnitude varies some with airfoil chord, having a hump centered at 60% of chord. Similar results are evident for $\hat{C}_p^2$ except that, for k=0.32, the hump is more pronounced and the lower surface magnitudes are significantly larger than those of the upper surface. These data are also

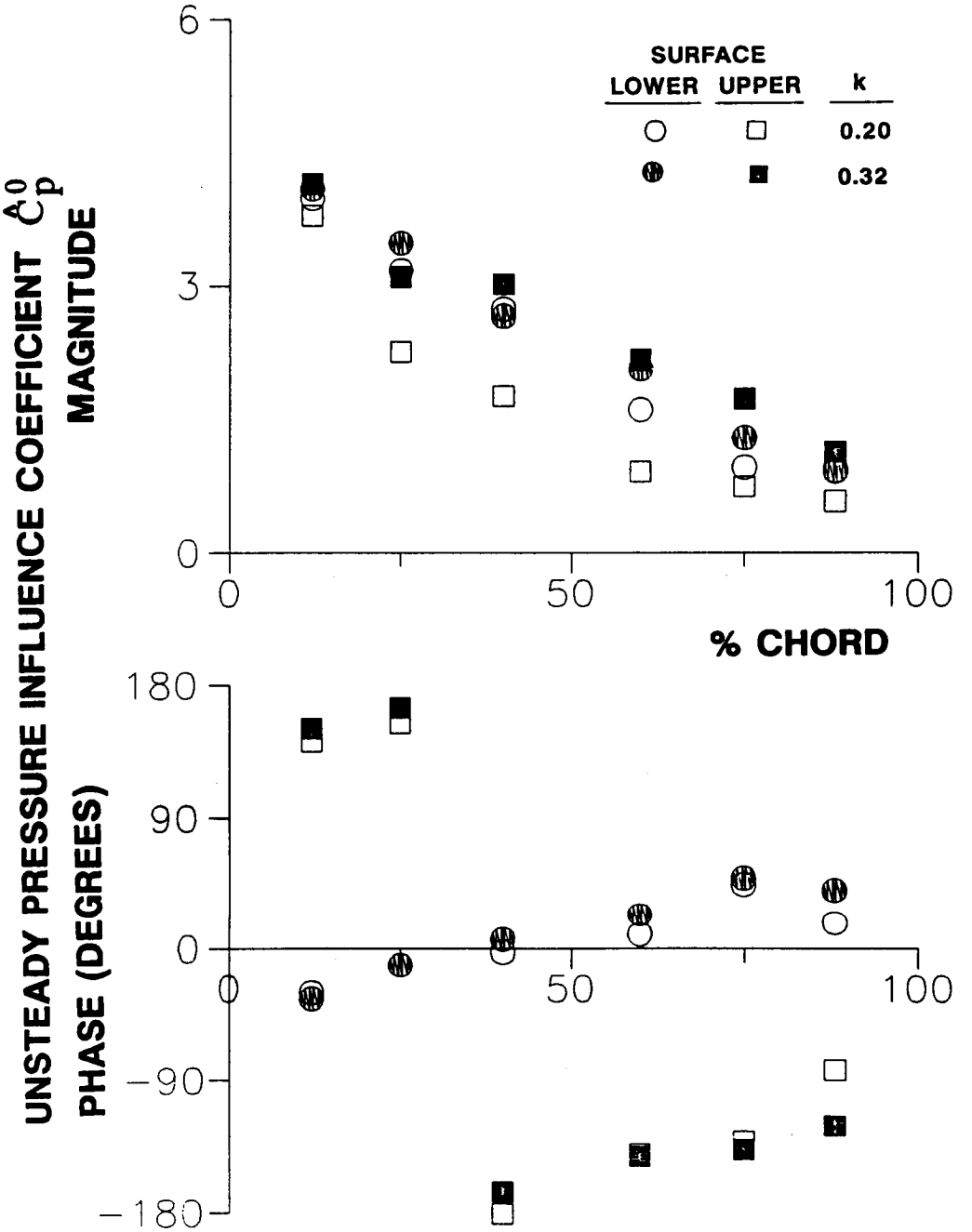

Figure 4.34 Effect of reduced frequency on unsteady pressure influence coefficient, oscillating airfoil in relative position 0, low solidity cascade, M = 0.80

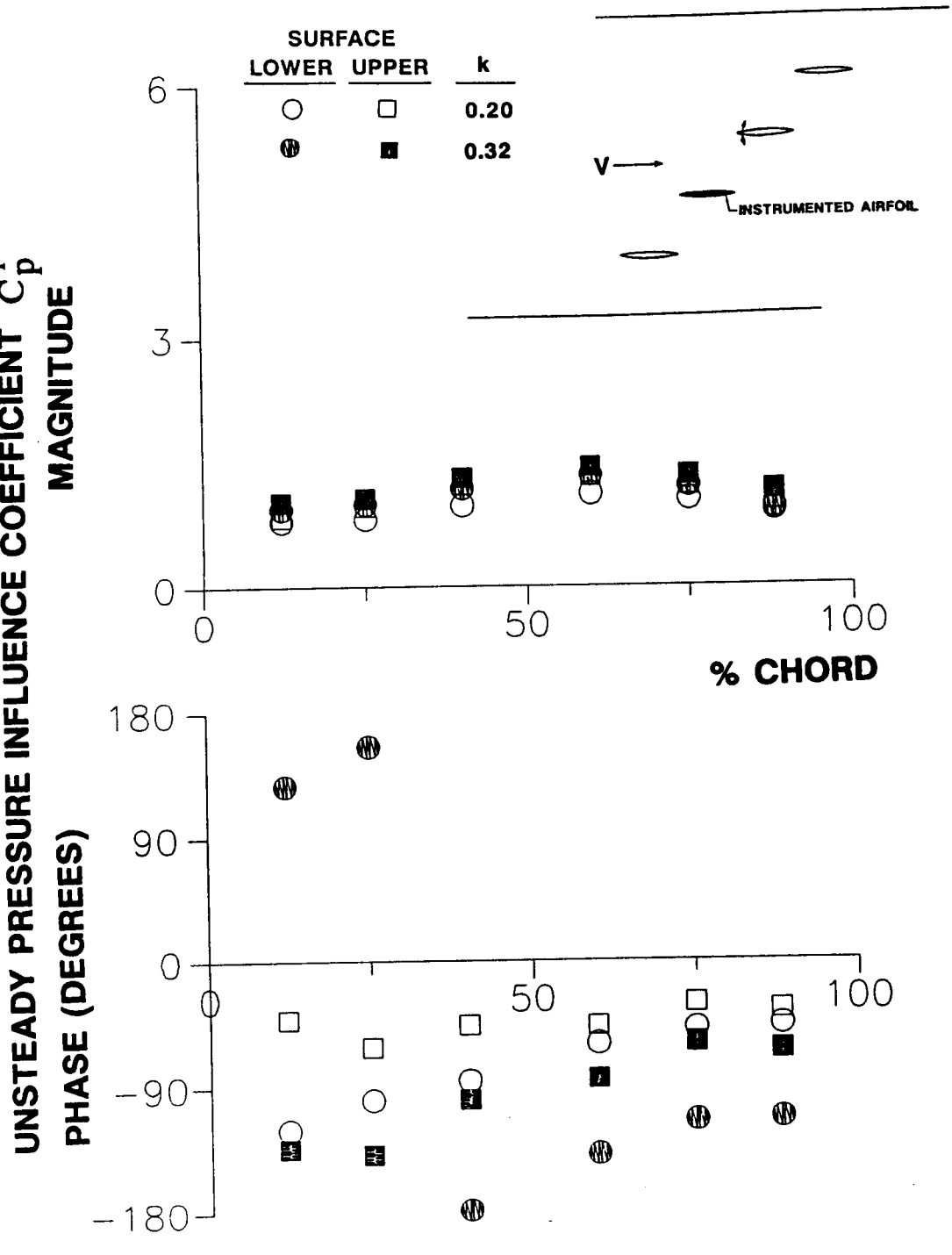

Figure 4.35 Effect of reduced frequency on unsteady pressure influence coefficient, oscillating airfoil in relative position 1, low solidity cascade, M = 0.80

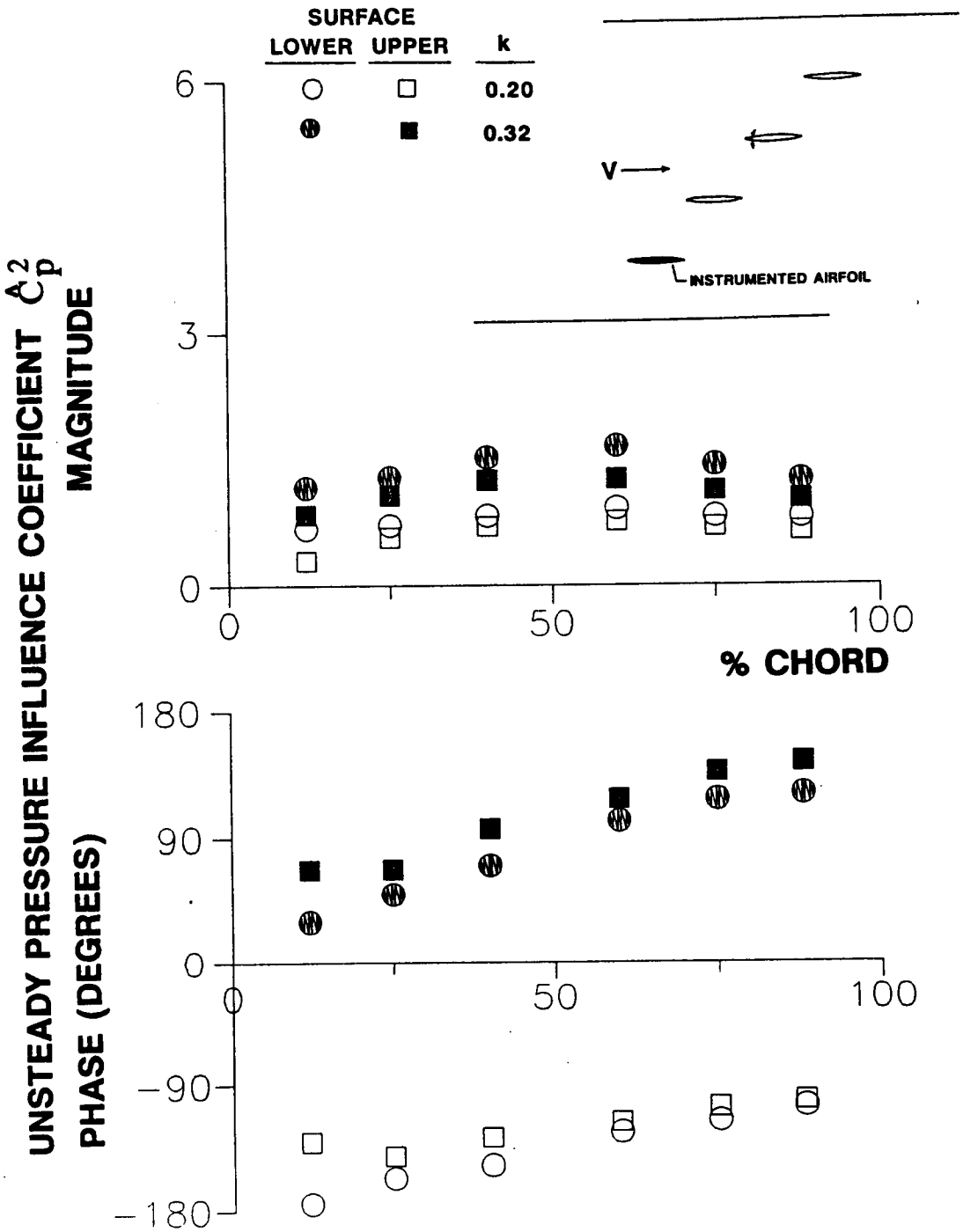

Figure 4.36 Effect of reduced frequency on unsteady pressure influence coefficient, oscillating airfoil in relative position 2, low solidity cascade, M=0.80

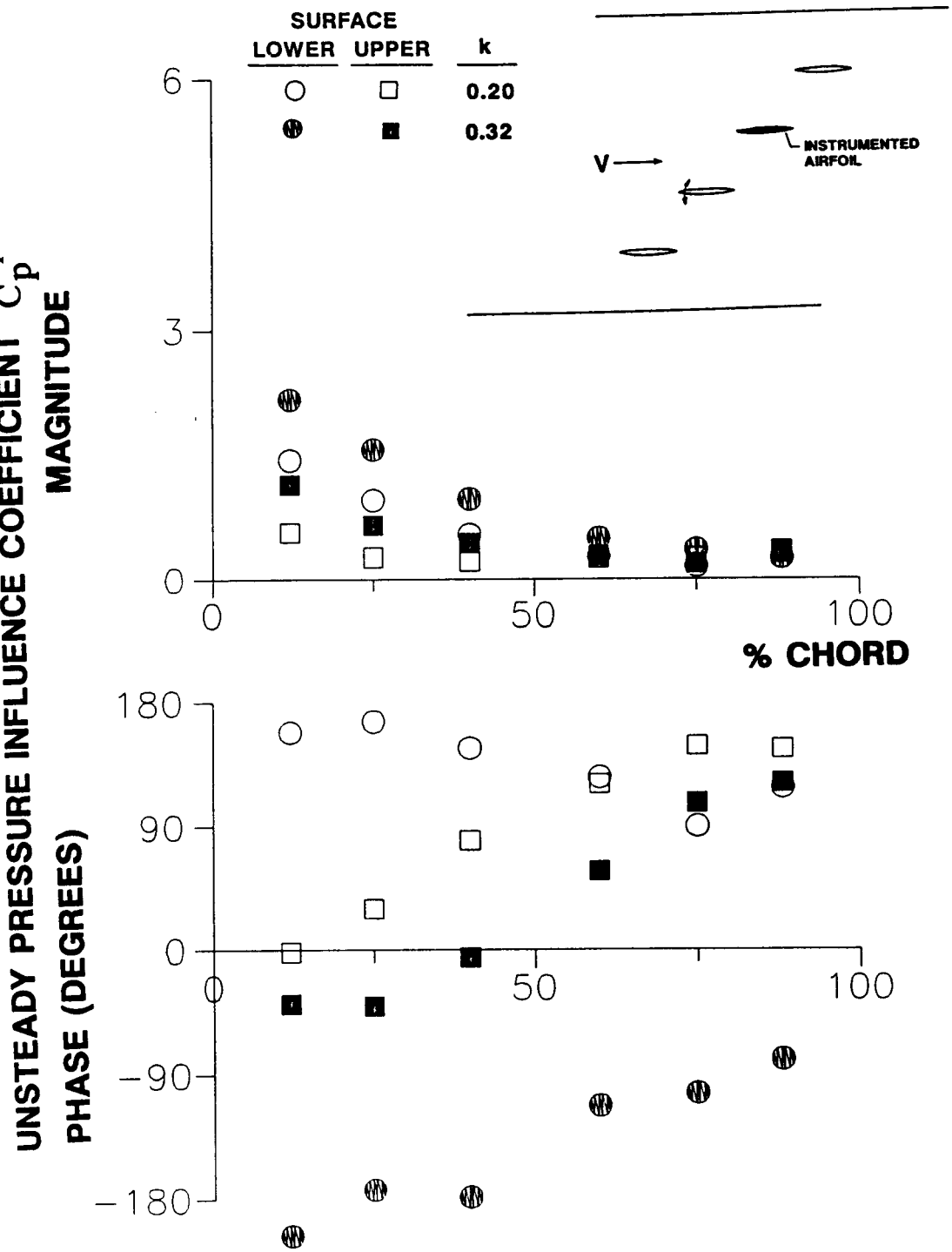

Figure 4.37 Effect of reduced frequency on unsteady pressure influence coefficient, oscillating airfoil in relative position -1, low solidity cascade, M=0.80

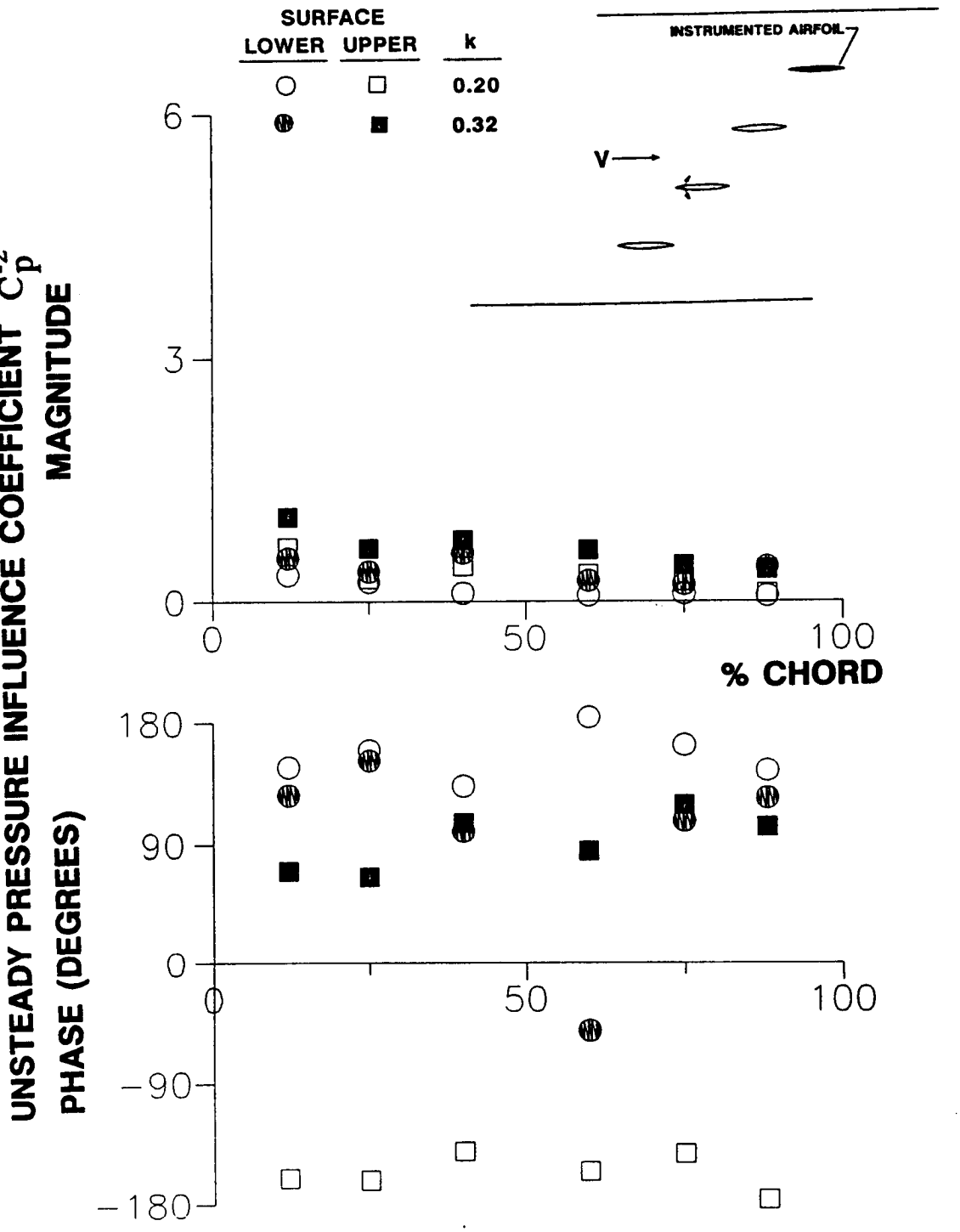

Figure 4.38 Effect of reduced frequency on unsteady pressure influence coefficient, oscillating airfoil in relative position -2, low solidity cascade, M=0.80

indicative of traveling wave phenomena, except that the mean flow field is distorting the waves and causing the nonuniform unsteady pressure magnitude distributions at this higher inlet Mach number.

(3) For either value of reduced frequency, oscillation of airfoil -1 causes unsteady pressure fluctuations on the nearest reference airfoil surface, the lower surface, which are larger than the opposite surface.

(4) When airfoil -2 is oscillating, larger unsteady pressures are found on the reference airfoil upper surface than the lower surface.

Effect of Inlet Mach Number

To determine the effects of inlet Mach number, a series of dynamic pressure influence coefficient plots having data for both M=0.55 and M=0.80 are presented for k=0.32. Each plot corresponds to a different oscillating airfoil relative position and includes data for both airfoil surfaces.

Inlet Mach number has a significant effect on the self-induced unsteady pressure coefficient magnitude distribution, Figure 4.39. Magnitudes are larger for the higher inlet Mach number, and there is little difference between the lower and upper surface magnitudes when M=0.8. When M=0.55, magnitudes are larger on the lower surface. The phase distributions are little affected by inlet Mach number.

Larger magnitudes also occur for M=0.80 when n=1 and n=2, Figures 4.40 and 4.41. Wave distortion by the mean flow field at the higher inlet Mach number is also apparent, as evidenced by the nonuniform magnitude distribution. This contrasts with the uniform distributions for M=0.55. One difference is that the upper and lower surface magnitudes for n=1 and M=0.55 are not equal.

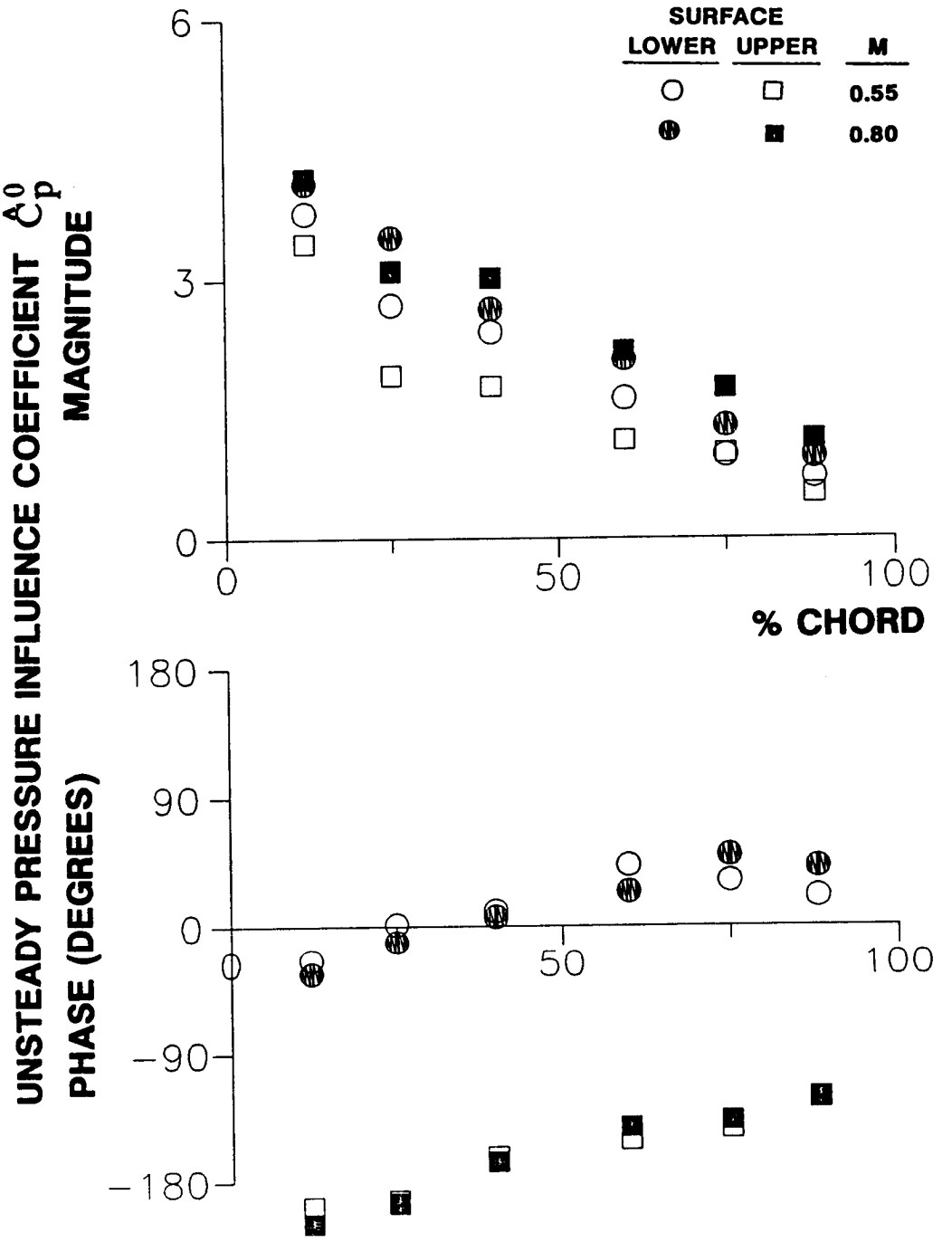

Figure 4.39 Effect of inlet Mach number on unsteady pressure influence coefficient, oscillating airfoil in relative position 0, low solidity cascade, k=0.32

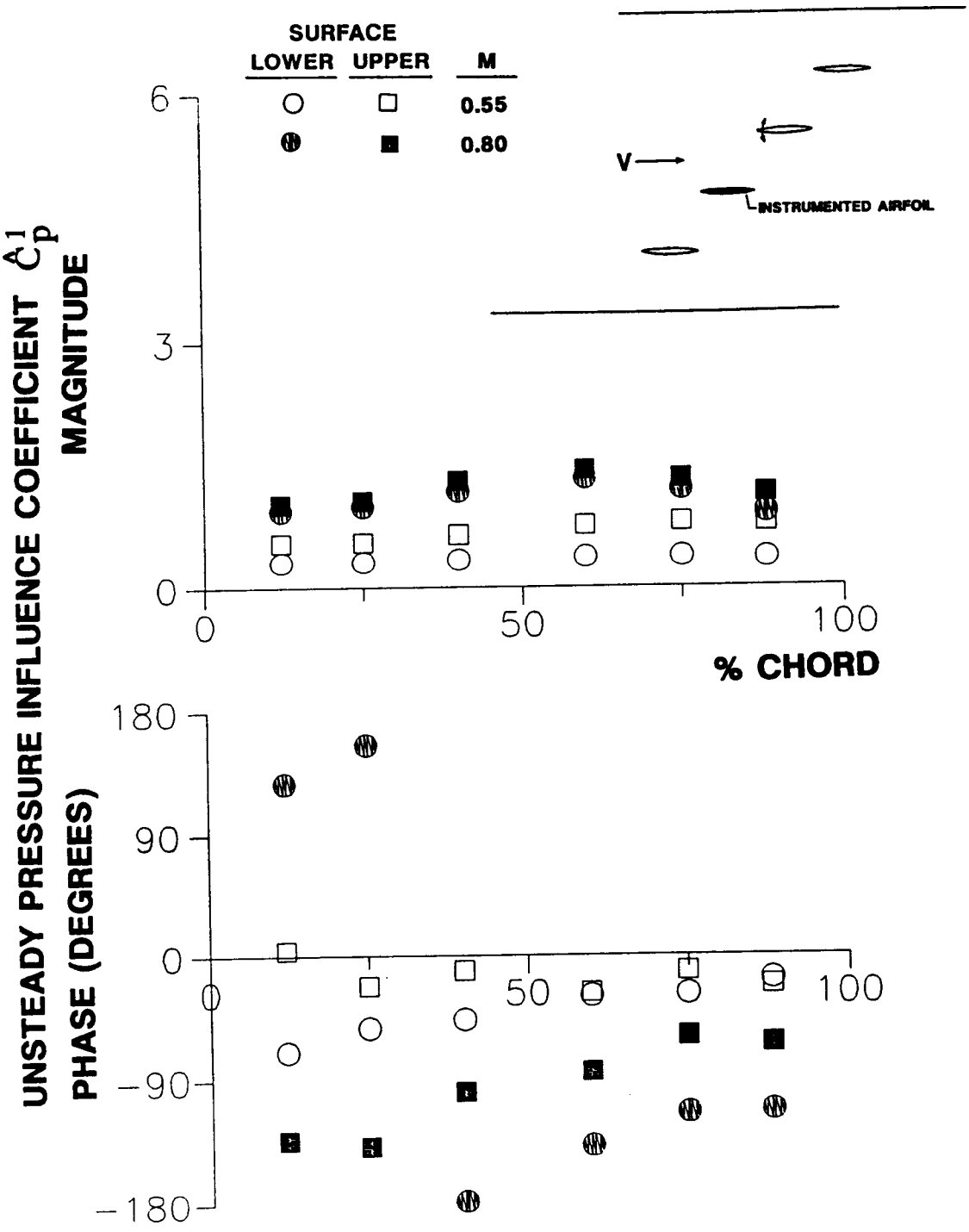

Figure 4.40 Effect of inlet Mach number on unsteady pressure influence coefficient, oscillating airfoil in relative position 1, low solidity cascade, k = 0.32

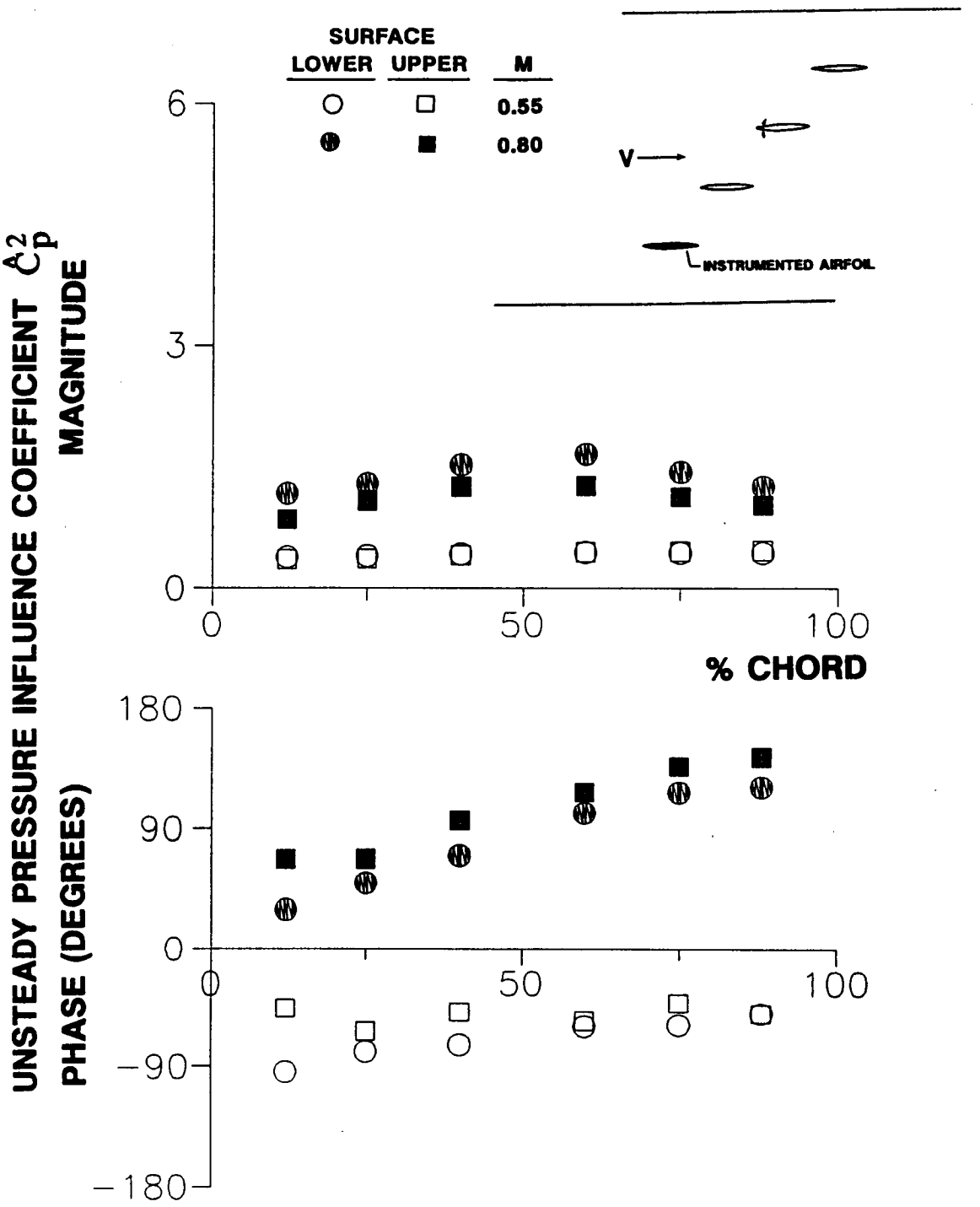

Figure 4.41 Effect of inlet Mach number on unsteady pressure influence coefficient, oscillating airfoil in relative position 2, low solidity cascade, k=0.32

For the other relative positions of the oscillating airfoil, n=-1 and n=-2, Figures 4.42 and 4.43, respectively, larger magnitudes are again found for the higher inlet Mach number. Inlet Mach number affects the phase data considerably, but no general trend is apparent.

Effect of Solidity and Number of Airfoils

The effect of cascade solidity and also the number of airfoils in the cascade is investigated by comparison of M=0.8 influence coefficient data for the low and high solidity cascades, Figures 4.44 through 4.48. Solidities of these cascades differ by a factor of two, the steady flow incidence angles are different, 2 degrees for the low solidity cascade and 7 degrees for the high solidity cascade, and the stagger angles also differ, 45 degrees for the low solidity configuration and 53 degrees for the high solidity configuration.

Despite all these differences, the self-induced unsteady pressure coefficient, Figure 4.44, is nearly independent of solidity. The main difference is on the upper surface at 12% of chord where an oscillating shock wave gives a spike in magnitude for the high solidity cascade. Otherwise, the magnitude and phase distributions are very similar.

Oscillating the airfoil in relative position 1, Figure 4.45, clearly shows the effect of reducing the spacing between the airfoils: the unsteady pressures on the adjacent surface of the instrumented airfoil, the upper surface, increase dramatically as the spacing is decreased. Magnitudes on the opposite surface are hardly affected. Phase distributions are similar in slope but shifted due to the difference in airfoil spacing. Note that, in the accompanying schematic, the locations of the cascade walls are accurate only for the low solidity (four airfoil) cascade; in the high solidity cascade, the center airfoil of the nine airfoils was oscillating.

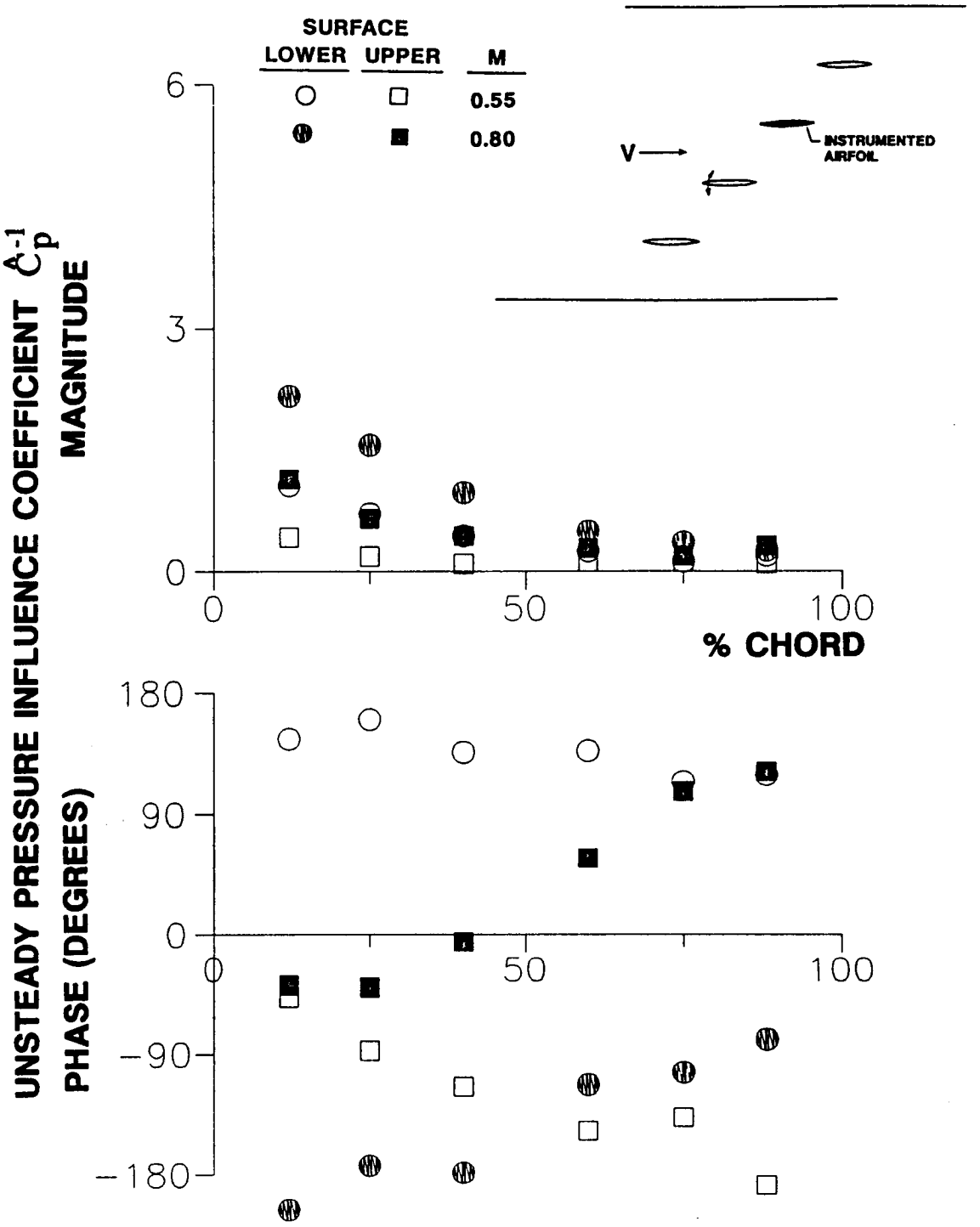

Figure 4.42 Effect of inlet Mach number on unsteady pressure influence coefficient, oscillating airfoil in relative position -1, low solidity cascade, k=0.32

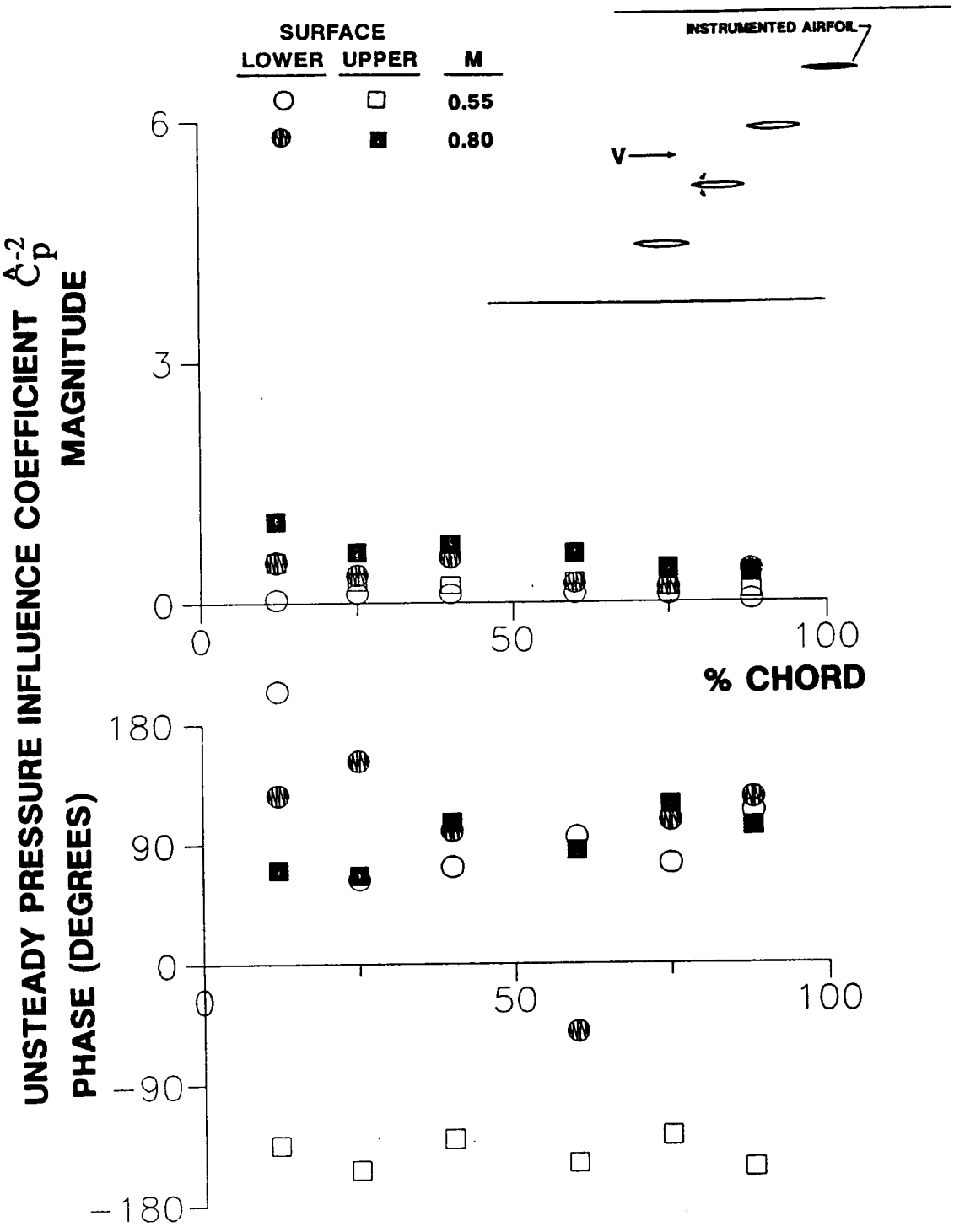

Figure 4.43 Effect of inlet Mach number on unsteady pressure influence coefficient, oscillating airfoil in relative position -2, low solidity cascade, k = 0.32

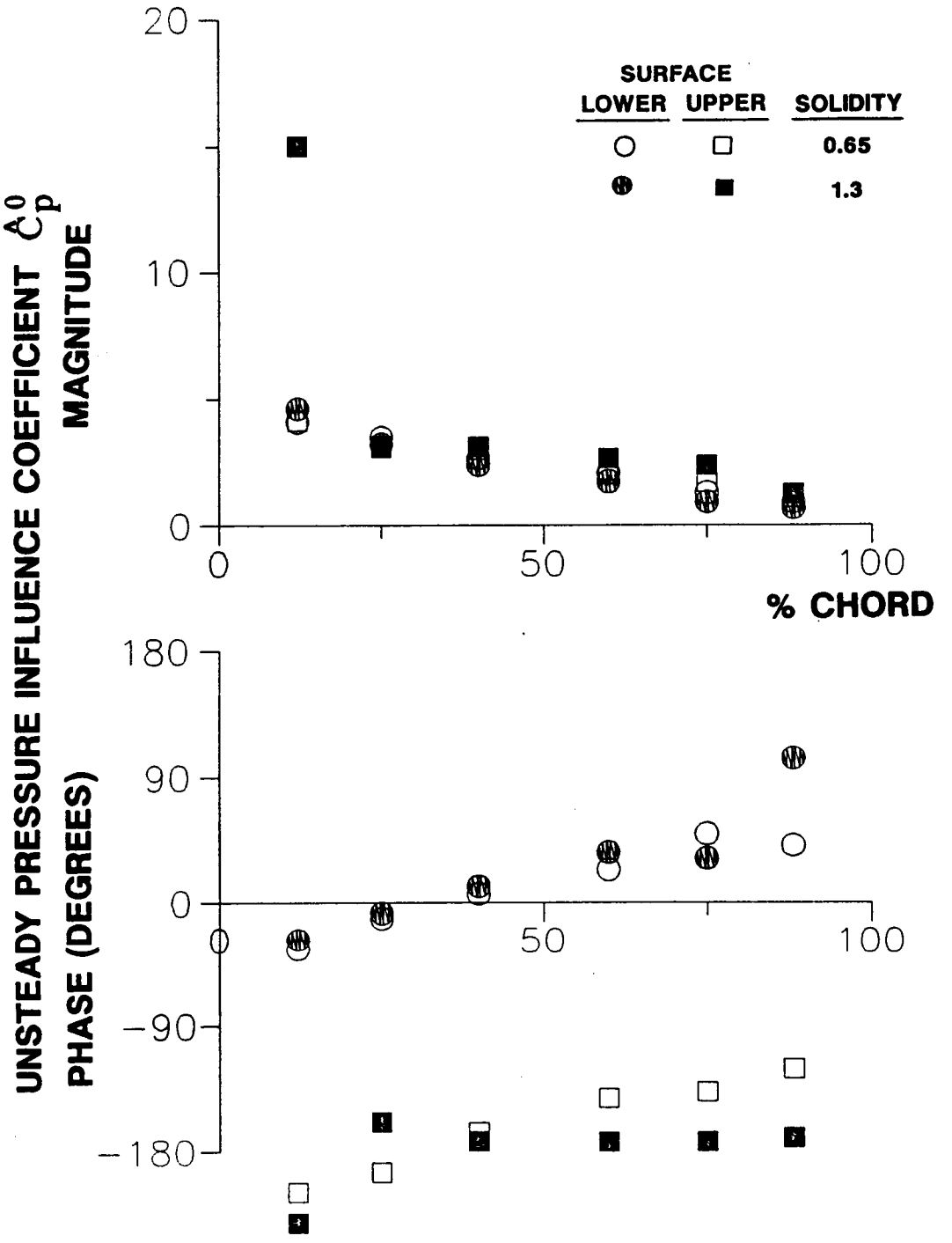

Figure 4.44 Effect of cascade solidity on unsteady pressure influence coefficient, oscillating airfoil in relative position 0, M = 0.80, k = 0.32

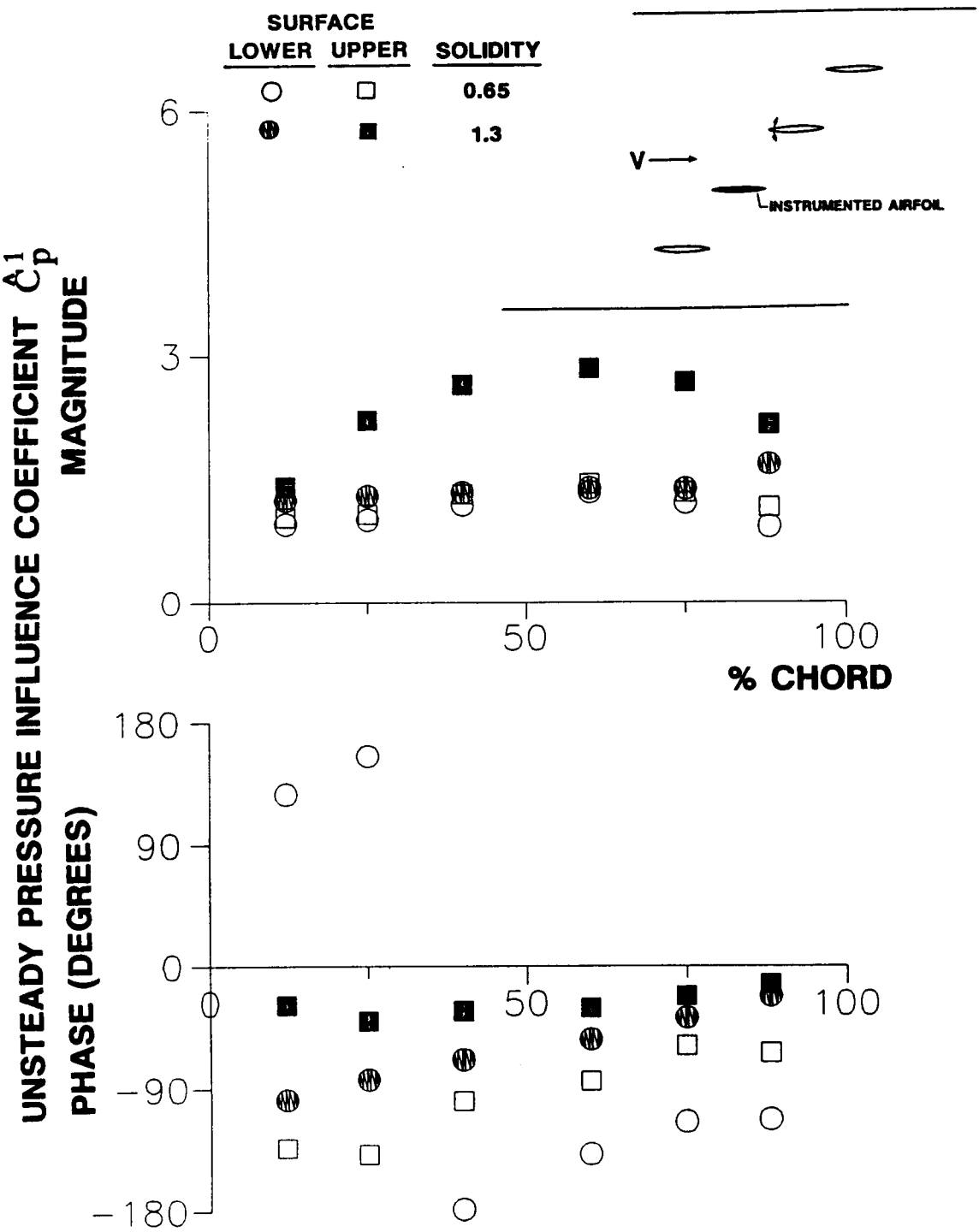

Figure 4.45 Effect of cascade solidity on unsteady pressure influence coefficient, oscillating airfoil in relative position 1, M = 0.80, k = 0.32

Solidity has little effect on the magnitude distribution of $\hat{C}_p^2$, Figure 4.46, but there is large shift in the phase angle due to the difference in airfoil spacing.

Oscillations of the airfoil immediately beneath the instrumented airfoil, Figure 4.47, causes larger lower surface unsteady pressures for the high solidity cascade, another consequence of the difference in airfoil spacing. The upper surface pressure magnitudes are approximately the same for the two cascades. The phase distributions are generally dissimilar except for the forward half of the airfoil lower surface.

Differences in $|\hat{C}_p^{-2}|$, Figure 4.48, confirm the adverse effect of the cascade wall on the upper surface pressures in the low solidity cascade. As discussed previously, reflections off the adjacent wall of the wind tunnel are believed to be the reason for values of $|\hat{C}_p^{-2}|$ which are, for the low solidity cascade, largest on the airfoil upper surface. In contrast, this figure shows that the high solidity cascade upper surface magnitudes are the smallest of all. That the airfoil upper surface was, in the high solidity cascade, separated from the wind tunnel wall by two airfoils is the critical factor.

Effect of Mean Flow Incidence Angle

Data taken in the high solidity cascade configuration for two incidence angles, 0 and 7 degrees, allow the effect of the mean flow incidence angle and the associated differences in the steady flow field on the unsteady aerodynamics to be investigated. For 0.65 inlet Mach number and 0.22 reduced frequency, incidence angle crossplots are presented for the various relative positions of the oscillating airfoil in Figures 4.49 through 4.53.

Mean flow incidence angle has little effect on the self-induced unsteady pressure coefficients, Figure 4.49. Except for the large magnitude on the upper surface at 12% of chord for 7 degrees of incidence, the distributions are the same. The large response

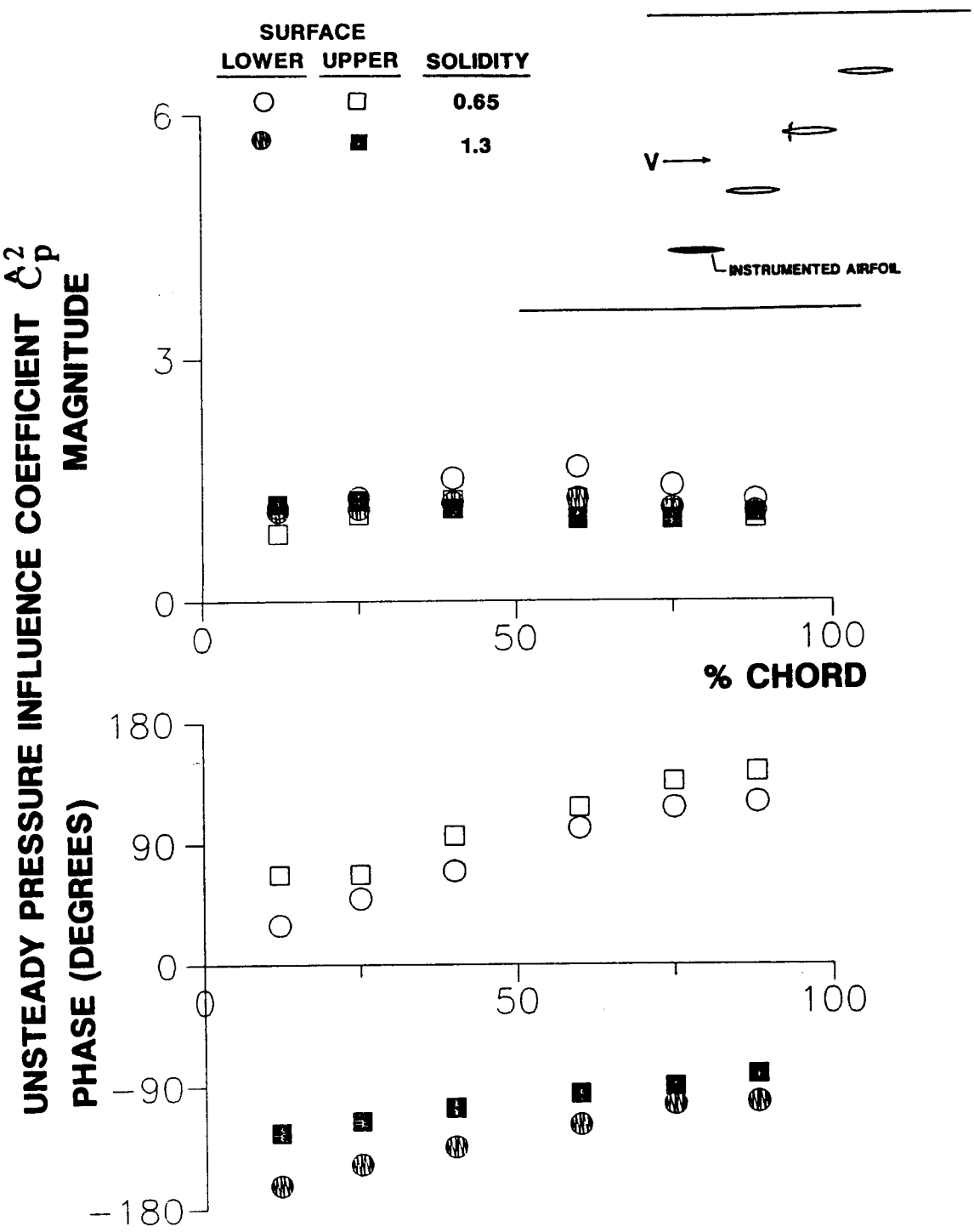

Figure 4.46 Effect of cascade solidity on unsteady pressure influence coefficient, oscillating airfoil in relative position 2, M = 0.80, k = 0.32

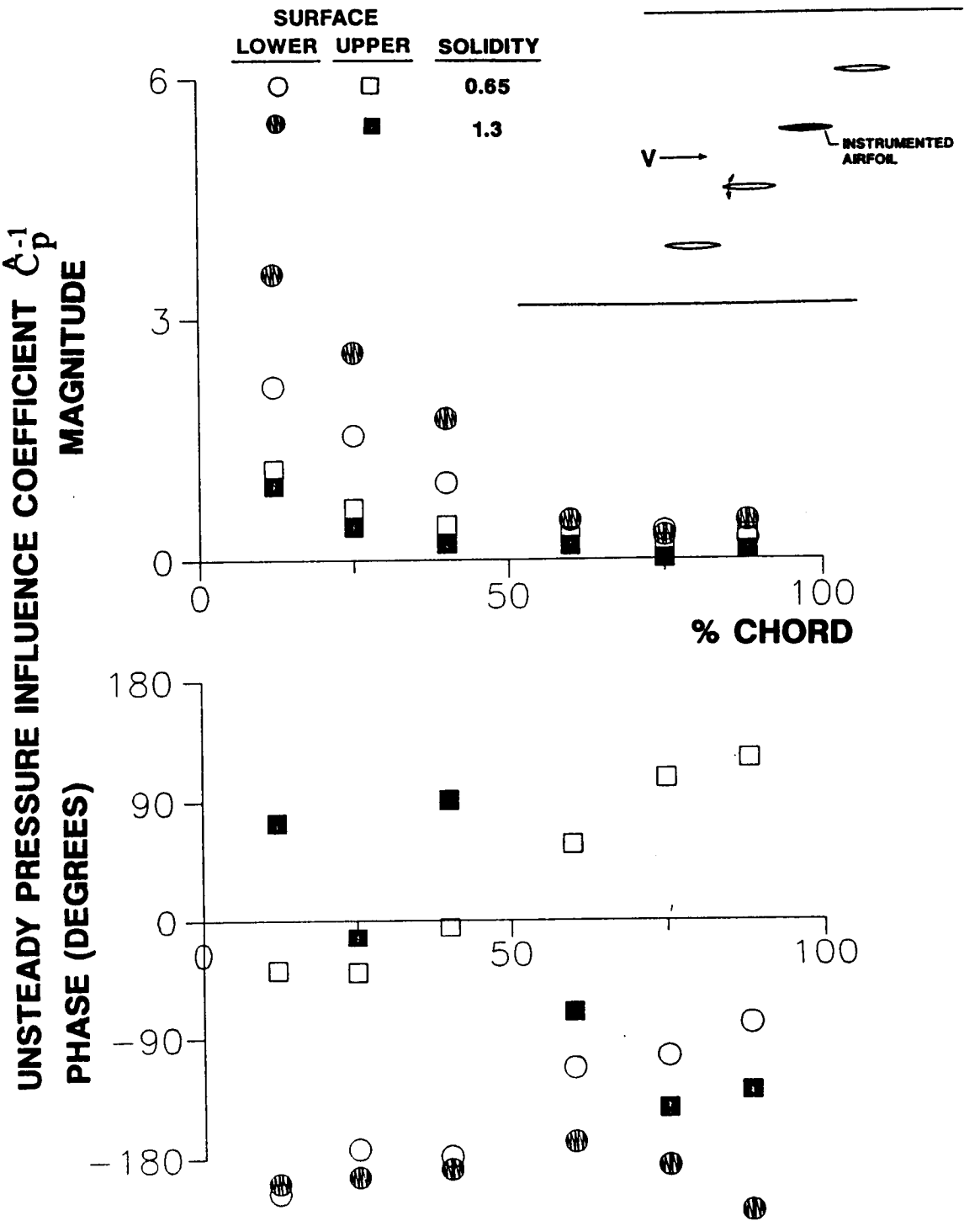

Figure 4.47 Effect of cascade solidity on unsteady pressure influence coefficient, oscillating airfoil in relative position -1, M=0.80, k=0.32

C-2

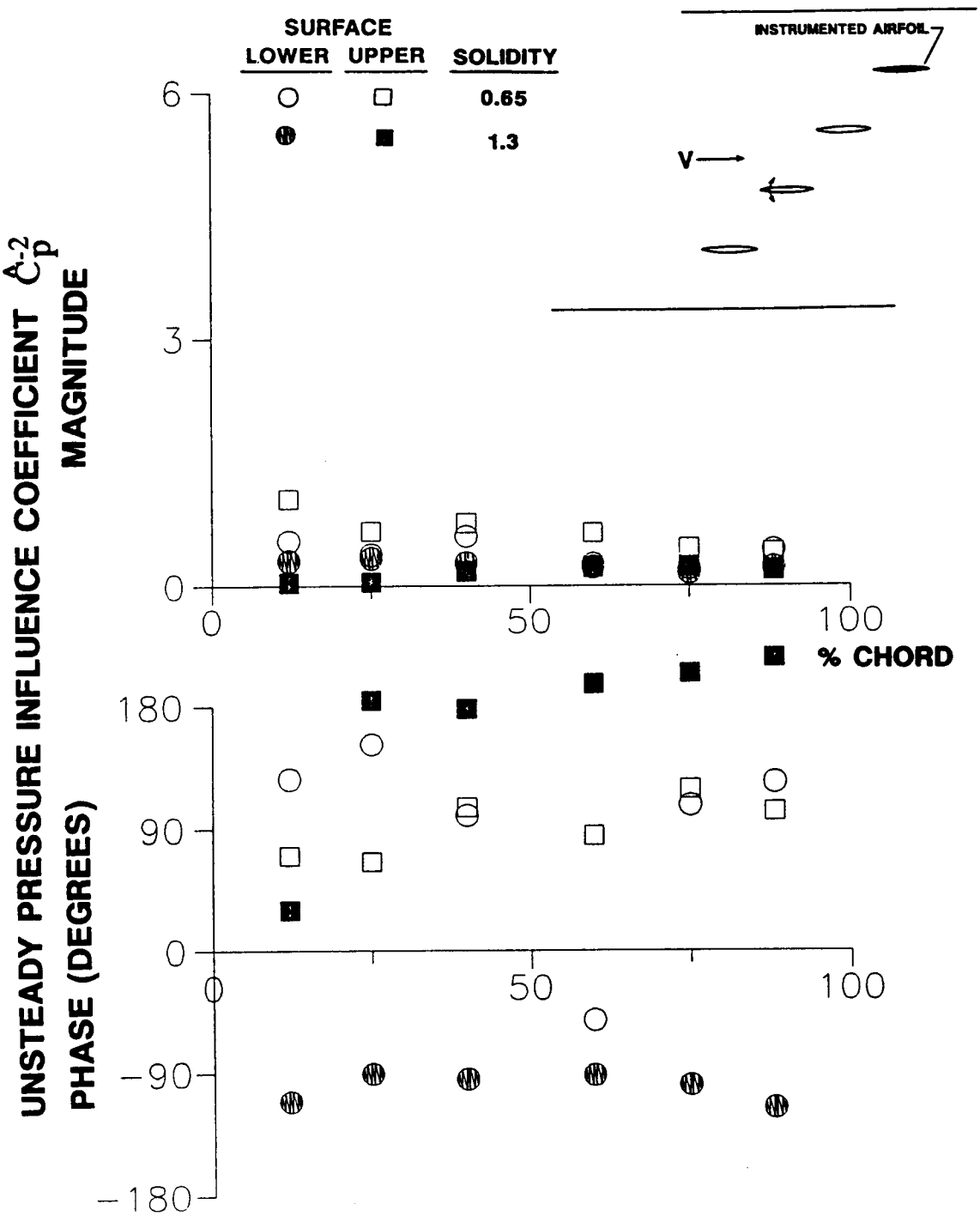

Figure 4.48 Effect of cascade solidity on unsteady pressure influence coefficient, oscillating airfoil in relative position -2, M = 0.80, k = 0.32

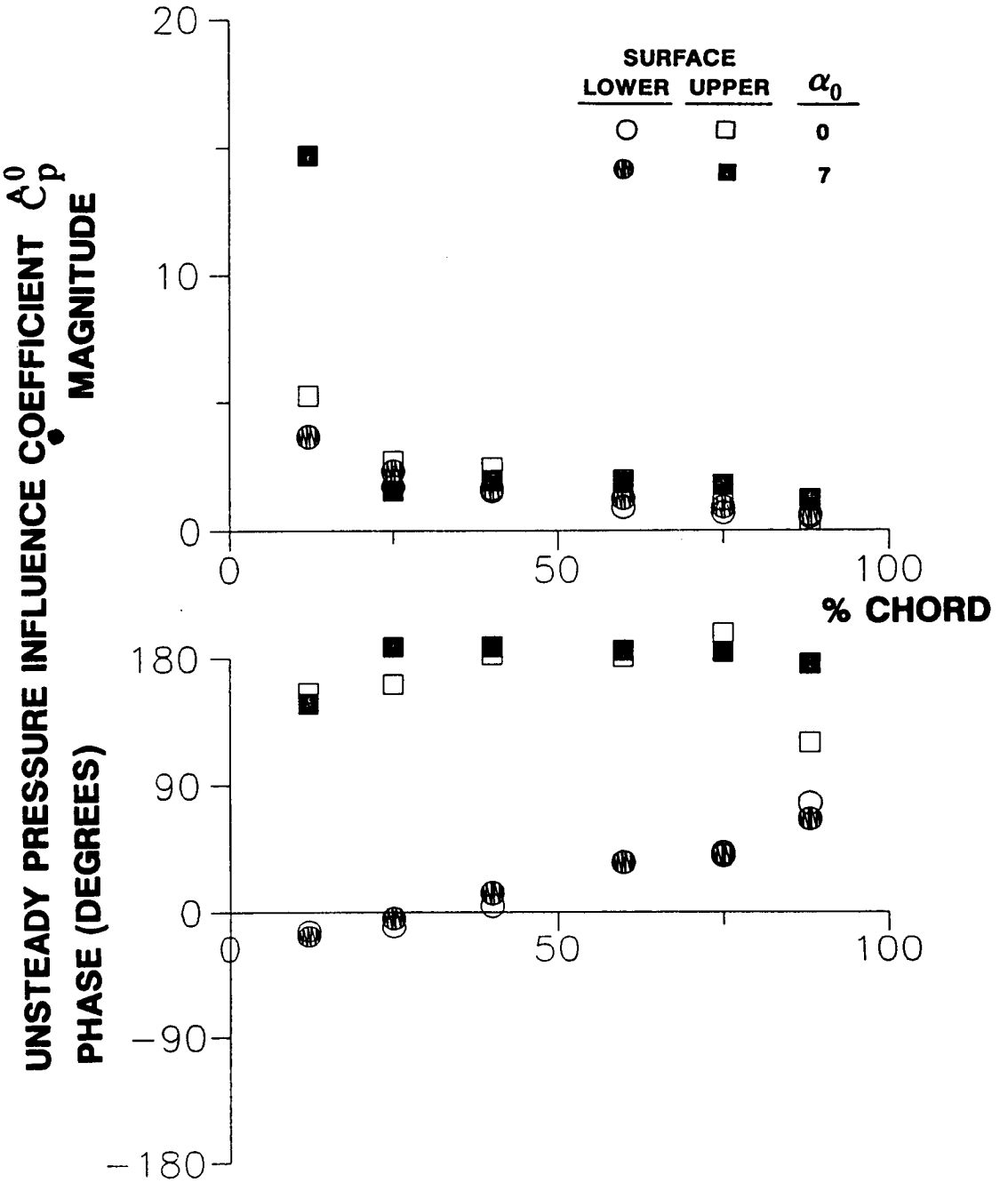

Figure 4.49 Effect of mean flow incidence angle on unsteady pressure influence coefficient, oscillating airfoil in relative position 0, high solidity cascade, M = 0.65, k = 0.22

there is due to a small, oscillating separation bubble near the leading edge on the upper surface. The presence of separation was first indicated by significant higher harmonic content in the leading upper surface pressure transducer signal. Steady state flow visualization with airfoil 0 at 8.2 degrees of incidence then confirmed the presence of a small separated region near the leading edge.

Differences in the other influence coefficients due to incidence angle are generally small. For $\hat{C}_p^1$, Figure 4.50, phase differences are small with only the magnitude on the aft half of the airfoil upper surface affected. Larger magnitudes occur there for zero incidence. Some differences in phase are found in the chordwise distribution of $\hat{C}_p^2$, Figure 4.51, but the magnitude differences are small. Incidence angle does affect $\hat{C}_p^{-1}$, Figure 4.52, to some extent: the lower surface magnitudes are generally larger for the higher incidence angle, and the upper surface separation bubble is caused to oscillate, resulting in a spike in the unsteady upper surface pressure at 12% of chord. There are also differences in the upper surface phase distributions, but the upper surface amplitudes are generally so small that these differences are insignificant. Values of $\hat{C}_p^{-2}$, Figure 4.53, are also very small except for some response on the lower surface for zero incidence.

4.2.3 Summation of Influence Coefficients

Summation of the experimentally-determined influence coefficients to determine the unsteady pressure difference coefficient is depicted in Figures 4.54 and 4.55 for low solidity cascade data. The 0.55 inlet Mach number, 0.45 reduced frequency data are presented as a dynamic pressure difference coefficient for interblade phase angles of 0 and 180 degrees, with N specifying the limits of the sum per Equation 1.1. Thus N = 0 corresponds to the self-induced unsteady aerodynamic

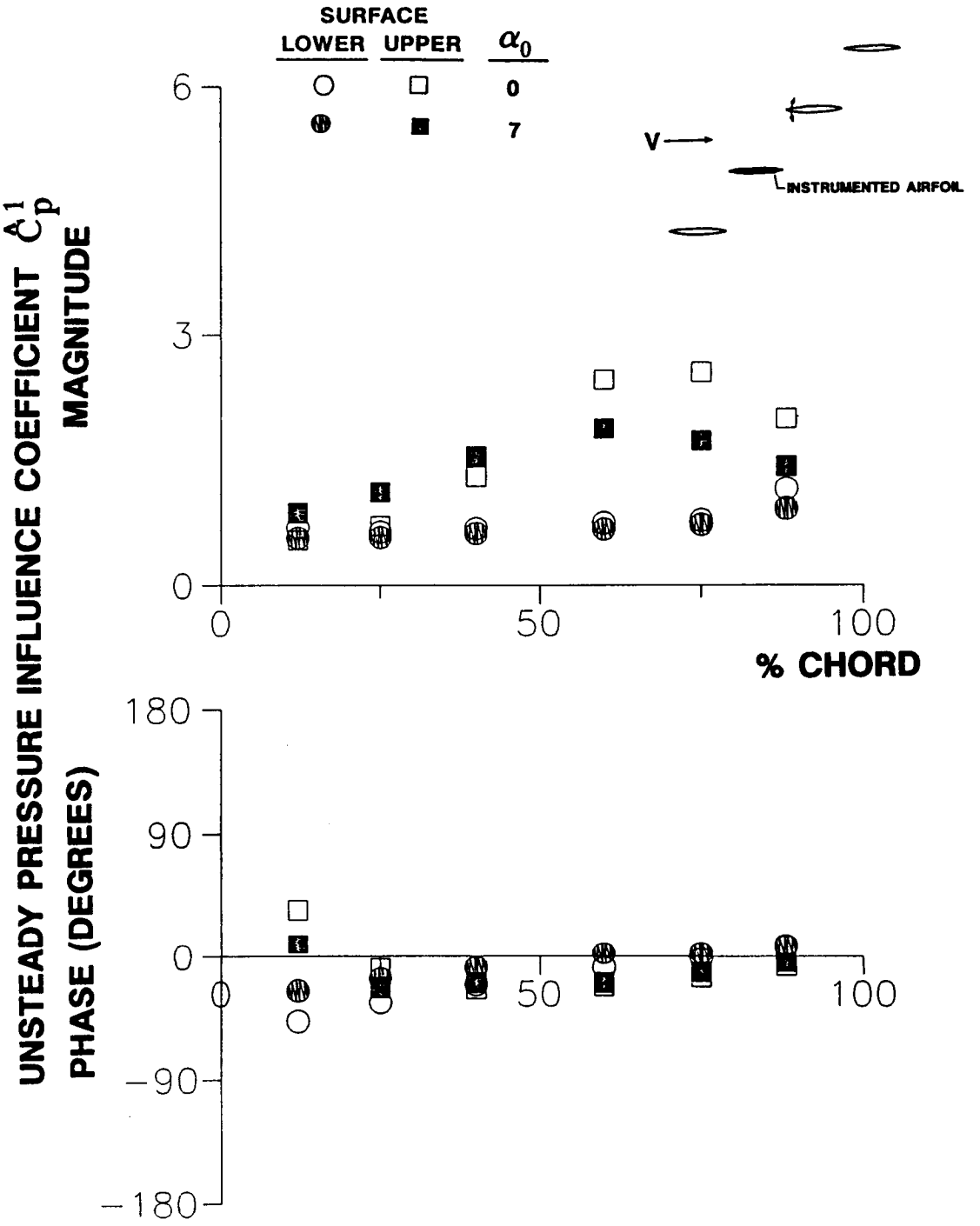

Figure 4.50 Effect of mean flow incidence angle on unsteady pressure influence coefficient, oscillating airfoil in relative position 1, high solidity cascade, M = 0.65, k = 0.22

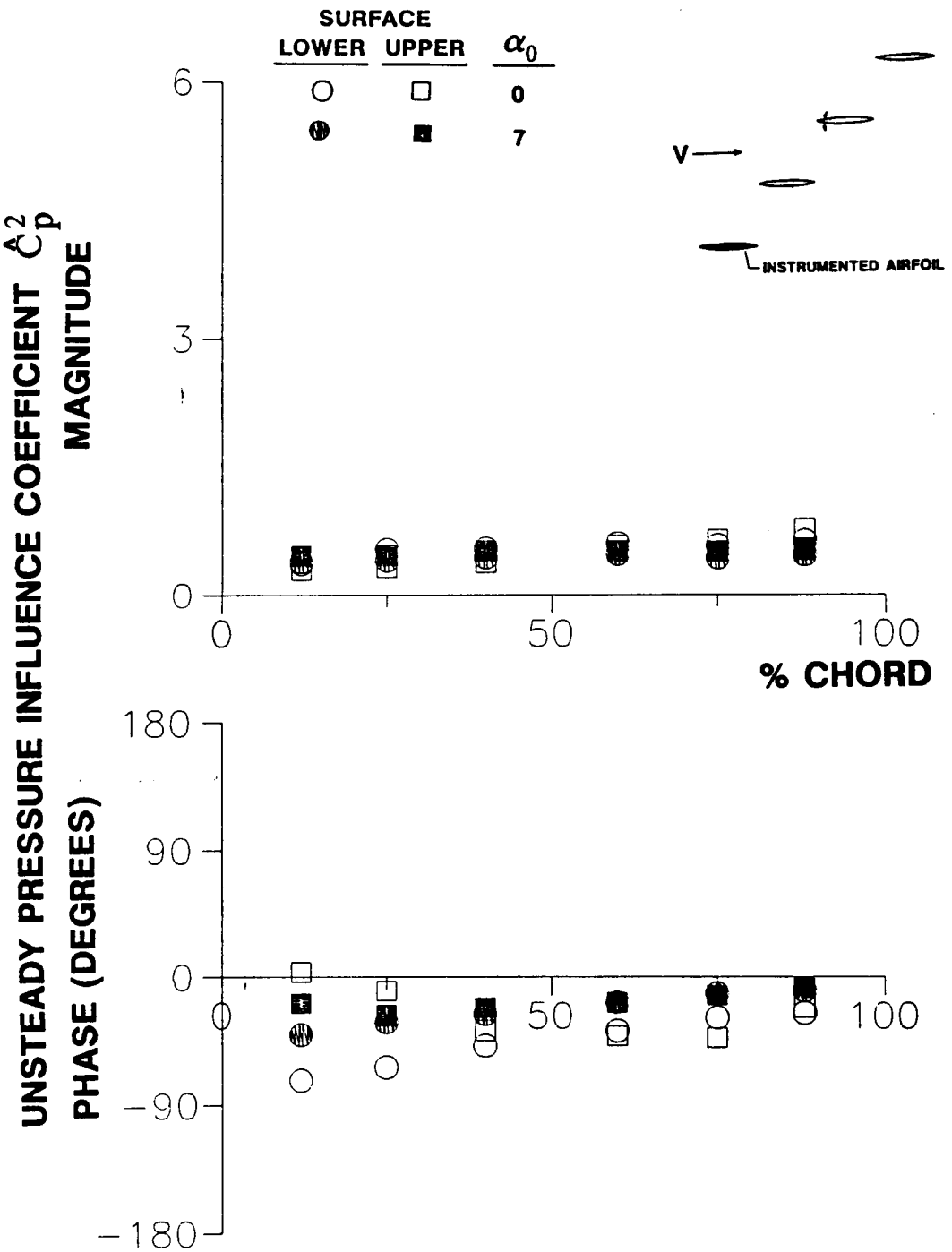

Figure 4.51 Effect of mean flow incidence angle on unsteady pressure influence coefficient, oscillating airfoil in relative position 2, high solidity cascade, M = 0.65, k = 0.22

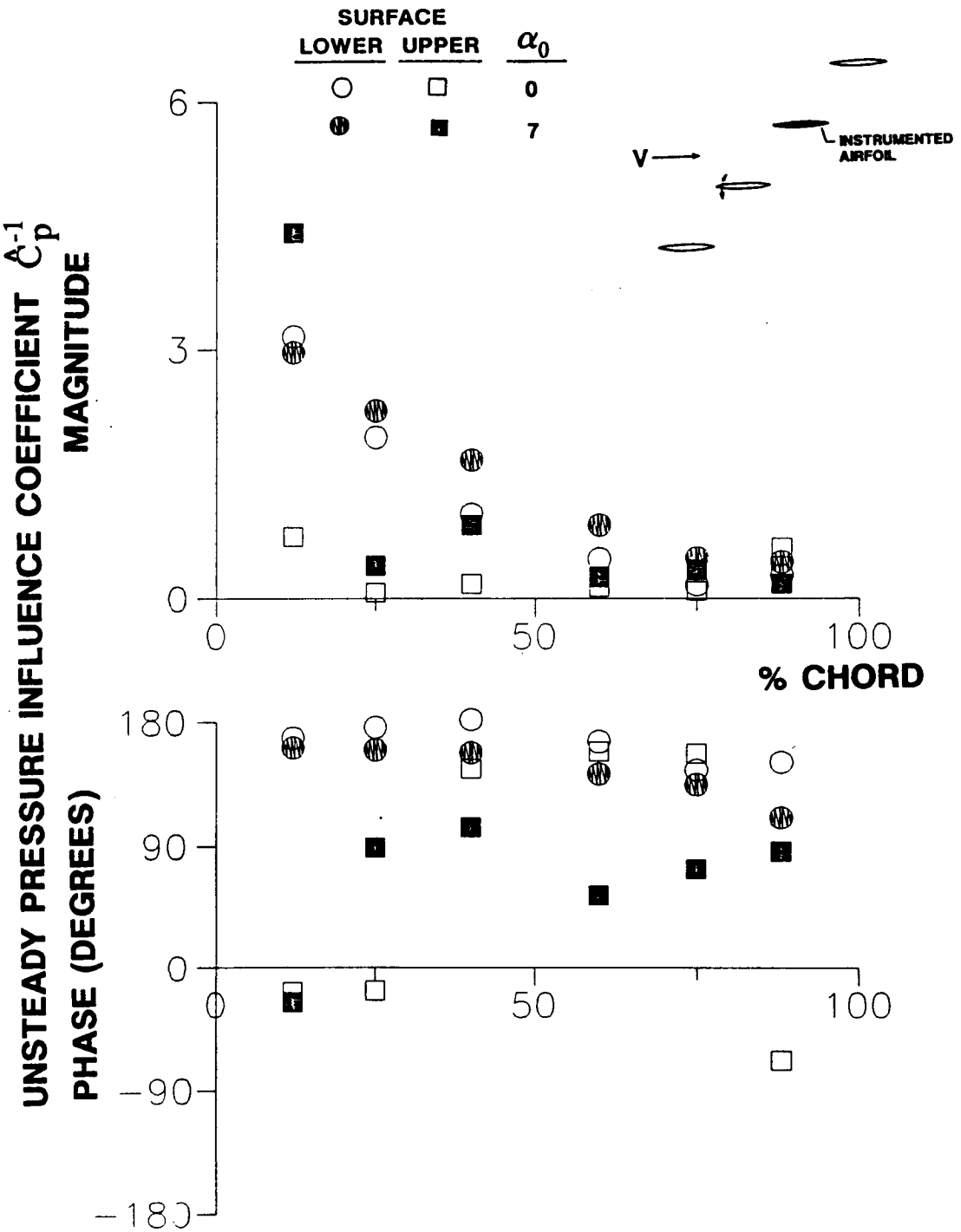

Figure 4.52 Effect of mean flow incidence angle on unsteady pressure influence coefficient, oscillating airfoil in relative position -1, high solidity cascade, M = 0.65, k = 0.22

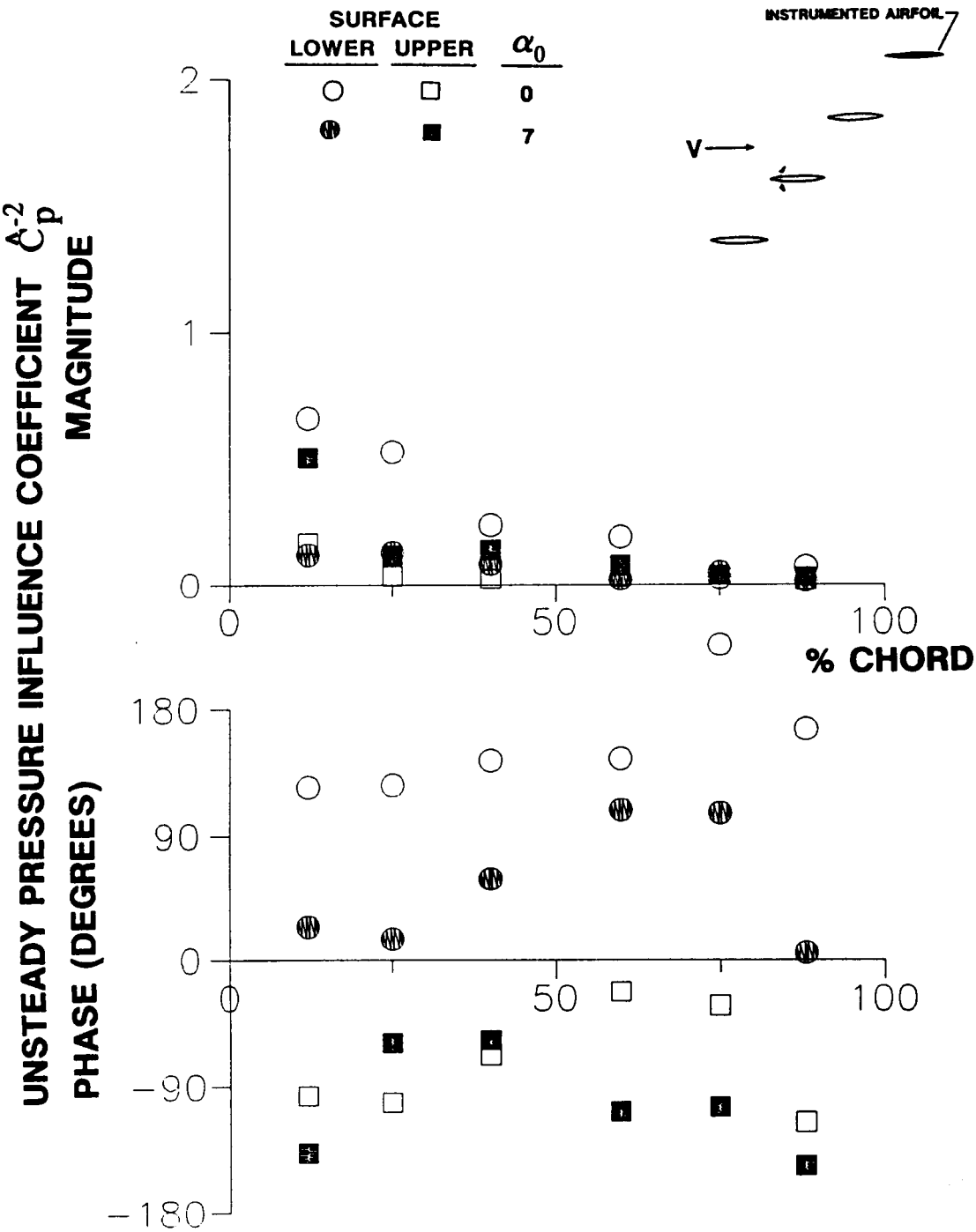

Figure 4.53 Effect of mean flow incidence angle on unsteady pressure influence coefficient, oscillating airfoil in relative position -2, high solidity cascade, M = 0.65, k = 0.22

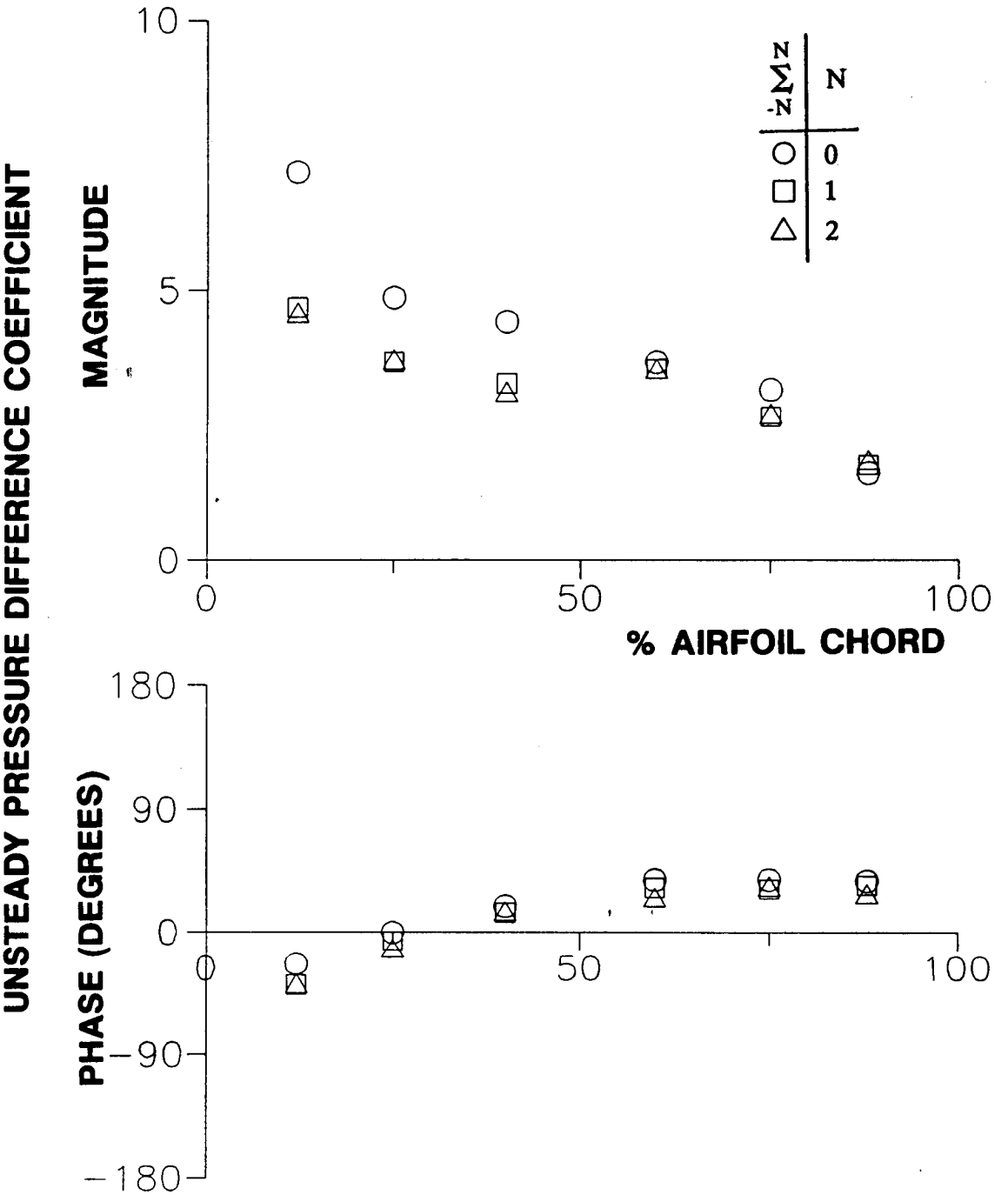

Figure 4.54 Summation of airfoil surface unsteady pressure difference influence coefficients, M=0.55, k=0.45, β=0 degrees

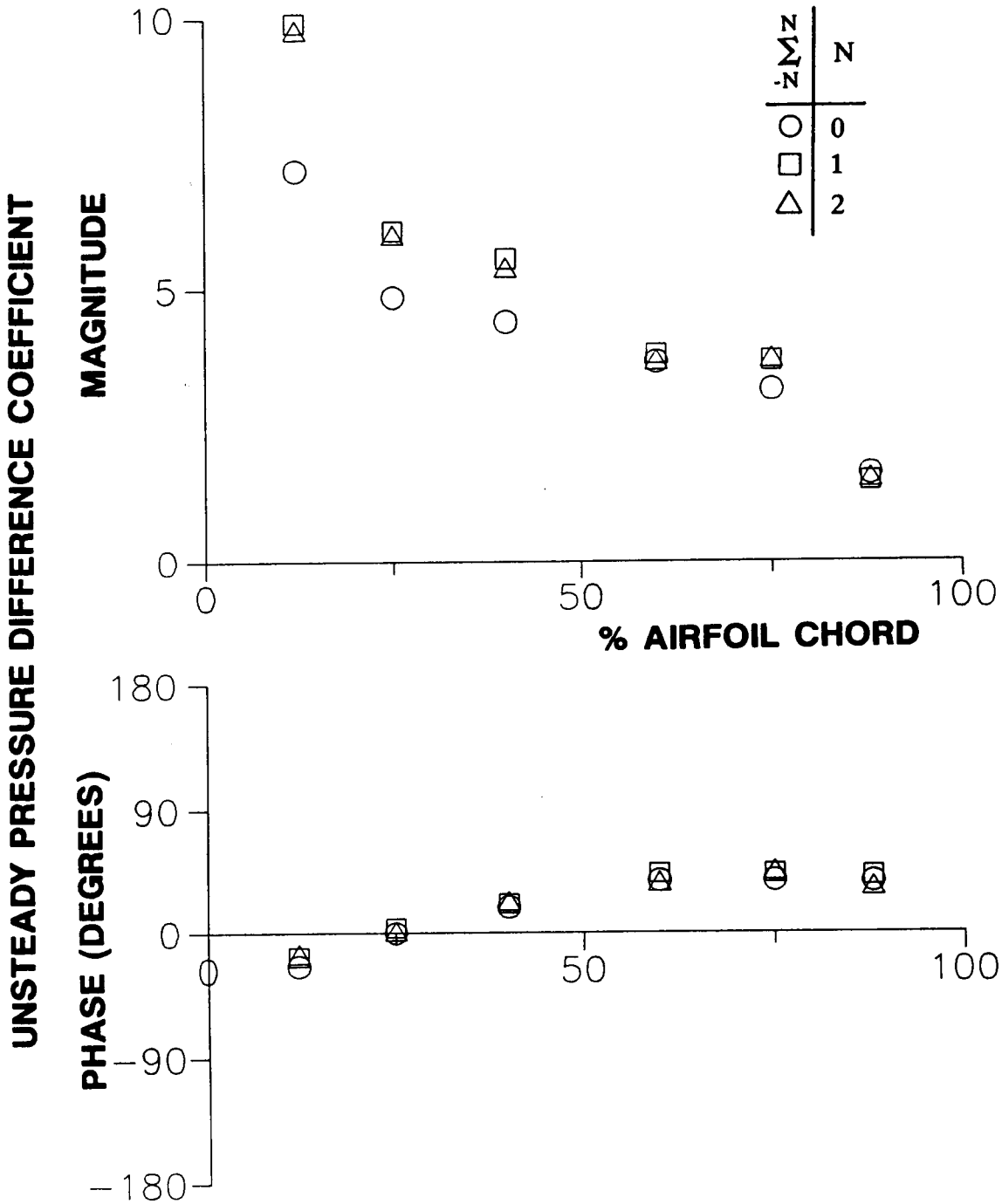

Figure 4.55 Summation of airfoil surface unsteady pressure difference influence coefficients, M=0.55, k=0.45, β=180 degrees

response. The influence coefficient series for ΔC_p is rapidly convergent, with only the reference airfoil and its two immediate neighbors having a significant effect on the resulting dynamic pressure differences.

In contrast, the series for the airfoil individual surface static pressure coefficient C_p is not necessarily convergent. For example, Figures 4.56 and 4.57 demonstrate summation of the lower surface pressure coefficients for M=0.55, k=0.45, in-phase and out-of-phase oscillations. In both of these cases, the series are not convergent over the range for which data are available: the phase is varying rapidly with N for $\beta = 0°$ while the magnitude is not converging for $\beta = 180°$. This is mainly due to the large magnitudes of $\hat{C}_p^n$ when $n>0$. That the series for the unsteady pressure difference coefficient is convergent despite this is because the pressures due to the upstream traveling wave largely cancel when the pressure difference is taken. This can be seen in Figures 4.31 and 4.36, where the complex individual surface values of $\hat{C}_p^2$ are approximately equal and thus cancel when the pressure difference is calculated. While the individual surface influence coefficients are of significant magnitude, the pressure difference influence coefficient is insignificant.

Since the amplitude of $\hat{C}_p^2$ increases with reduced frequency, lowering the reduced frequency should result in a C_p series with better convergence properties. This effect is shown in Figures 4.58 and 4.59, where a reduction in k to 0.20 while keeping the same Mach number and interblade phase angles results in good convergence for the airfoil lower surface unsteady pressure coefficient.

4.2.4 Correlation of Data

Experimental results consisting of unsteady airfoil surface pressure difference coefficients obtained via summation of influence coefficients and the corresponding data obtained when all the airfoils are oscillating simultaneously with a constant

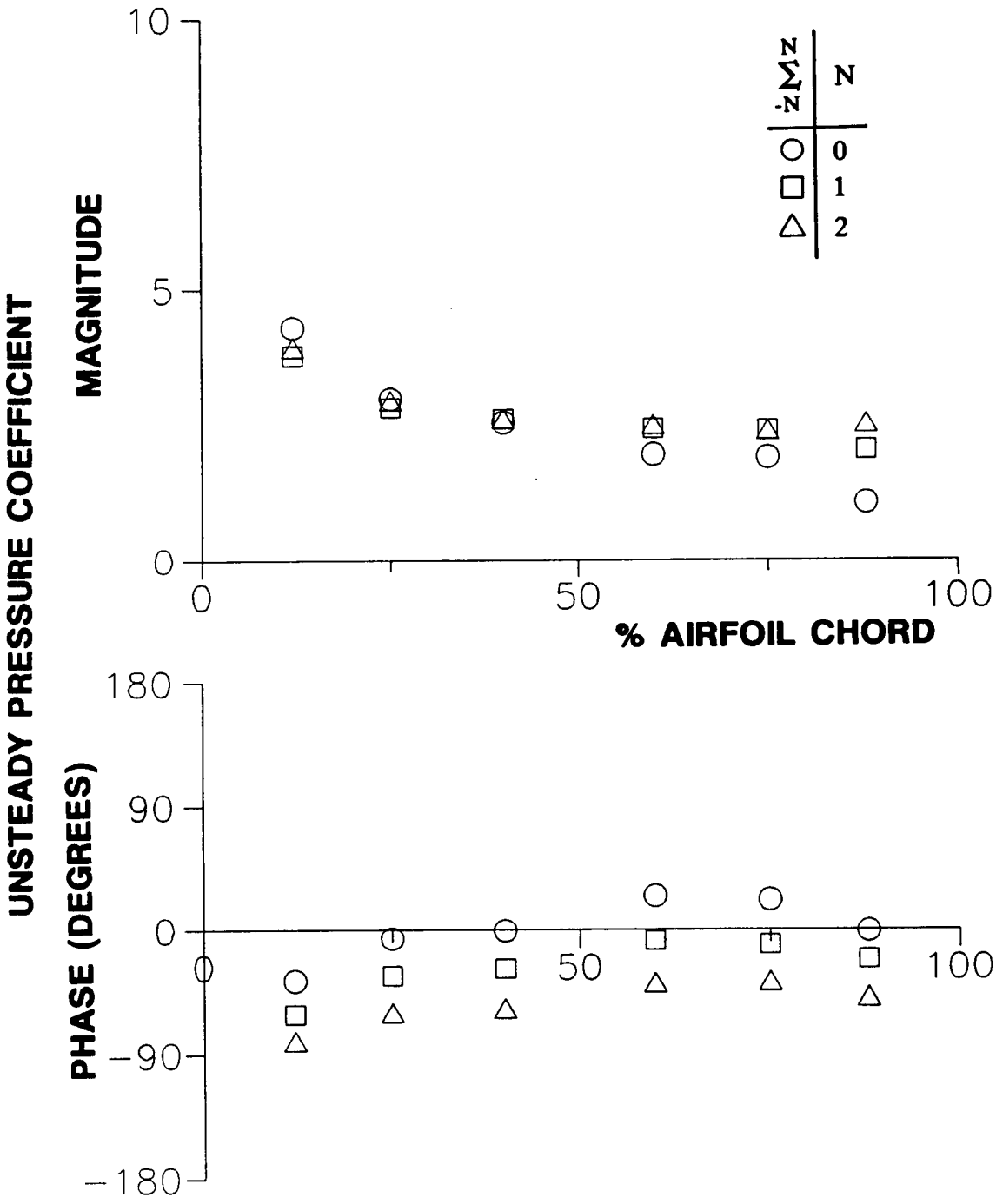

Figure 4.56 Summation of airfoil lower surface unsteady pressure influence coefficients, M = 0.55, k = 0.45, β = 0 degrees

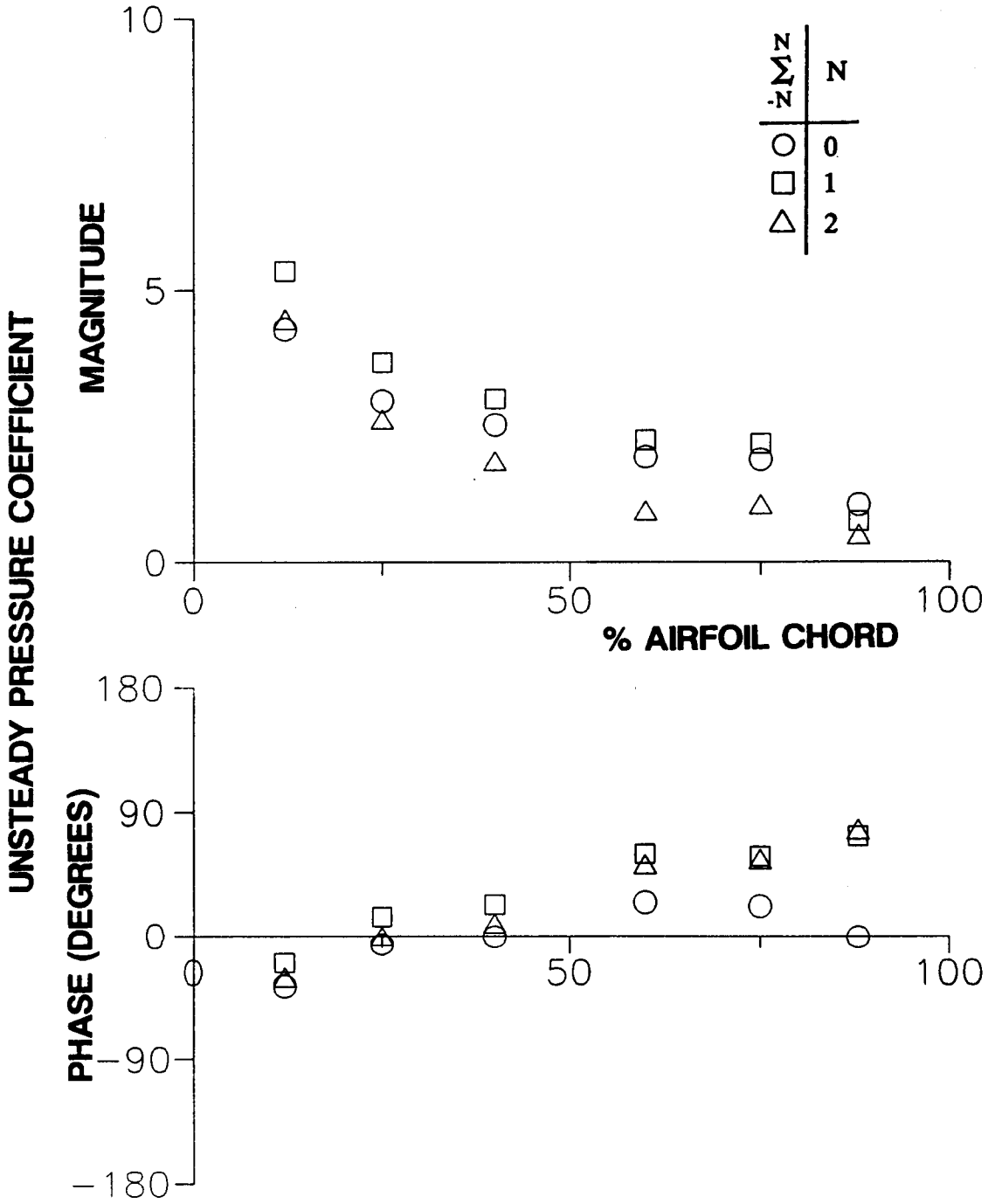

Figure 4.57 Summation of airfoil lower surface unsteady pressure influence coefficients, M = 0.55, k = 0.45, β = 180 degrees

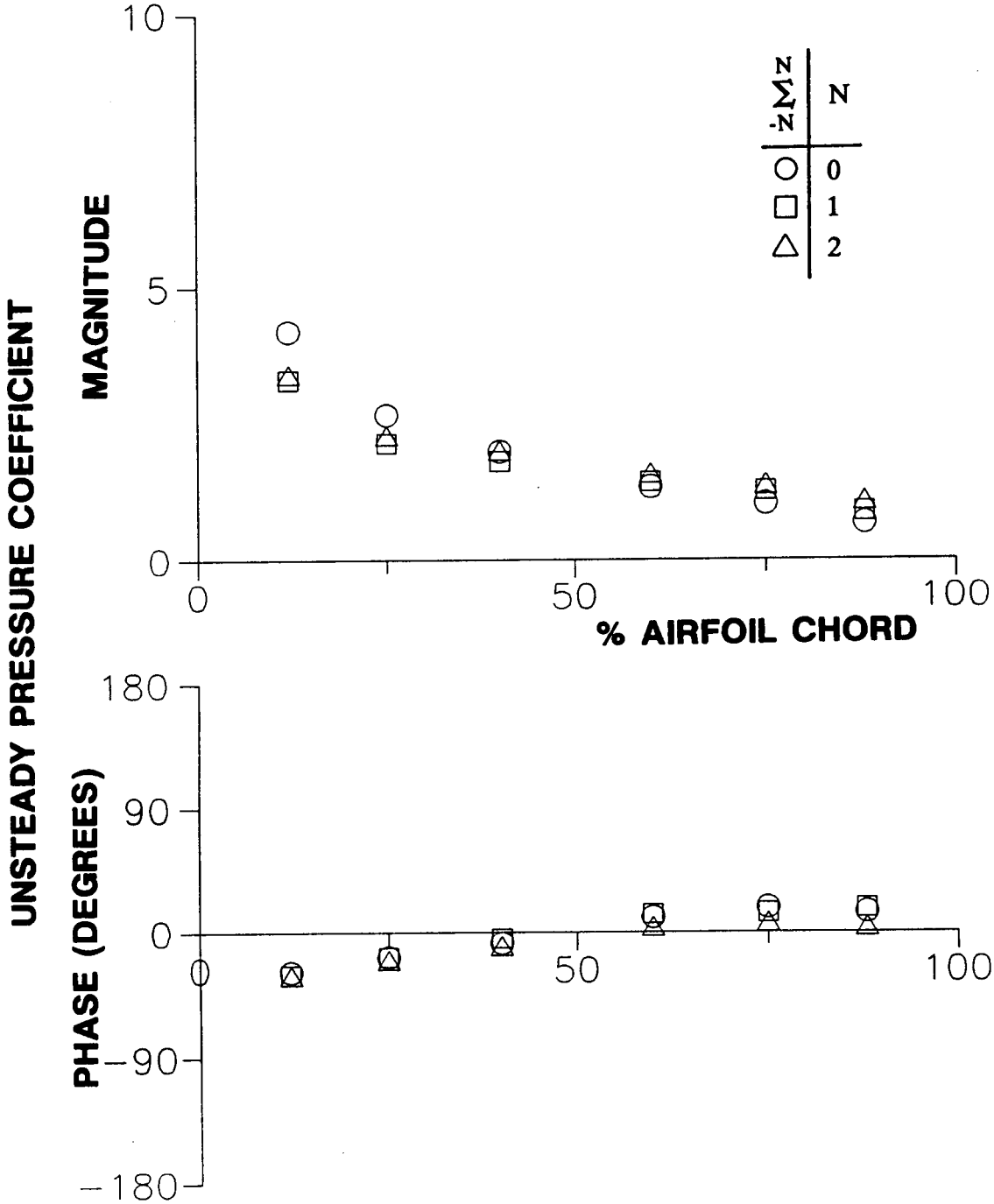

Figure 4.58 Summation of airfoil lower surface unsteady pressure influence coefficients, M=0.55, k=0.20, β=0 degrees

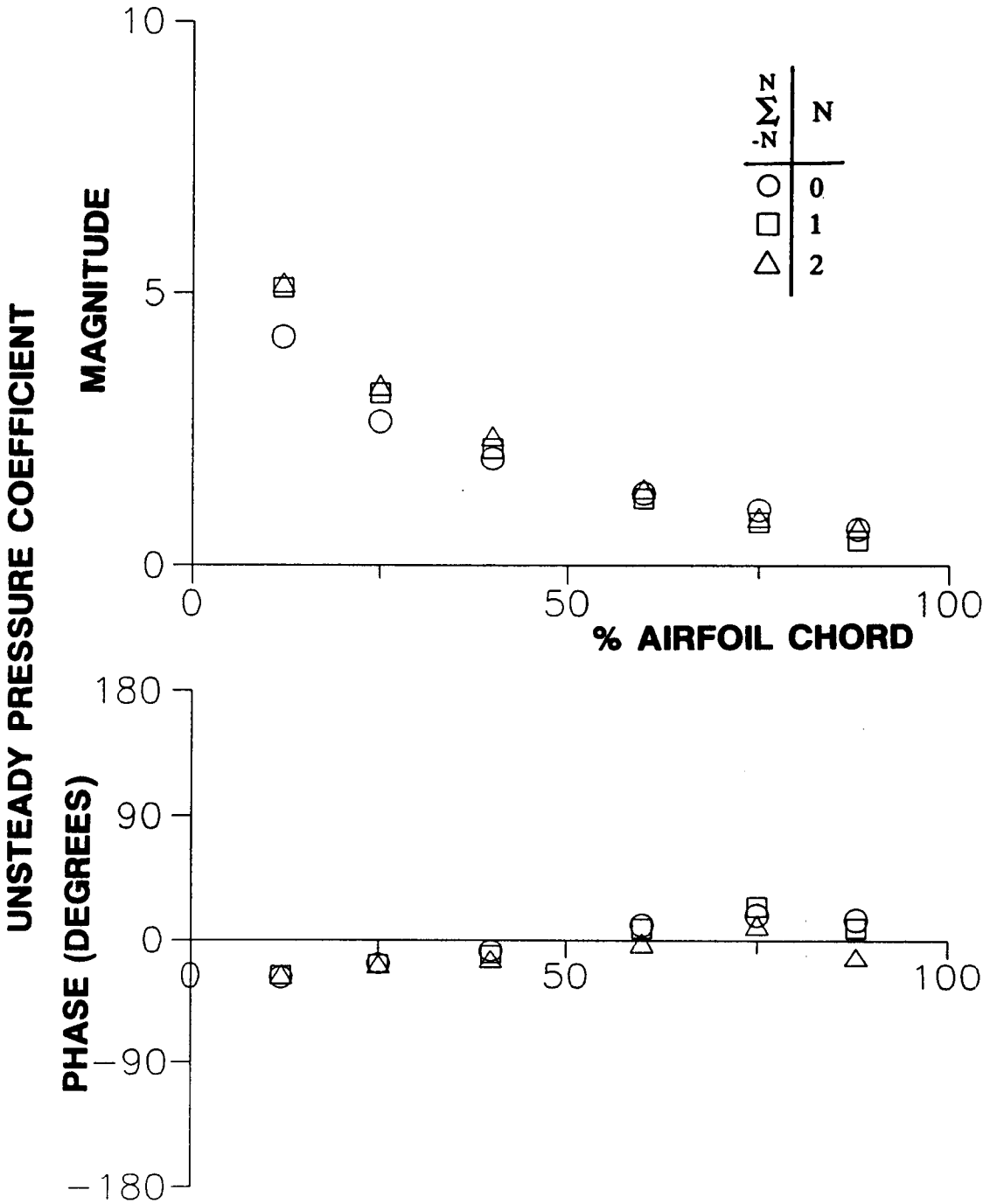

Figure 4.59 Summation of airfoil lower surface unsteady pressure influence coefficients, M = 0.55, k = 0.20, β = 180 degrees

interblade phase angle are presented. These experimental data are correlated with the analysis of Smith, reference 3. Smith's analysis is based upon the assumptions of inviscid, isentropic, subsonic flow through an infinite cascade of flat plate airfoils. The analysis also assumes that the airfoils are at zero mean incidence, and that the airfoil oscillations create small unsteady disturbances to the uniform mean flow. Summation of the influence coefficient experimental data makes use of all the available experimental data, that is, N=2 in Equation 1.1. Predictions obtained from Smith's analysis via the influence coefficient technique, as explained in Chapter 1, are also presented for N=2.

Low Solidity Cascade

For a reduced frequency of 0.32 and a range of interblade phase angles from -90 degrees to 180 degrees, Figures 4.60 through 4.71 present low solidity cascade results for inlet Mach numbers of 0.55 and 0.80. For superresonant in-phase oscillations with M=0.55, Figure 4.60, the two experimental data sets correlate very well with each other in both magnitude and phase. The magnitudes predicted by Smith's linearized analysis are in very good agreement with the experimental data and the analytical influence coefficient predictions for $N=2$. The analytically-determined phase distributions are offset from the experimental data by a small amount. The good overall correlation found here is surprising considering the poor dynamic periodicity found for $\beta = 0°$ and M=0.55, Figure 4.8.

When the inlet Mach number is increased to 0.80, Figure 4.61, the correlation is not as good as for M=0.55. The two sets of experimental data are in good mutual agreement along the forward half of the airfoil, but aft of there, the experimentally-determined influence coefficient magnitudes are relatively small in comparison with the experimental all-airfoils-oscillating data. The analytical predictions are in very good mutual agreement, indicating that only a few oscillating

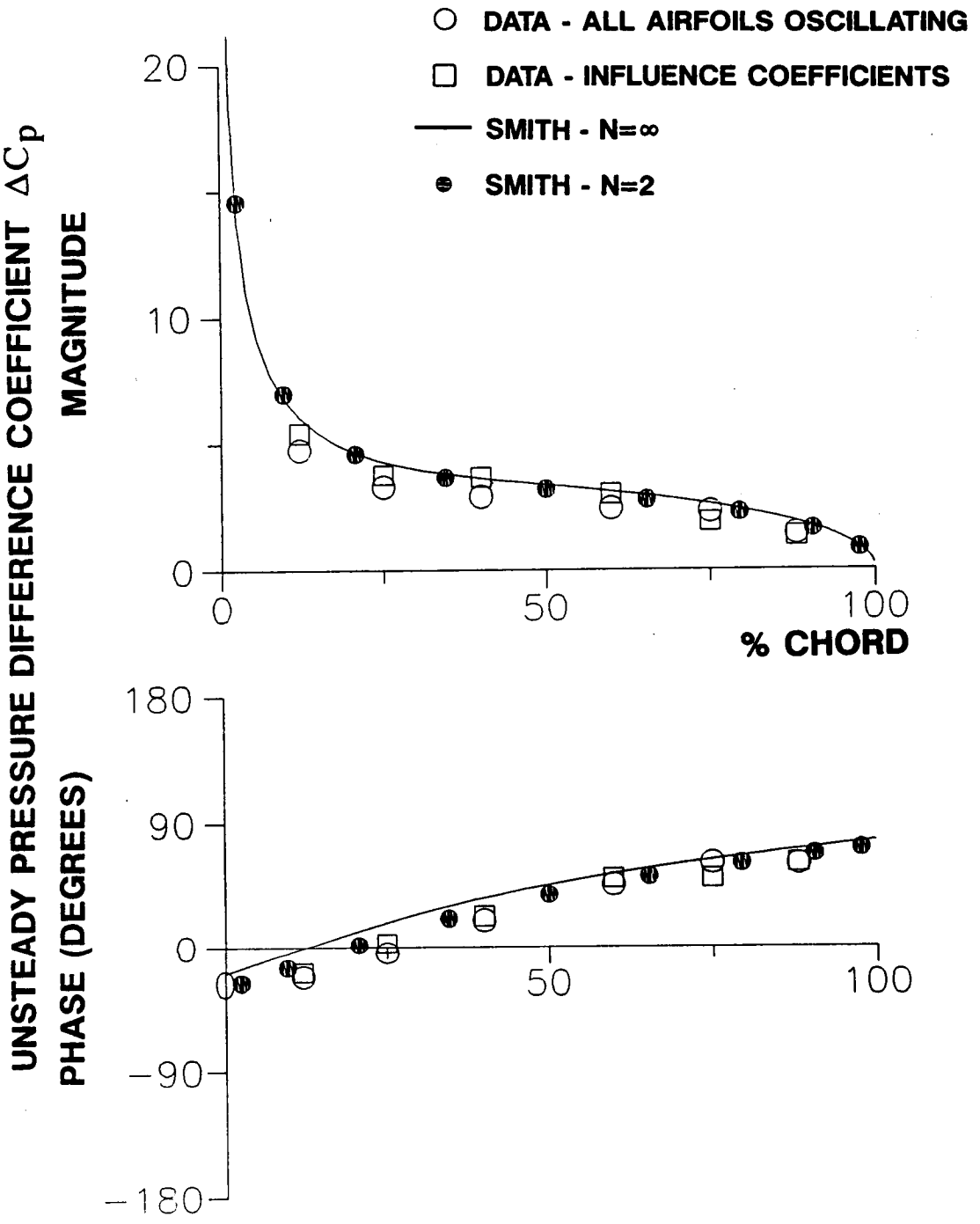

Figure 4.60 Unsteady pressure difference coefficient distribution, low solidity cascade, M=0.55, k=0.32, β=0

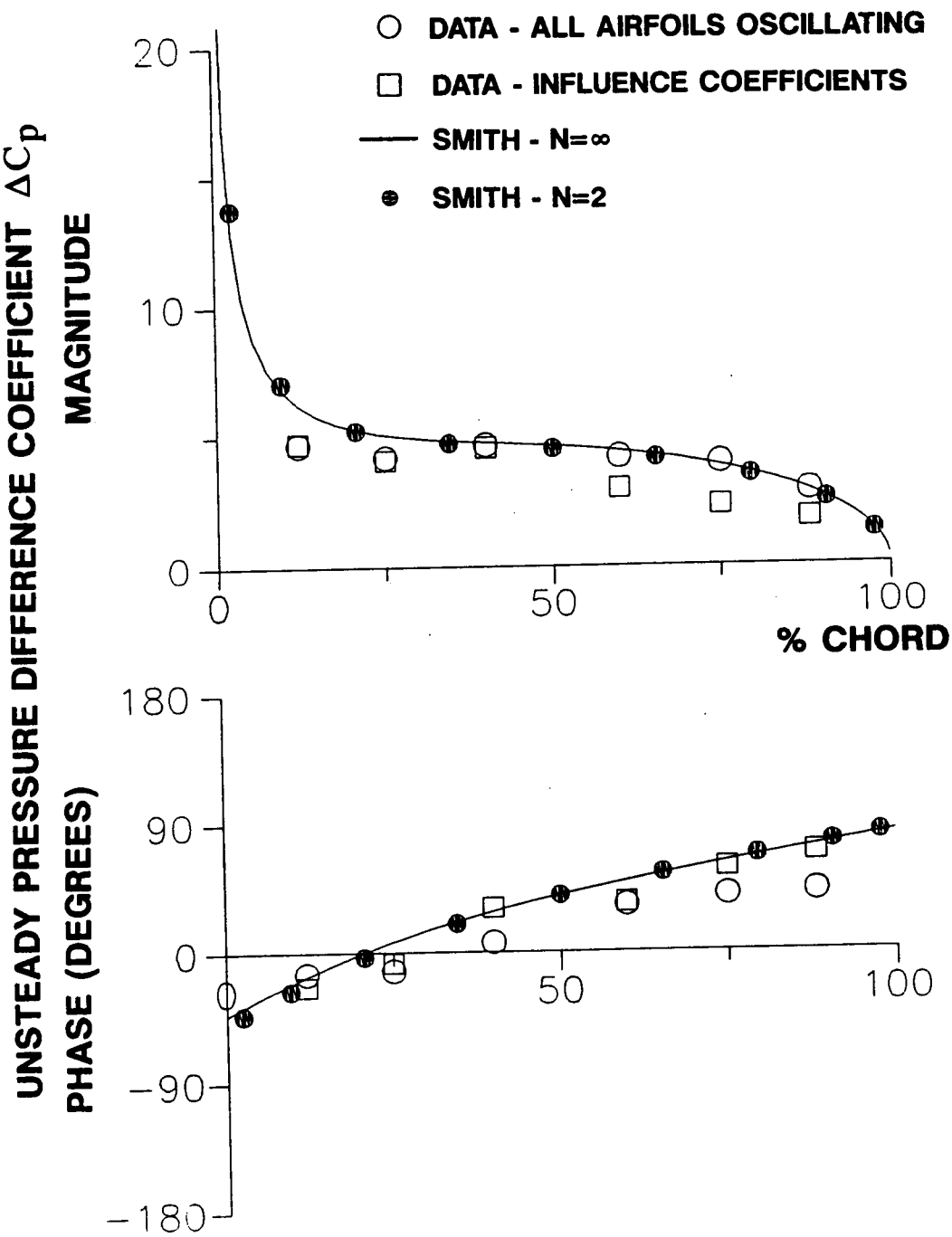

Figure 4.61 Unsteady pressure difference coefficient distribution, low solidity cascade, M=0.80, k=0.32, β=0

airfoils are required to accurately quantify the oscillating cascade aerodynamics at this flow condition. The correlation of the experimental data and the analytical predictions varies: the predicted magnitudes are in better agreement with the experimental all-airfoils-oscillating data than with the experimental influence coefficient data, but the predicted phase distributions better agree with the experimental influence coefficient data. Poor dynamic periodicity was found for this superresonant condition, Figure 4.14.

The data correlation for $\beta = 45°$ also varies with inlet Mach number. For both inlet Mach numbers, $\beta = 45°$ is superresonant. For M=0.55, Figure 4.62, the magnitude correlation is good but the phase variations are large. In particular, while the analytical results and the experimental influence coefficient phase data are in good agreement, the experimental all-airfoils-oscillating phase data generally have much more of a phase lead. For M=0.80, Figure 4.63, the level of correlation is reduced. The good magnitude correlation of the all-airfoils-oscillating experimental data and the analytical predictions is offset by their poor phase correlation. The influence coefficient data result in magnitudes about half that of the data for all-airfoils-oscillating, and phases which fall between the experimental all-airfoils-oscillating data and the analytical predictions. For both of these inlet Mach numbers, the dynamic periodicity for $\beta = 45°$ was found to be poor. This is shown in Figure 4.9 for an inlet Mach number of 0.55 and in Figure 4.15 for an inlet Mach number of 0.80.

In contrast, the correlation is very good for $\beta = -45°$, a subresonant condition, Figures 4.64 and 4.65. The only significant differences are found at the higher Mach number where there are some relatively small differences in the experimental

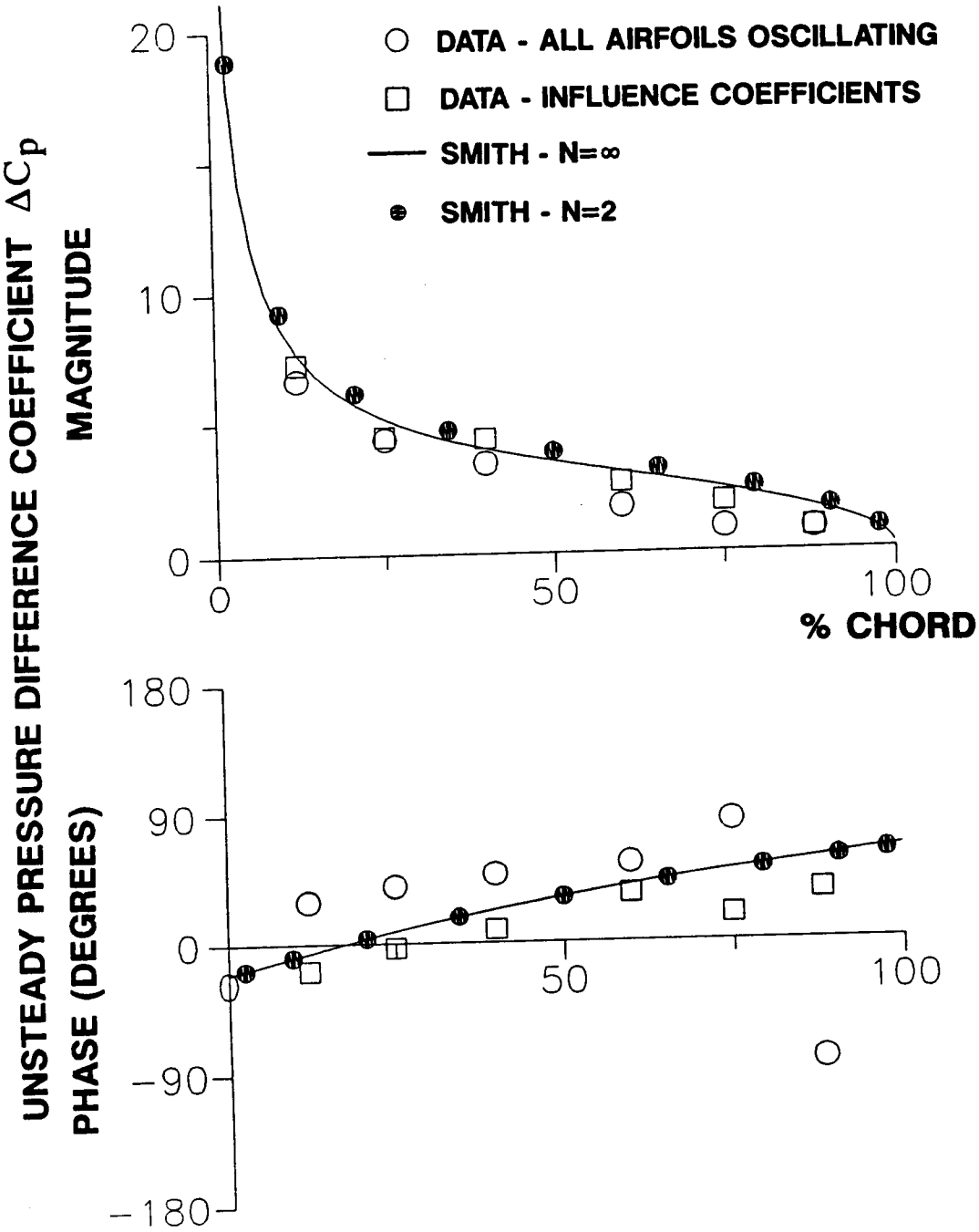

Figure 4.62 Unsteady pressure difference coefficient distribution, low solidity cascade, M = 0.55, k = 0.32, β = 45 degrees

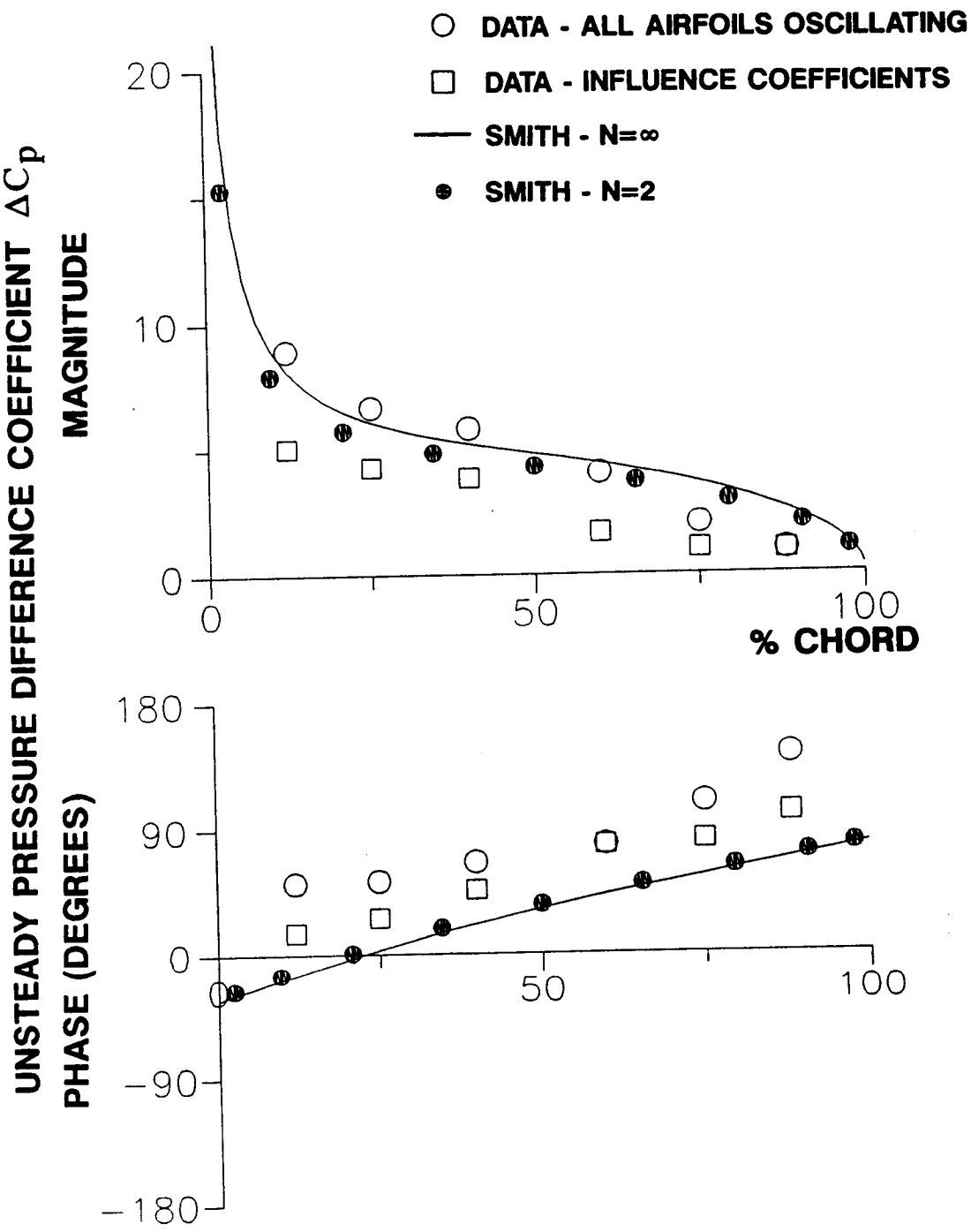

Figure 4.63 Unsteady pressure difference coefficient distribution, low solidity cascade, M=0.80, k=0.32, β=45 degrees

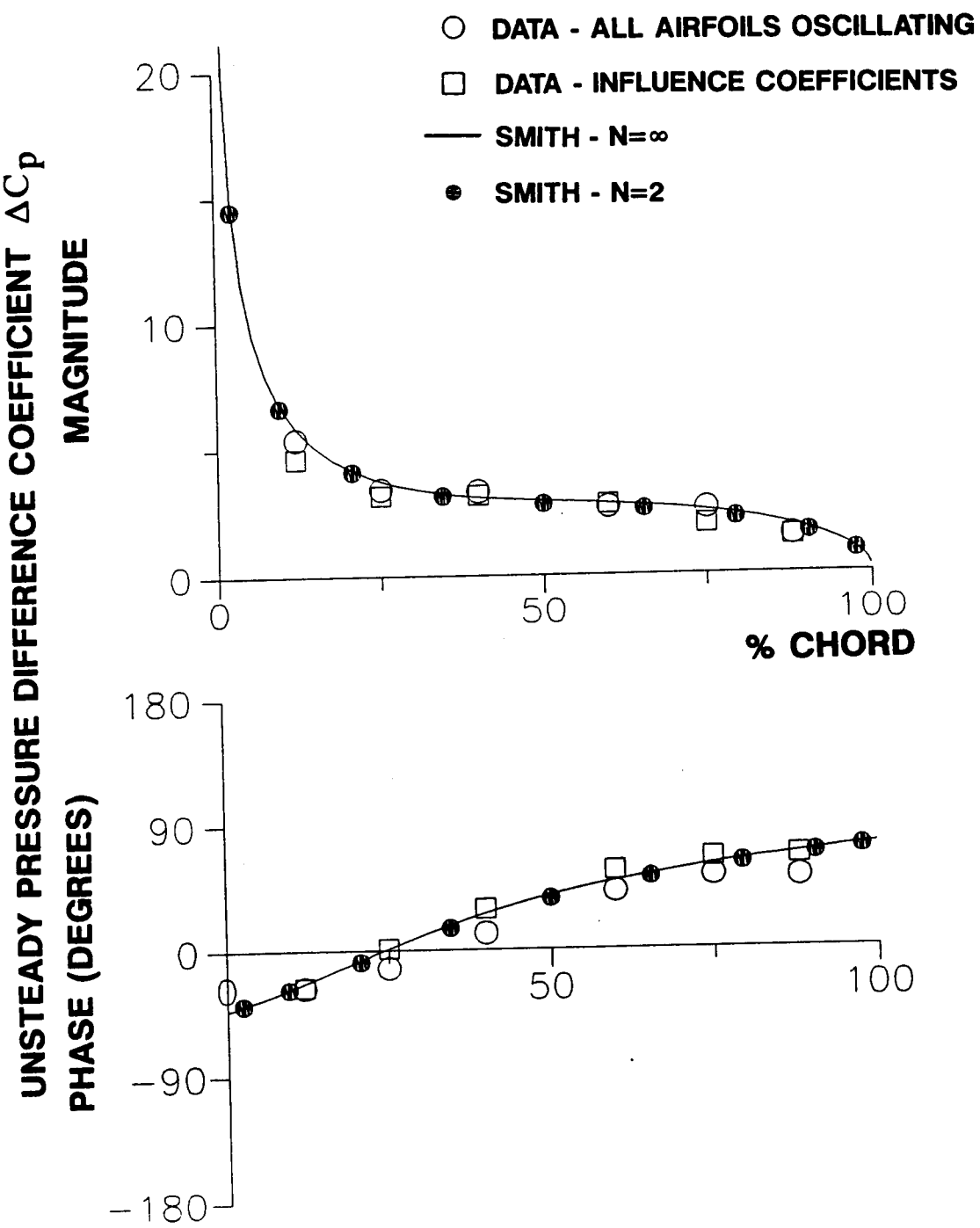

Figure 4.64 Unsteady pressure difference coefficient distribution, low solidity cascade, M=0.55, k=0.32, β=-45 degrees

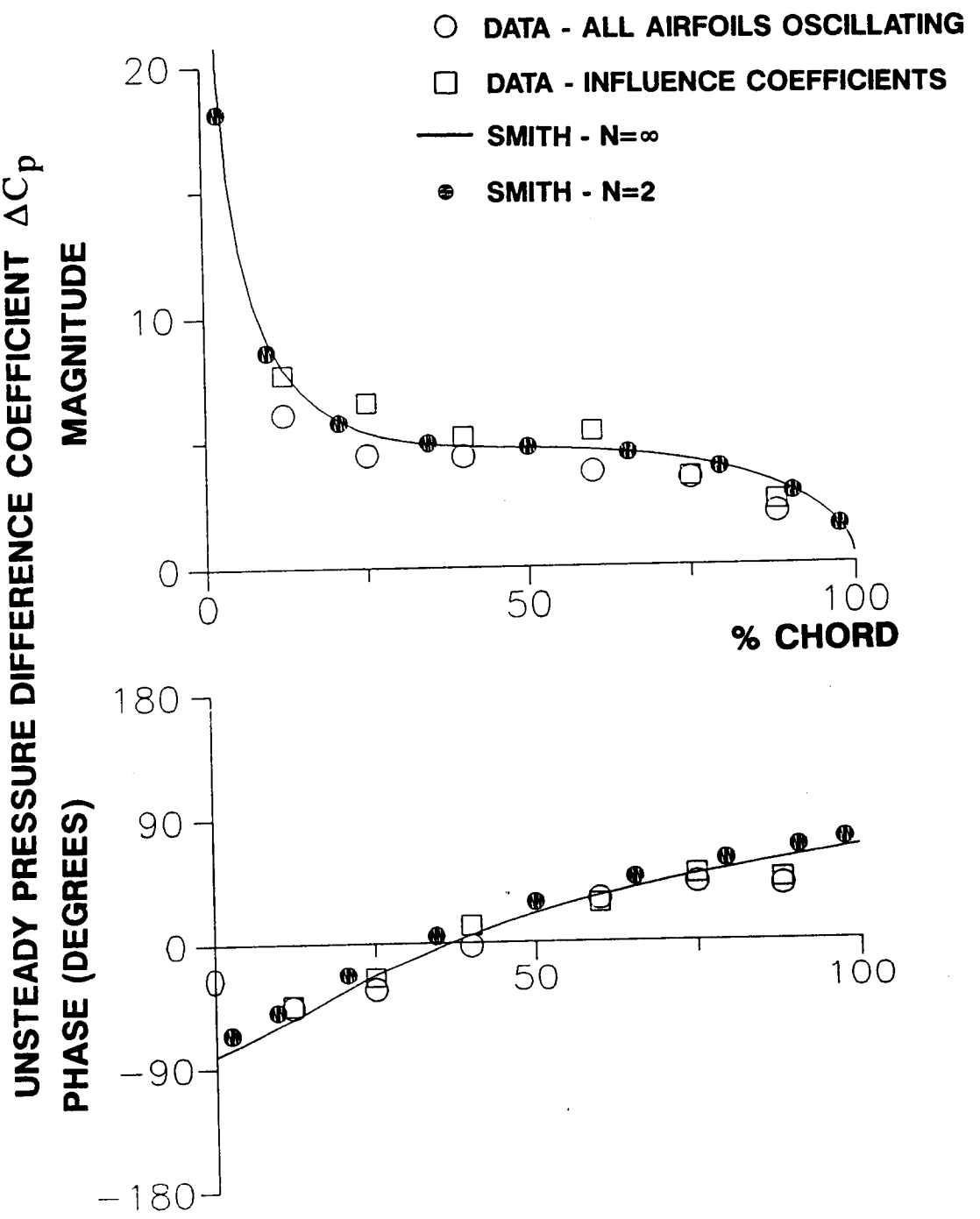

Figure 4.65 Unsteady pressure difference coefficient distribution, low solidity cascade, M=0.80, k=0.32, β=-45 degrees

magnitude data. As discussed in Section 4.2.1, relatively good dynamic periodicity was found at this value of interblade phase angle, Figure 4.10 for M=0.55 and Figure 4.16 for M=0.80.

Correlations for $\beta = 90°$ are shown in Figures 4.66 and 4.67 for M=0.55 (subresonant) and M=0.80 (superresonant), respectively. These correlations are quite similar to their respective correlations for $\beta = 45°$, Figures 4.62 and 4.63. One exception is that the experimental magnitude data and the analytical magnitude predictions are reduced in agreement for M=0.55, $\beta = 90°$, a subresonant condition, as compared to M=0.55, $\beta = 45°$, a superresonant condition. Poor dynamic periodicity was found for these conditions, Figures 4.11 and 4.17, respectively, for M=0.55 and M=0.80.

As for $\beta = -45°$, the data-theory correlation is very good for $\beta = -90°$, Figures 4.68 and 4.69. Good dynamic periodicity was found for $\beta = -90°$, Figure 4.12 for M=0.55 and Figure 4.18 for M=0.80.

The correlation for out-of-phase, subresonant, oscillations varies with inlet Mach number. For M=0.55, Figure 4.70, both sets of the experimental magnitude data and the analytical predictions are in good agreement. The influence coefficient experiment phase data and the analytical predictions are in very good agreement, but the all-airfoils-oscillating experiment phase data are shifted from the analytical predictions and the influence coefficient experiment phase data. Note that while relatively good periodicity was found for M=0.55 and $\beta = 180°$, Figure 4.13, this correlation is not as good as the correlations found for $\beta = -45°$ and $\beta = -90°$, the other interblade phase angle values where relatively good periodicity was found.

At M=0.80 and $\beta = 180°$, Figure 4.71, the correlation is reduced. The two sets of experimental magnitude data are in good agreement with each other but are

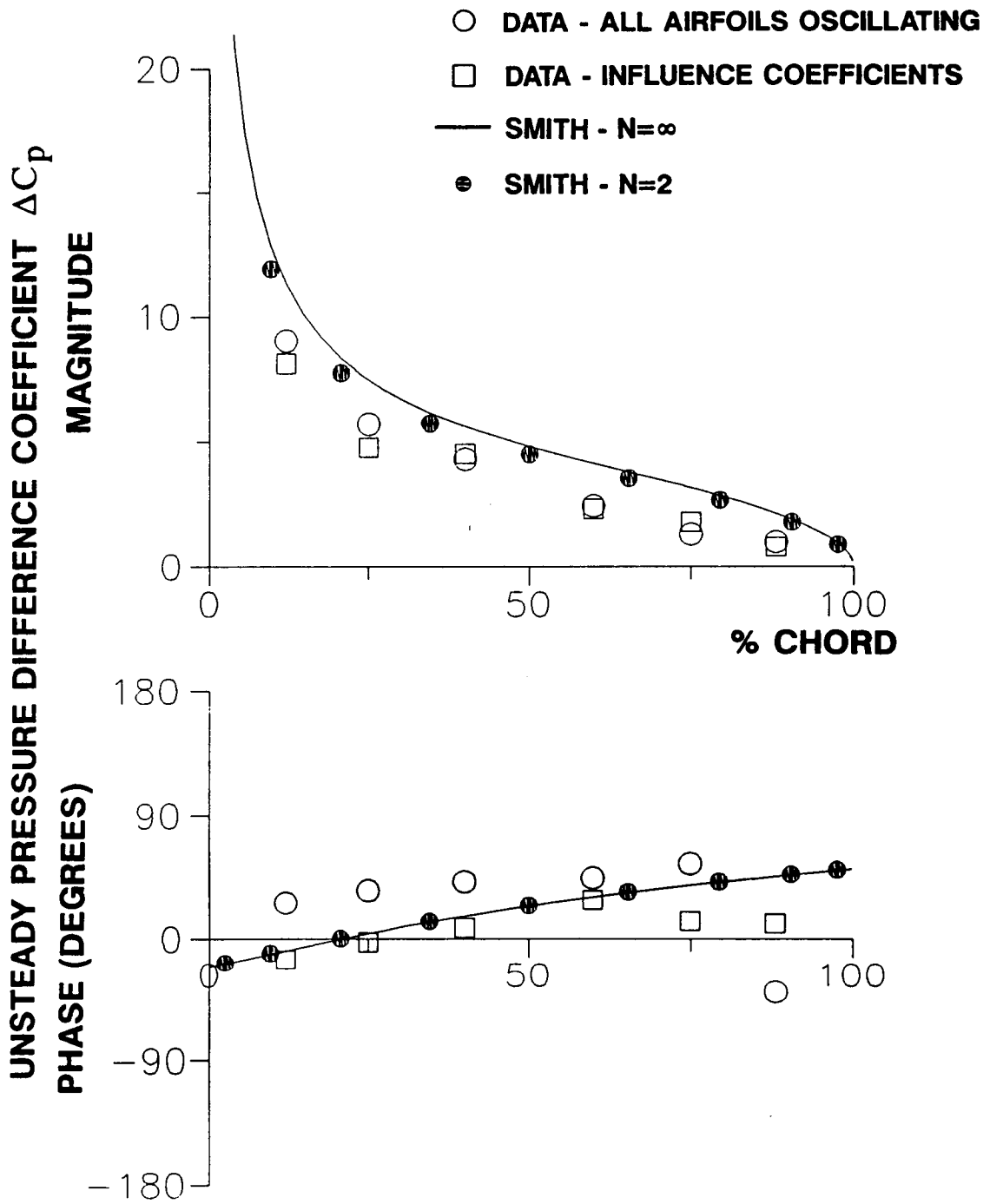

Figure 4.66 Unsteady pressure difference coefficient distribution, low solidity cascade, M=0.55, k=0.32, β=90 degrees

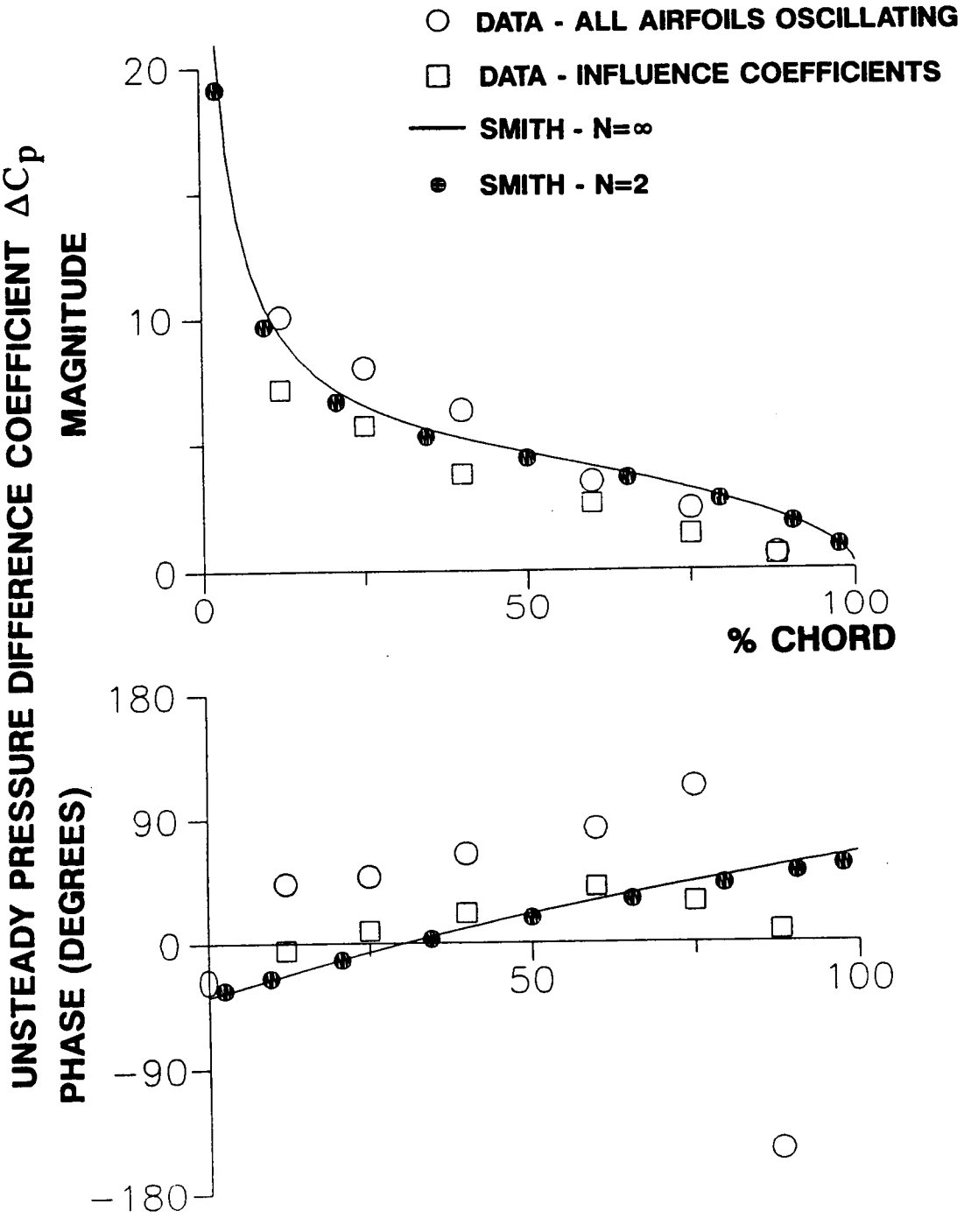

Figure 4.67 Unsteady pressure difference coefficient distribution, low solidity cascade, M = 0.80, k = 0.32, β = 90 degrees

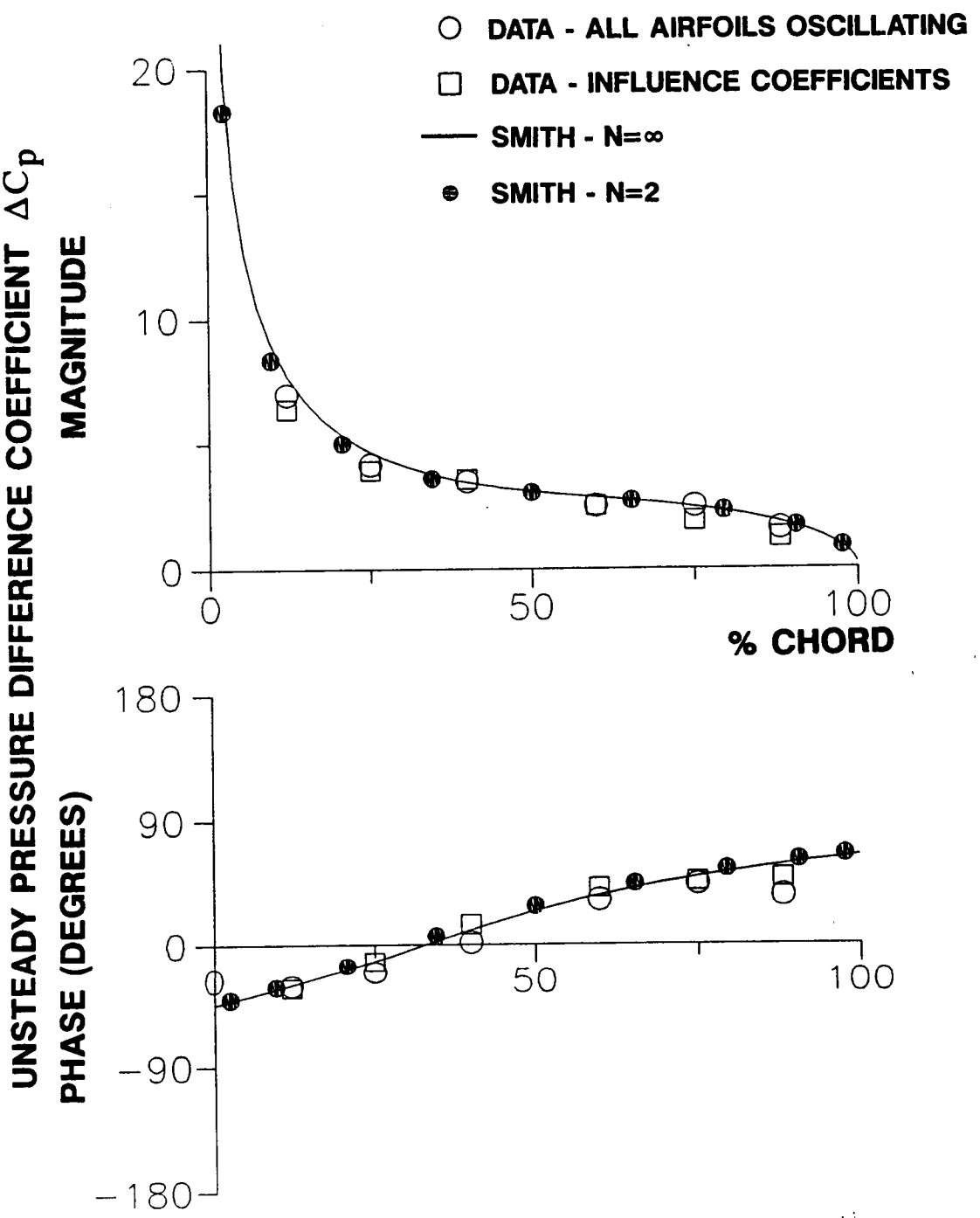

Figure 4.68 Unsteady pressure difference coefficient distribution, low solidity cascade, M=0.55, k=0.32, β=-90 degrees

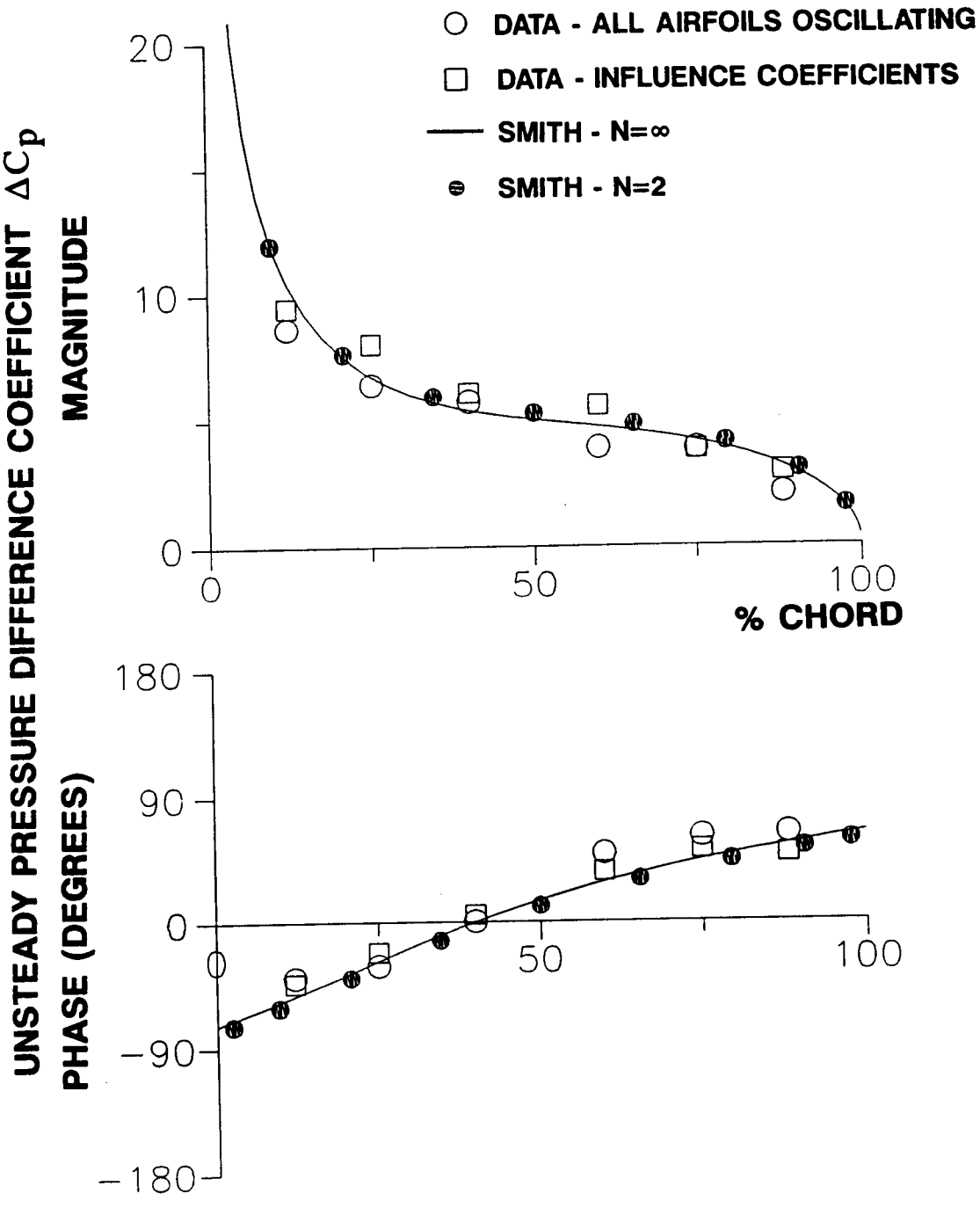

Figure 4.69 Unsteady pressure difference coefficient distribution, low solidity cascade, M = 0.80, k = 0.32, β = -90 degrees

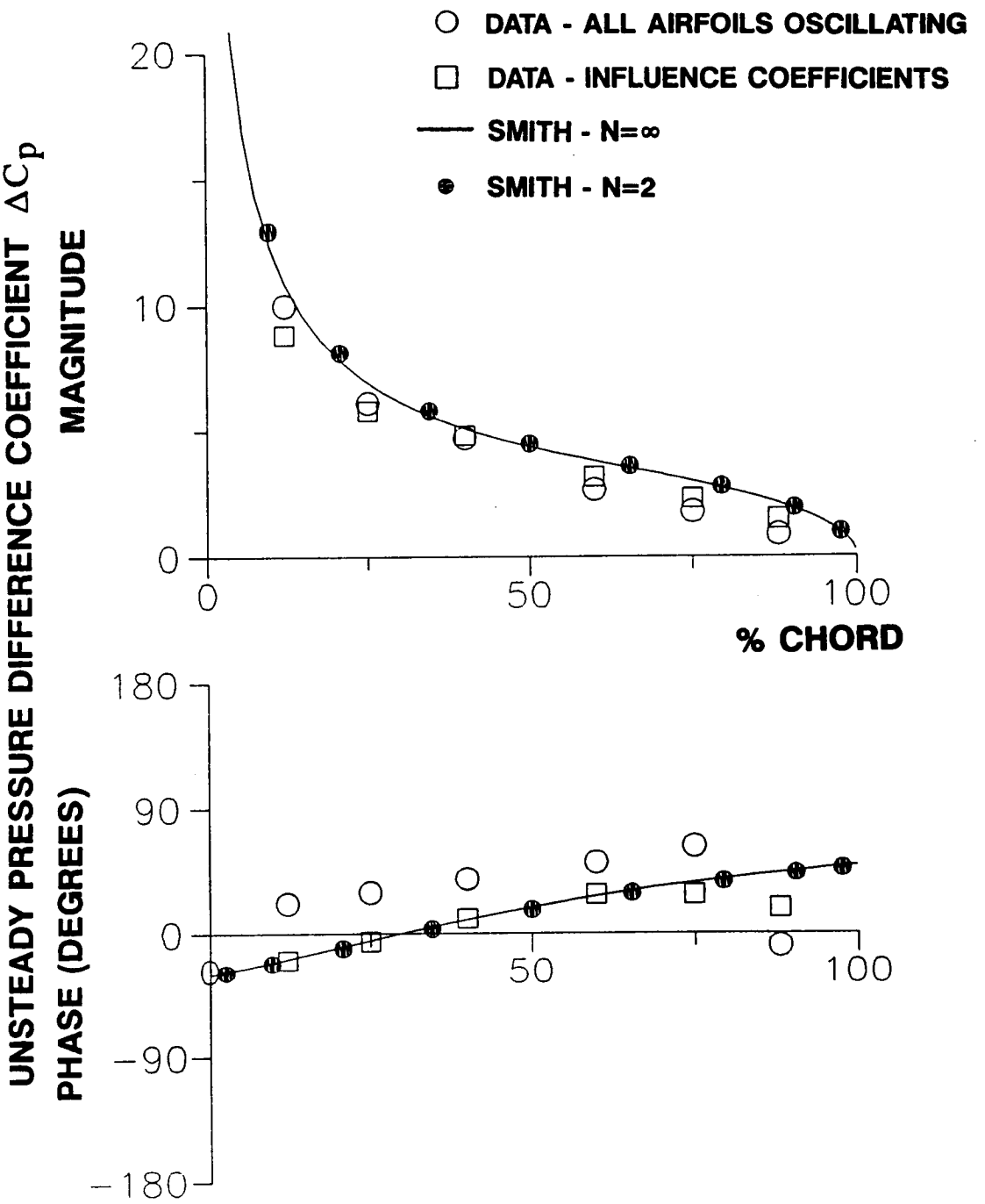

Figure 4.70 Unsteady pressure difference coefficient distribution, low solidity cascade, M = 0.55, k = 0.32, β = 180 degrees

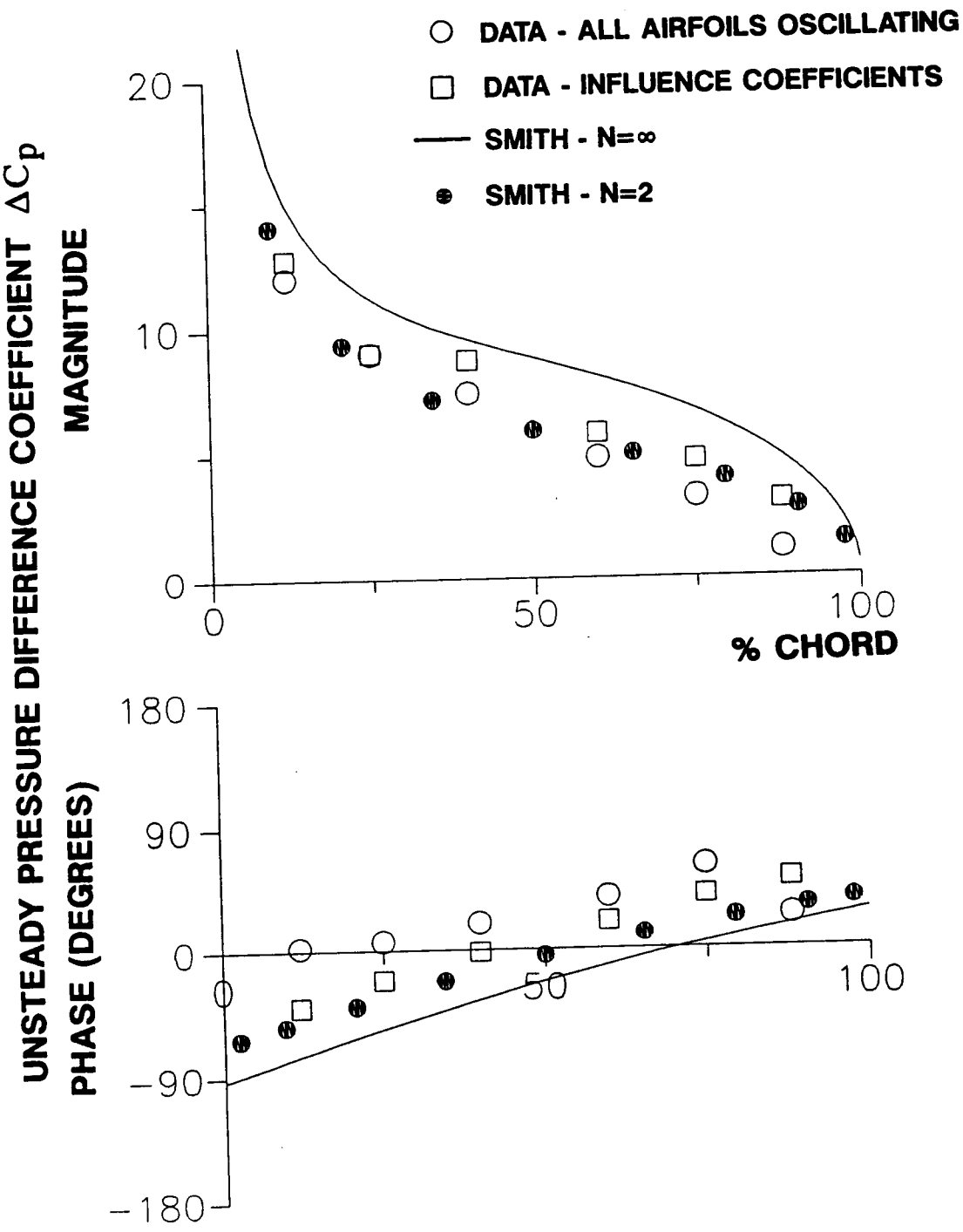

Figure 4.71 Unsteady pressure difference coefficient distribution, low solidity cascade, M = 0.80, k = 0.32, β = 180 degrees

significantly less in magnitude than the analytical prediction for an infinite cascade. The experimental phase data and the analytical predictions all have significant differences despite similar trends. Because this condition falls very near an acoustic resonance at 178.4 degrees, the predictions of Smith's analysis for an infinite cascade and the analytical influence coefficient predictions for N=2 are quite different. However, the experimental influence coefficient data and the analytical influence coefficient predictions are in good agreement.

To summarize these low solidity cascade results, several trends are evident from these plots of the dynamic pressure difference coefficient distributions:

(1) The best correlation is achieved at interblade phase angle values where the best unsteady cascade periodicity is found, -90 and -45 degrees. The two sets of experimental data are in good agreement with each other and also in good agreement with the analytical predictions. All of these conditions are subresonant.

(2) The level of correlation is generally poorest at interblade phase angle values of 45 and 90 degrees, values for which the unsteady cascade periodicity was generally poor. One of these conditions is subresonant, thus subresonance does not guarantee good correlation.

(3) Surprisingly good correlation is found for in-phase oscillations considering that relatively poor dynamic periodicity was found for that interblade phase angle value.

(4) Correlation is reduced at the higher inlet Mach number, M=0.8, as compared to the lower inlet Mach number, M=0.55.

(5) There is generally good agreement between the values of ΔC_p determined using the experimental influence coefficient technique and those predicted by the linearized analysis.

(6) The analytical influence coefficient predictions for N=2 are generally in very good agreement with the analytical predictions for an infinite cascade, indicating that only a few oscillating airfoils are generally required to model an infinite cascade. This approximation fails in the vicinity of acoustic resonances. Also, because the analyses predict ΔC_p, not C_p, the number of oscillating airfoils required to accurately determine the airfoil surface C_p distributions is not determined.

High Solidity Cascade

In a similar fashion, ΔC_p experimental data from the high solidity cascade are presented along with the analytical predictions in Figures 4.72 through 4.80. The 0.39 reduced frequency results are presented for an inlet Mach number of 0.65, 0 and 7 degrees mean incidence. The 0.32 reduced frequency results are presented for an inlet Mach number of 0.8 and 7 degrees mean incidence. Due to the failure of several dynamic pressure transducers, some data points from the all-airfoils-oscillating experiments are omitted from these figures.

Superresonant in-phase oscillations result in varied correlations. For 0.65 inlet Mach number and 0 mean incidence, Figure 4.72, the predicted magnitudes tend to fall between the two sets of experimental data, with the largest magnitudes from the all-airfoils-oscillating experiment. The experimental phase data are in good mutual agreement except in the midchord region, but there is a large offset between the predictions and the experimental data. The analytical influence coefficient predictions for N=2 are in good agreement with the analytical predictions for an infinite cascade.

Changing the mean flow incidence angle to 7 degrees, Figure 4.73, results in improved magnitude and phase correlations except for the magnitude near the leading

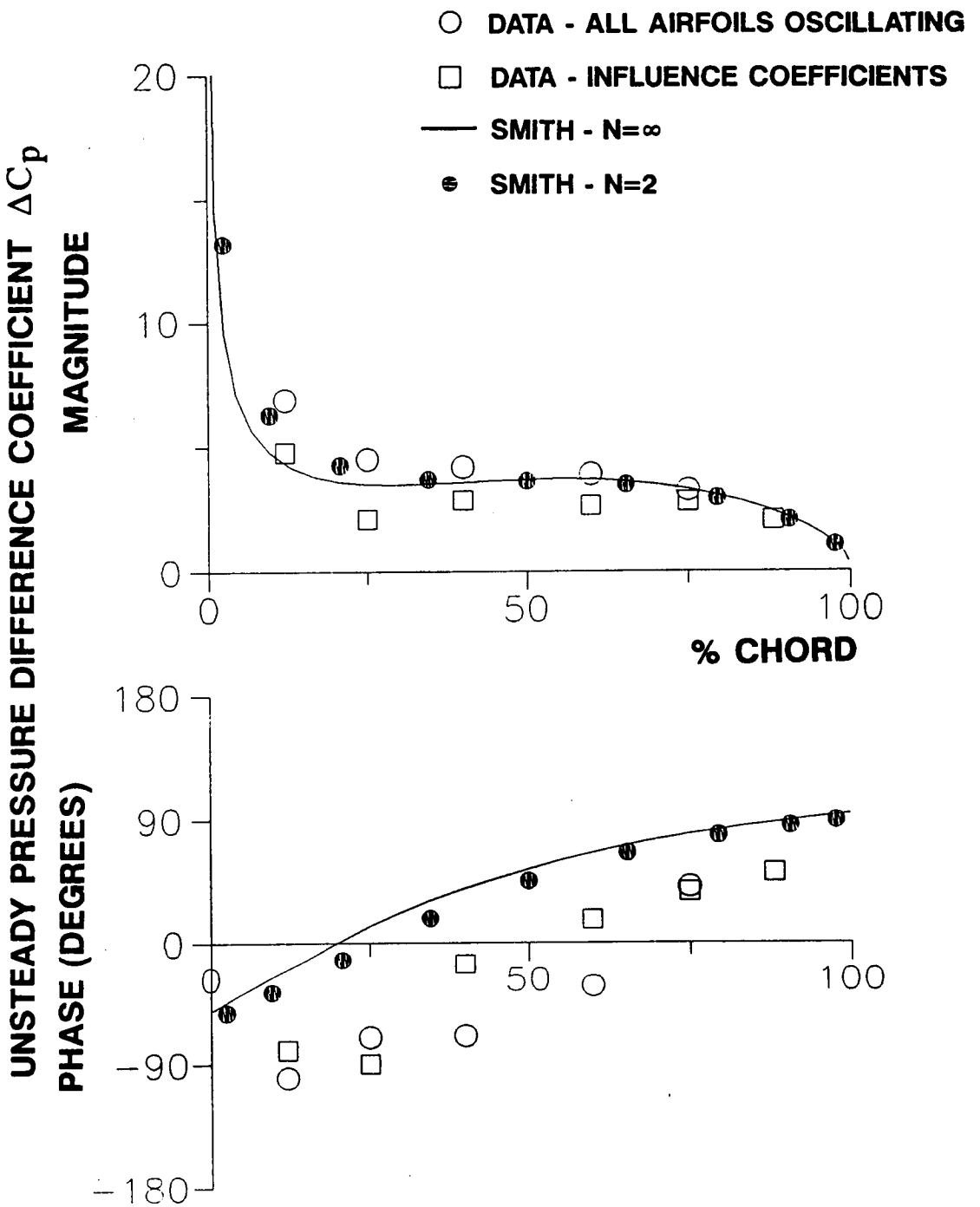

Figure 4.72 Unsteady pressure difference coefficient distribution, high solidity cascade, M=0.65, α_0=0, k=0.39, β=0

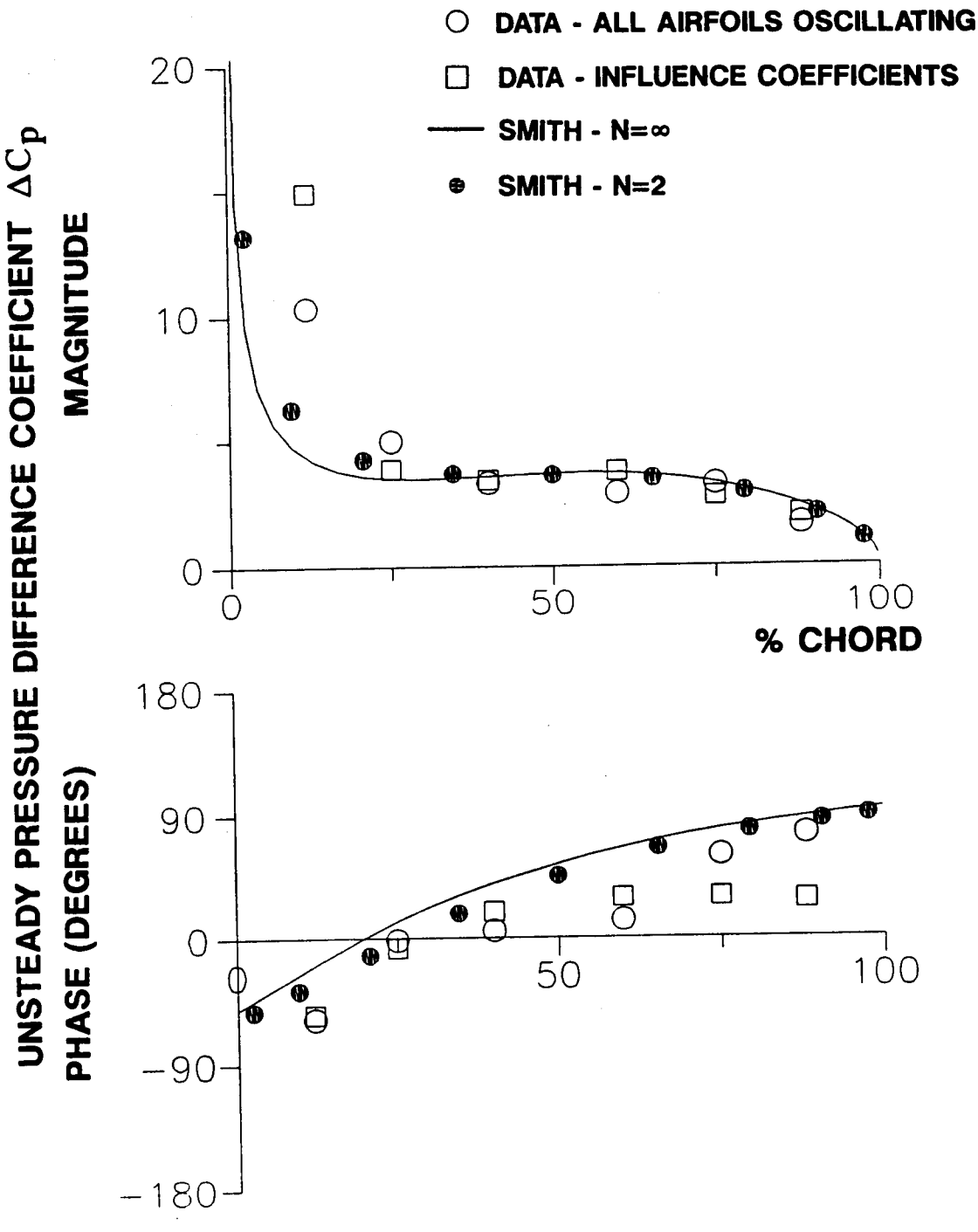

Figure 4.73 Unsteady pressure difference coefficient distribution, high solidity cascade, M=0.65, α_0=7 degrees, k=0.39, β=0

edge and the phase near the trailing edge. The peak in the influence-coefficient-determined magnitude at 12% of chord is due to the oscillating separation bubble as discussed in Section 4.2.2.

For M=0.8 at 7 degrees of incidence and k=0.32, Figure 4.74, the two sets of experimental magnitude data are in fairly good mutual agreement except at the leading edge. There, the peak in the influence-coefficient-determined magnitude at 12% of chord is due to oscillations of the upper surface shock wave. That shock wave oscillations were not evident at 12% of chord in the corresponding all-airfoils-oscillating experiments may be due to small differences in the steady flow field between the two experiments. The analyses predict larger magnitudes than the experimental data except at 12% of chord. The experimental phase data are in good mutual agreement near the leading and trailing edges but differ in between. The predictions correlate reasonably well with the experimental phase data except for the experimental influence coefficient data at 25 and 75% of chord and the all-airfoils-oscillating experiment data at 60% of chord.

Changing the interblade phase angle to 90 degrees, the oscillating cascade is predicted to be subresonant for M=0.65 and k=0.39, but superresonant for M=0.80 and k=0.32. For M=0.65 and $\alpha_0 = 0°$, Figure 4.75, the influence coefficient experiment data and the predictions correlate very well, but the experiment phase data for all-airfoils-oscillating are offset from the rest. The influence coefficient experiment data and the analytical predictions are also in relatively good agreement when the mean incidence angle is changed to 7 degrees, Figure 4.76, although the magnitude correlation is reduced over the forward half of the airfoil. For M=0.8, k=0.32, Figure 4.77, the magnitude correlation is good except near the leading edge where the influence coefficient magnitude is large due to the oscillating shock wave. Differences between the phase data and the analysis results occupy a wide band.

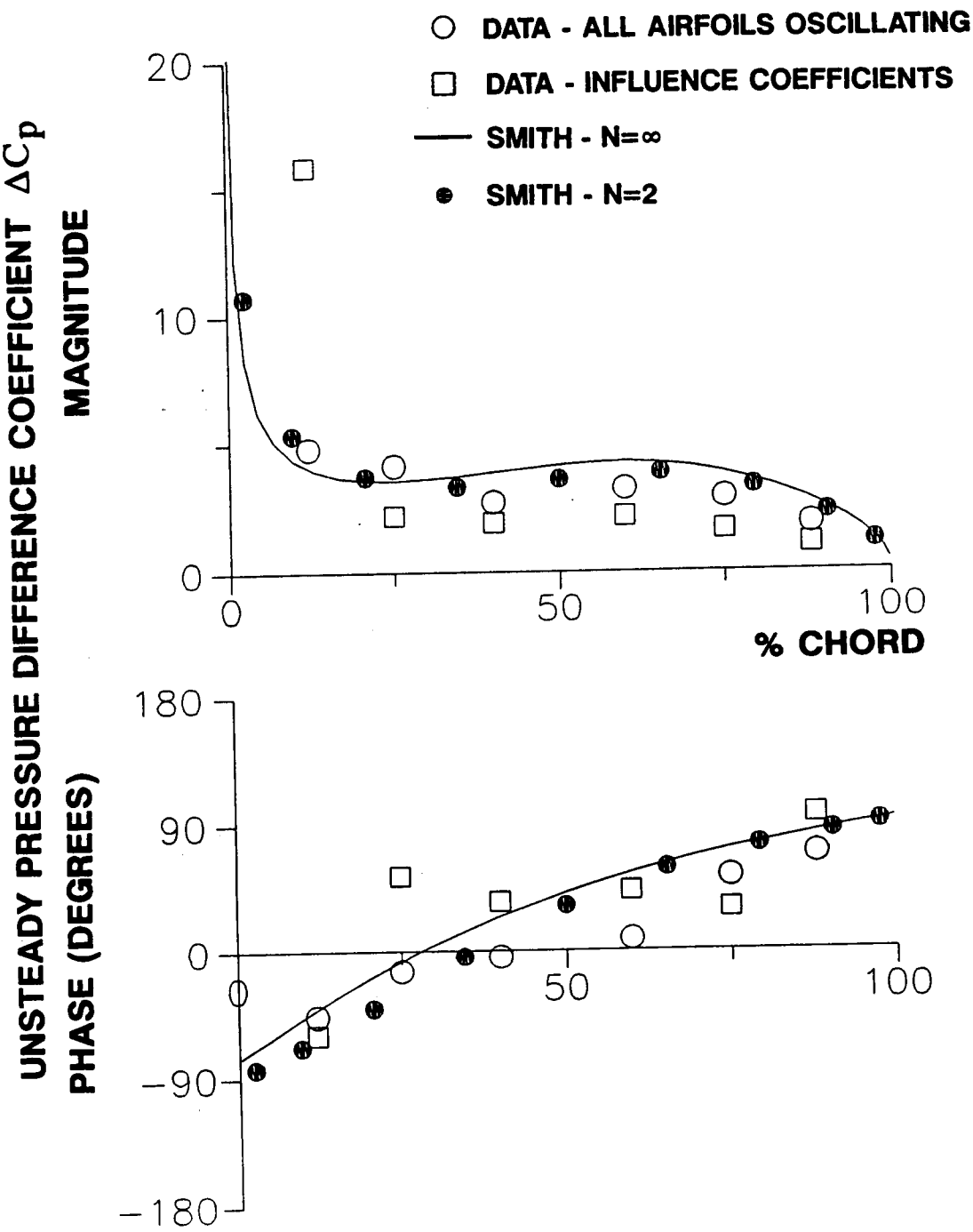

Figure 4.74 Unsteady pressure difference coefficient distribution, high solidity cascade, M=0.80, α_0=7 degrees, k=0.32, β=0

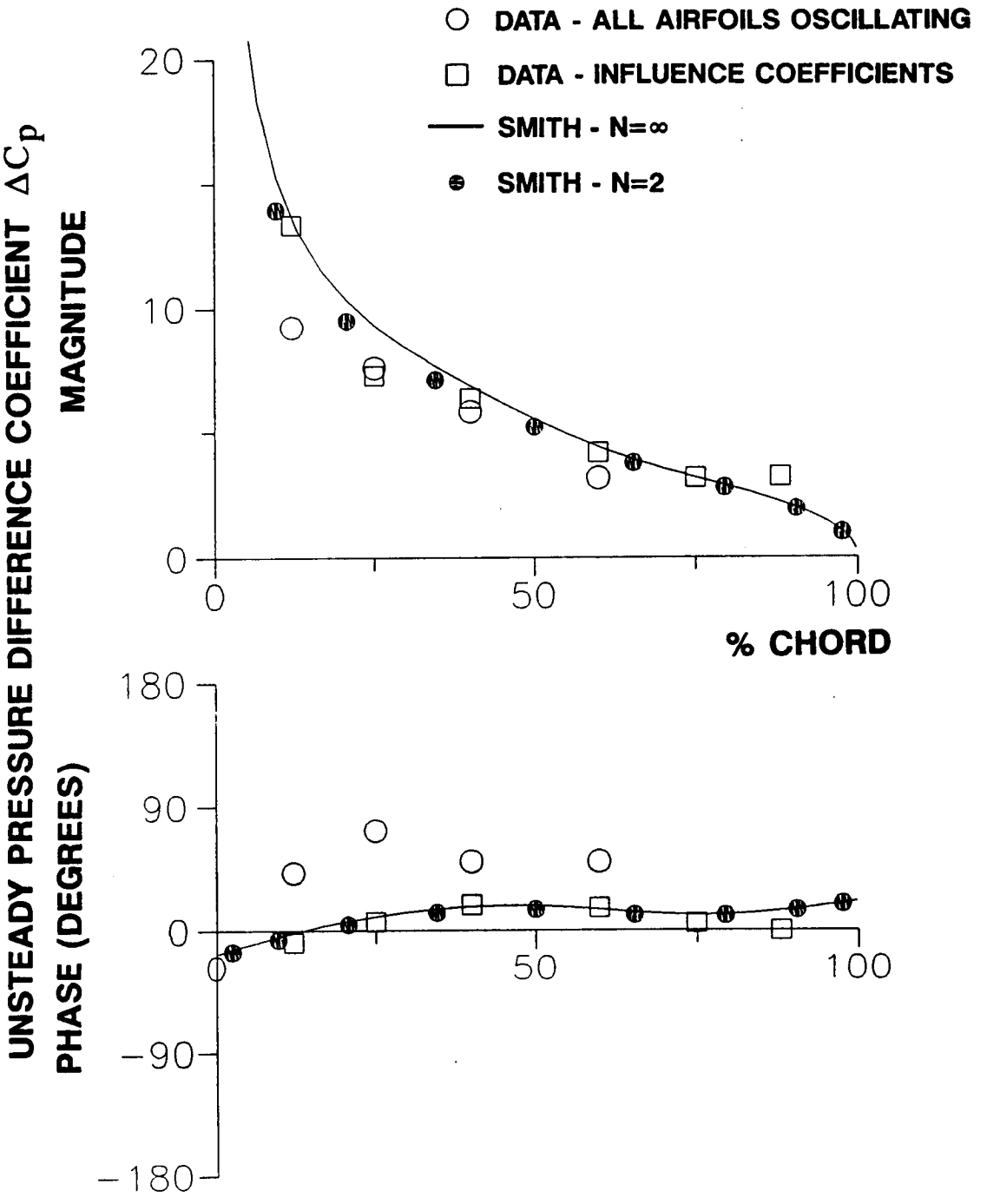

Figure 4.75 Unsteady pressure difference coefficient distribution, high solidity cascade, M=0.65, α_0=0, k=0.39, β=90 degrees

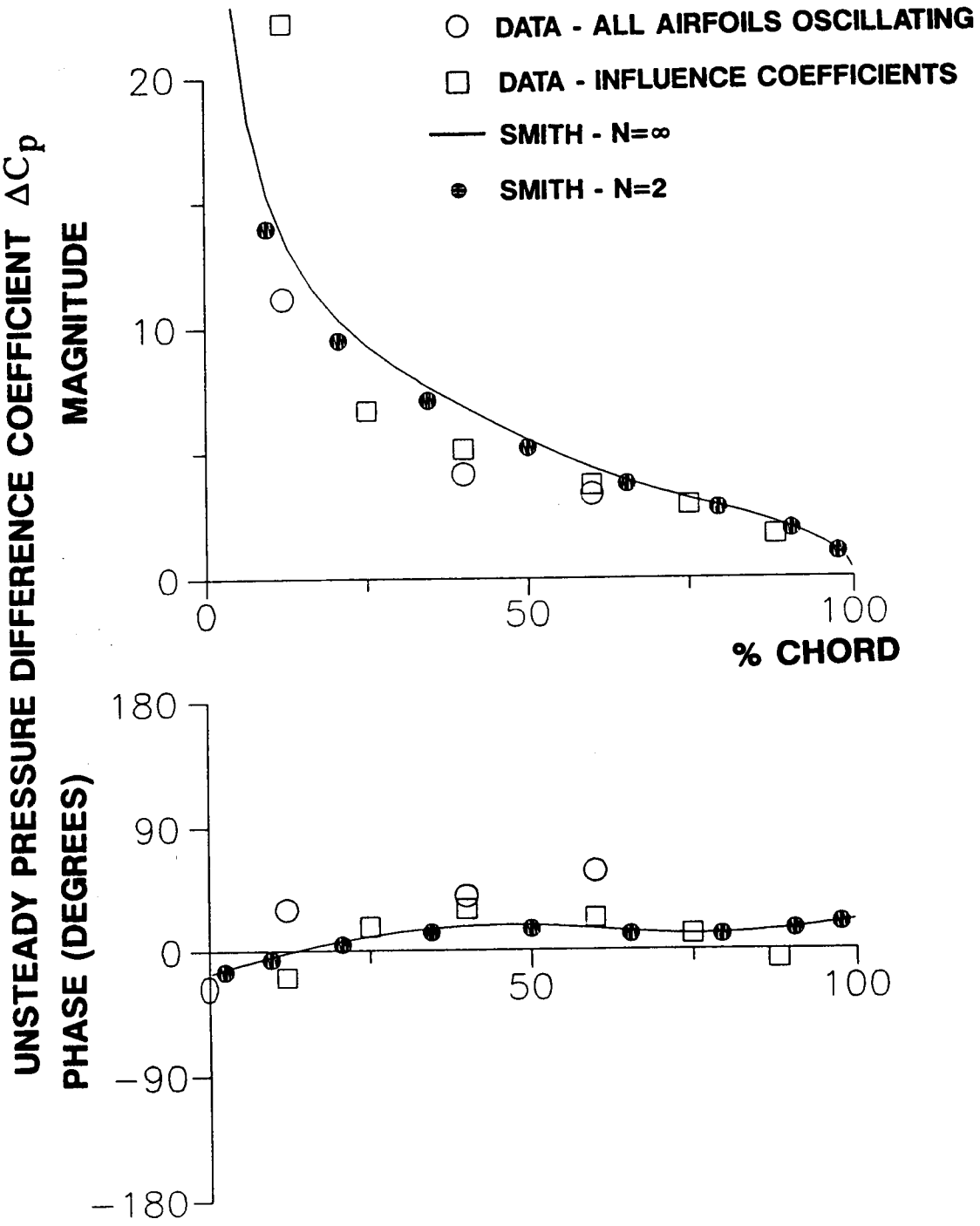

Figure 4.76 Unsteady pressure difference coefficient distribution, high solidity cascade, M=0.65, α_0=7 degrees, k=0.39, β=90 degrees

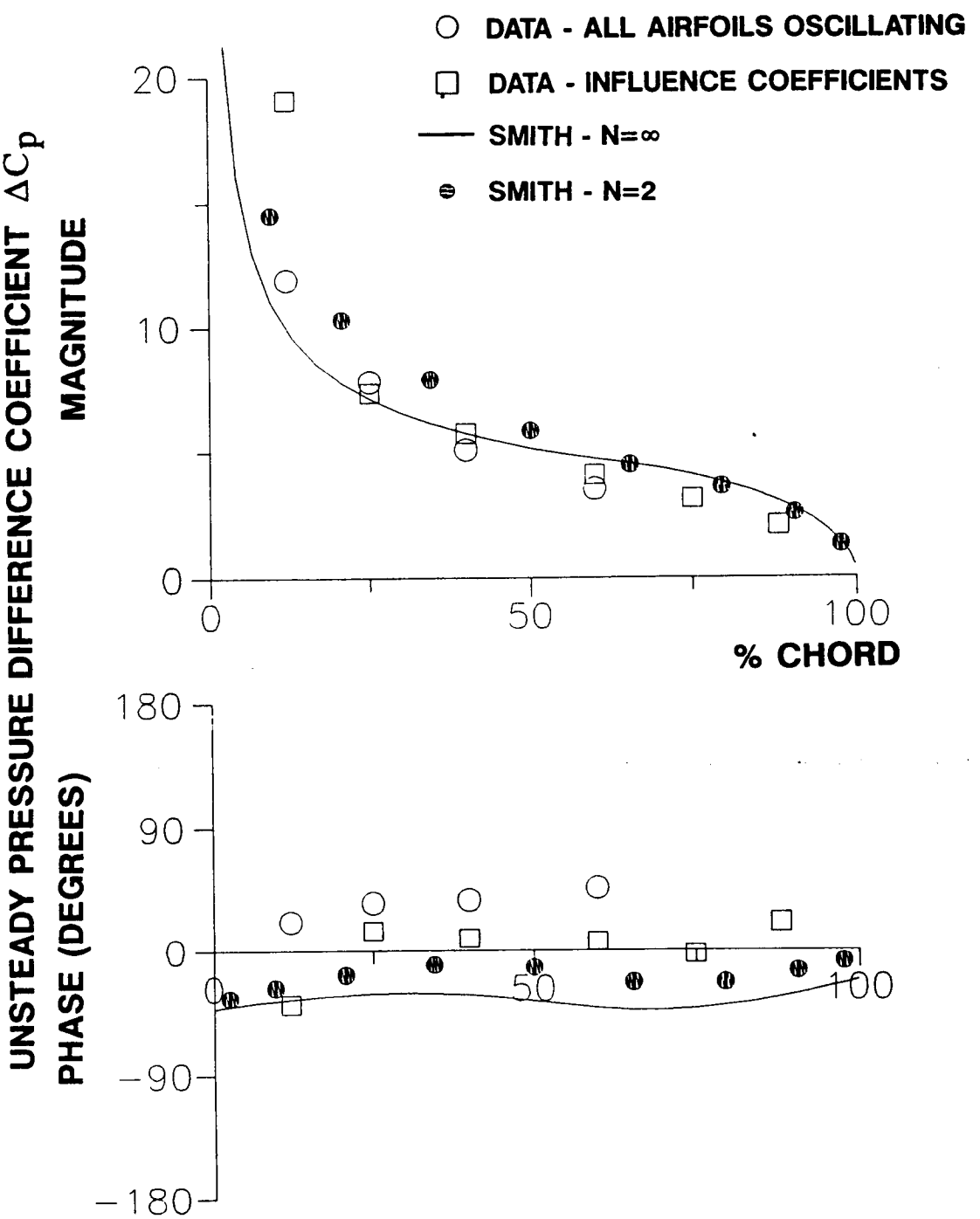

Figure 4.77 Unsteady pressure difference coefficient distribution, high solidity cascade, M=0.80, α_0=7 degrees, k=0.32, β=90 degrees

For $\beta = -90°$, subresonant conditions are predicted for both inlet Mach numbers. The two sets of experimental data and the predictions correlate well in both magnitude and phase for 0.65 inlet Mach number and 0 mean incidence, Figure 4.78. Increasing the mean incidence to 7 degrees, Figure 4.79, the correlation is still good except that the predicted magnitudes are, except near the leading edge, greater than the experiment data. Again, the peak in the influence-coefficient-determined magnitude at 12% of chord is due to the oscillating separation bubble. There is good phase correlation for M = 0.8, Figure 4.80, but the predicted magnitude distributions are again generally greater than measured. The peak in the influence-coefficient-determined magnitude at 12% of chord is due to oscillations of the upper surface shock wave.

In summary, there are several trends from these plots of the dynamic pressure difference coefficient distributions for the high solidity cascade:

(1) The experimental data-linearized analysis magnitude correlation is generally good. The primary exceptions are due to the M = 0.80 oscillating shock wave or the M = 0.65 oscillating separation bubble present at 12% of chord in the influence coefficient experiments.

(2) The best correlation of both experimental data sets and the analytical results is generally achieved at $\beta = -90°$, a subresonant interblade phase angle.

(3) Significant differences in the phase angle distributions are generally found at interblade phase angle values of 0 (superresonant) and 90 degrees (subresonant for M = 0.65, superresonant for M = 0.80).

(4) The correlations between the experimental influence coefficient data and the linearized analysis predictions for the high solidity cascade vary considerably.

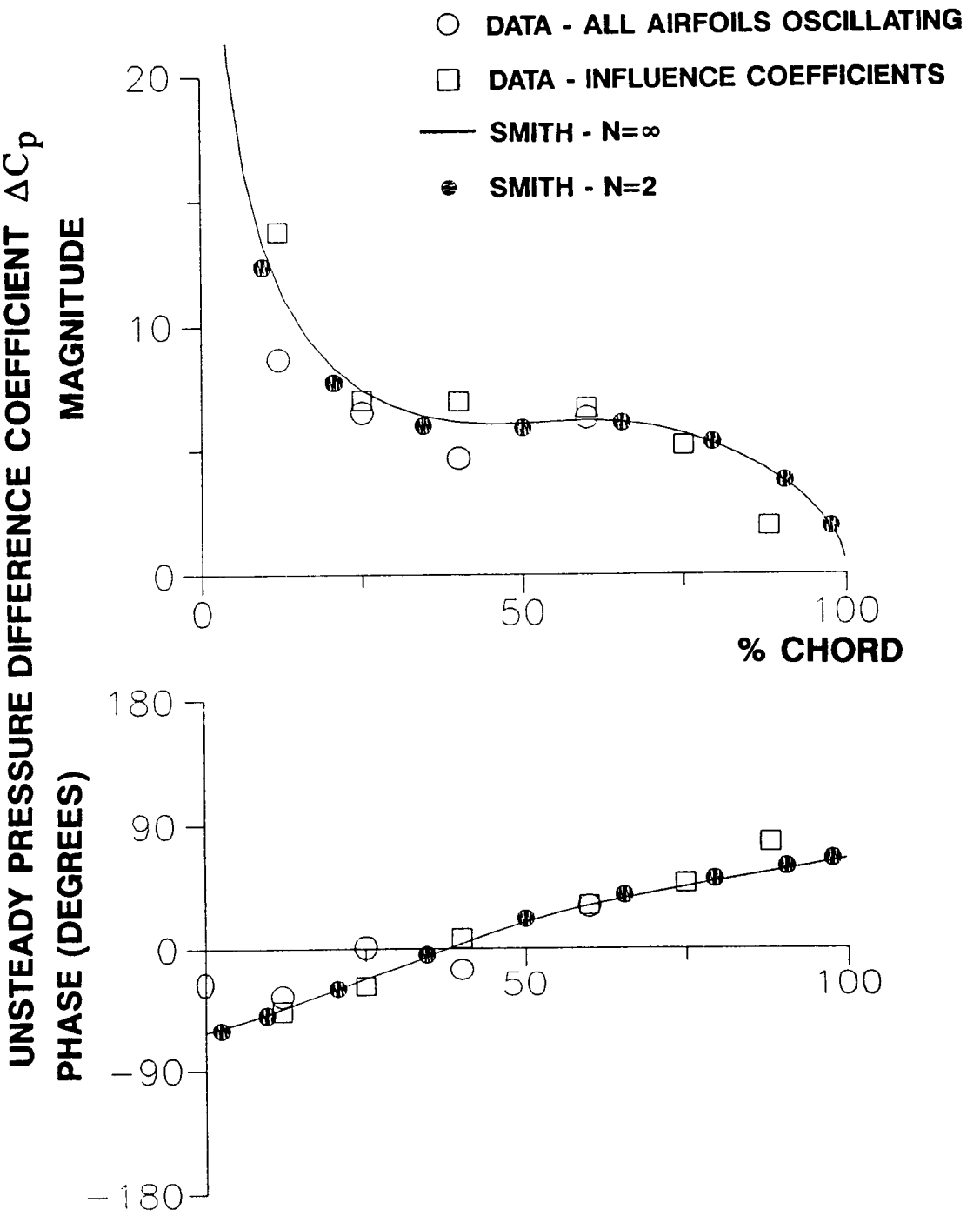

Figure 4.78 Unsteady pressure difference coefficient distribution, high solidity cascade, M=0.65, α_0=0, k=0.39, β=-90 degrees

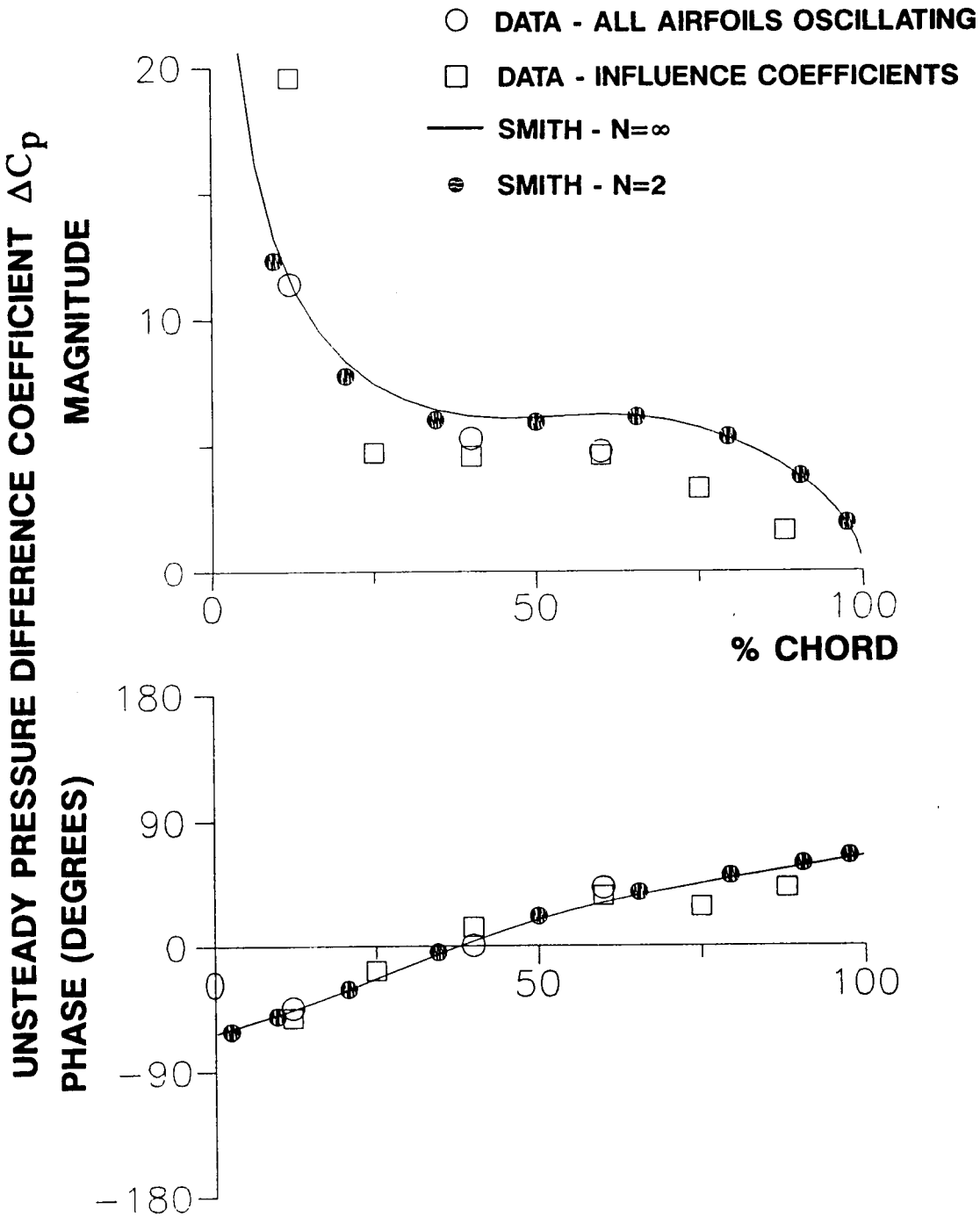

Figure 4.79 Unsteady pressure difference coefficient distribution, high solidity cascade, M=0.65, α_0=7 degrees, k=0.39, β=-90 degrees

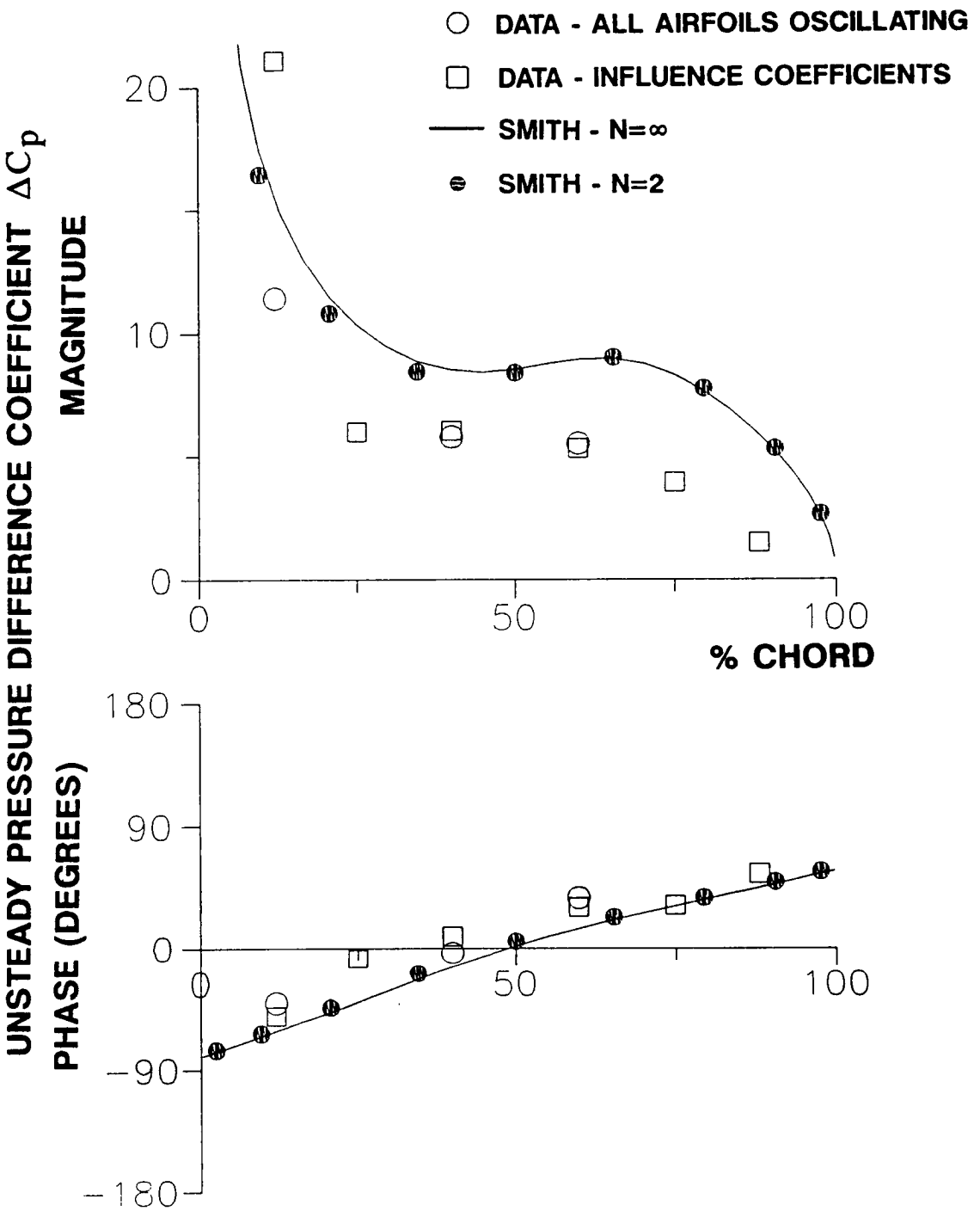

Figure 4.80 Unsteady pressure difference coefficient distribution, high solidity cascade, M=0.80, α_0=7 degrees, k=0.32, β=-90 degrees

4.2.5 Finite Linear Cascade Effects

The cascade dynamic periodicity and correlation of the experimental all-airfoils-oscillating data with the results of Smith's analysis have been shown to vary greatly with interblade phase angle. How these correlations can be very good for some interblade phase angles but poor for others leads one to question the validity of conducting oscillating cascade experiments in a linear cascade. Two specific areas of concern which will now be considered are: (1) the effect of having a finite number of airfoils in the cascade; (2) the effect of the wind tunnel walls. Both experimental data and linearized analysis will be used to address these concerns.

The effect of a finite number of airfoils has, in effect, already been considered. In Section 4.2.3, the convergence properties of the experimentally-determined influence coefficient series were investigated. Because the experiment C_p series is, for some conditions, slowly convergent at best, a large number of airfoils is generally required to determine the unsteady pressure distribution on the oscillating cascaded airfoils. But the series convergence depends mainly upon the upstream-traveling wave, which may not truly be a cascade phenomenon. That is, the wave may be a consequence of the rectangular duct which encloses the cascade. Thus there is insufficient experimental evidence to assess the effect of a limited number of cascaded airfoils. From a theoretical standpoint, it was found in Section 4.2.4 that the analytical predictions for N=2 are generally in good agreement with infinite cascade predictions. But the analyses predict ΔC_p, not C_p, so the convergence properties of the C_p series may not be determined from the analyses.

The effect of the wind tunnel walls on the cascade unsteady aerodynamics is addressed by considering both the experimental data and the linearized unsteady aerodynamic analysis. The analysis, as explained in Appendix C, is used to predict the cascade wave generation characteristics which, although for an infinite cascade,

will give insight into possible cascade/wind tunnel interactions. Algebraic expressions are used to calculate the wavelength, propagation direction and decay rate of the pressure disturbances produced by an oscillating cascade. The initial amplitudes of these disturbances are calculated using Smith's analysis.

Low Solidity Cascade

Figures 4.81 through 4.84 present these results for an inlet Mach number of 0.55 and 0.32 reduced frequency. Referring to Figure 4.81, the direction of wave propagation is expressed relative to axial (ξ) and tangential (η) coordinates so that a wave moving away from the cascade in the $-\xi$ direction is said to be upstream-traveling while a wave moving in the ξ direction is traveling downstream. Both upstream-traveling and downstream-traveling waves are produced in the superresonant region which brackets $\beta = 0°$. Outside this region, the oscillating cascade produces subresonant waves which travel only downstream. Acoustic resonances occur at the boundaries between the subresonant and superresonant regions, with pressure disturbances propagating along the cascade in the $\pm\eta$ directions.

Computed values of the initial magnitude of the outgoing pressure disturbance are shown in Figure 4.82 for M = 0.55 and k = 0.32. These results are presented in the format of an unsteady pressure coefficient magnitude at the leading edge of the cascade, $|C_p(\xi = 0)|$. The largest initial disturbance amplitudes are found in the vicinity of β_r^*. Outside the near-resonance regions, relatively large amplitudes occur at positive subresonant values of the interblade phase angle, $\beta > \beta_r^*$. As shown in Appendix C, these pressure disturbances will either propagate unattenuated or decay exponentially as a function of the axial distance ξ:

$$\frac{|C_p(\xi)|}{|C_p(\xi = 0)|} = e^{-|\iota'\xi|}. \qquad (4.4)$$

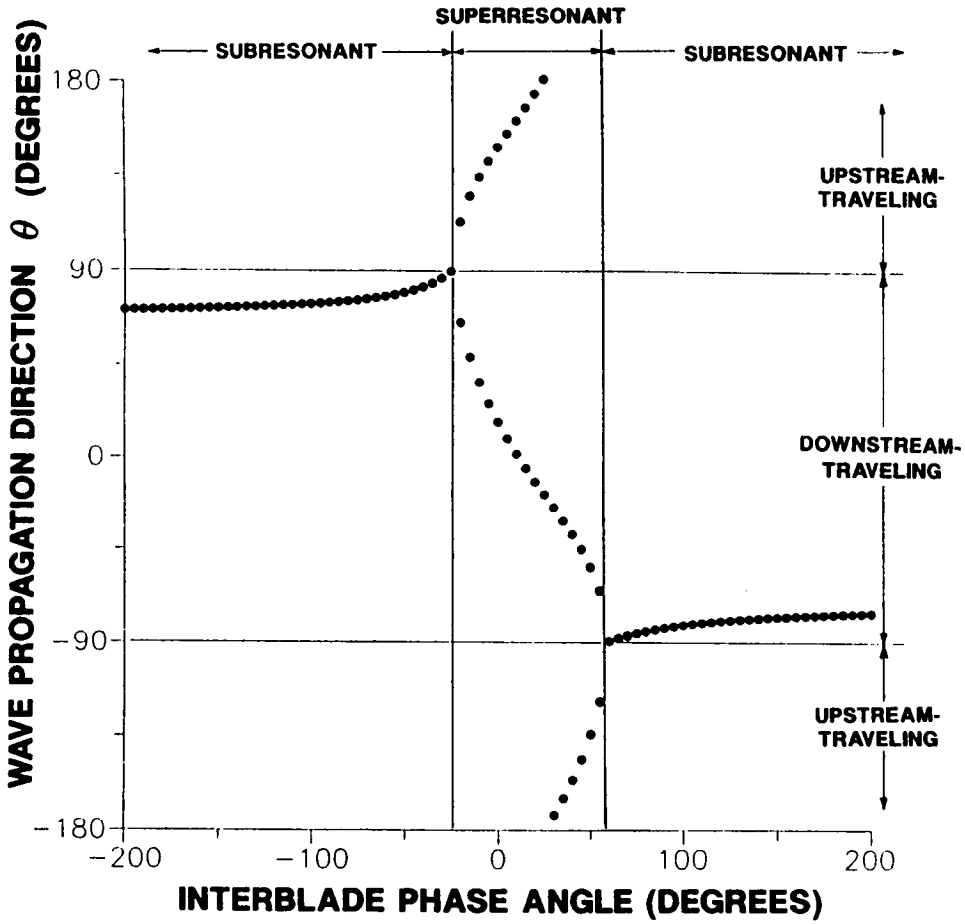

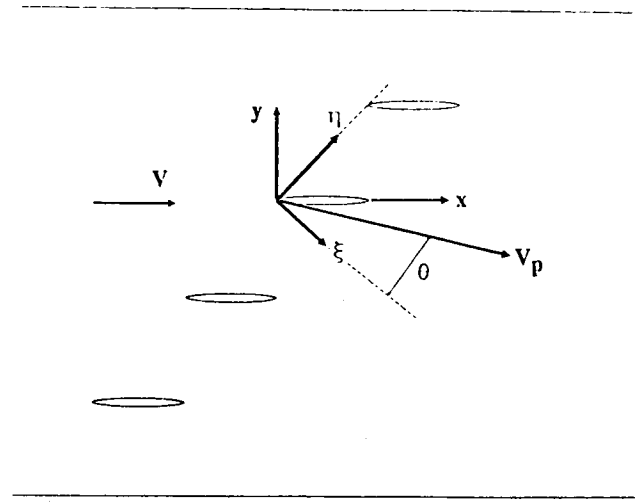

Figure 4.81 Pressure disturbance propagation direction, low solidity cascade, M=0.55, k=0.32

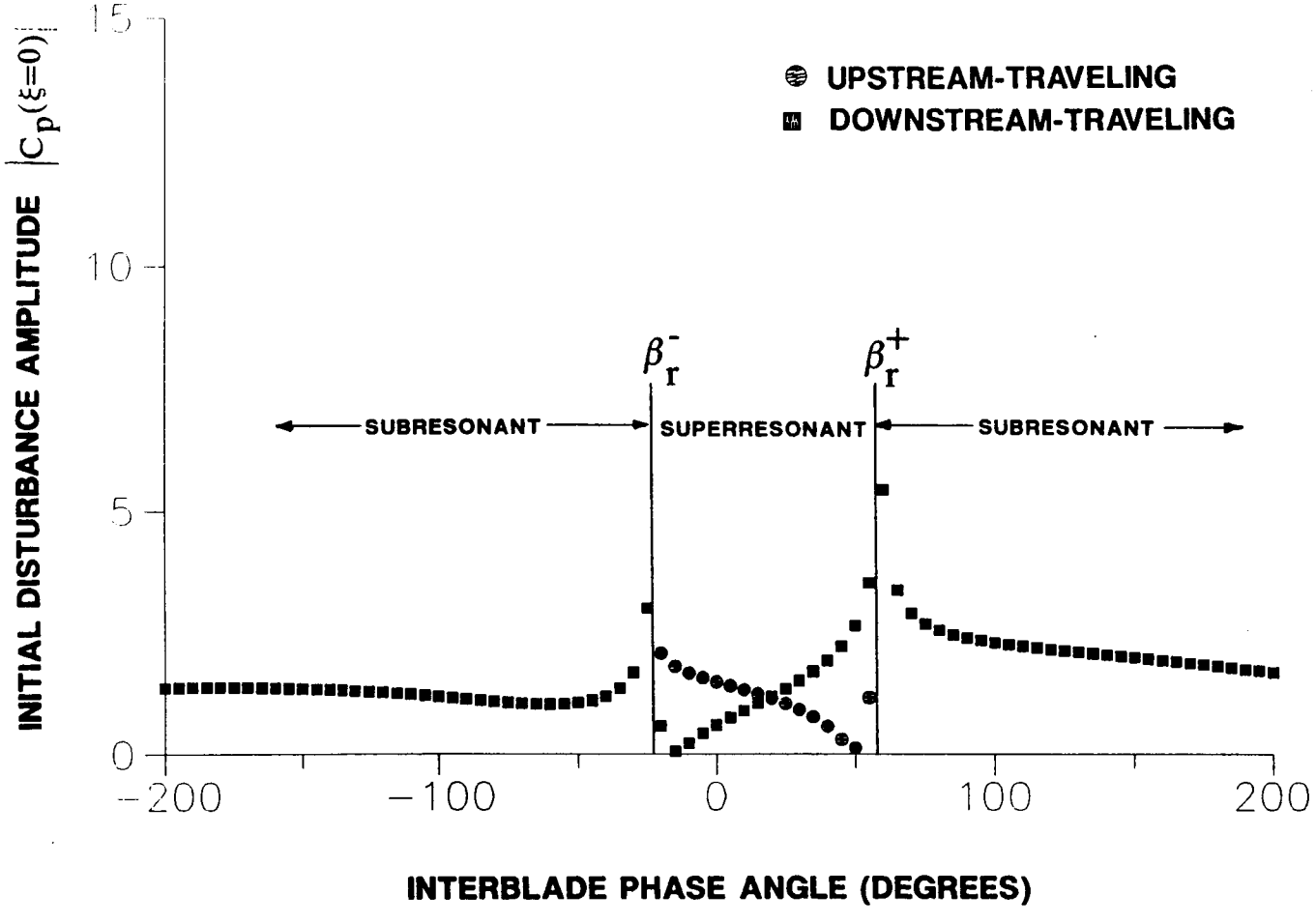

Figure 4.82 Initial pressure disturbance amplitude, low solidity cascade, M = 0.55, k = 0.32

l' is the imaginary part of the axial wavenumber. Figure 4.83 presents l' for M=0.55 and k=0.32. As shown, $l' = 0$ in the superresonant region, hence superresonant disturbances propagate away from the cascade unattenuated. Outside this region, l' is nonzero, thus the subresonant waves decay with distance away from the cascade. In addition, l' increases monotonically with the absolute value of the interblade phase angle in the subresonant regions.

Figure 4.84 presents the disturbance wavelength for M=0.55 and k=0.32. The wavelengths are an order of magnitude greater than the airfoil chord, and the subresonant waves for $\beta < 0$ are about 2.5 times longer than the subresonant waves for $\beta > 0$.

Insight into possible cascade/wind tunnel wall interactions is gained by considering the predicted pressure disturbance characteristics along with the correlation of the experimental data and Smith's analysis. Specifically, for 0.55 inlet Mach number and 0.32 reduced frequency, Figures 4.81 through 4.84, decaying waves traveling at $\theta \approx 80°$ with $|C_p(\xi = 0)| \approx 1.5$ are predicted for $\beta = -45°$ and $\beta = -90°$, the interblade phase angle values for which good ΔC_p data-analysis correlation was found. These waves are directed at the upper cascade wall. Since the angle of reflection of a wave off a plane surface is equal to the angle of incidence [32], the reflected disturbances exit the cascade and thus will have little effect on the oscillating cascade aerodynamics. Decaying waves are also predicted for $\beta = 90°$, an interblade phase angle at which there was poor correlation between the data for all airfoils oscillating and the theory. But the predicted cascade wave generation characteristics for $\beta = 90°$ are much different than for $\beta = -90°$: the initial wave amplitude is about twice as large, the wave decays less rapidly than that for $\beta = -90°$, and it is traveling at almost the opposite direction, $\theta = -83°$, such that waves reflected off the lower wind tunnel wall could reflect into the cascade and thereby affect the

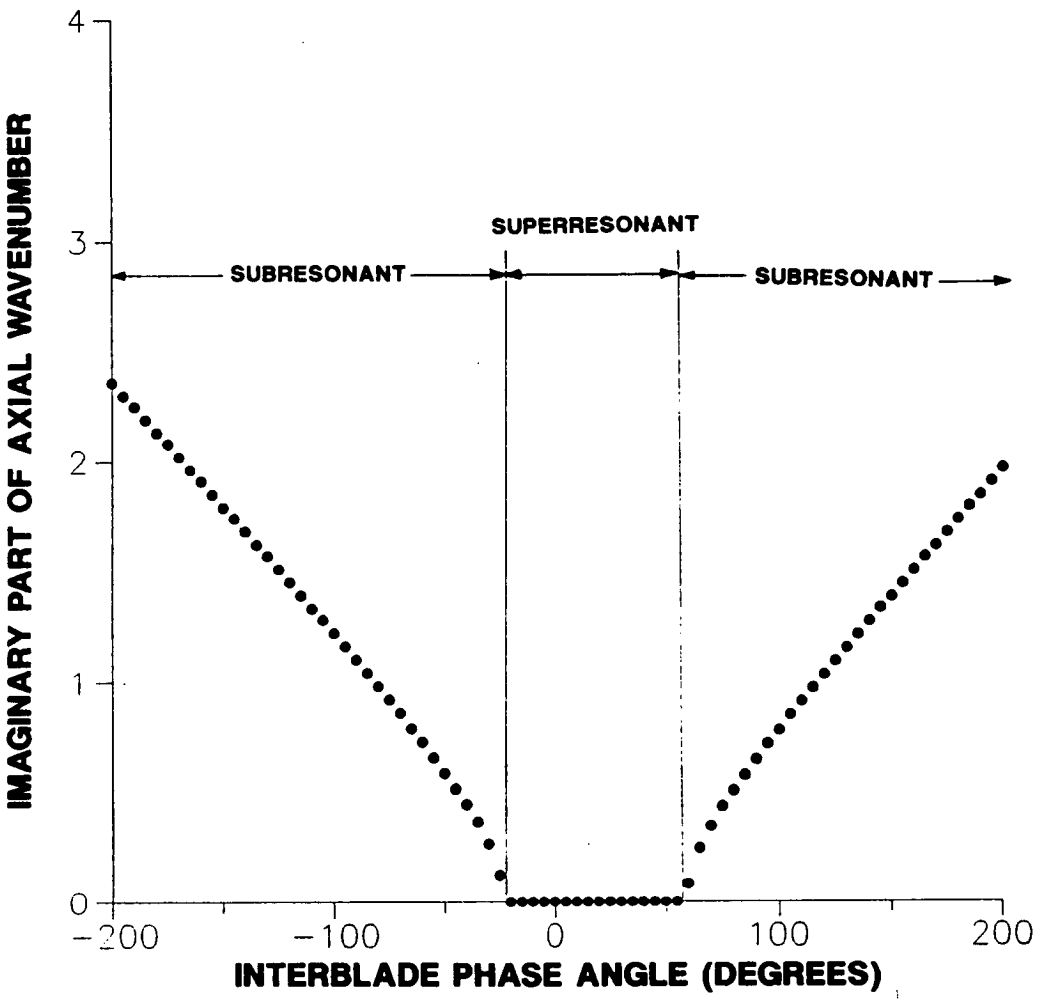

Figure 4.83 Imaginary part of axial wavenumber, low solidity cascade, M = 0.55, k = 0.32

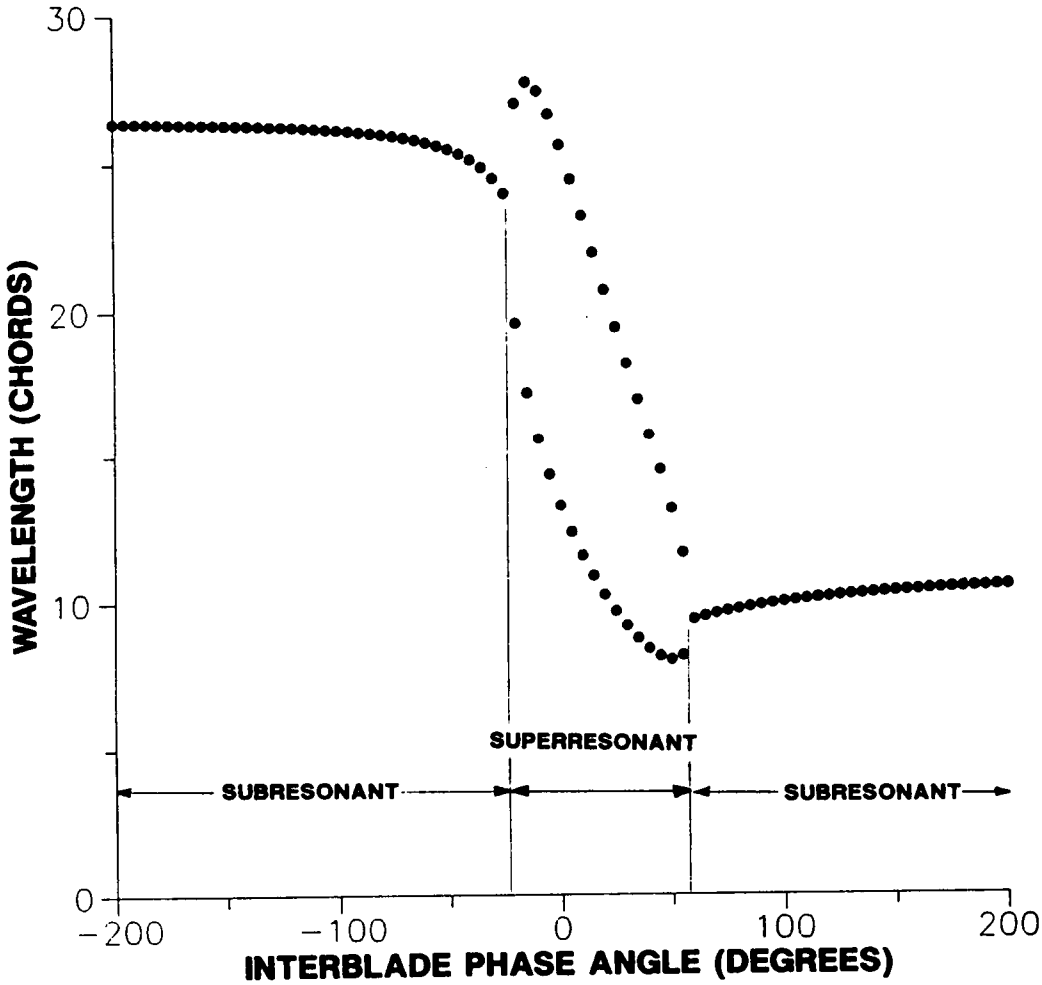

Figure 4.84 Pressure disturbance wavelength, low solidity cascade, M = 0.55, k = 0.32

cascade unsteady aerodynamics. Out-of-phase oscillations also produce decaying waves of similar amplitude and direction as $\beta = 90°$, except that the imaginary part of the axial wavenumber is more than doubled, so the waves generated at $\beta = 180°$ will decay more rapidly. Thus the cascade walls should have less of an effect at $\beta = 180°$, and the result is slightly better correlation between the data for all airfoils oscillating and the analysis at $\beta = 180°$, Figure 4.70, than at $\beta = 90°$, Figure 4.66. Interblade phase angle values of 0 and 45 degrees are predicted to be superresonant, propagating waves unattenuated in both the upstream and downstream directions. The data-analysis correlation is good for $\beta = 0°$, but this is considered fortuitous because the cascade periodicity was poor. The upstream-traveling wave for in-phase oscillations is predicted to travel at an angle of 140 degrees; reflection of this wave off the upper cascade wall could affect the cascade unsteady aerodynamics. The data-analysis correlation is poor for $\beta = 45°$. In this case, the downstream-traveling wave, directed at an angle of -48 degrees, might disturb the cascade unsteady aerodynamics after reflection off the lower wall.

Increasing the inlet Mach number to 0.8 while maintaining k=0.32, Figures 4.85 through 4.88, results in an expanded range of superresonant interblade phase angles, but the trends are similar to M=0.55. As for M=0.55, at $\beta = -45°$ and $\beta = -90°$ there is good data-analysis correlation, and the predicted wave characteristics at these two interblade phase angles are very similar to those for M=0.55. The direction of propagation of the subresonant wave at $\beta = 180°$ has not changed much, but the wave produced at 0.8 inlet Mach number is of about twice the initial amplitude and decays much more slowly than the wave of M=0.55, thus the poorer data-theory correlation for M=0.8 is understandable. In-phase oscillations at the higher inlet Mach number produce an upstream-traveling wave of larger amplitude than M=0.55, and the correlation between the data for all-airfoils-oscillating and the analysis is

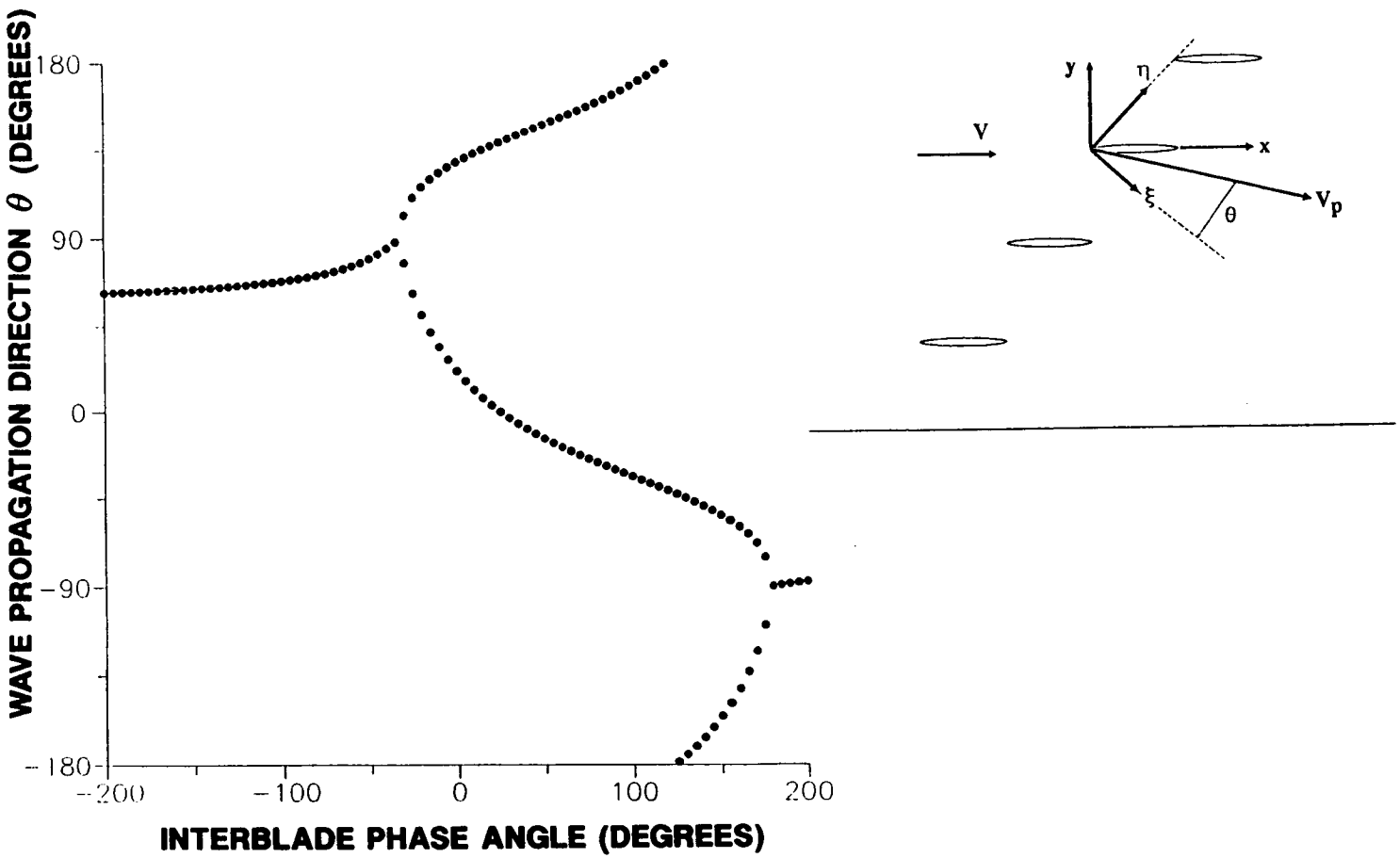

Figure 4.85 Pressure disturbance propagation direction, low solidity cascade, M=0.80, k=0.32

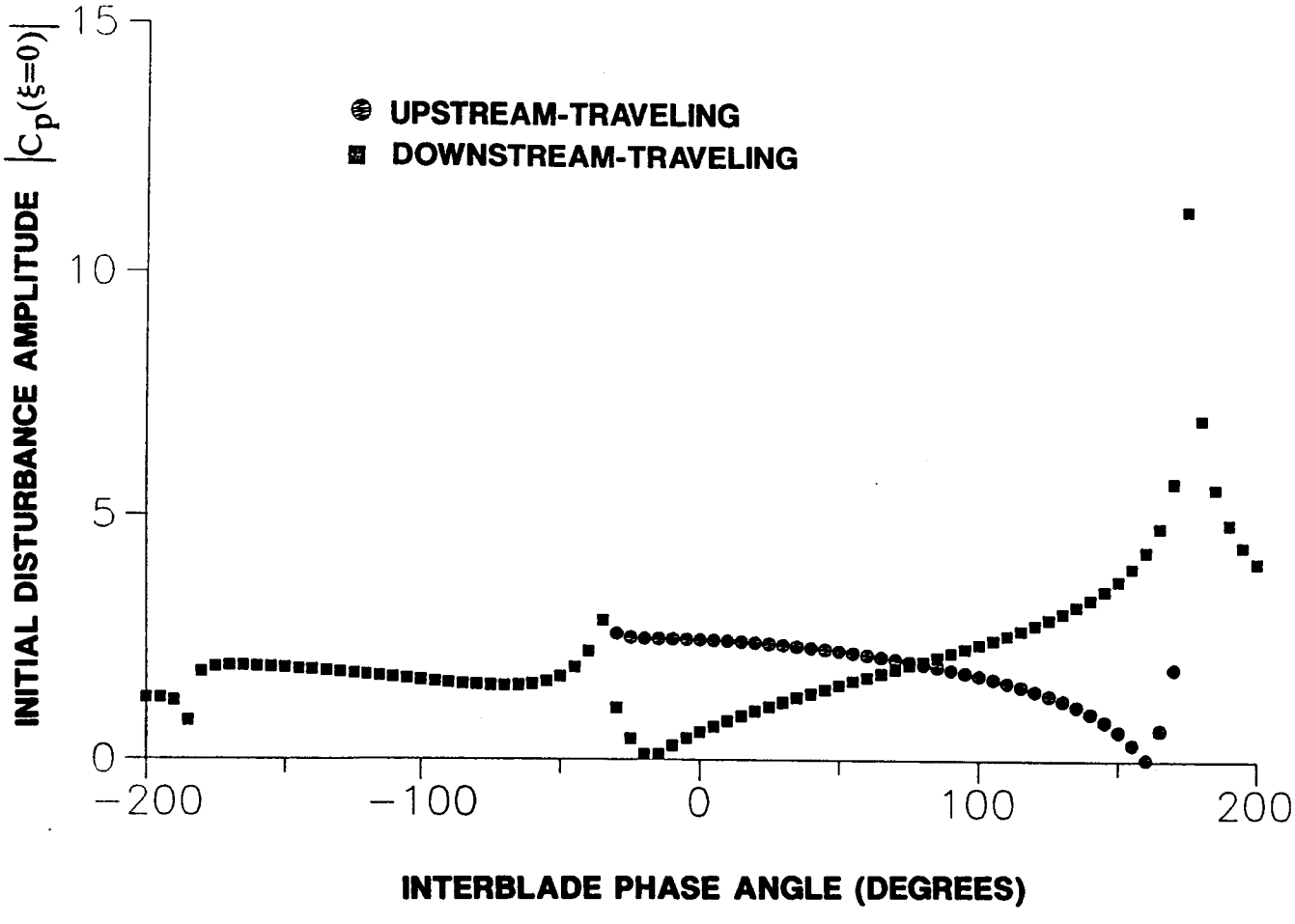

Figure 4.86 Initial pressure disturbance amplitude, low solidity cascade, M=0.80, k=0.32

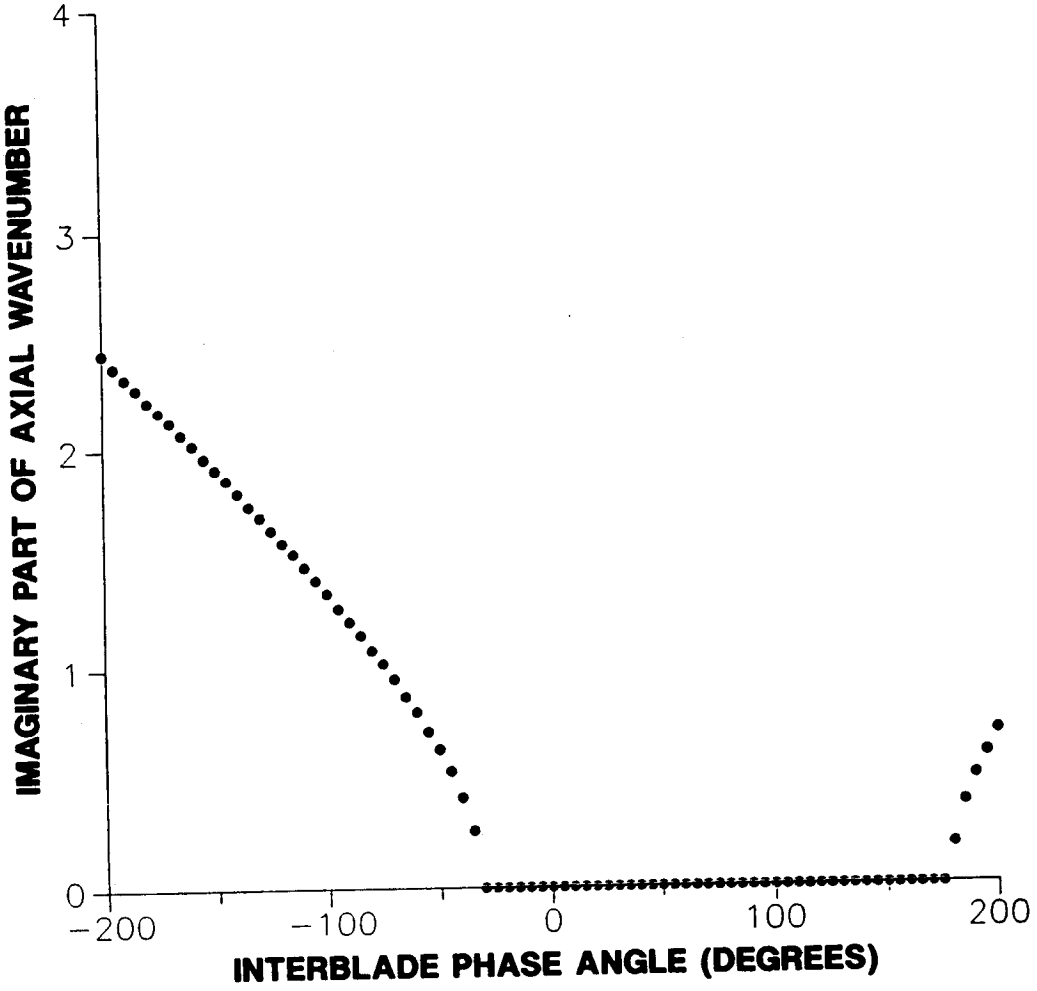

Figure 4.87 Imaginary part of axial wavenumber, low solidity cascade, M = 0.80, k = 0.32

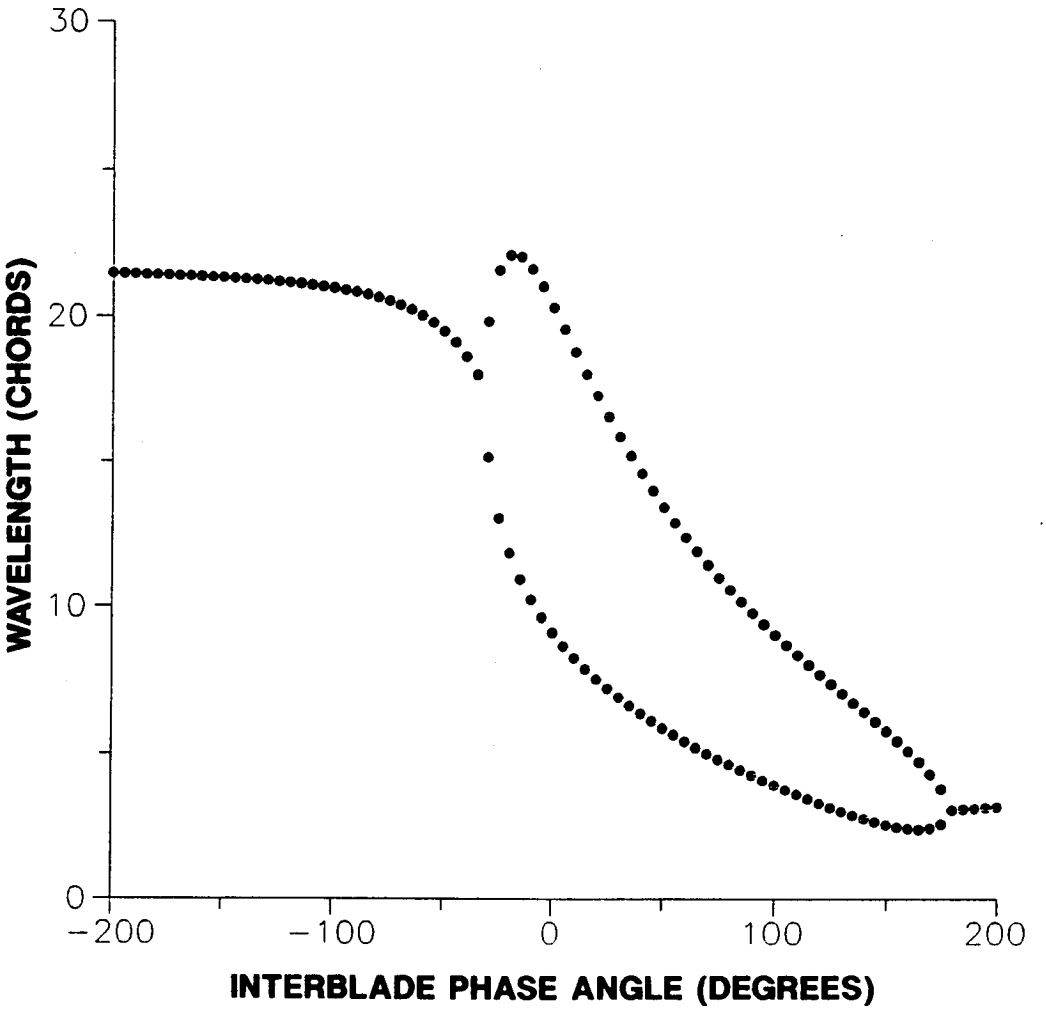

Figure 4.88 Pressure disturbance wavelength, low solidity cascade, M = 0.80, k = 0.32

reduced in comparison to M=0.55. For $\beta = 45°$, the wave propagation directions are quite different than for M=0.55, but the overall correlation is similar. In this case, the upstream-traveling wave ($\theta = 145°$) appears to be responsible. $\beta = 90°$ is now superresonant. The wave amplitudes are smaller at M=0.8 than M=0.55, but aren't predicted to decay, and the level of correlation is reduced.

High Solidity Cascade

The predicted acoustic wave propagation characteristics for the high solidity cascade with M=0.65, $\alpha_0=0$ and k=0.39 are presented in Figures 4.89 through 4.92. In comparison to the predictions for the low solidity cascade, the peak values of the initial disturbance amplitude are relatively large when $\beta > \beta_r^*$, but values of l' are also relatively large, so the high solidity cascade waves may initially be of larger amplitude, but tend to decay more rapidly. The all-airfoils-oscillating experiment phase data correlate poorly with the predictions for $\beta = 0°$, Figure 4.72, and for $\beta = 90°$, Figure 4.75. In both cases, waves are predicted which may reflect off a wind tunnel wall and back into the cascade, thus affecting the unsteady aerodynamics. The wave predicted for $\beta = -90°$ is directed at the upper cascade wall and will reflect away from the cascade.

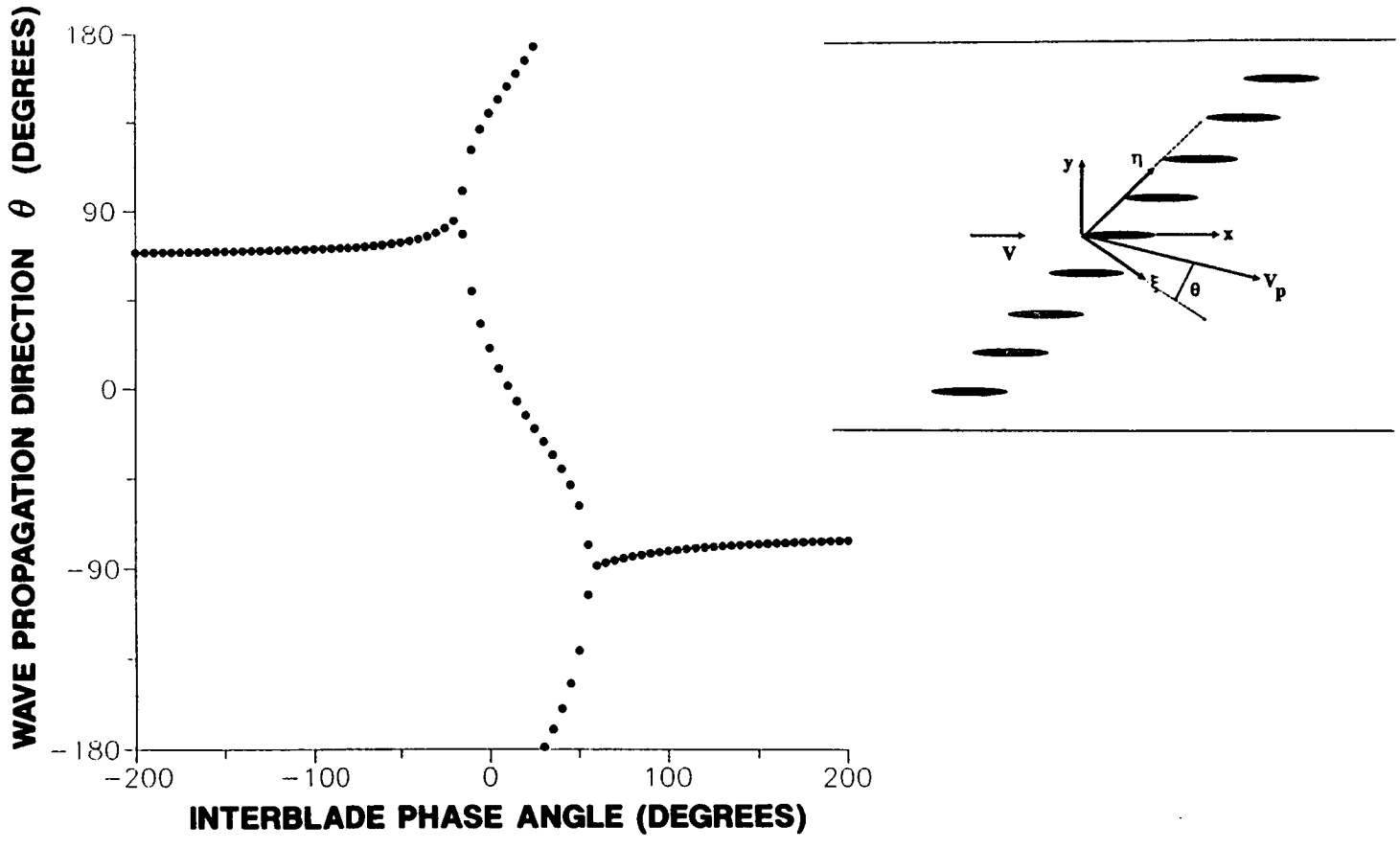

Figure 4.89 Pressure disturbance propagation direction, high solidity cascade, M=0.65, α_0=0 degrees, k=0.39

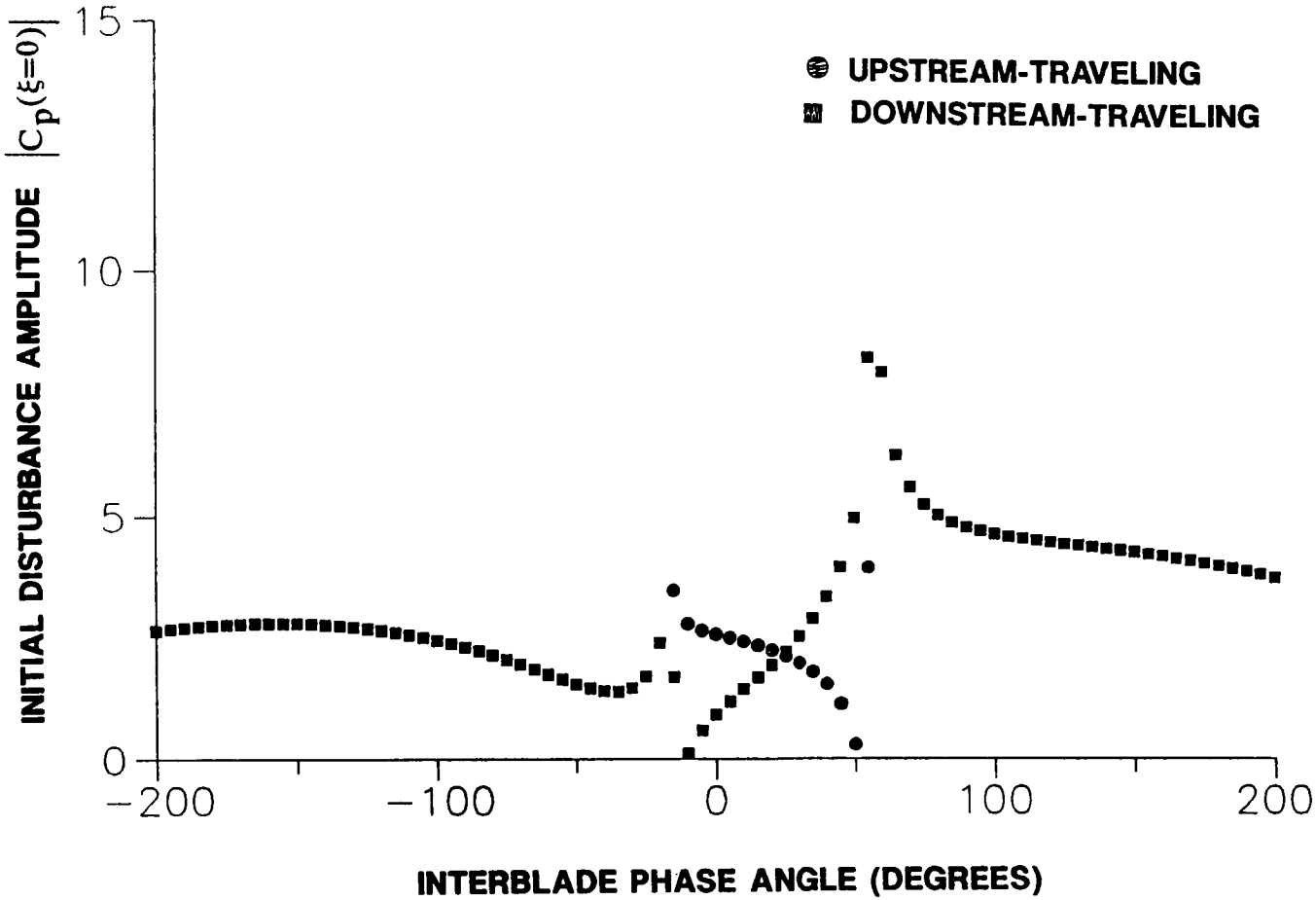

Figure 4.90 Initial pressure disturbance amplitude, high solidity cascade, M=0.65, α_0=0 degrees, k=0.39

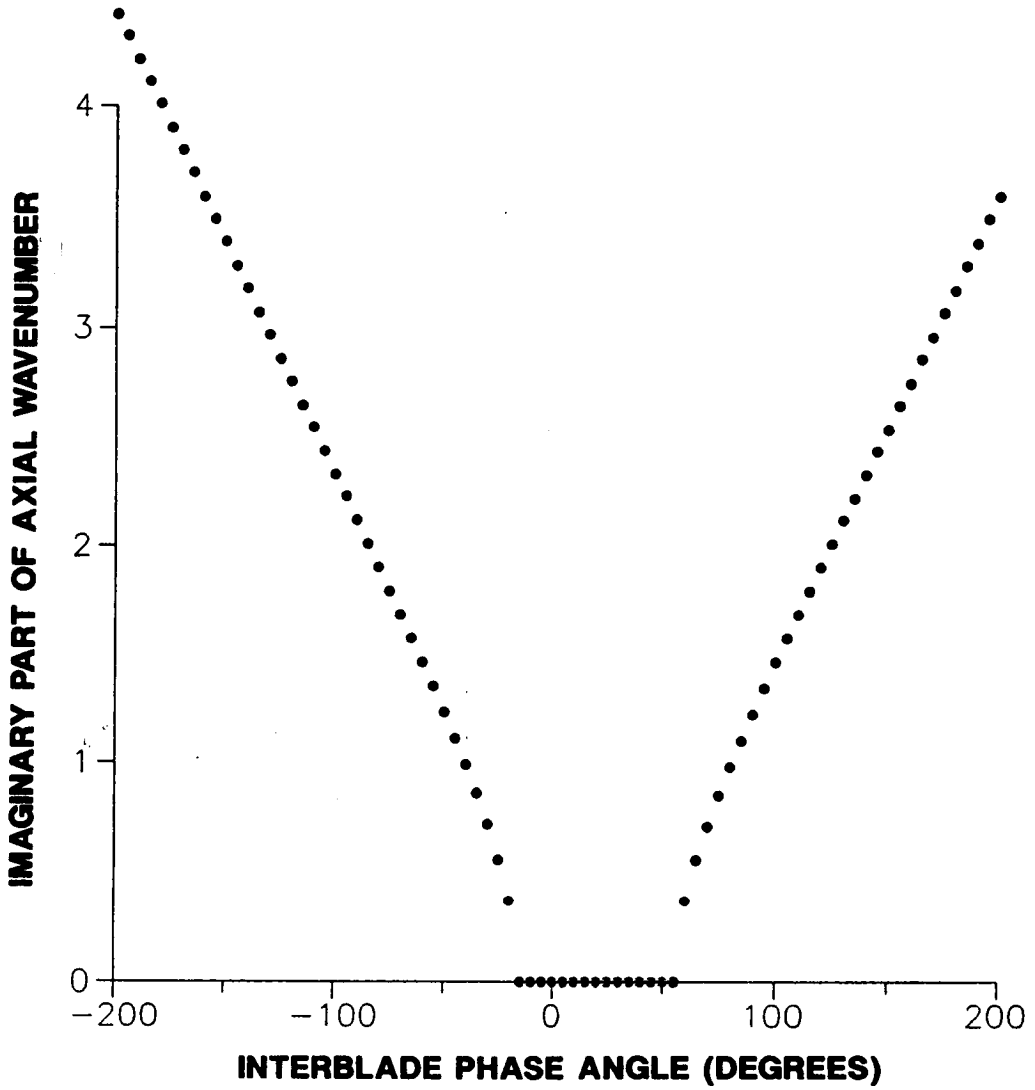

Figure 4.91 Imaginary part of axial wavenumber, high solidity cascade, M = 0.65, $\alpha_0 = 0$ degrees, k = 0.39

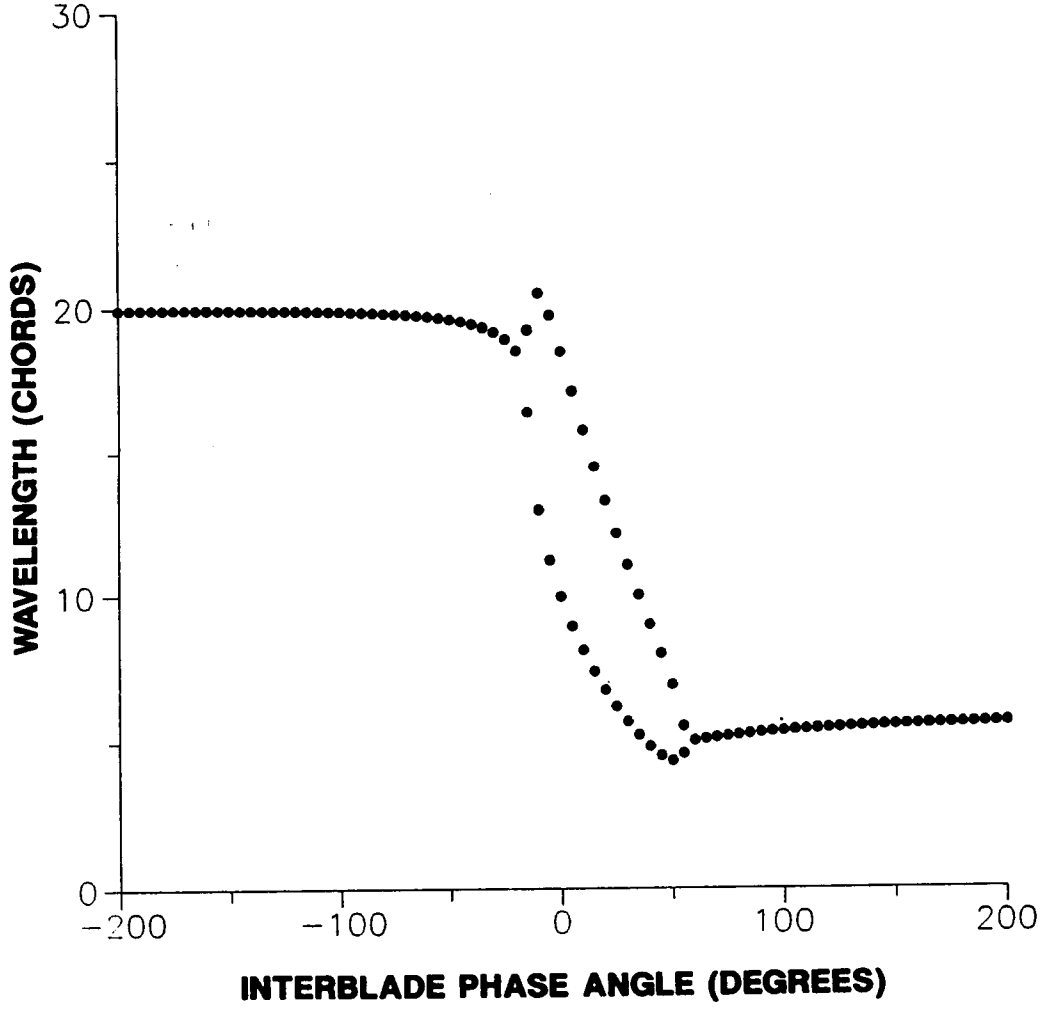

Figure 4.92 Pressure disturbance wavelength, high solidity cascade, M=0.65, α_0=0 degrees, k=0.39

CHAPTER 5
COMPUTATIONAL UNSTEADY AERODYNAMIC INFLUENCE COEFFICIENT TECHNIQUE

An Euler solver for oscillating cascaded airfoils is modified to implement the computational unsteady aerodynamic influence coefficient technique. First, a description of the baseline code is presented along with a description of boundary condition modifications which improve the ability of the code to predict oscillating cascade aerodynamics and sample results. Then the code, as modified for the unsteady aerodynamic influence coefficient technique, is described and results are correlated with both experimental data and linearized analysis predictions.

5.1 Euler Solver for Oscillating Cascaded Airfoils

Solutions of the time-dependent equations for the conservation of mass, momentum and energy for the two-dimensional flow of an inviscid, non-heat-conducting calorically perfect gas are obtained for a body-fitted coordinate system via an implicit finite difference procedure. The flow solver was initially coded for isolated pitching airfoils by Sankar and Tang [33], extended by Wu [34] and adapted to cascade flows by Huff [13].

5.1.1 Mathematical Model

A body-fitted C-grid, Figure 5.1, is transformed from the spatial coordinates x, y and time t into the ξ, η, τ coordinate system which depends upon the x, y, t coordinates.

$$\xi = \xi(x, y, t), \eta = \eta(x, y, t), \tau = \tau(t) \qquad (5.1)$$

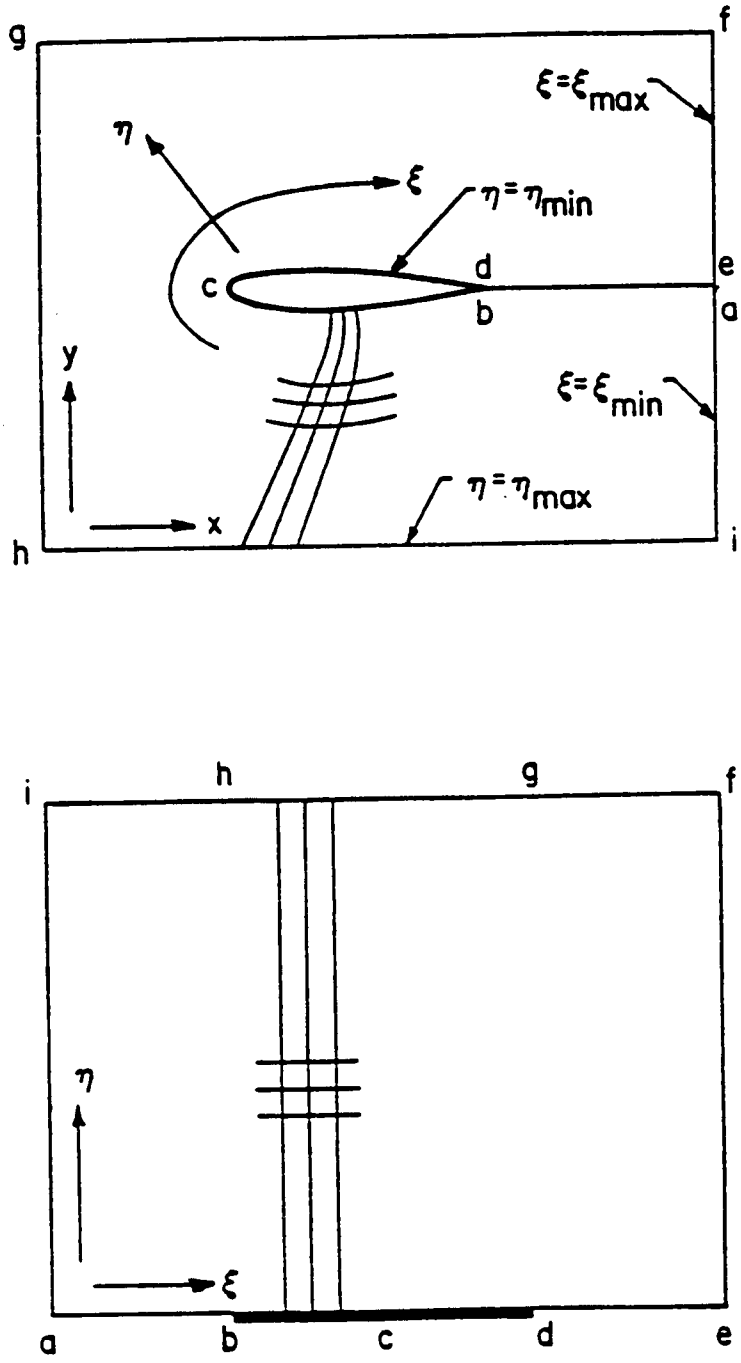

Figure 5.1 Body-fitted coordinate transformation

The conservation of mass, momentum and energy in the transformed coordinate system, the Euler equations, are expressed in matrix conservation-law form, Equation 5.2.

$$\frac{\partial \mathbf{Q}}{\partial \tau} + \frac{\partial \mathbf{E}}{\partial \xi} + \frac{\partial \mathbf{F}}{\partial \eta} = 0 \tag{5.2}$$

The unknown quantities ρ, the density, u and v, the x and y components of velocity and e, the total energy per unit volume, are components of the vector $\mathbf{Q}$.

$$\mathbf{Q} = J^{-1}\begin{pmatrix} \rho \\ \rho u \\ \rho v \\ e \end{pmatrix} \tag{5.3}$$

where

$$e = \rho\left(c_v T + \frac{1}{2}(u^2 + v^2)\right) \tag{5.4}$$

All quantities in these equations are nondimensional. Lengths are divided by the airfoil chord, velocity components are divided by the inlet speed of sound, time is multiplied by the inlet speed of sound divided by the airfoil chord, and the total energy per unit volume is divided by the product of the inlet density and the square of the inlet speed of sound.

The transformation Jacobian is given in equation 5.5, with the E and F vectors defined in Equations 5.6 and 5.7.

$$J = \frac{\partial \xi}{\partial x}\frac{\partial \eta}{\partial y} - \frac{\partial \xi}{\partial y}\frac{\partial \eta}{\partial x} \tag{5.5}$$

$$\mathbf{E} = J^{-1}\begin{pmatrix} \rho u_\xi \\ \rho u u_\xi + p\dfrac{\partial \xi}{\partial x} \\ \rho v u_\xi + p\dfrac{\partial \xi}{\partial y} \\ u_\xi(e+p) - p\dfrac{\partial \xi}{\partial t} \end{pmatrix} \tag{5.6}$$

$$\mathbf{F} = J^{-1}\begin{pmatrix} \rho v_\eta \\ \rho u v_\eta + p\dfrac{\partial \eta}{\partial x} \\ \rho v v_\eta + p\dfrac{\partial \eta}{\partial y} \\ v_\eta(e+p) - p\dfrac{\partial \eta}{\partial t} \end{pmatrix} \tag{5.7}$$

The ξ and η components of velocity are, respectively,

$$u_\xi = \frac{\partial \xi}{\partial t} + u\frac{\partial \xi}{\partial x} + v\frac{\partial \xi}{\partial y}, \quad v_\eta = \frac{\partial \eta}{\partial t} + u\frac{\partial \eta}{\partial x} + v\frac{\partial \eta}{\partial y}. \tag{5.8}$$

The pressure is related to the total energy and the velocity components by

$$p = (\gamma - 1)\left(e - \frac{\rho}{2}(u^2 + v^2)\right). \tag{5.9}$$

Baseline Boundary Conditions

To complete the mathematical model, boundary conditions are specified on the airfoil surface, the wake-region cut-line, the cascade periodic boundaries and the upstream and downstream boundaries. On the airfoil surface, line b-c-d of Figure 5.1, the relative normal velocity, v_η, must be zero. u_ξ and ρ are extrapolated from the interior of the computational domain, and the surface normal pressure gradient is approximately

$$\frac{\partial p}{\partial \eta} = 0. \tag{5.10}$$

The surface pressure is determined from adjacent grid points using a one-sided difference approximation to Equation 5.10.

The wake-region cut-line consists of segments a-b and d-e, Figure 5.1. To preserve continuity of the variables across this cut, the variables along the cut are the averages of those one point above and below the cut.

Cascade periodic boundary conditions are satisfied by stacking airfoil grids and passing information between adjacent grids. This is achieved by expanding the grids with ghost points in the η direction so the grids overlap along the periodic boundaries.

Figure 5.2 shows how the ghost points are chosen to be coincident with interior points in the adjacent grid. The ghost points are used as the boundaries to the interior solution scheme which is applied to each airfoil grid sequentially for each time step. Thus the solution at the periodic boundaries is determined as part of the interior solution.

With the airfoils oscillating at a fixed nonzero interblade phase angle, the minimum number of airfoils, N_a, which satisfy the periodicity requirement

$$N_a|\beta| = 360^\circ \tag{5.11}$$

is used to define the cascade. Thus a 90 degree interblade phase angle requires modeling 4 airfoils. For in-phase oscillations, only one airfoil is required.

At the upstream boundary of the computational domain, the values of ρ, u and v are specified and e is extrapolated from the interior. At the downstream boundary, the static pressure is specified and ρ, u and v are extrapolated from the interior.

Modified Boundary Conditions

Improved boundary conditions at the cascade inflow and outflow boundaries are obtained using a one-dimensional approximation to the Euler equations as in reference 35. The Euler equations in primitive variable form (see Appendix B for details)

$$\frac{\partial \mathbf{q}}{\partial \tau} + \tilde{A}\frac{\partial \mathbf{q}}{\partial \xi} + \tilde{B}\frac{\partial \mathbf{q}}{\partial \eta} = 0 \tag{5.12}$$

with

$$\mathbf{q} = J^{-1}\begin{pmatrix} \rho \\ u \\ v \\ p \end{pmatrix} \tag{5.13}$$

are used to derive the boundary conditions. At the inflow boundary, derivatives with respect to ξ are neglected. Equation 5.12 becomes

$$\frac{\partial \mathbf{q}}{\partial \tau} + \tilde{B}\frac{\partial \mathbf{q}}{\partial \eta} = 0. \tag{5.14}$$

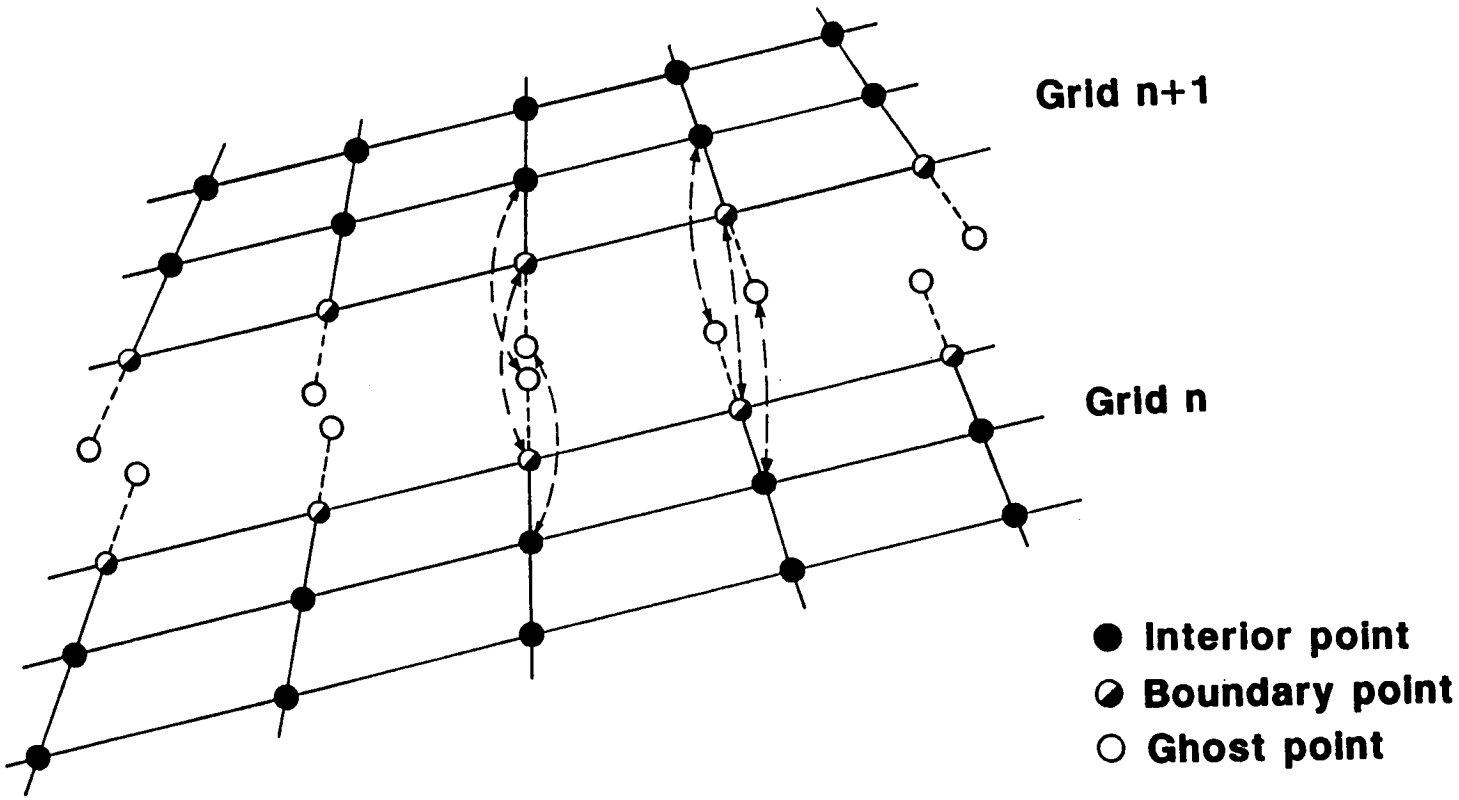

Figure 5.2 Overlapping grid

$\tilde{\mathbf{B}}$ may be expressed by the similarity transform $\tilde{\mathbf{B}} = \mathbf{R}_\eta \Lambda_\eta \mathbf{R}_\eta^{-1}$. Λ_η is a diagonal matrix of the eigenvalues of $\tilde{\mathbf{B}}$.

$$\Lambda_\eta = \begin{pmatrix} v_\eta & 0 & 0 & 0 \\ 0 & v_\eta & 0 & 0 \\ 0 & 0 & v_\eta + a|\nabla\eta| & 0 \\ 0 & 0 & 0 & v_\eta - a|\nabla\eta| \end{pmatrix} \tag{5.15}$$

where $|\nabla\eta| = \sqrt{(\partial\eta/\partial x)^2 + (\partial\eta/\partial y)^2}$.

The columns of $\mathbf{R}_\eta$ are right eigenvectors of $\tilde{\mathbf{B}}$ corresponding in order to the eigenvalues in Equation 5.15 and the rows of $\mathbf{R}_\eta^{-1}$ are corresponding left eigenvectors. Substituting for $\tilde{\mathbf{B}}$ and multiplying by $\mathbf{R}_\eta^{-1}$ gives

$$\mathbf{R}_\eta^{-1}\frac{\partial \mathbf{q}}{\partial \tau} + \Lambda_\eta \mathbf{R}_\eta^{-1}\frac{\partial \mathbf{q}}{\partial \eta} = 0. \tag{5.16}$$

$\mathbf{R}_\eta^{-1}$ is assumed to be constant (indicated by the subscript 0), so

$$\frac{\partial \mathbf{R}_{\eta 0}^{-1}\mathbf{q}}{\partial \tau} + \Lambda_\eta \frac{\partial \mathbf{R}_{\eta 0}^{-1}\mathbf{q}}{\partial \eta} = 0 \tag{5.17}$$

with

$$\mathbf{R}_{\eta 0}^{-1} = \begin{pmatrix} 1 & 0 & 0 & -1/a_0^2 \\ 0 & \tilde{\eta}_y & -\tilde{\eta}_x & 0 \\ 0 & \tilde{\eta}_x/\sqrt{2} & \tilde{\eta}_y/\sqrt{2} & 1/(\sqrt{2}\rho_0 a_0) \\ 0 & -\tilde{\eta}_x/\sqrt{2} & -\tilde{\eta}_y/\sqrt{2} & 1/(\sqrt{2}\rho_0 a_0) \end{pmatrix}. \tag{5.18}$$

$\tilde{\eta}_y = (\partial\eta/\partial y)/|\nabla\eta|$, for example, and $a = \sqrt{\gamma p/\rho}$ is the speed of sound. Letting

$$\mathbf{W}_\eta = \mathbf{R}_{\eta 0}^{-1}\mathbf{q} = J^{-1}\begin{pmatrix} \rho - \dfrac{p}{a_0^2} \\ u\tilde{\eta}_y - v\tilde{\eta}_x \\ \dfrac{u\tilde{\eta}_x}{\sqrt{2}} + \dfrac{v\tilde{\eta}_y}{\sqrt{2}} + \dfrac{p}{\sqrt{2}\rho_0 a_0} \\ \dfrac{-u\tilde{\eta}_x}{\sqrt{2}} - \dfrac{v\tilde{\eta}_y}{\sqrt{2}} + \dfrac{p}{\sqrt{2}\rho_0 a_0} \end{pmatrix} \tag{5.19}$$

results in Equation 5.20.

$$\frac{\partial W_\eta}{\partial \tau} + \Lambda_\eta \frac{\partial W_\eta}{\partial \eta} = 0 \tag{5.20}$$

Because Λ_η is diagonal, the individual equations of Equation 5.20 are decoupled and each component equation may be expressed as

$$\frac{\partial W_{\eta j}}{\partial \tau} + \Lambda_{\eta jj} \frac{\partial W_{\eta j}}{\partial \eta} = 0 \tag{5.21}$$

where $\Lambda_{\eta jj} = \frac{d\eta_j}{d\tau}$ is the speed of propagation of $W_{\eta j}$, the j-th component of W_η.

The sign of $\Lambda_{\eta jj}$ thus determines the propagation of information for $W_{\eta j}$. For subsonic flow at the inflow boundary, $\Lambda_{\eta 11}$, $\Lambda_{\eta 22}$ and $\Lambda_{\eta 44}$ are each less than zero. Thus $W_{\eta 1}$, $W_{\eta 2}$ and $W_{\eta 4}$ all travel into the computational domain from upstream, and their values at the upstream boundary are specified using the inlet values of ρ, u, v and p. $\Lambda_{\eta 33}$ is greater than zero, so $W_{\eta 3}$ waves travel from the interior of the computational domain toward the boundary. At the boundary, $W_{\eta 3}$ is calculated using values ρ, u, v and p extrapolated from the adjacent interior node in the η direction. Once the values of $W_{\eta j}$ are calculated, the simultaneous equations composing Equation 5.19 are solved for the boundary values of ρ, u, v and p.

Boundary conditions at the computational exit plane are determined in an analogous manner except that variations are neglected in the η direction. As a result,

$$\frac{\partial W_\xi}{\partial \tau} + \Lambda_\xi \frac{\partial W_\xi}{\partial \xi} = 0 \tag{5.22}$$

is obtained with

$$\Lambda_\xi = \begin{pmatrix} u_\xi & 0 & 0 & 0 \\ 0 & u_\xi & 0 & 0 \\ 0 & 0 & u_\xi + a|\nabla\xi| & 0 \\ 0 & 0 & 0 & u_\xi - a|\nabla\xi| \end{pmatrix} \tag{5.23}$$

and

$$W_\xi = R_{\xi 0}^{-1} q = J^{-1} \begin{pmatrix} \rho - \dfrac{p}{a_0^2} \\ u\xi_y - v\xi_x \\ \dfrac{u\xi_x}{\sqrt{2}} + \dfrac{v\xi_y}{\sqrt{2}} + \dfrac{p}{\sqrt{2}\rho_0 a_0} \\ \dfrac{-u\xi_x}{\sqrt{2}} - \dfrac{v\xi_y}{\sqrt{2}} + \dfrac{p}{\sqrt{2}\rho_0 a_0} \end{pmatrix}. \qquad (5.24)$$

The three of these quantities which propagate toward the boundary from the interior are extrapolated from the interior. One of $W_{\xi 3}$ and $W_{\xi 4}$ will propagate upstream. That quantity which propagates upstream is set equal to the mean flow value at the exit plane. The simultaneous equations for $W_{\xi j}$ are then solved for the boundary values of ρ, u, v and p.

5.1.2 Numerical Solution Technique

Equation 5.2 is solved numerically using an implicit finite difference technique. The time derivative is approximated by a first order accurate difference and the spatial derivatives are approximated by second order accurate central differences.

$$\frac{\Delta Q}{\Delta \tau} + \delta_\xi E^{n+1} + \delta_\eta F^{n+1} + O(\Delta\tau, \Delta\xi^2, \Delta\eta^2) \qquad (5.25)$$

with

$$\Delta Q = Q^{n+1} - Q^n$$

$$\Delta \tau = \tau^{n+1} - \tau^n$$

$$\delta_\xi E^{n+1} = \frac{E_{i+1,j}^{n+1} - E_{i-1,j}^{n+1}}{2\Delta\xi}$$

$$\delta_\eta F^{n+1} = \frac{F_{i,j+1}^{n+1} - F_{i,j-1}^{n+1}}{2\Delta\eta}$$

The nonlinear terms E and F are expanded in Taylor series.

$$E^{n+1} = E^n + \left(\frac{\partial E}{\partial Q}\right)^n \Delta Q + O(\Delta\tau^2) \qquad (5.26)$$

$$F^{n+1} = F^n + \left(\frac{\partial F}{\partial Q}\right)^n \Delta Q + O(\Delta\tau^2) \qquad (5.27)$$

Substituting Equations 5.26 and 5.27 into 5.25 and letting $A = \partial E/\partial Q$ and $B = \partial F/\partial Q$, a system of linear equations in ΔQ is obtained.

$$(I + \Delta\tau\delta_\xi A^n + \Delta\tau\delta_\eta B^n)\Delta Q = -\Delta\tau(\delta_\xi E^n + \delta_\eta F^n) \qquad (5.28)$$

Expressions for A and B are in Appendix B.

Application of Equation 5.28 to the interior of the computational domain results in a sparse block pentadiagonal matrix which must be solved at each time step. A more efficient solution technique is to factor the left hand side of Equation 5.28 into a product of ξ and η derivatives. Since

$$(I + \Delta\tau\delta_\xi A^n)(I + \Delta\tau\delta_\eta B^n) = I + \Delta\tau\delta_\xi A^n + \Delta\tau\delta_\eta B^n + \Delta\tau^2\delta_\xi A^n\delta_\eta B^n$$

Equation 5.28 may be approximated by

$$(I + \Delta\tau\delta_\xi A^n)(I + \Delta\tau\delta_\eta B^n)\Delta Q = -\Delta\tau(\delta_\xi E^n + \delta_\eta F^n) \qquad (5.29)$$

without degrading the formal accuracy of the equation.

The linear system of Equation 5.29 is solved in alternating directions by first solving

$$(I + \Delta\tau\delta_\xi A^n)\Delta Q' = -\Delta\tau(\delta_\xi E^n + \delta_\eta F^n) \qquad (5.30)$$

then

$$(I + \Delta\tau\delta_\eta B^n)\Delta Q = \Delta Q'. \qquad (5.31)$$

A system of block tridiagonal equations is obtained for each of these sweeps.

Implicit and explicit damping terms, as described in reference 34, are added to the discretized equations to suppress high frequency oscillations arising from the central differences.

A deforming grid is used to capture the oscillating airfoil motion, reference 13. A linear weighting function w is defined which allows the grid points on the airfoil

surface, $\eta = \eta_{min}$, to follow the airfoil motion while the grid points at the outer boundary, $\eta = \eta_{max}$, remain fixed.

$$w_{ij} = 1 - \frac{s(\xi,\eta)}{s(\xi,\eta_{max})} \tag{5.32}$$

$s(\xi,\eta)$ is the arc length in the physical plane of the grid line ξ = constant from the airfoil surface ($\eta = \eta_{min}$) to η. Then the grid deformation for one time step is

$$\Delta x_{ij} = w_{ij}\Delta x'_{ij}$$

$$\Delta y_{ij} = w_{ij}\Delta y'_{ij}$$

$\Delta x'_{ij}$ and $\Delta y'_{ij}$ are changes in the grid coordinates for a solid body motion of the grid.

The C grid is generated using the GRAPE program (GRids about Airfoils using Poisson's Equation), reference 36. This program allows the user to specify the grid intersection angles at the boundaries, so orthogonality at the boundaries may be specified if desired, and also the mesh spacing at the boundaries. The code has been modified to better model turbomachine blades, reference 37, including enforced periodicity of the cascade C grid.

5.1.3 Results

To ascertain the effectiveness of the modified boundary conditions, test cases are considered for a cascade of flat plates oscillating in torsion about the midchord. The results from the modified Euler code are compared to results obtained from the baseline, unmodified code and the fully linearized subsonic oscillating cascade analysis [3].

The cascade consists of flat plates staggered at 53 degrees with 1.3 solidity. The inlet Mach number is 0.65, the mean flow incidence angle is zero and the reduced frequency is 0.22. For the codes, 1% thick flat plates with rounded leading and trailing edges are used to facilitate fitting the 199x33 C grid, Figure 5.3. Initially, the flow variables are set equal to the previously determined steady-state values. Then the

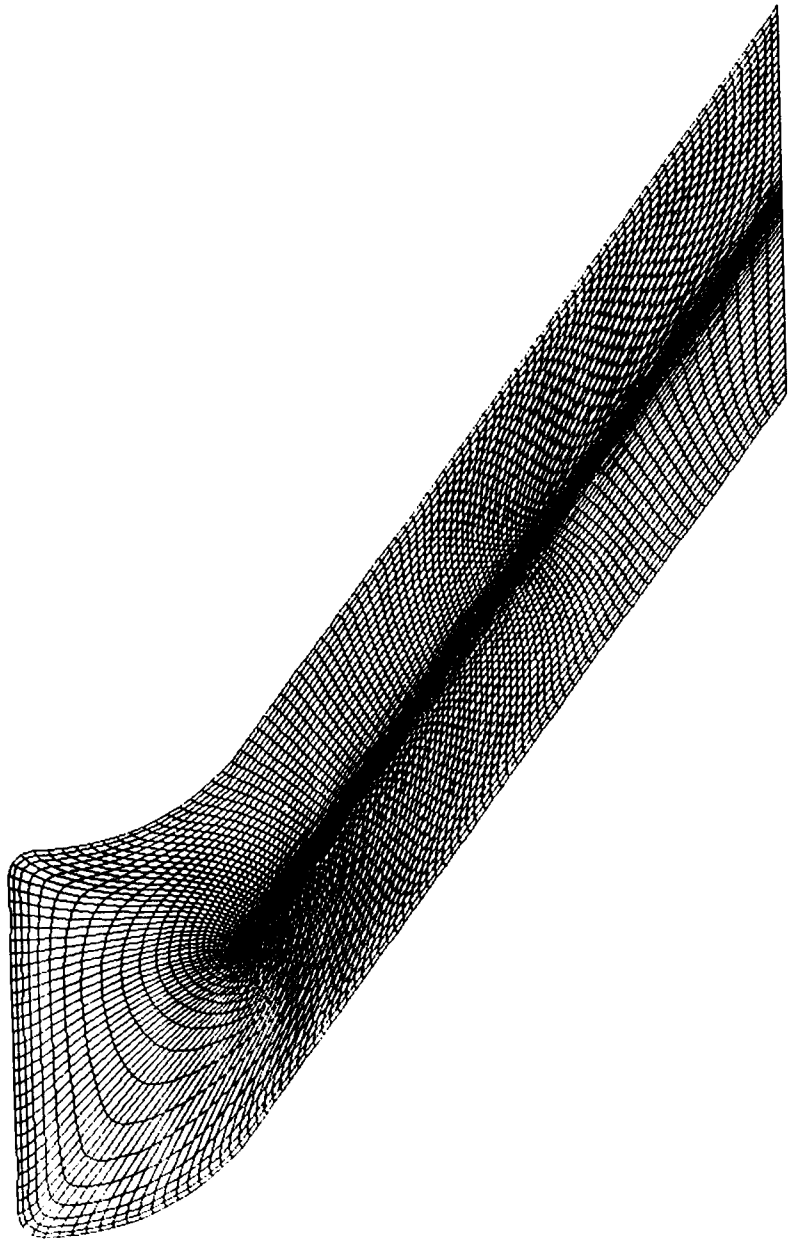

Figure 5.3 Flat plate cascade grid

airfoils oscillate for a number of cycles sufficient to reach a periodic unsteady solution. The airfoil surface unsteady pressures for the last cycle of oscillation are Fourier transformed to determine the first harmonic unsteady pressure distribution.

To illustrate the rapid convergence of the time-marching solution, results for in-phase oscillations are considered. As shown in Figure 5.4, the moment coefficient rapidly becomes periodic and varies in a sinusoidal manner. Figure 5.5, which shows that the first harmonic dynamic pressure difference coefficients for the third and fourth cycles of airfoil oscillation are essentially identical, further confirms the rapid convergence of the solution.

Predicted first harmonic unsteady pressure difference coefficients are compared with the baseline Euler code predictions and the linearized theory for interblade phase angle values of -90, 0 and 90 degrees, Figures 5.6 through 5.8. Running on the NASA Lewis CRAY-XMP, the Euler calculations required 2500 seconds to complete 3570 time steps (3.25 cycles of airfoil oscillation) for the -90 and 90 degree interblade phase angles. Since the in-phase oscillations require modeling only one airfoil as opposed to four, the computer time was roughly 625 seconds.

There is little difference between the unsteady pressure difference coefficients predicted by the Euler codes for $\beta = -90°$, Figure 5.6, a subresonant interblade phase angle, with both code results in good agreement with the predictions of Smith's analysis. In particular, the baseline code predictions for the ΔC_p magnitude are in excellent agreement with the theory but there are small differences between the magnitude predicted by the modified Euler code and the analysis. The phase distributions predicted by the Euler codes are almost identical except near the trailing edge. They agree well with the analytical predictions except for a small offset of about 10 degrees.

The modified boundary conditions have a large effect on the Euler code predictions for in-phase (superresonant) oscillations, Figure 5.7. While the predictions of the modified code are in very good agreement with the analytical predictions, the baseline Euler code predicts much larger magnitudes than Smith's analysis, and the

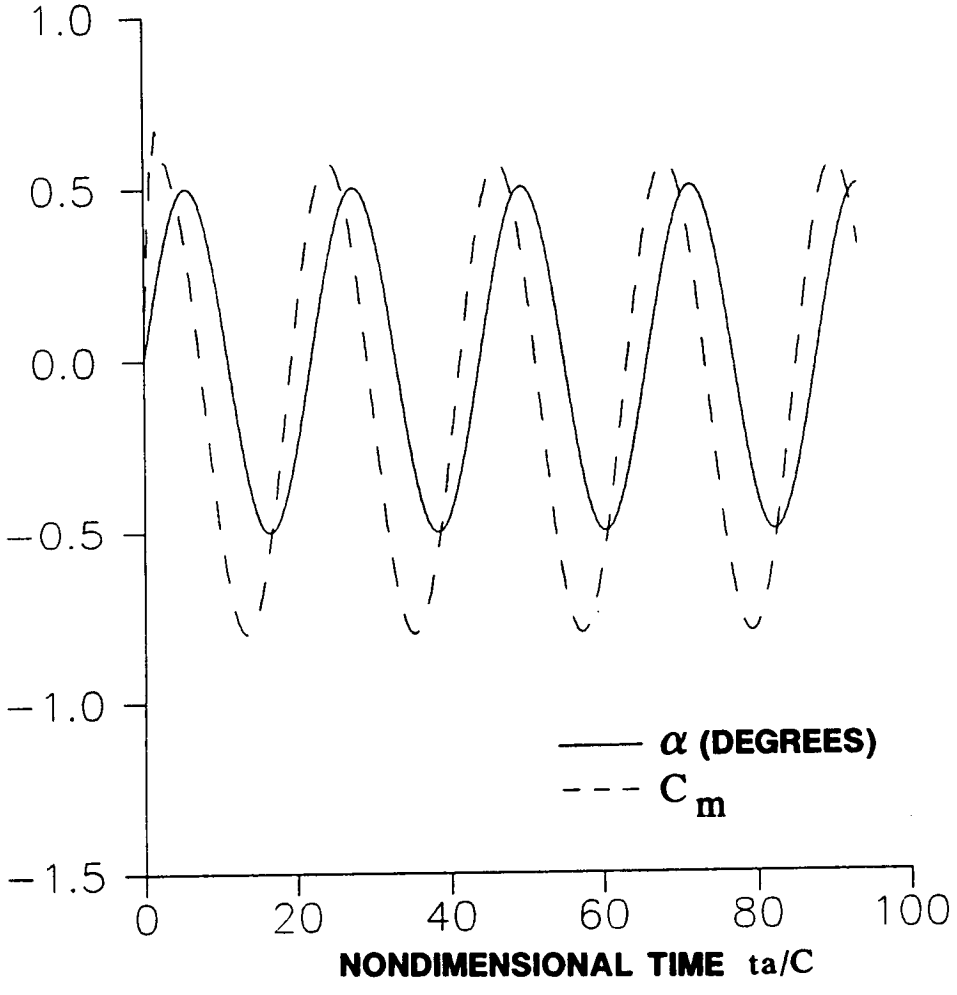

Figure 5.4 Incidence angle and moment coefficient versus time

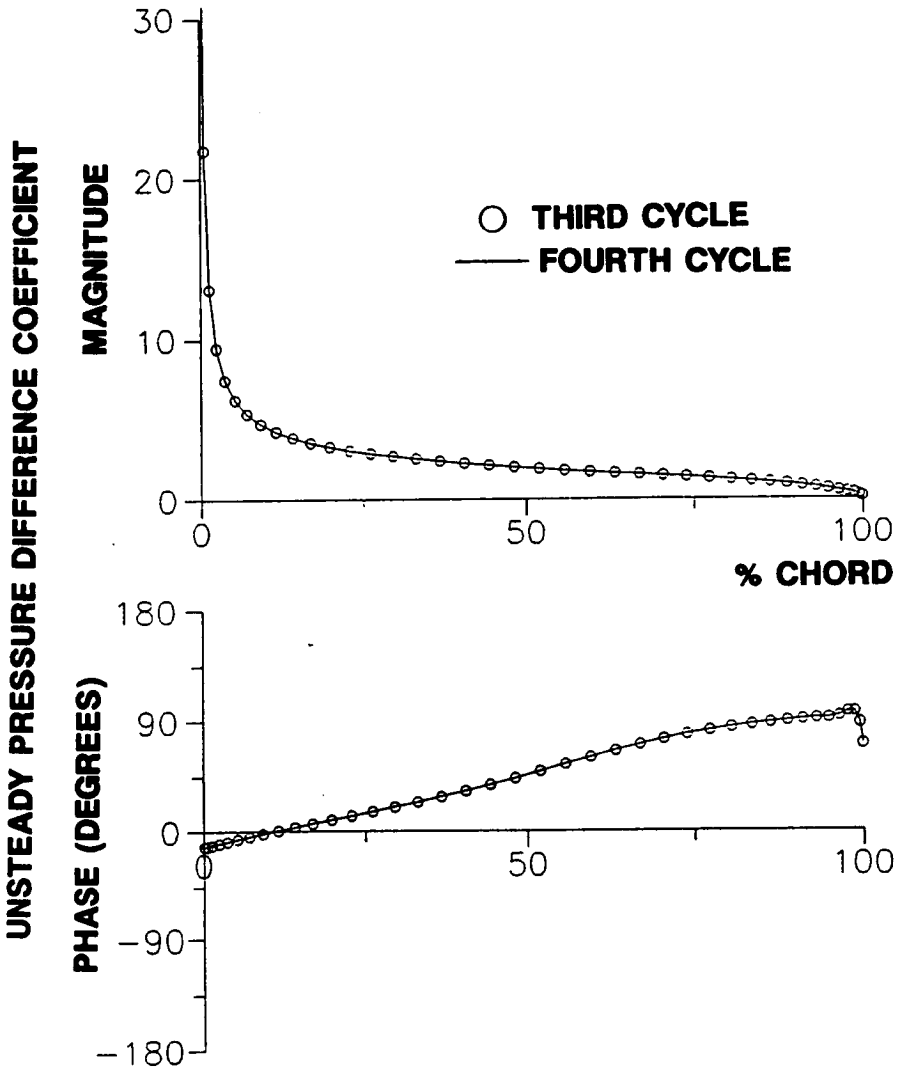

Figure 5.5 Comparison of unsteady pressure difference coefficients for third and fourth cycles of oscillation

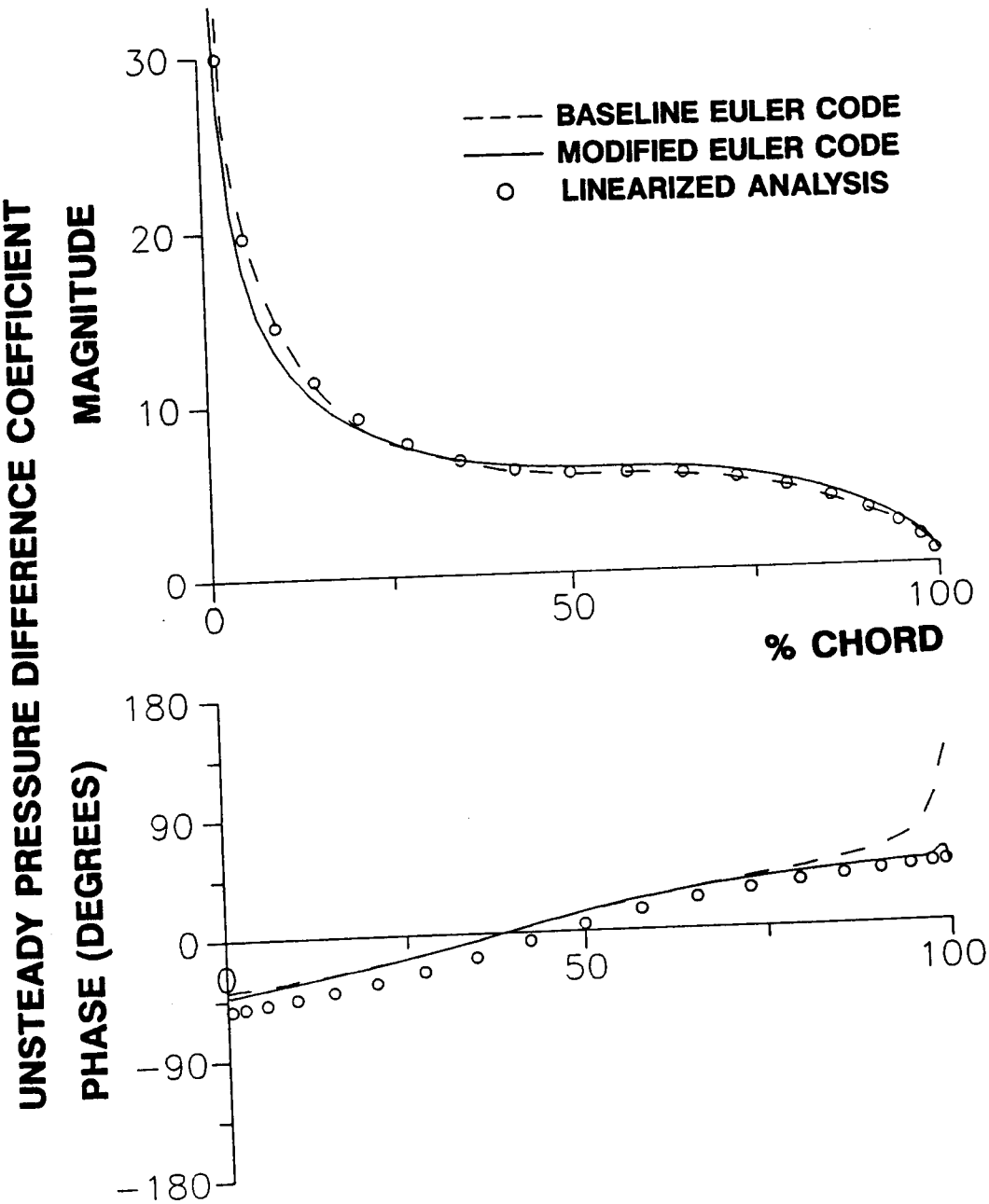

Figure 5.6 Comparison of Euler code predictions with linearized analysis, flat plate cascade, M=0.65, k=0.22, β=-90 degrees

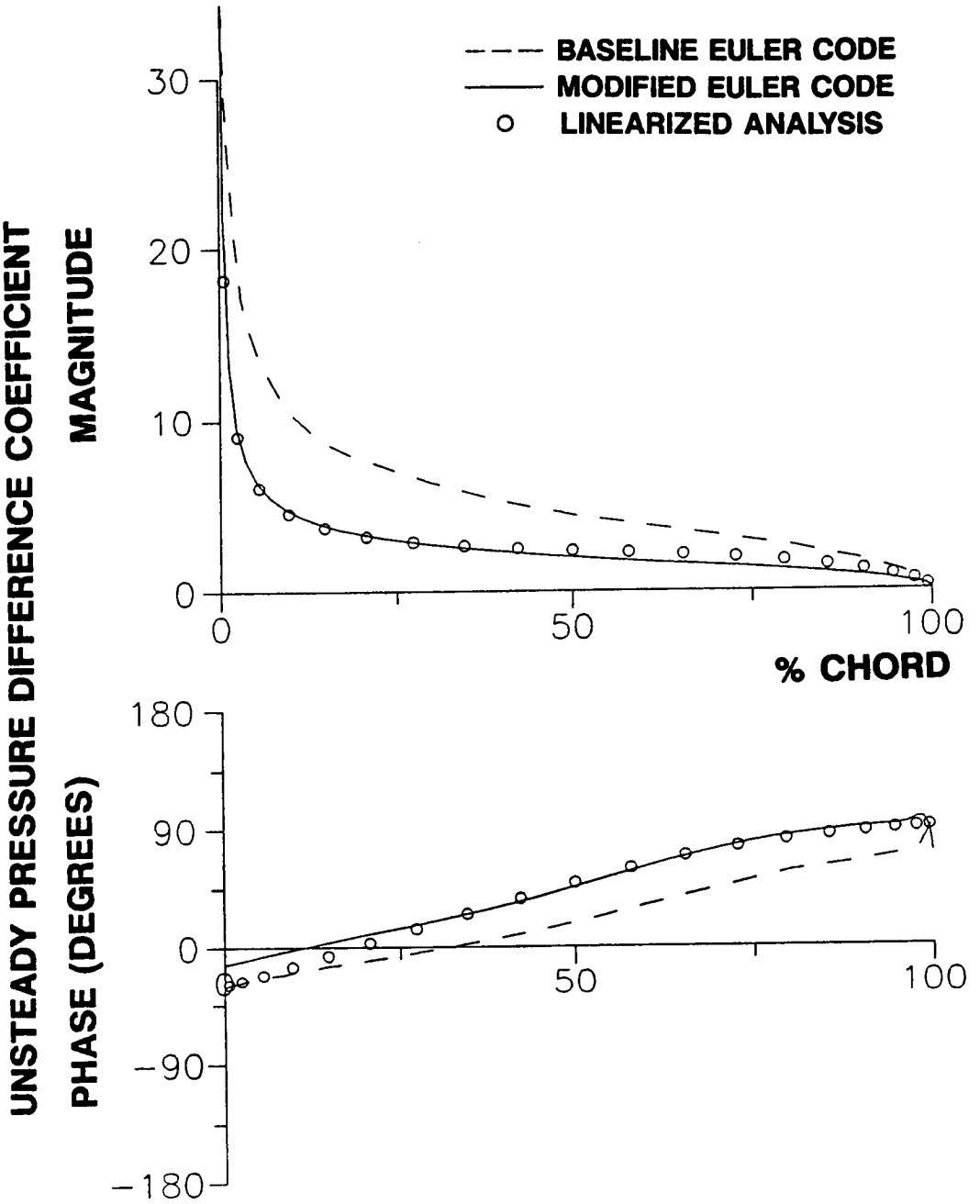

Figure 5.7 Comparison of Euler code predictions with linearized analysis, flat plate cascade, M=0.65, k=0.22, β=0 degrees

phase distribution is offset from the analytical predictions. Apparently, wave reflections from the upstream and downstream boundaries in the baseline code are detrimental to the predicted airfoil surface unsteady pressure distributions.

For $\beta = 90°$, a subresonant condition, the levels of agreement between the two codes and the theory are similar, Figure 5.8. The magnitude distribution predicted by the modified Euler code is in better agreement with the linearized analysis predictions over the forward half of the airfoil, but the baseline Euler code better agrees with the analytical predictions over the aft half. The phase distributions predicted by the codes are nearly identical except for the trailing edge region. These predictions are in very good trendwise agreement with the theory but there is some offset, particularly over the aft half of the airfoil where the corresponding magnitudes are relatively small.

5.2 Influence Coefficient Technique

Modifications to the Euler code allow implementation of the unsteady aerodynamic influence coefficient technique. After these modifications are described, calculated unsteady aerodynamic influence coefficients are presented for a cascade of oscillating flat plate airfoils and compared to the linearized theory. Summation of these influence coefficients is used to predict the cascade unsteady aerodynamics for various interblade phase angle values, with these results also correlated with the linearized analysis predictions. Then the influence coefficient technique is used to predict the biconvex airfoil cascade unsteady aerodynamics, and the results are correlated with the corresponding experimental data.

5.2.1 Euler Code Modifications

Just as when the airfoils are oscillating at a fixed interblade phase angle, grids are stacked for the desired number of airfoils. However, now only the center airfoil in the cascade oscillates. The one-dimensional boundary conditions are used at the inlet and exit. Overlapping grids are used to pass information between adjacent grids.

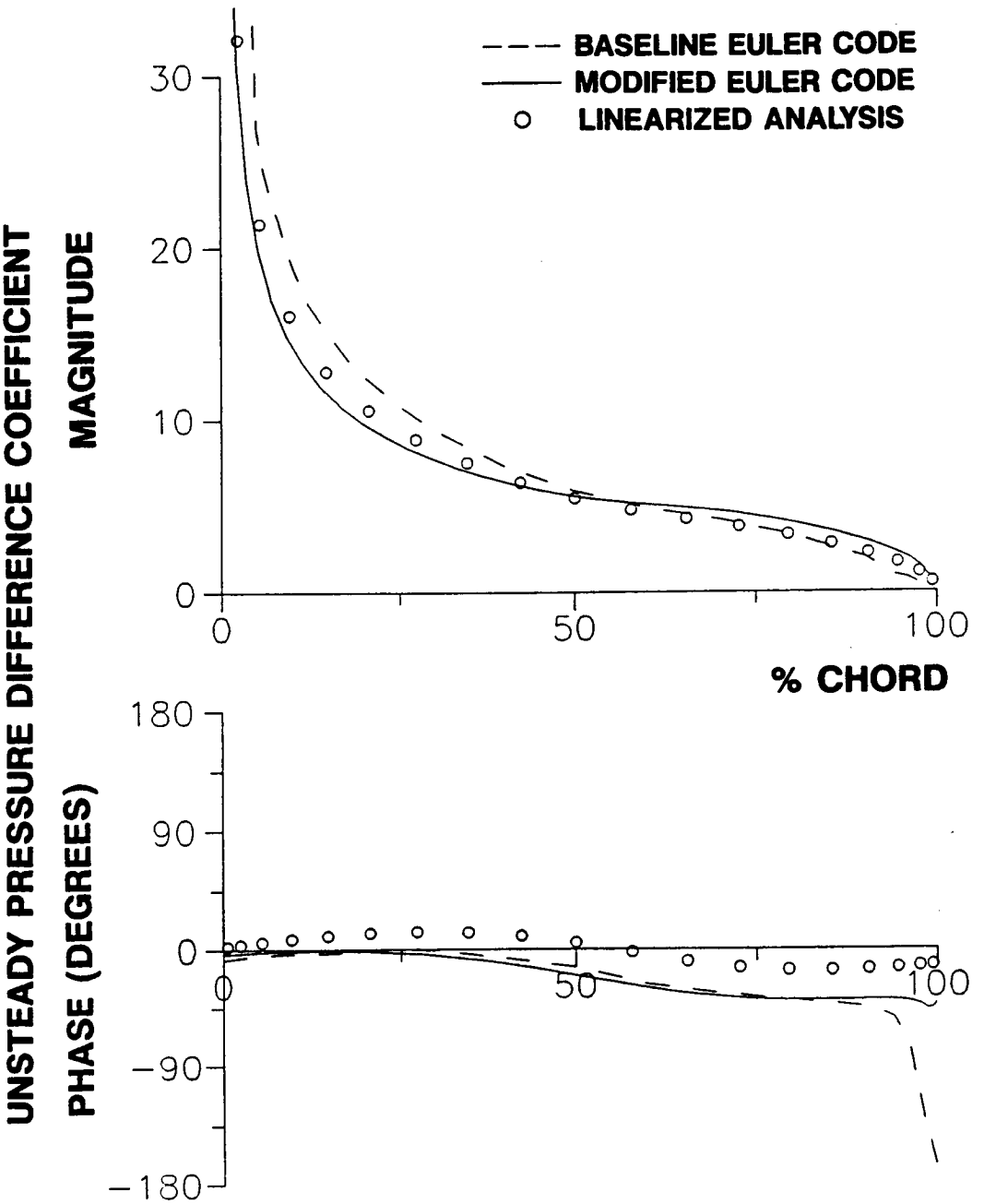

Figure 5.8 Comparison of Euler code predictions with linearized analysis, flat plate cascade, M=0.65, k=0.22, β=90 degrees

The two outermost airfoils in the cascade have open boundaries: boundary f-g in Figure 5.1 for the top airfoil, and boundary h-i for the bottom airfoil. These boundaries are treated by setting the flow variables at the ghost points equal to those from the steady-state solution.

Initially, the flow variables are set equal to the previously determined steady-state values. Then the center airfoil oscillates for an amount of time sufficient to reach a periodic unsteady solution. The airfoil surface unsteady pressures for the last cycle of oscillation are Fourier transformed in order to determine the first harmonic unsteady pressure distribution on each airfoil in the cascade. Predicted results for any value of interblade phase angle are obtained via summation of the influence coefficients.

5.2.2 Comparison with Linearized Analysis Results

First harmonic unsteady pressure difference influence coefficients predicted by the code for a cascade of oscillating flat plate airfoils are presented, then these influence coefficients are summed to predict unsteady aerodynamic moment coefficients over the entire range of interblade phase angle values. These predictions are correlated with influence coefficient results obtained from the linearized analysis using the technique described in Chapter 1. To study the effect of the number of cascaded airfoils, code results are presented for 5 airfoil and 7 airfoil cascades.

Unsteady pressure difference influence coefficients for a cascade of flat plates are presented in Figures 5.9 through 5.15 for values of n ranging from -3 to 3. The cascade has a stagger angle of 53 degrees and 1.3 solidity. The Mach number is 0.65, the incidence angle is 0 and the reduced frequency of oscillation is 0.5. The center airfoil is oscillating in torsion about the mid-chord. 1600 seconds of CPU time on the NASA Lewis CRAY-XMP were required to complete 1570 time steps (3.25 cycles of oscillation of the center airfoil) of the Euler solution for the 7 airfoil cascade.

For the self-induced unsteady pressure difference coefficients, Figure 5.9, there is good agreement between the code predictions and the linearized analysis. The code under-predicts the magnitude by a small amount, and there are small differences in the predicted phase angle distribution and the analysis. Differences between the code predictions for five and seven airfoils are negligible.

For the oscillating airfoil in relative position 1, Figure 5.10, the Euler code-linearized analysis correlation is very good in both magnitude and phase over the aft half of the reference airfoil. Significant phase differences occur over the forward half, but the predicted magnitudes are in good agreement with the theory except for the first 15% of the airfoil. The code predictions are the same for five and seven airfoil cascades.

Large phase differences are found for $\Delta\hat{C}_p^2$, Figure 5.11. The Euler code-linearized analysis magnitude correlation is good except in the leading edge region. There are small differences in the code predictions depending upon the number of cascaded airfoils, but these differences are small compared to the differences with the linearized analysis.

Large phase differences are also found for $\Delta\hat{C}_p^3$, Figure 5.12. The magnitude correlation is not good, either, with the code predicting magnitudes over the forward half of the airfoil which are large relative to the linearized analysis values.

With the oscillating airfoil immediately below the reference airfoil, Figure 5.13, the correlation is good in both magnitude and phase over the forward half of the airfoil. Aft of there, the correlation is poor due to large differences in the phase angle values. Fortunately, the corresponding magnitudes are relatively small, so the differences are not crucial.

The correlation is poor for $\Delta\hat{C}_p^{-2}$, Figure 5.14. Magnitudes predicted by the linearized analysis are negligible everywhere except near the leading edge, but the Euler code predictions are much larger. Differences between the predictions for five airfoil and seven airfoil cascades are insignificant.

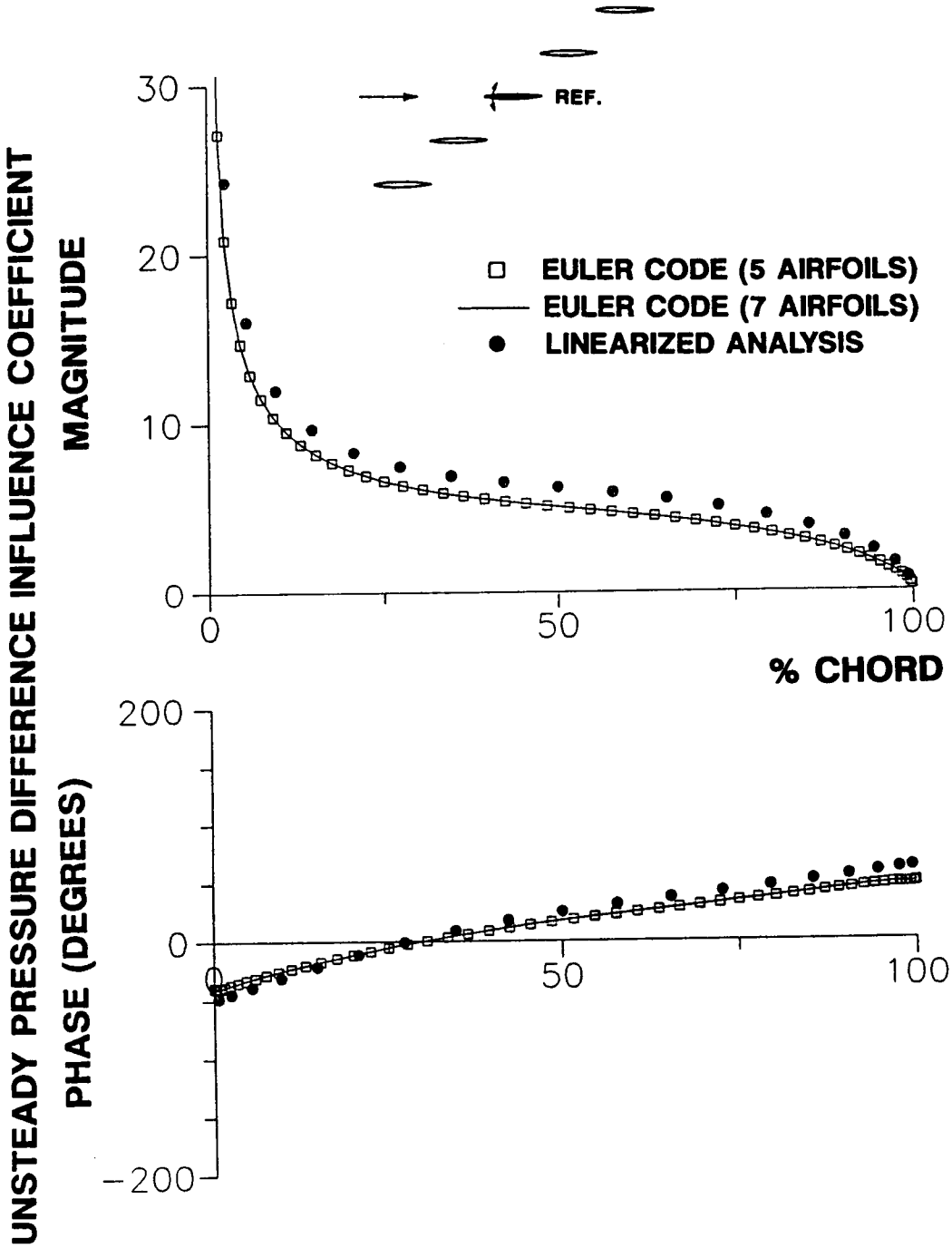

Figure 5.9 Predicted unsteady aerodynamic influence coefficient distributions, flat plate airfoil cascade, oscillating airfoil in relative position 0, M = 0.65, k = 0.50

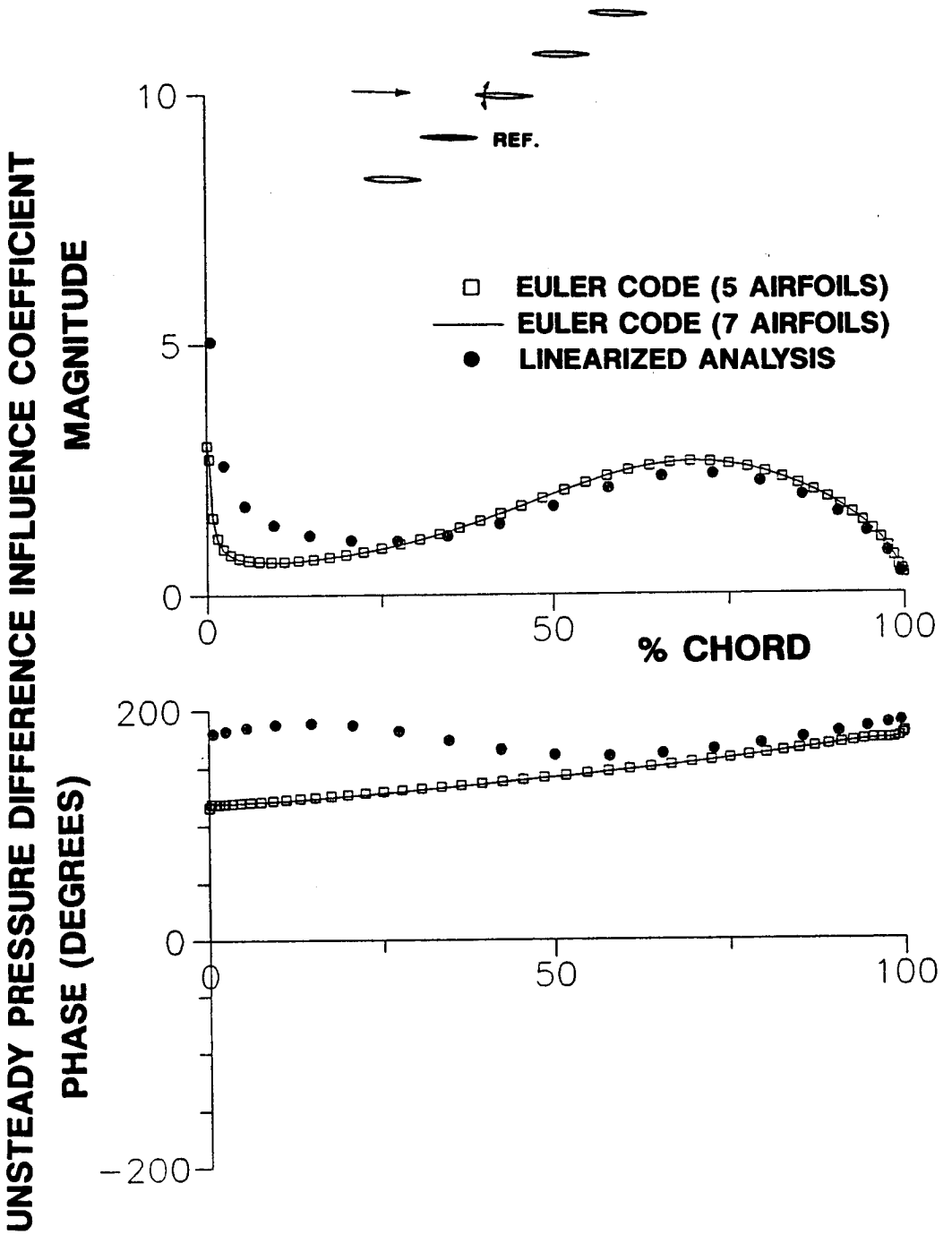

Figure 5.10 Predicted unsteady aerodynamic influence coefficient distributions, flat plate airfoil cascade, oscillating airfoil in relative position 1, M=0.65, k=0.50

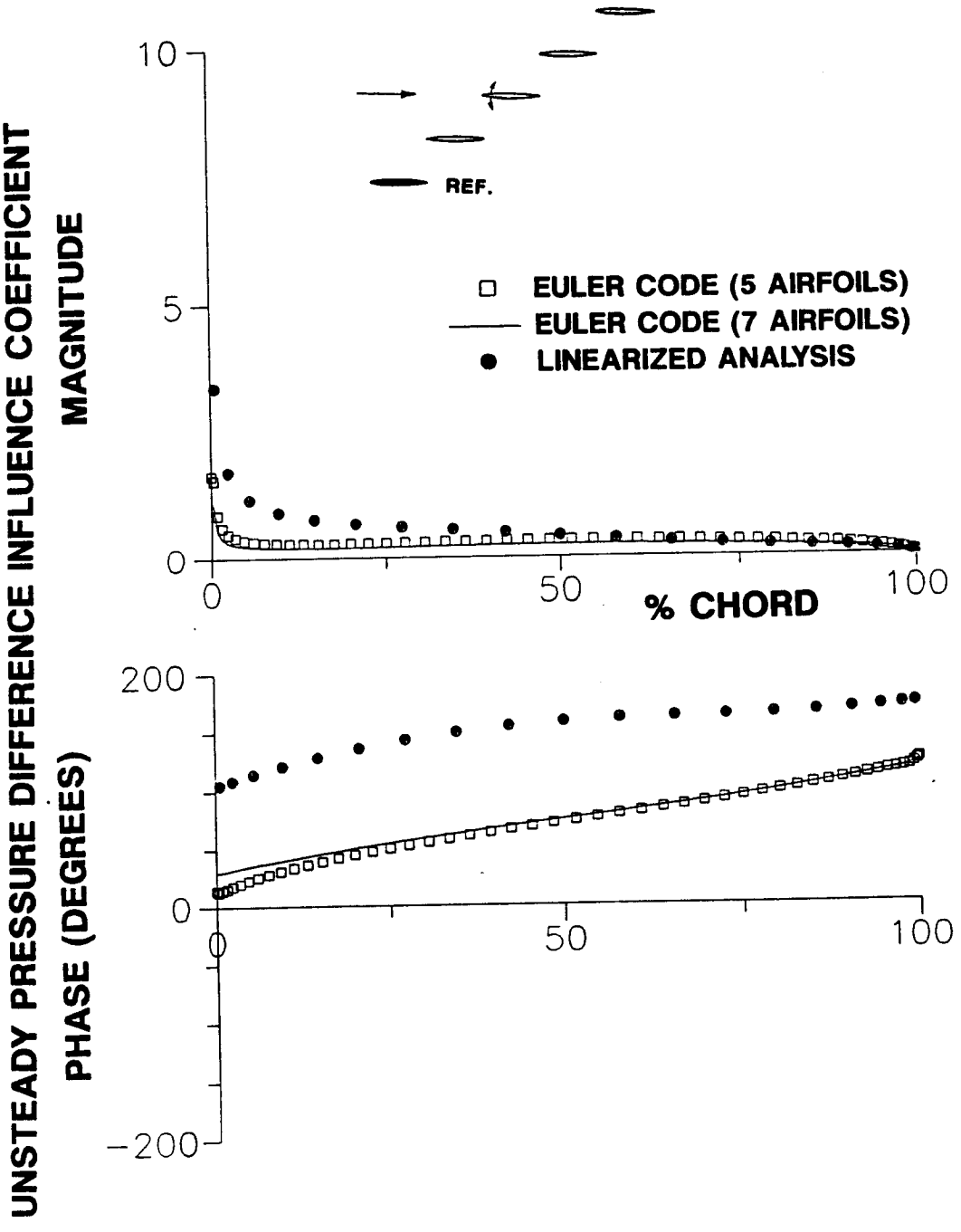

Figure 5.11 Predicted unsteady aerodynamic influence coefficient distributions, flat plate airfoil cascade, oscillating airfoil in relative position 2, M=0.65, k=0.50

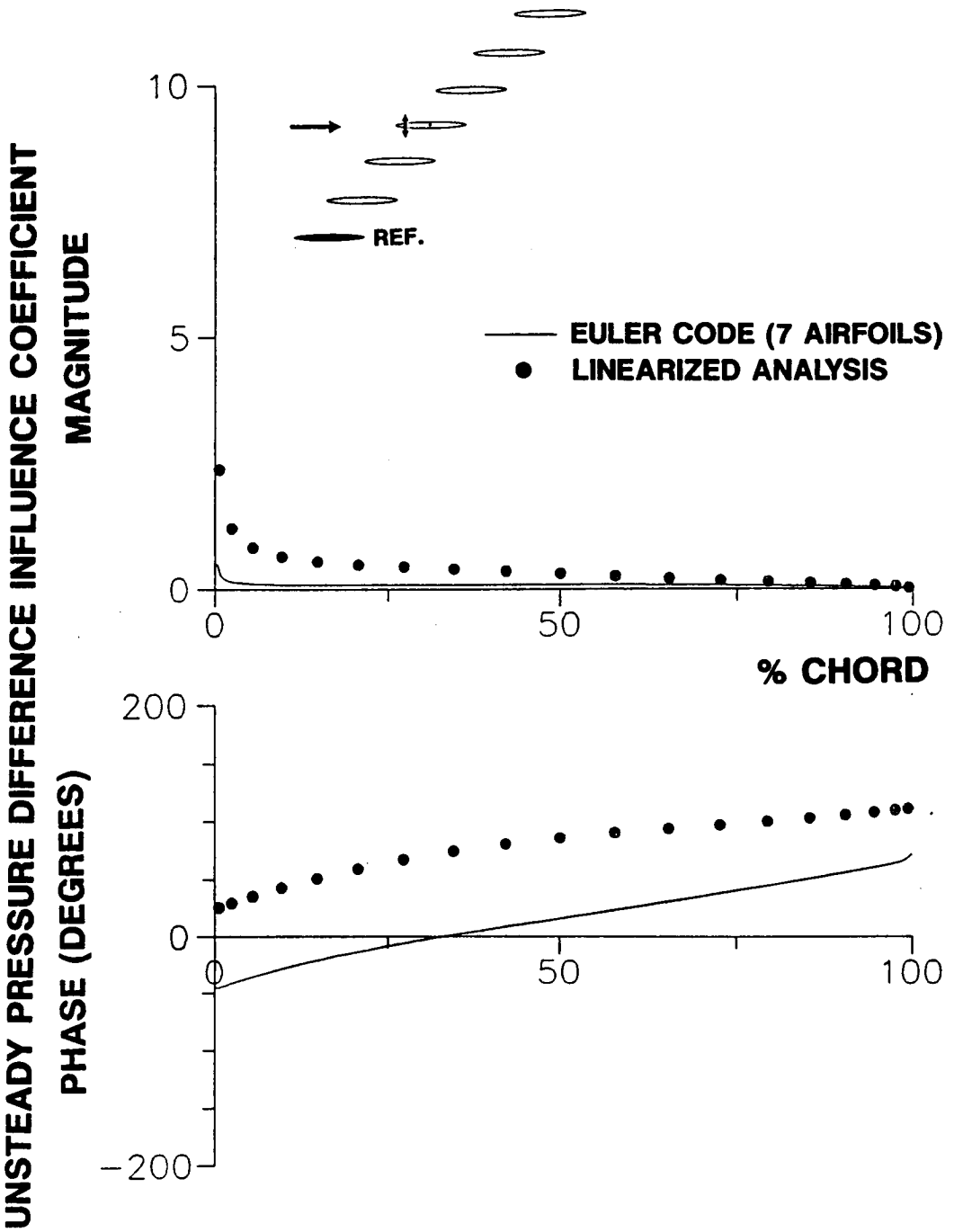

Figure 5.12 Predicted unsteady aerodynamic influence coefficient distributions, flat plate airfoil cascade, oscillating airfoil in relative position 3, M = 0.65, k = 0.50

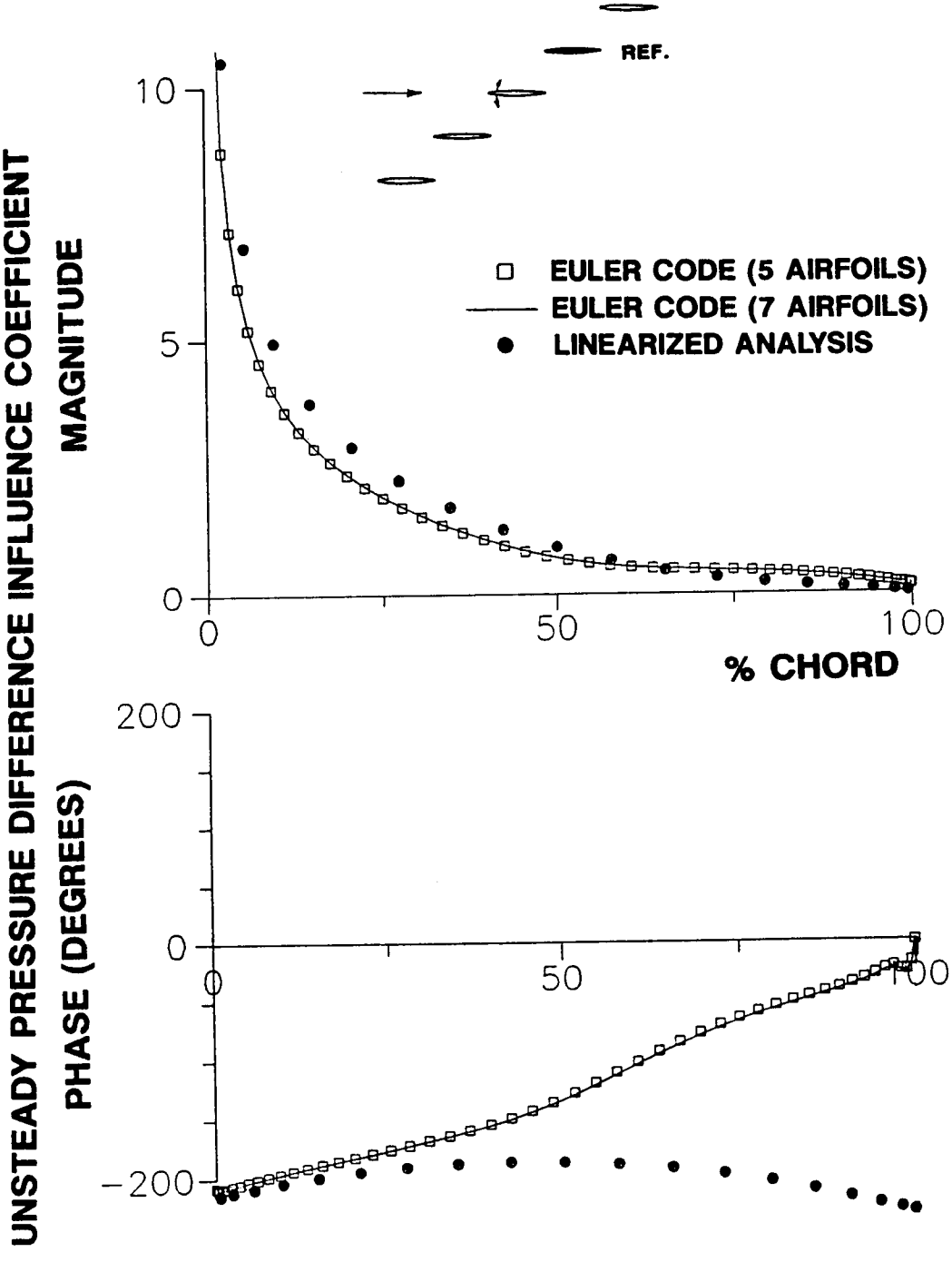

Figure 5.13 Predicted unsteady aerodynamic influence coefficient distributions, flat plate airfoil cascade, oscillating airfoil in relative position -1, M=0.65, k=0.50

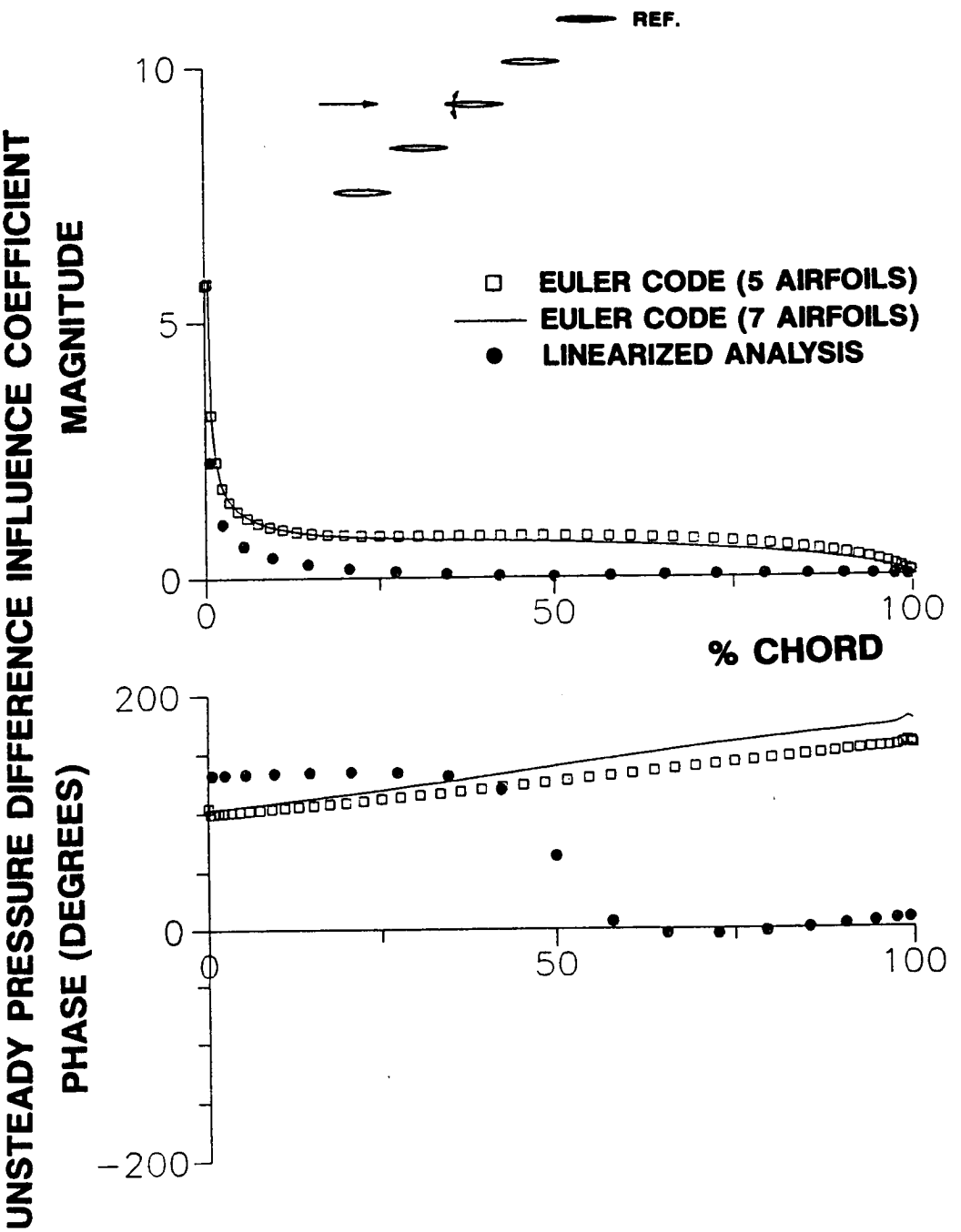

Figure 5.14 Predicted unsteady aerodynamic influence coefficient distributions, flat plate airfoil cascade, oscillating airfoil in relative position -2, M=0.65, k=0.50

Similar results are found for $\Delta \hat{C}_p^{-3}$, Figure 5.15: while the magnitudes predicted by the linearized analysis are mostly negligible, the magnitudes predicted by the Euler code are relatively large.

Equation 5.35 defines the unsteady aerodynamic moment coefficient about the midchord for a flat plate airfoil.

$$C_m = \int_0^1 \left(\frac{1}{2} - x^*\right) \Delta C_p(x^*) dx^* \tag{5.35}$$

x^* is the nondimensional chordwise coordinate, x/C. Accordingly, the unsteady aerodynamic moment influence coefficient resulting from oscillations of the airfoil in relative position n is given in Equation 5.36.

$$\hat{C}_m^n = \int_0^1 \left(\frac{1}{2} - x^*\right) \Delta \hat{C}_p^n(x^*) dx^*. \tag{5.36}$$

Unsteady aerodynamic moment influence coefficients obtained by integration of the Euler code seven airfoil cascade predictions of Figures 5.9 through 5.15 are presented in Figure 5.16 along with linearized analysis results. The unsteady aerodynamic moment on the reference airfoil is shown to be a strong function of the unsteady aerodynamics associated with oscillating the reference airfoil itself and the two adjacent airfoils. There is generally good agreement between the influence coefficients predicted by the code and the linearized analysis, but the difference in the imaginary part of $\hat{C}_m^0$ is significant.

The consequence of differences between the Euler code predictions and the results of the linearized analysis is shown in Figure 5.17, a plot of the imaginary part of the unsteady aerodynamic moment coefficient versus interblade phase angle. As demonstrated in reference 17, the work per cycle of oscillation done by the fluid on the airfoil is proportional to the imaginary part of C_m. Thus, when C_m^I is greater than 0, the work per cycle is positive, and flutter may occur. The curve predicted by

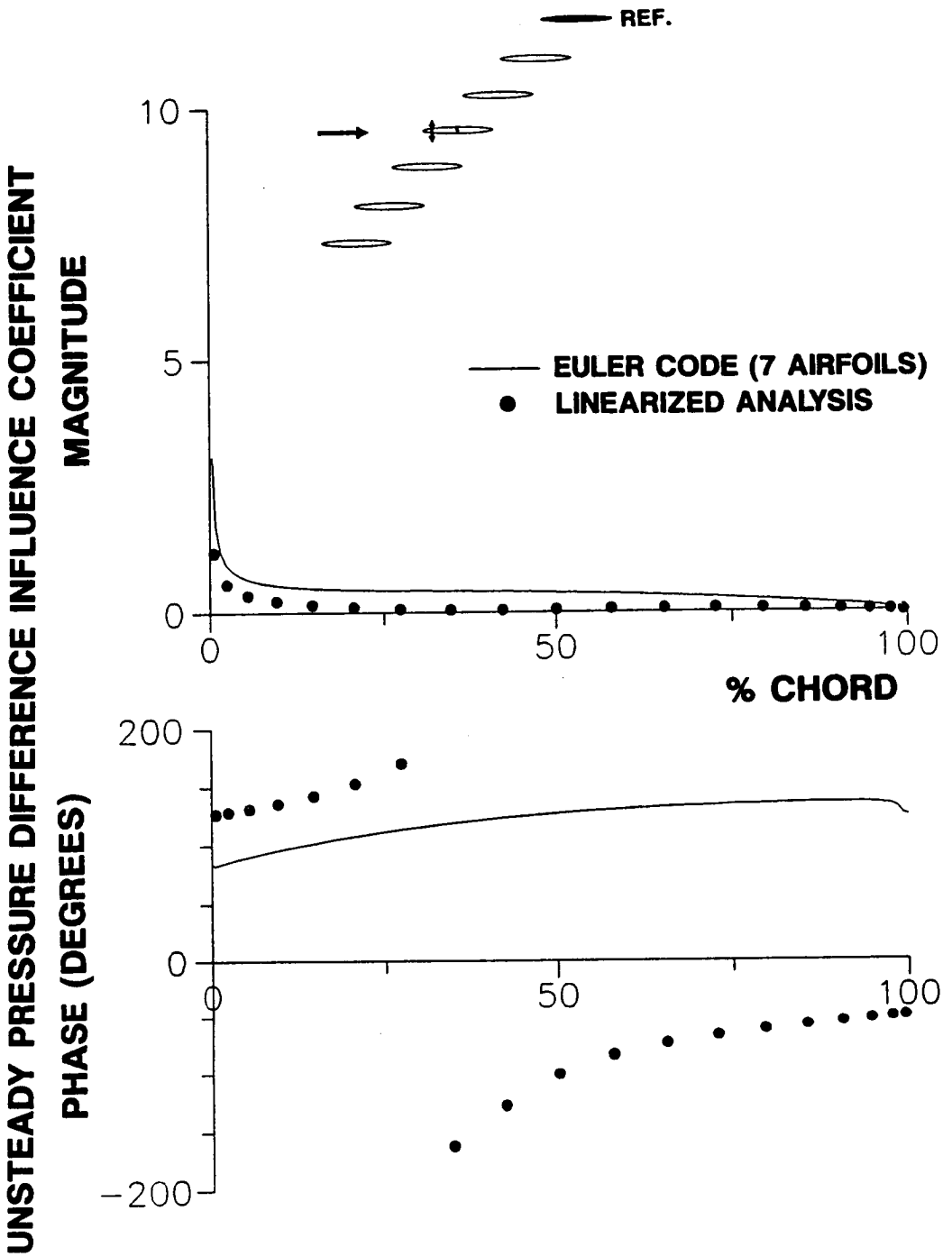

Figure 5.15 Predicted unsteady aerodynamic influence coefficient distributions, flat plate airfoil cascade, oscillating airfoil in relative position -3, M=0.65, k=0.50

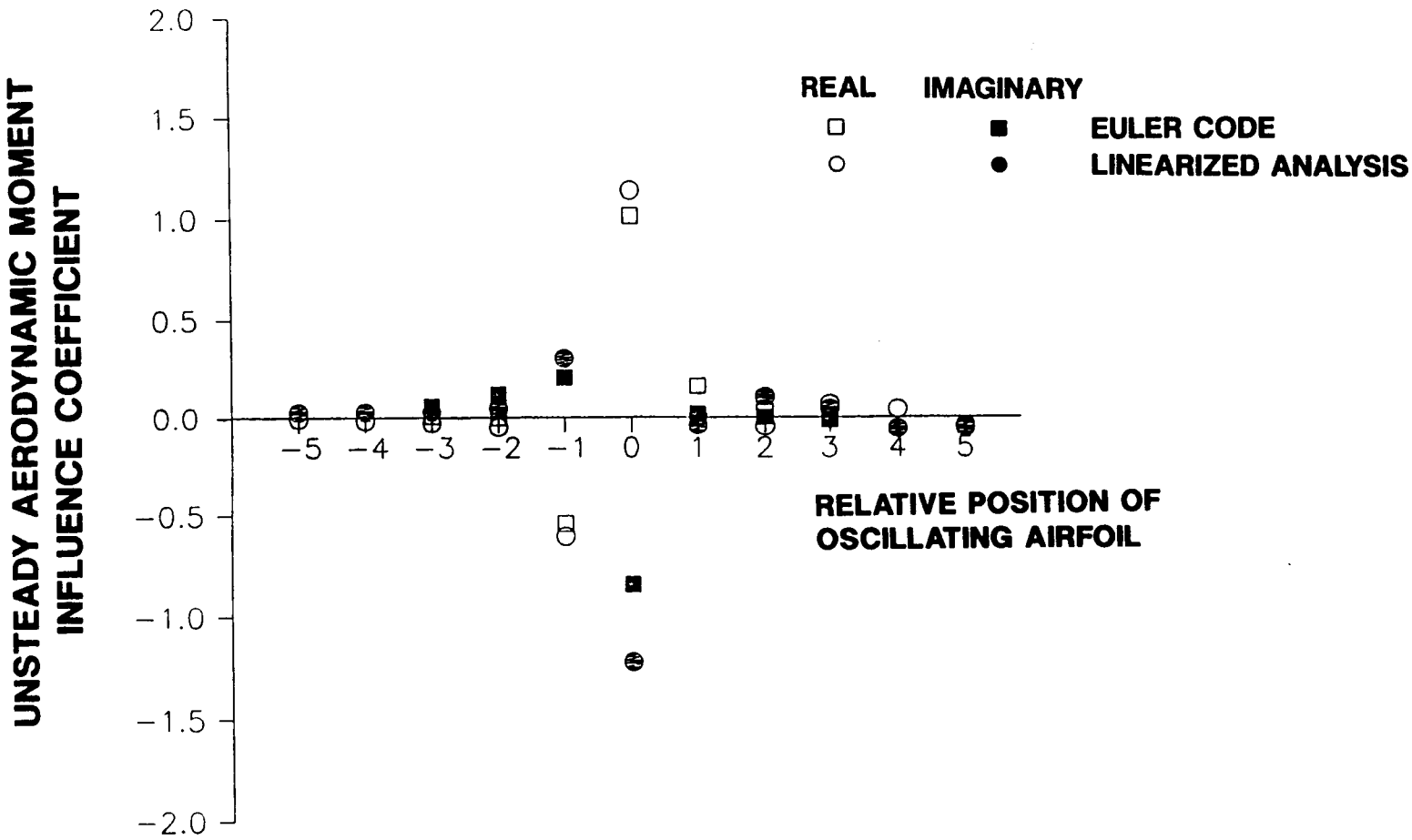

Figure 5.16 Unsteady aerodynamic moment influence coefficients, flat plate airfoil cascade, M=0.65, k=0.50

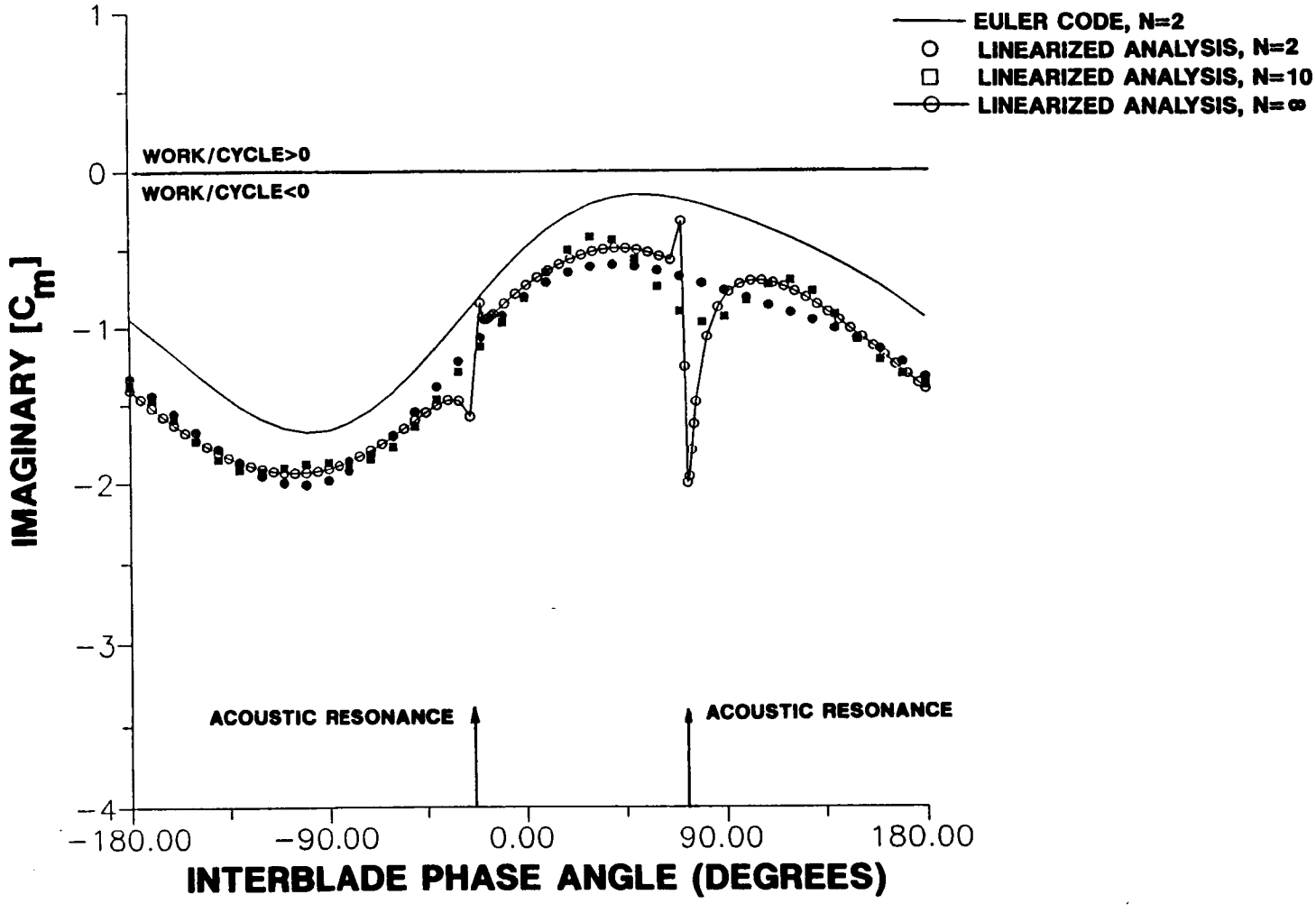

Figure 5.17 Unsteady aerodynamic moment coefficients, flat plate airfoil cascade, M=0.65, k=0.50

the Euler code is in good agreement with the analysis values except for an offset between them. This offset is a direct consequence of the differences in the imaginary part of $\hat{C}_m^0$ shown in Figure 5.16.

Results of the linearized analysis are shown in Figure 5.17 for limits of summation ranging from $N=2$ to $N=\infty$. C_m^I for an infinite cascade varies smoothly except in the vicinity of acoustic resonances, where rapid changes with the interblade phase angle occur. Results for $N=2$ are in good agreement with the infinite cascade results except near the acoustic resonances. To capture the rapidly changing unsteady aerodynamic response in these regions, many more airfoils are required: variations near the resonant interblade phase angles are better predicted when the influences of more airfoils are taken into account, $N=10$. Consequently, acoustic resonances will not occur in linear cascade experiments due to the limited number of cascaded airfoils.

5.2.3 Comparison with Experimental Data

Airfoil surface steady pressure coefficients and unsteady aerodynamic influence coefficients predicted by the Euler code are correlated with experimental data from the biconvex airfoil cascade. Following that, the influence coefficients are summed for comparison with the experimental data and linearized analysis predictions for various values of interblade phase angle.

Steady State

Steady state airfoil surface pressure coefficient distributions are correlated with the experimental data for the low solidity cascade at 2 degrees of incidence with inlet Mach numbers of 0.55 and 0.80. A 199x33 C-grid is used, as shown in Figure 5.18.

Figure 5.19 illustrates the prediction-data correlation for M=0.55. The best correlation is obtained on the forward half of the airfoil upper surface, where the data and the predictions are in good agreement. Beyond 50% of chord, the predicted upper surface pressure coefficients are greater in value than the data. The lower

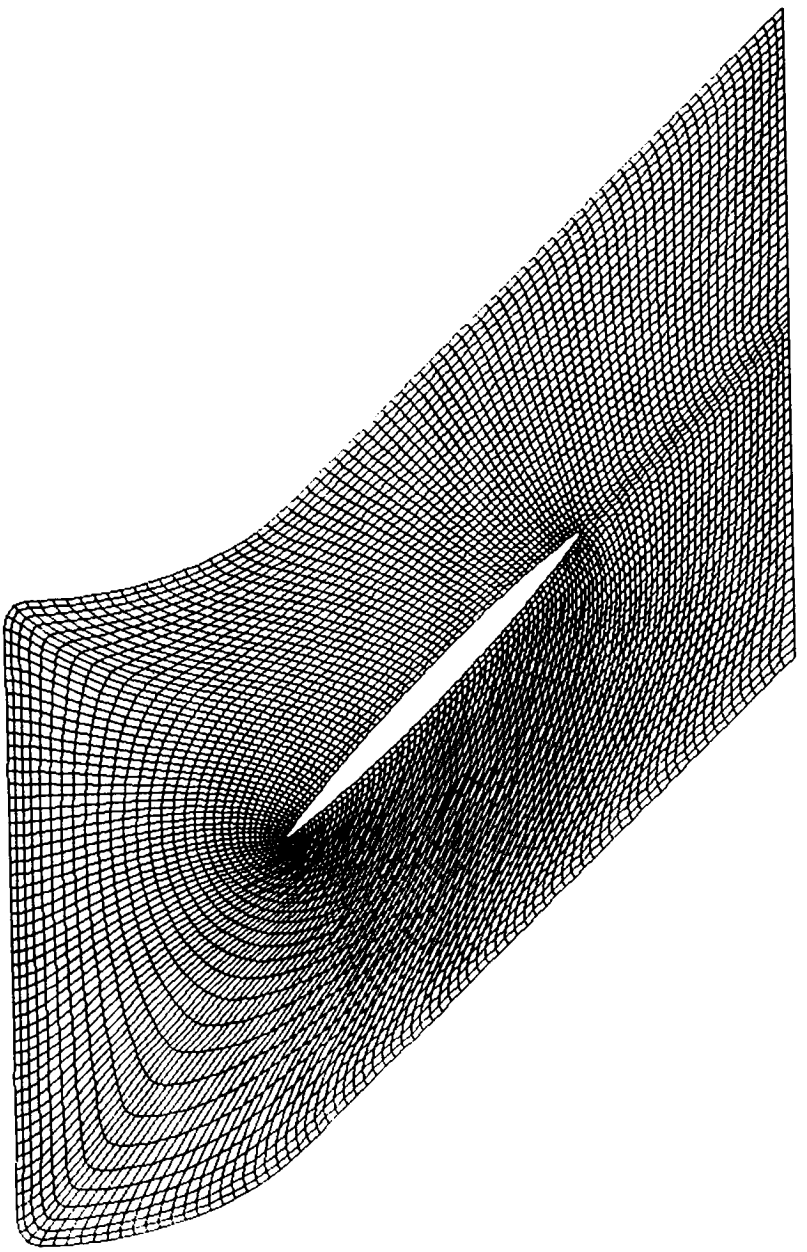

Figure 5.18 Low solidity biconvex airfoil cascade grid

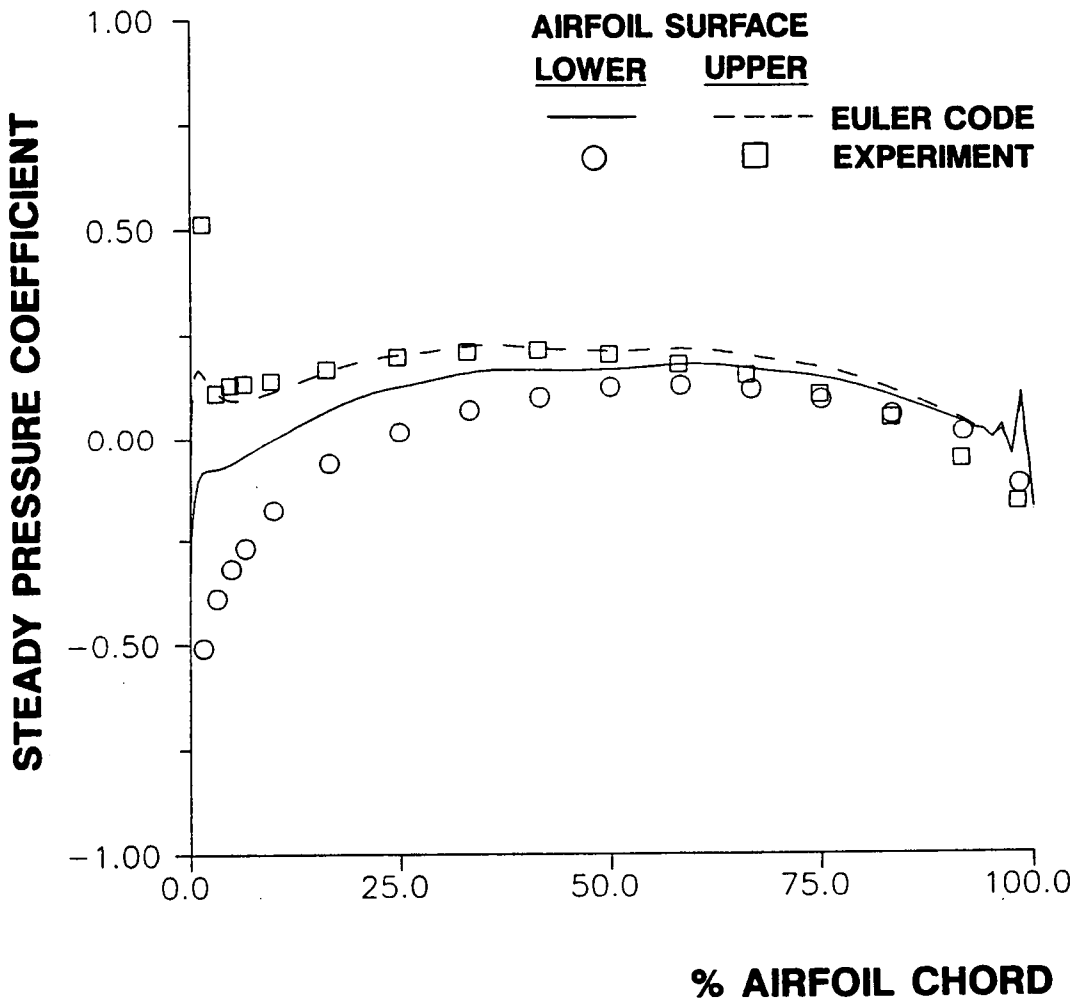

Figure 5.19 Correlation of predicted airfoil surface steady pressure coefficient distribution with experiment data, low solidity cascade, M=0.55, α_0=2 degrees

surface predictions are in fairly good agreement with the data along the aft half of the airfoil. Forward of there, the predicted values of the steady pressure coefficient are considerably greater than the data.

A similar correlation is obtained for M=0.80, Figure 5.20. For both of Figures 5.19 and 5.20, the inlet and exit boundary conditions are specified according to the experiment values of inlet Mach number, inlet flow angle and exit static pressure. It was found that relatively small changes in these boundary conditions could improve the correlation between the lower surface predictions and the data. However, this was at the expense of the upper surface correlation, thus no overall improvement was found.

The degree of correlation between the code predictions and the high solidity cascade data varies with incidence angle. For an inlet Mach number of 0.65 and an incidence angle of 0 degrees, Figure 5.21, the correlation is good. Predictions for the airfoil upper surface are in very good agreement with the data except when close to the leading edge. Lower surface trends are correctly predicted, but differences are found in the region extending from 10 to 50% of chord.

For M=0.65 with 7 degrees of incidence, Figure 5.22, the correlation is poor for both surfaces. The predicted pressure distributions shown here were obtained using the experiment values of inlet Mach number, inlet flow angle and exit static pressure for the inlet and exit boundary conditions, respectively. Altering these boundary values did not improve the correlation.

Influence Coefficients

In Figures 5.23 through 5.27, the predicted unsteady pressure influence coefficients are compared with the experimental data for the low solidity cascade for 0.55 inlet Mach number and 0.20 reduced frequency. The Euler solution took 3400 seconds of CPU time to complete 4642 time steps (3.25 cycles of airfoil oscillation) for a 5 airfoil cascade.

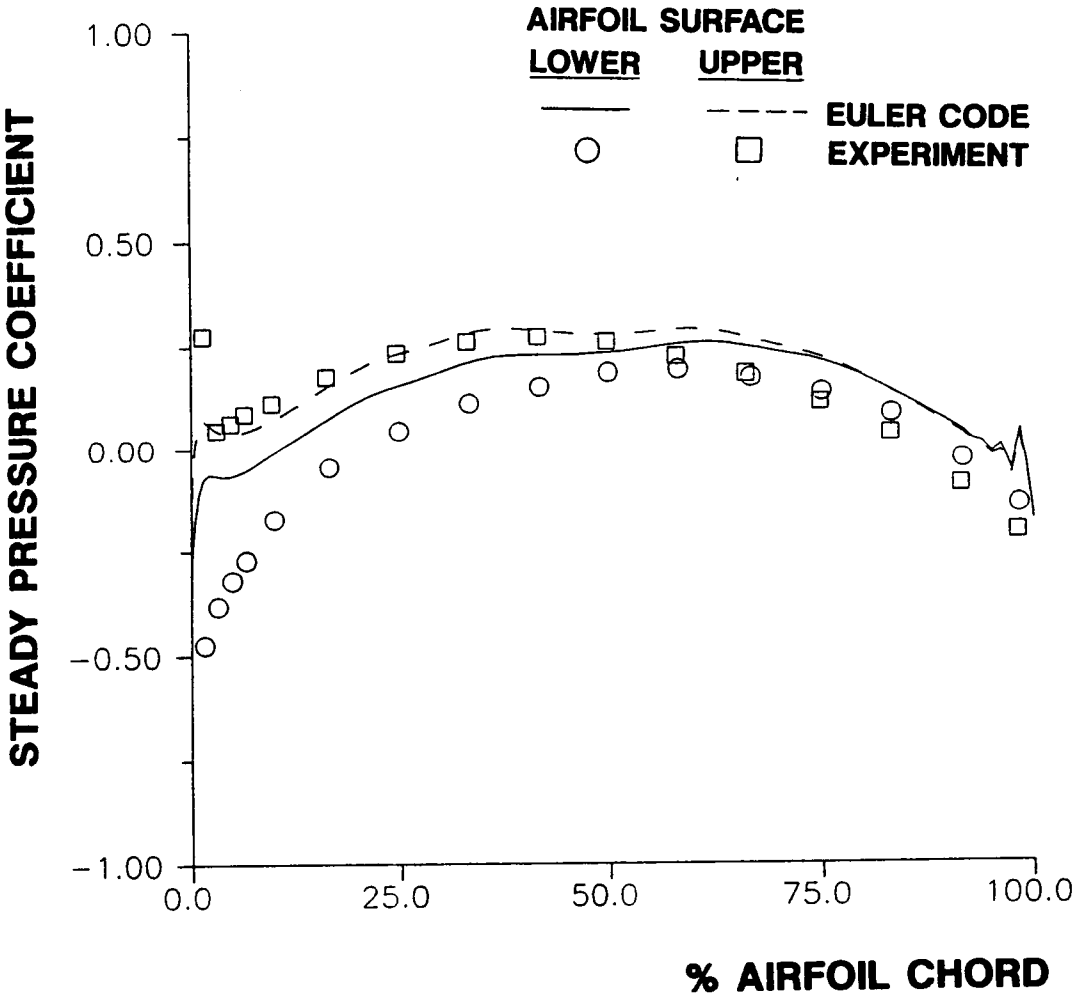

Figure 5.20 Correlation of predicted airfoil surface steady pressure coefficient distribution with experiment data, low solidity cascade, M=0.80, α_0=2 degrees

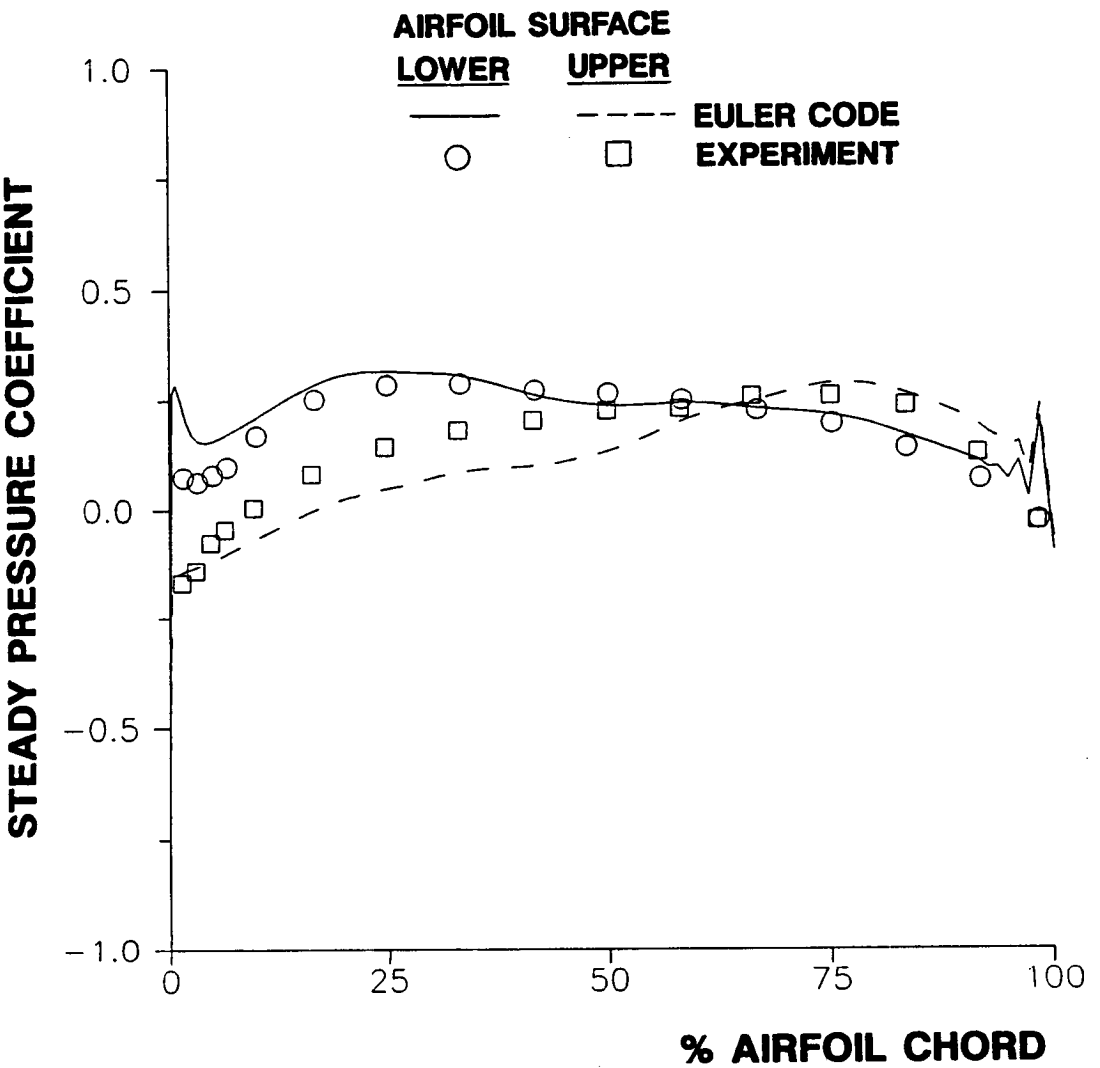

Figure 5.21 Correlation of predicted airfoil surface steady pressure coefficient distribution with experiment data, high solidity cascade, M=0.65, α_0=0 degrees

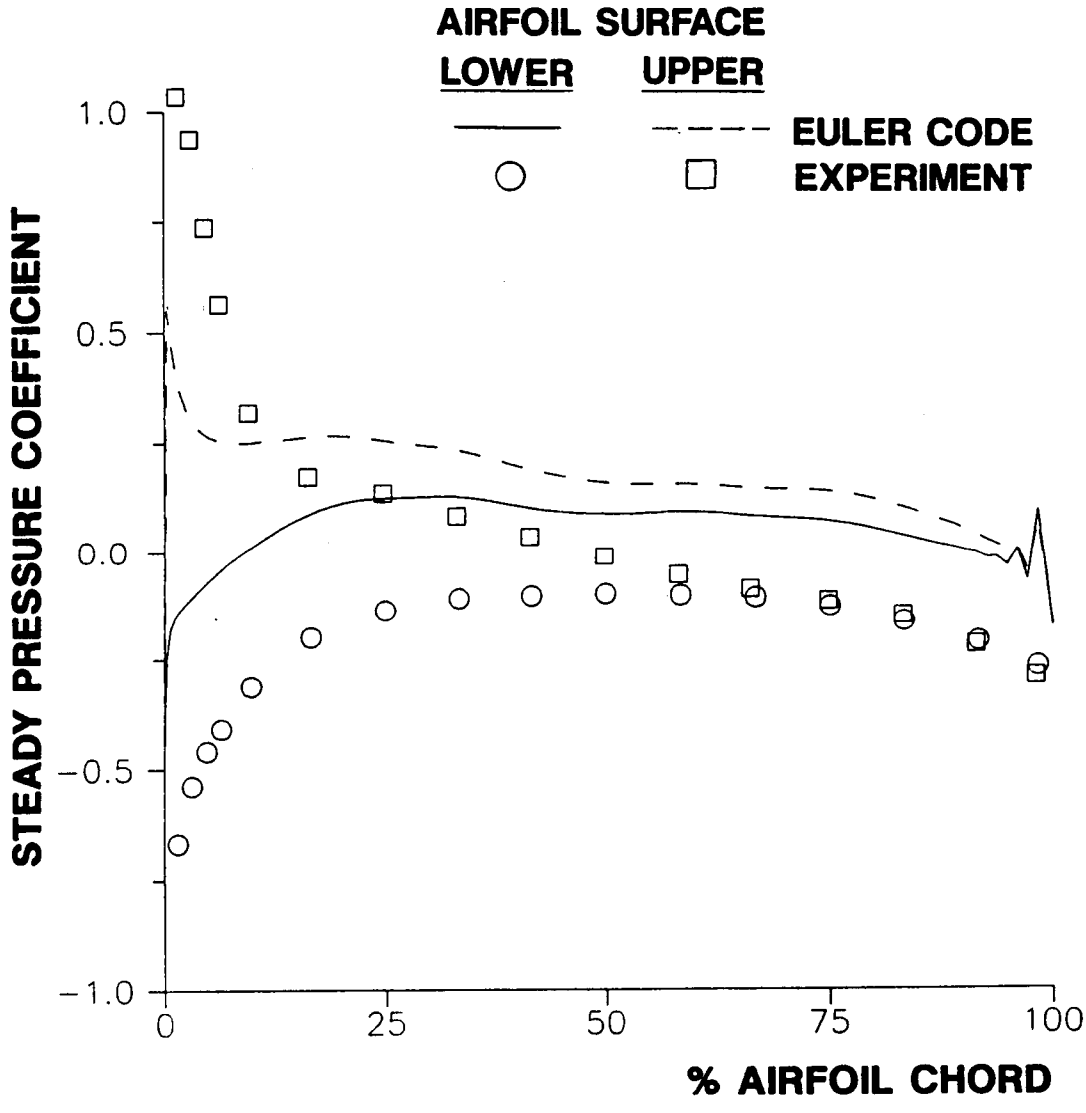

Figure 5.22 Correlation of predicted airfoil surface steady pressure coefficient distribution with experiment data, high solidity cascade, M=0.65, α_0=7 degrees

C-3

Correlation of the self-induced unsteady pressure distribution is generally very good, Figure 5.23. The magnitude trends predicted for both airfoil surfaces are in very good agreement with the data although the predicted magnitudes are slightly larger. The phase correlation is also very good with the only significant differences at 88% of chord. The magnitudes are so small there that those differences are not very significant.

The experimental data fall between the predicted magnitudes for $\hat{C}_p^1$, Figure 5.24. Note that the cascade schematic indicates walls which were present in the experiments but not simulated in the computations. While the differences in magnitude between the lower and upper surfaces are small for the data, the predicted magnitudes are largest on the upper surface, as one would expect. The phase data and predictions are in good agreement except near the leading edge.

Both the predicted magnitudes for $\hat{C}_p^2$ are smaller than the measured values, Figure 5.25. Similar to $\hat{C}_p^1$, there is little difference in experiment magnitudes between the two surfaces, but the code predicts magnitudes larger on the airfoil upper surface than the lower surface. The phase correlation is very similar to that for $\hat{C}_p^1$, being very good except on the upper surface at 12% of chord.

Oscillations of the airfoil in relative position -1, Figure 5.26, cause relatively large unsteady pressure coefficient magnitudes on the lower surface of the reference airfoil. The correlation of the predictions with the data is very good, particularly for the airfoil upper surface. For the lower surface, the predicted magnitudes are generally larger than the data, but these differences are fairly small. The lower surface phase correlation is very good except for the aft portion of the airfoil.

Moving the oscillating airfoil further away from the reference airfoil to relative position -2, Figure 5.27, correlation of the Euler code predictions with the data is fairly good. Because the magnitudes are quite small, the differences between the

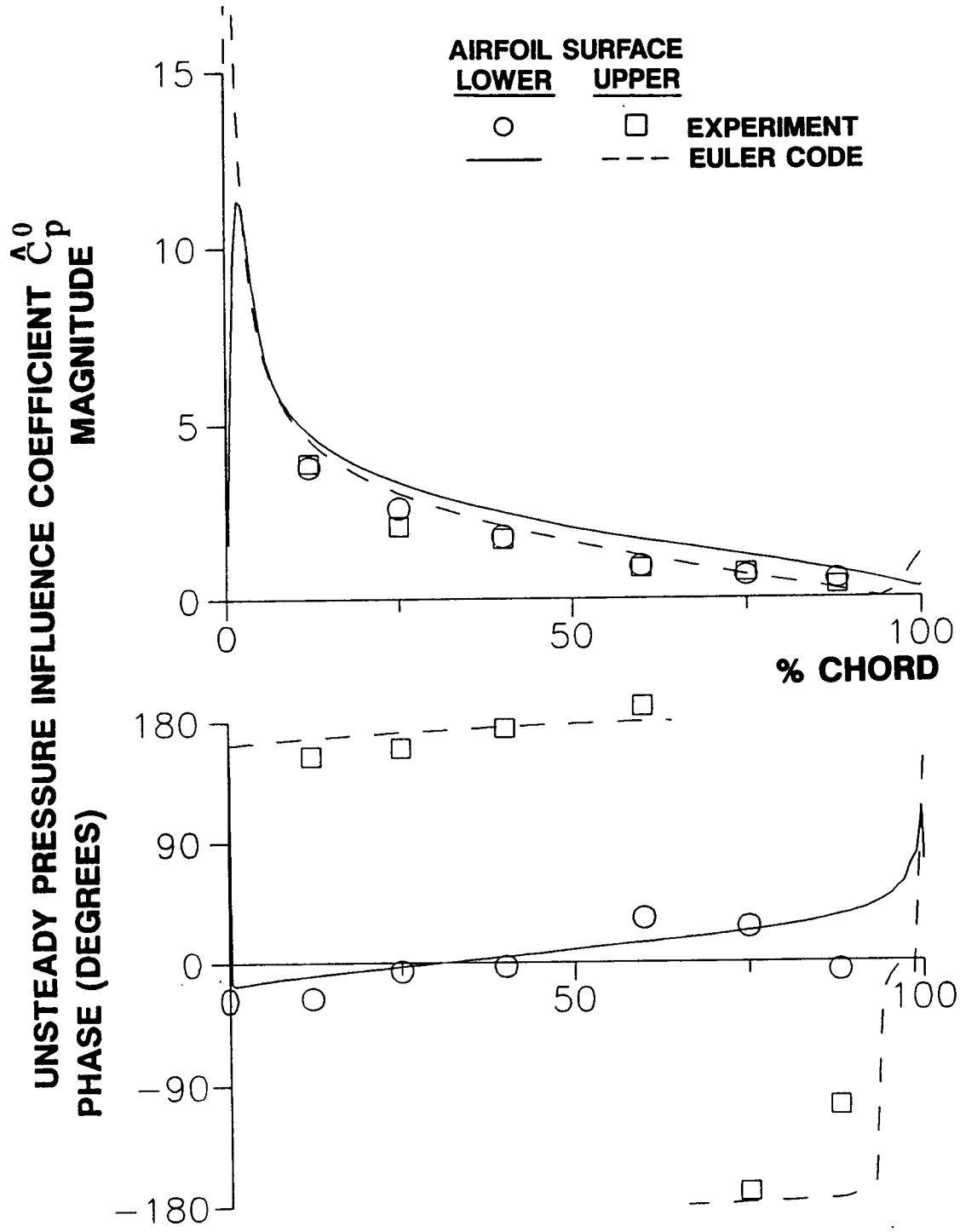

Figure 5.23 Unsteady pressure influence coefficient distribution, oscillating airfoil in relative position 0, low solidity cascade, M = 0.55, k = 0.20

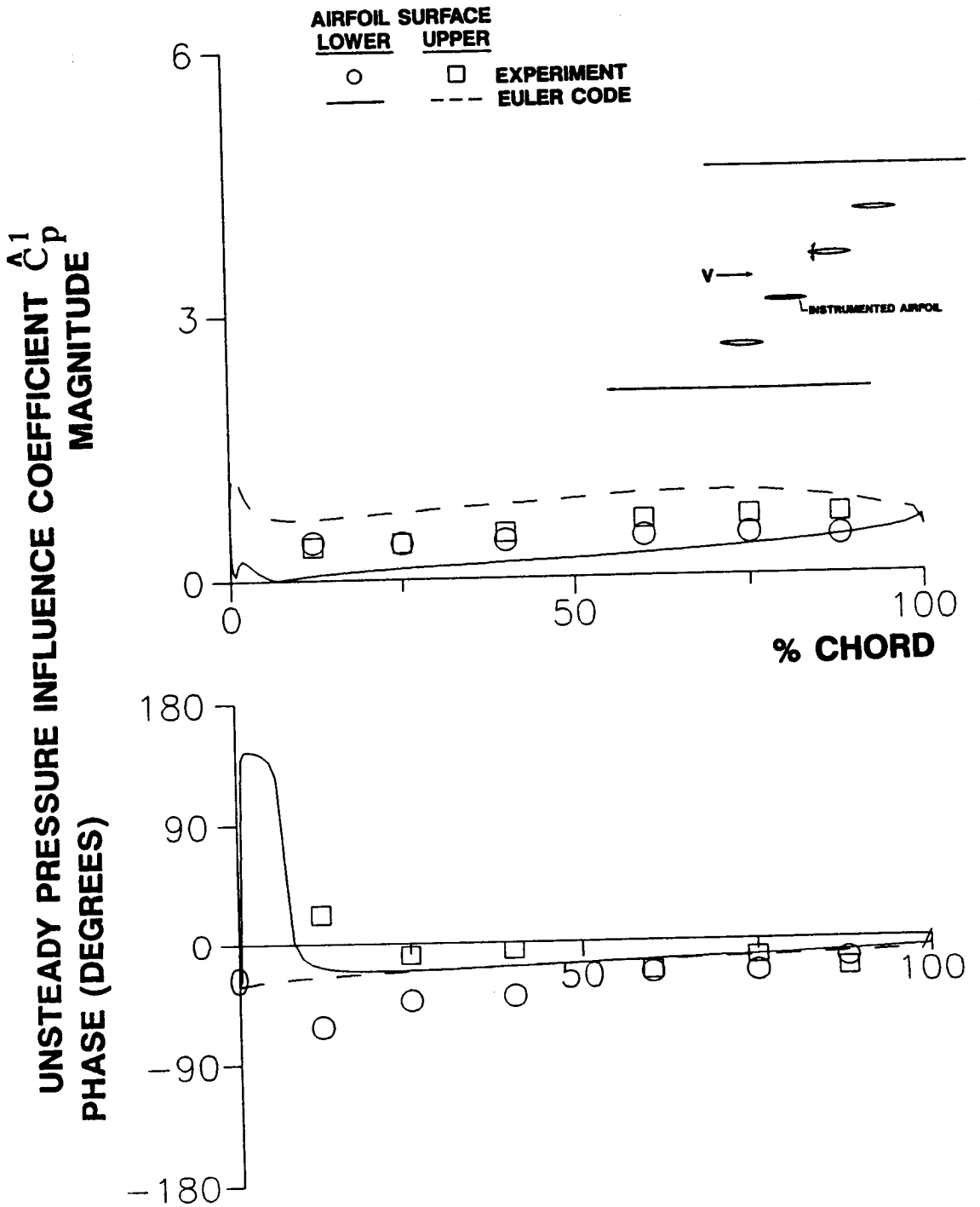

Figure 5.24 Unsteady pressure influence coefficient distribution, oscillating airfoil in relative position 1, low solidity cascade, M=0.55, k=0.20

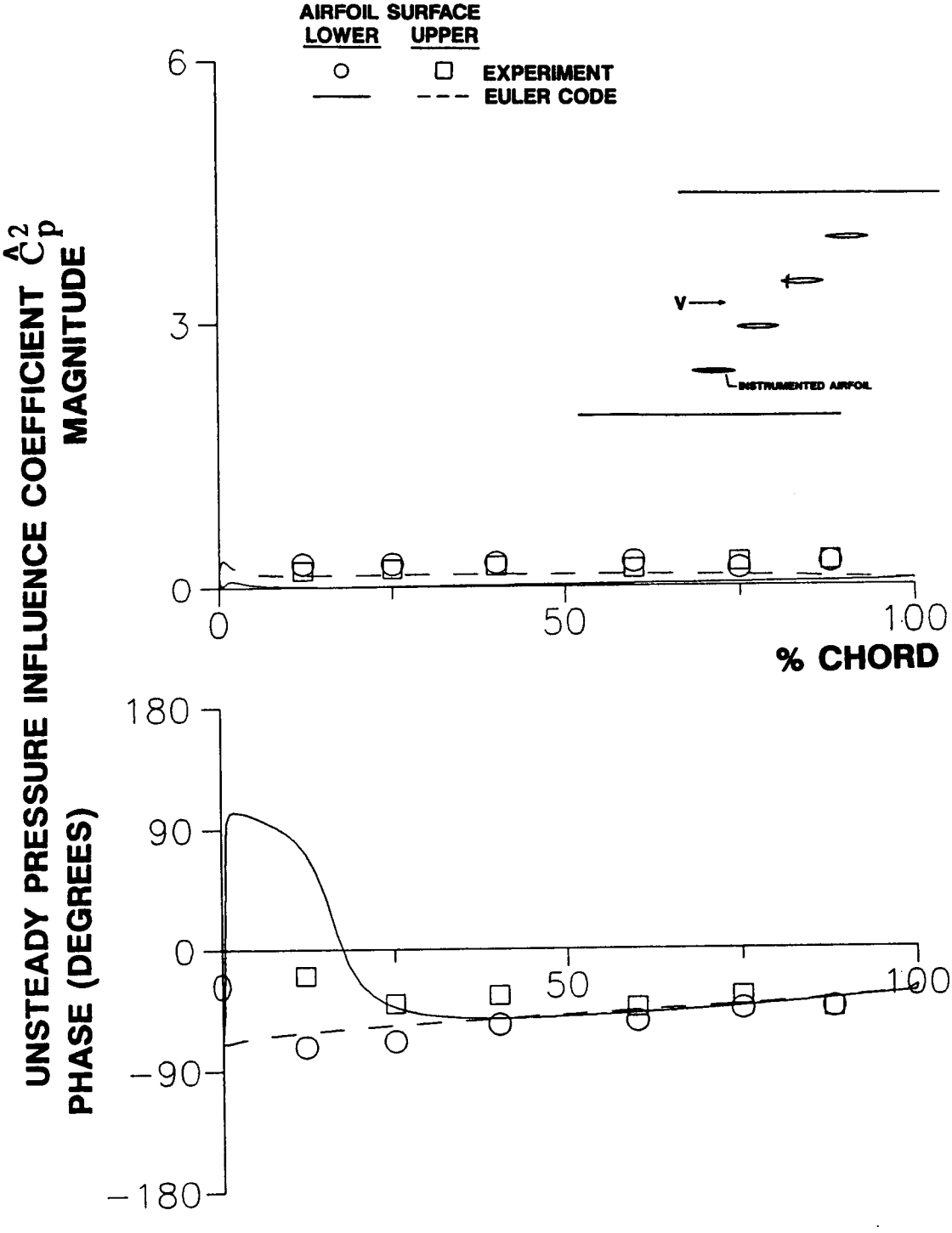

Figure 5.25 Unsteady pressure influence coefficient distribution, oscillating airfoil in relative position 2, low solidity cascade, M = 0.55, k = 0.20

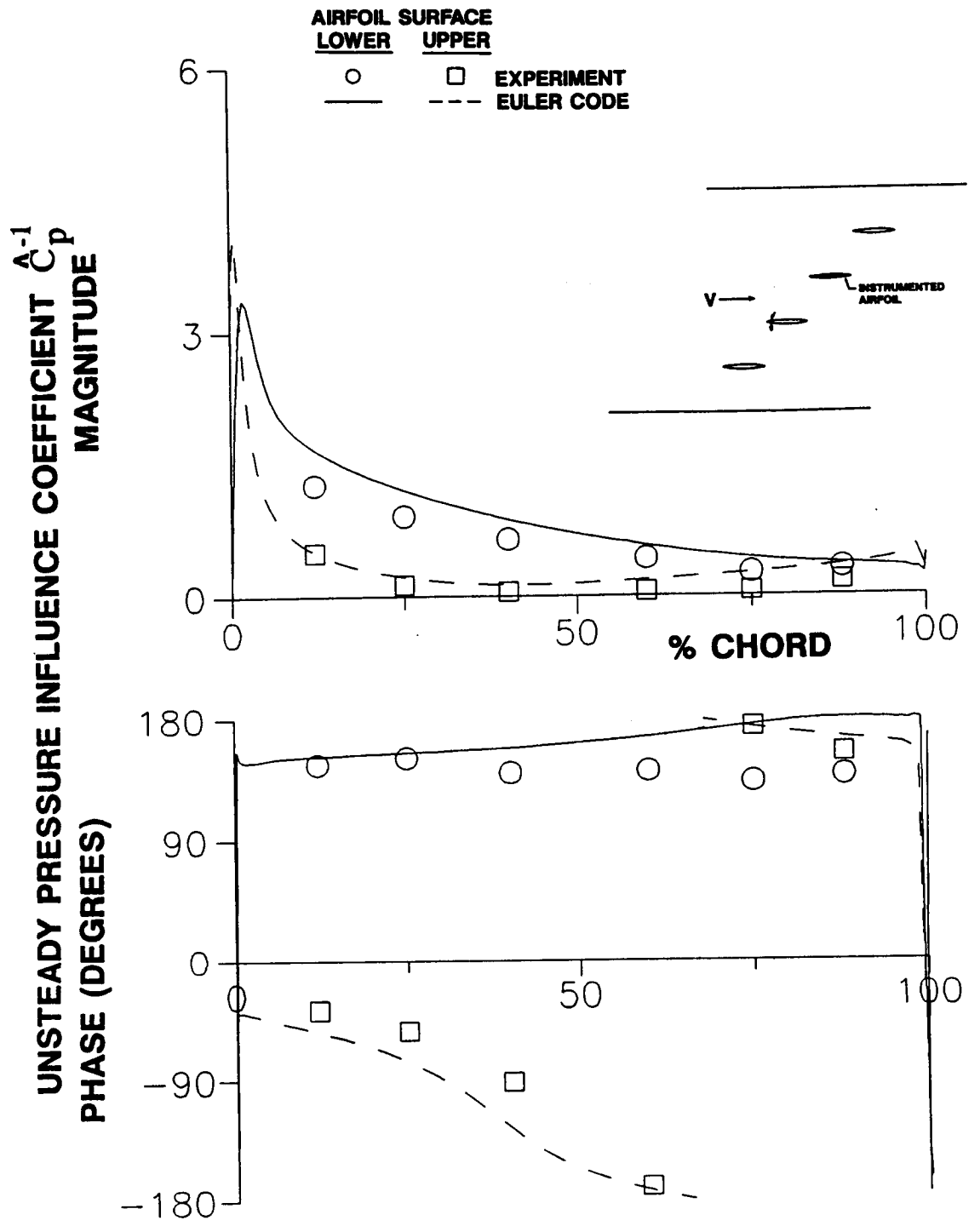

Figure 5.26 Unsteady pressure influence coefficient distribution, oscillating airfoil in relative position -1, low solidity cascade, M = 0.55, k = 0.20

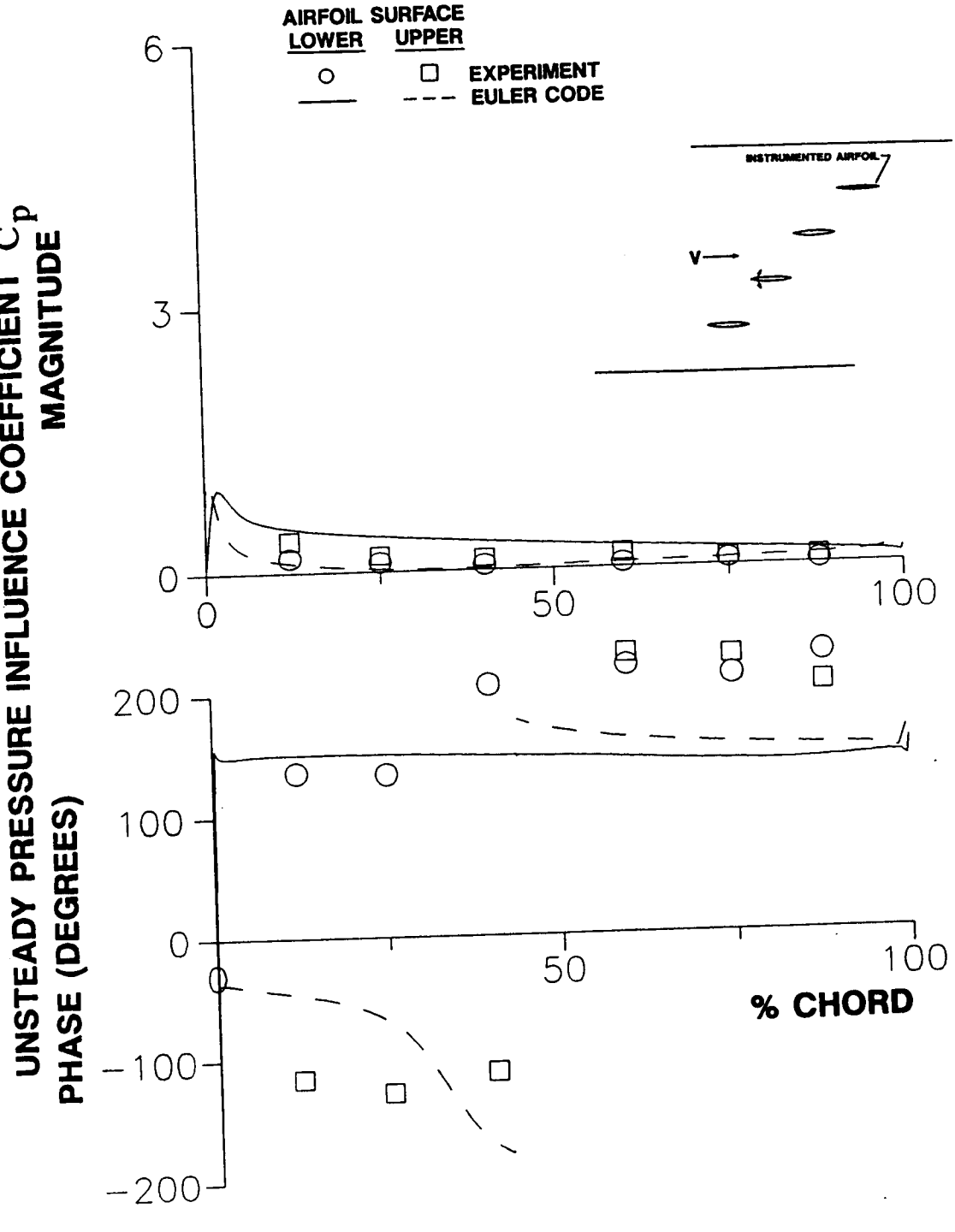

Figure 5.27 Unsteady pressure influence coefficient distribution, oscillating airfoil in relative position -2, low solidity cascade, M = 0.55, k = 0.20

predictions and the data are of little significance. However, while the predicted upper surface magnitudes are essentially zero, the experimental data indicate small but finite responses which may be due to reflections off the adjacent wind tunnel wall.

Correlation of the predicted unsteady pressure influence coefficients with experimental data is also made for the low solidity cascade with 0.80 inlet Mach number and 0.32 reduced frequency. The results for the first harmonic unsteady pressure coefficients, shown in Figures 5.28 through 5.32, are in many ways very similar to the results just seen for M=0.55 and k=0.20.

(1) The correlation for $\hat{C}_p^0$ is very good, Figure 5.28. The only differences of note are on the aft half of the upper surface, where the predicted magnitudes are less than the data.

(2) The predicted upper surface distribution for $\hat{C}_p^{-1}$ is in very good agreement with the data, Figure 5.29. The lower surface magnitude data-prediction correlation is also very good, but the phase correlation is poor along the airfoil aft half.

The main differences between these results and those for M=0.55, k=0.20 are due to the upstream-traveling wave phenomenon occurring in the experiments, an effect which was found to intensify with increasing Mach number and reduced frequency.

(1) Differences in the magnitude correlation for $\hat{C}_p^1$, Figure 5.30, are mainly a consequence of this wave phenomenon. While the wave causes experimental pressure distributions of approximately equal amplitude on the two airfoil surfaces, the predicted unsteady pressure differences are relatively large. The magnitude and phase correlations are good for the airfoil upper surface, but the predicted magnitudes for the lower surface are much less than the data.

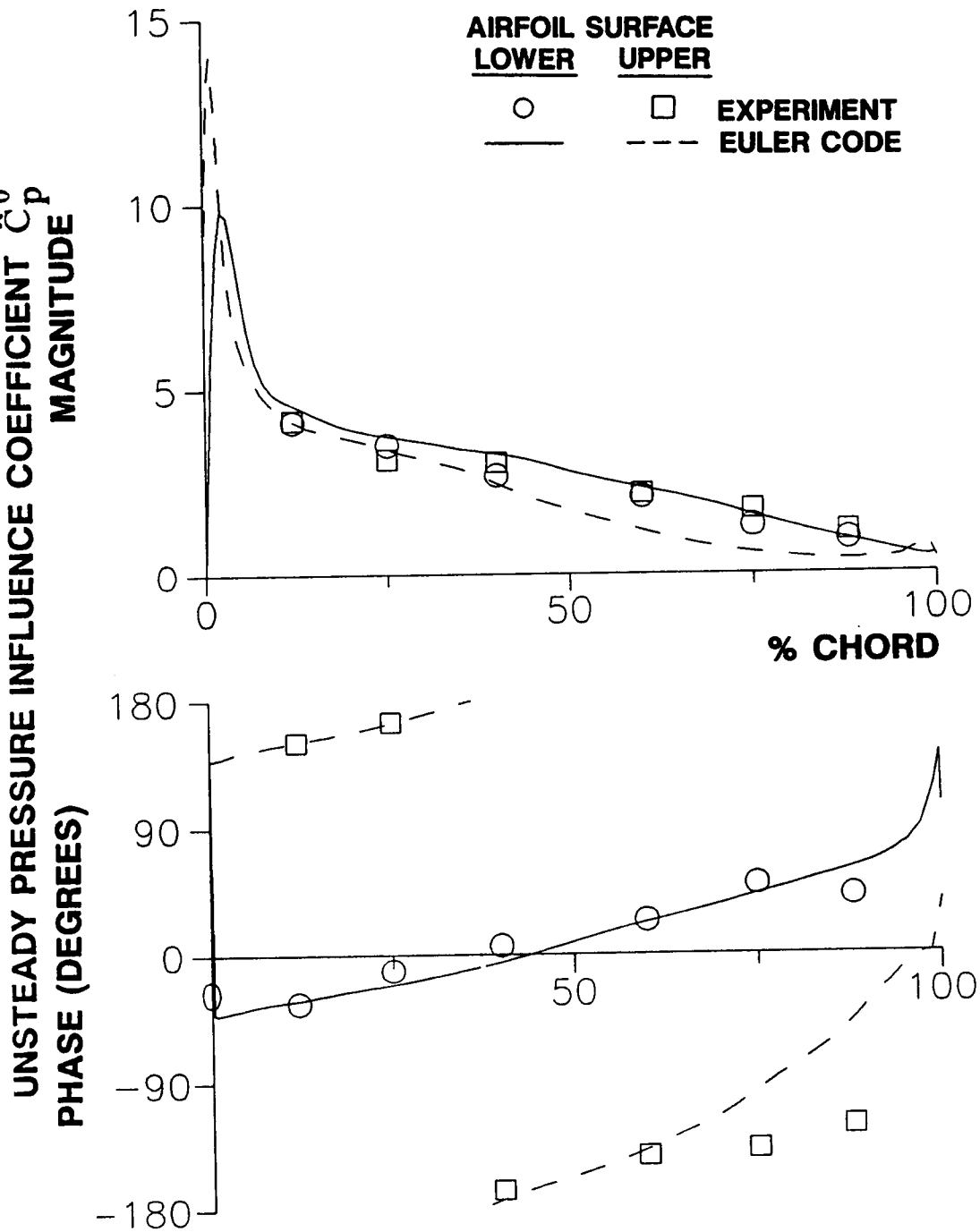

Figure 5.28 Unsteady pressure influence coefficient distribution, oscillating airfoil in relative position 0, low solidity cascade, M = 0.80, k = 0.32

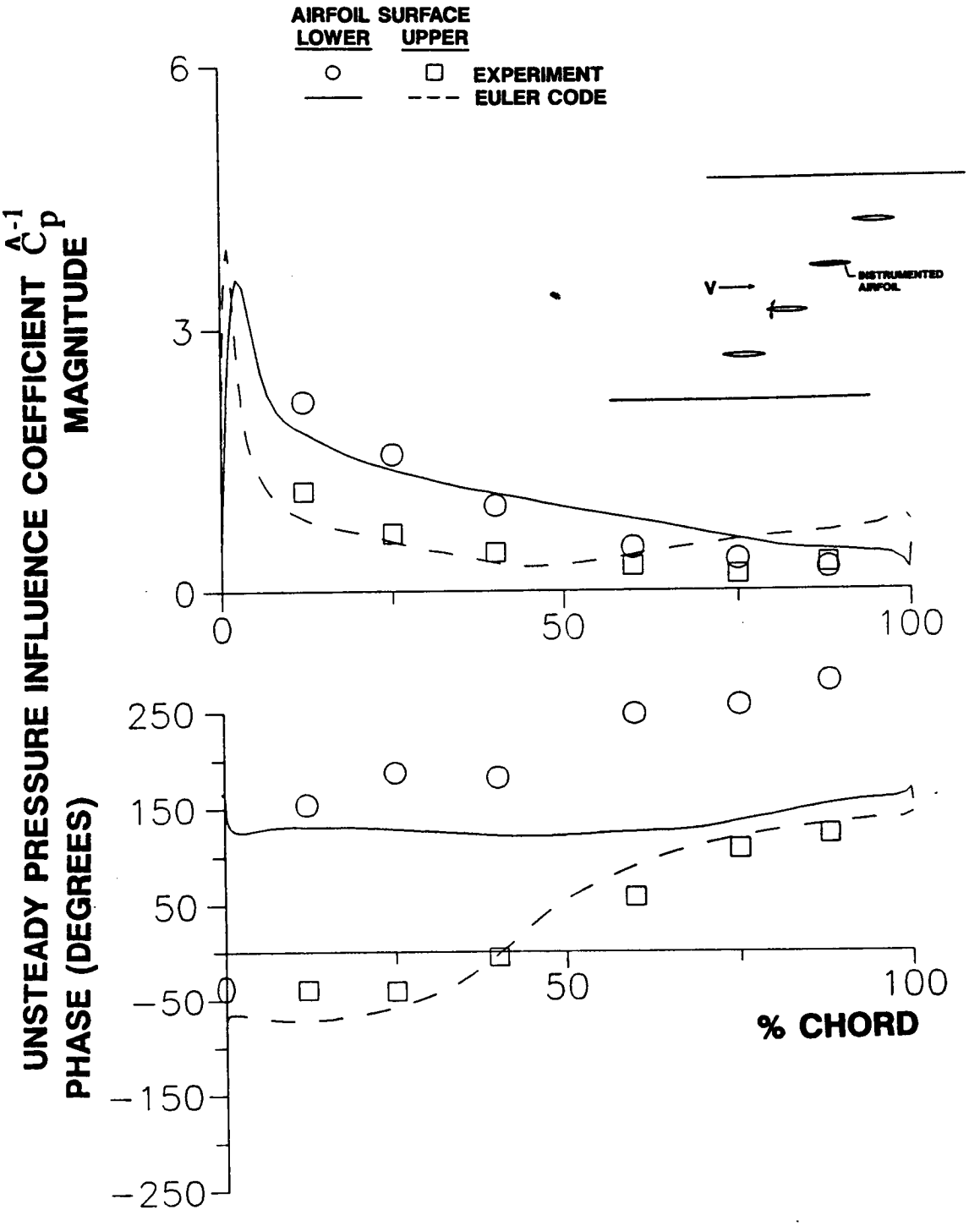

Figure 5.29 Unsteady pressure influence coefficient distribution, oscillating airfoil in relative position -1, low solidity cascade, M=0.80, k=0.32

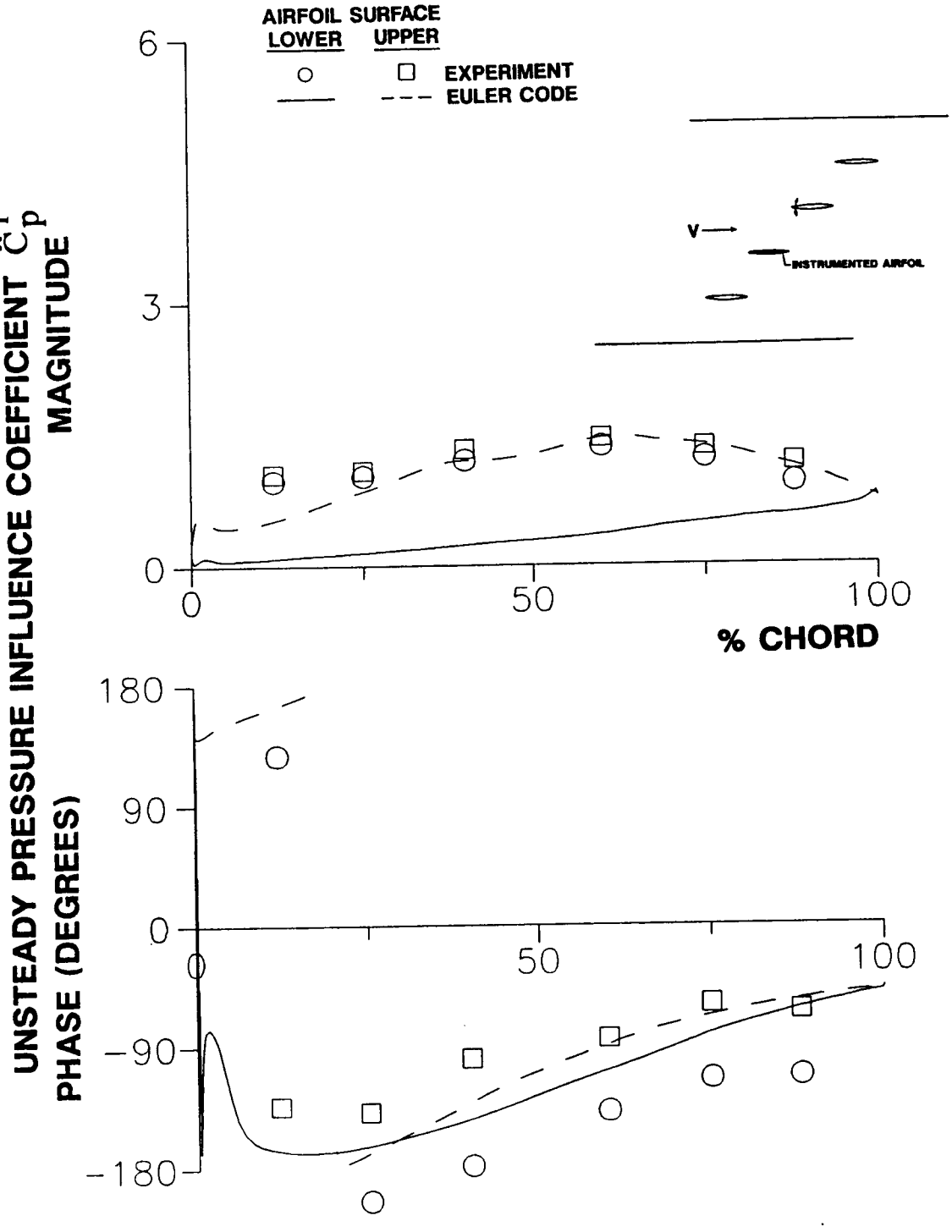

Figure 5.30 Unsteady pressure influence coefficient distribution, oscillating airfoil in relative position 1, low solidity cascade, M=0.80, k=0.32

(2) The upstream-traveling wave effect is even more evident for $\hat{C}_p^2$, Figure 5.31. The predicted unsteady pressure magnitudes are negligible while the experimentally-determined values are relatively large.

These results indicate that the upstream traveling wave is actually a duct phenomenon rather than a cascade phenomenon. That is, the wave exists in the experiments only because the cascade of airfoils is enclosed in a duct. Because the influence coefficient Euler code does not simulate this duct, the wave is not predicted.

Finally, for $\hat{C}_p^{-2}$, Figure 5.32, the correlation is generally poor. Nowhere on the airfoil lower surface are the magnitude and phase correlations simultaneously good. On the upper surface, the experimentally-determined magnitudes are much larger than the predicted magnitudes, possibly due to reflections off the adjacent wall of the wind tunnel.

For the high solidity cascade, correlations for a steady flow condition defined by an inlet Mach number of 0.65 and a mean flow incidence angle of 0 degrees are presented in Figures 5.33 through 5.37. The reduced frequency is 0.39. The correlation is, once again, good for $\hat{C}_p^0$, Figure 5.33. The predicted effect of oscillating the airfoil in relative position 1, Figure 5.34, is in trendwise agreement with the data, but the predicted upper surface magnitude distribution has a larger peak than the data, and the predicted lower surface magnitudes are less than the data. For $\hat{C}_p^2$, Figure 5.35, the predicted magnitudes are smaller than the experimental data due to the upstream-traveling wave. The response due to oscillations of the airfoil in relative position -1 is relatively large on the adjacent, lower surface of the reference airfoil, Figure 5.36. The magnitude correlation is very good for both airfoil surfaces, but the phase correlation is good only at 12 and 25% of chord. For $\hat{C}_p^{-2}$, Figure 5.37, the upper surface correlation is good, but the predicted lower surface magnitudes are much larger than the measured values.

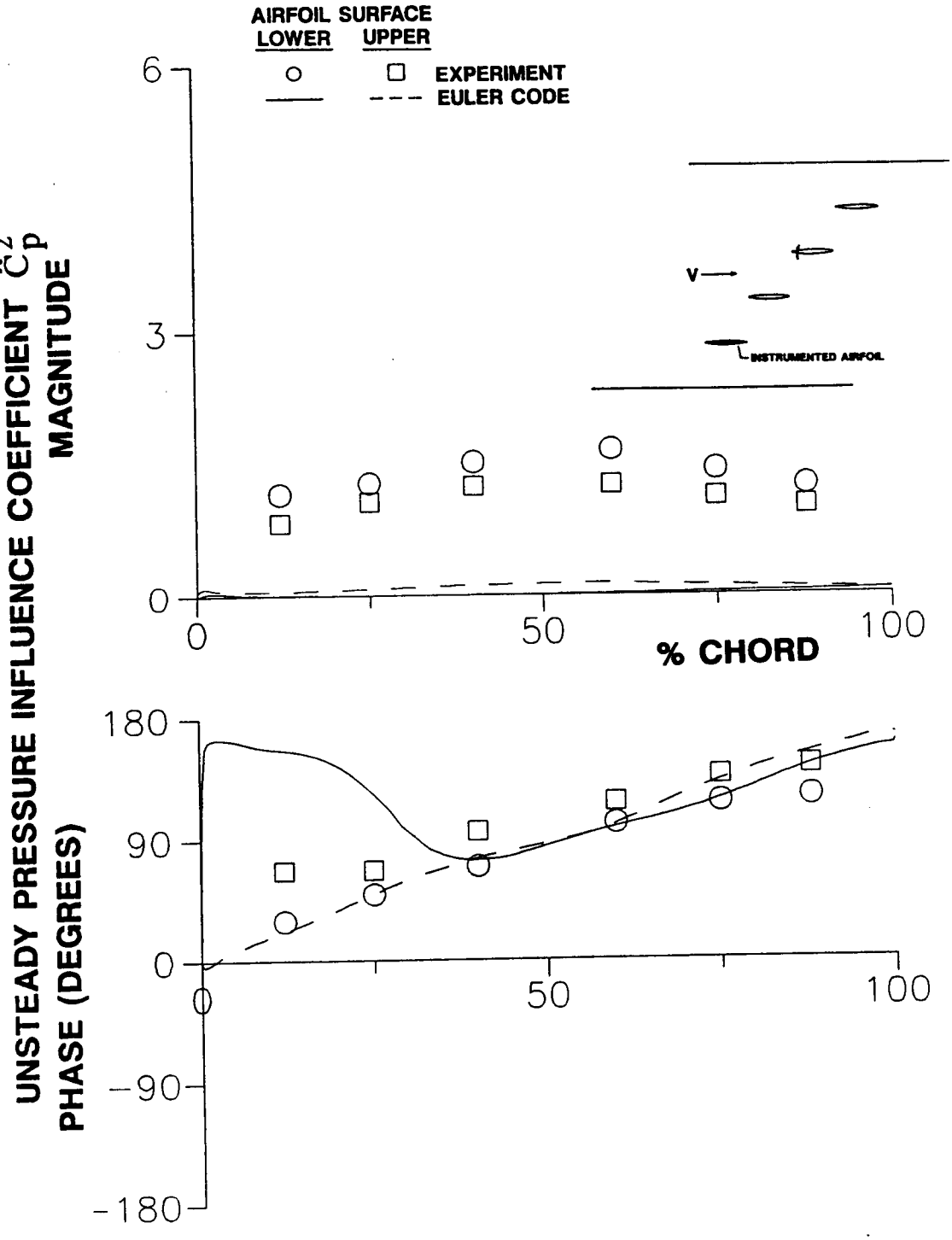

Figure 5.31 Unsteady pressure influence coefficient distribution, oscillating airfoil in relative position 2, low solidity cascade, M=0.80, k=0.32

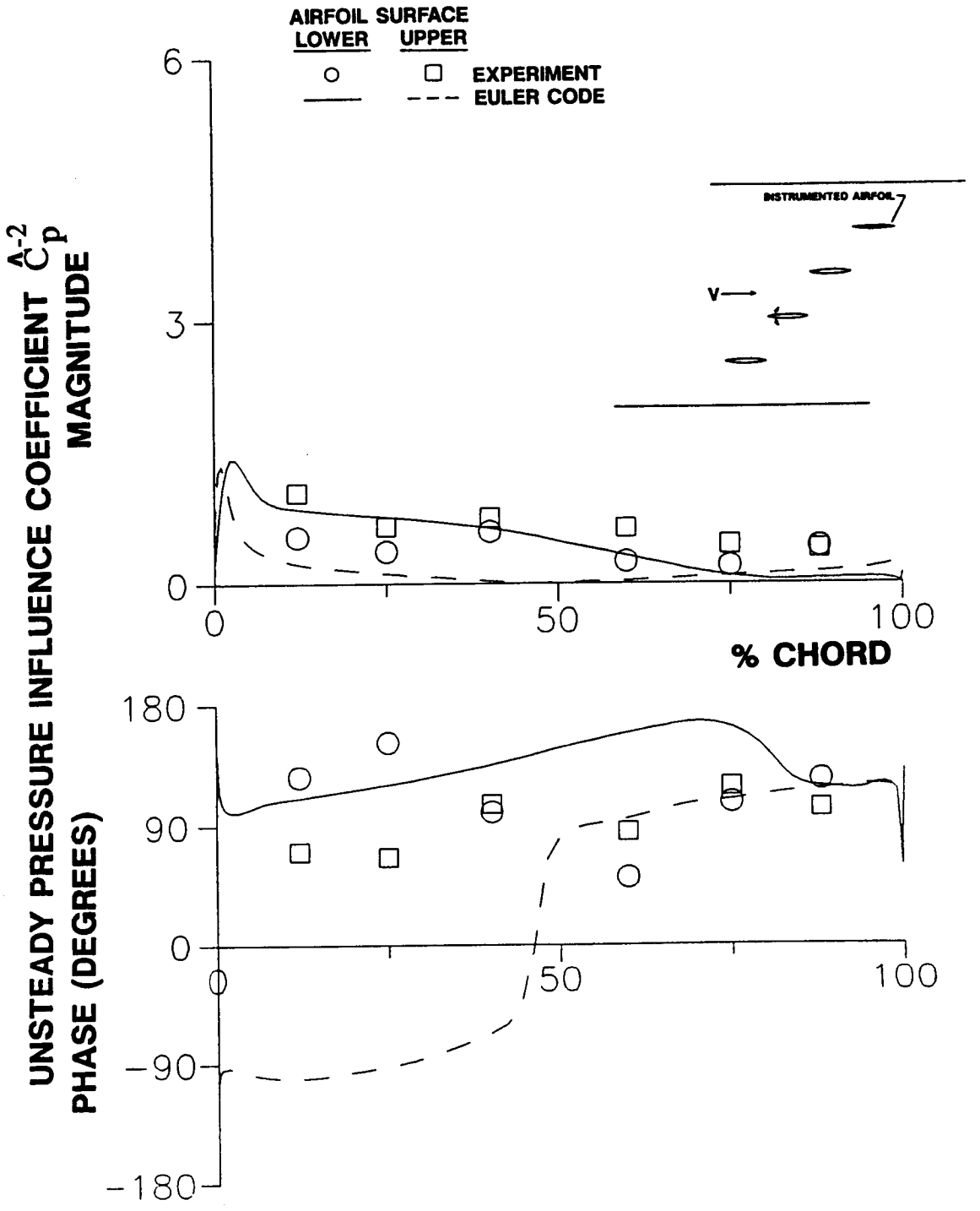

Figure 5.32 Unsteady pressure influence coefficient distribution, oscillating airfoil in relative position -2, low solidity cascade, M=0.80, k=0.32

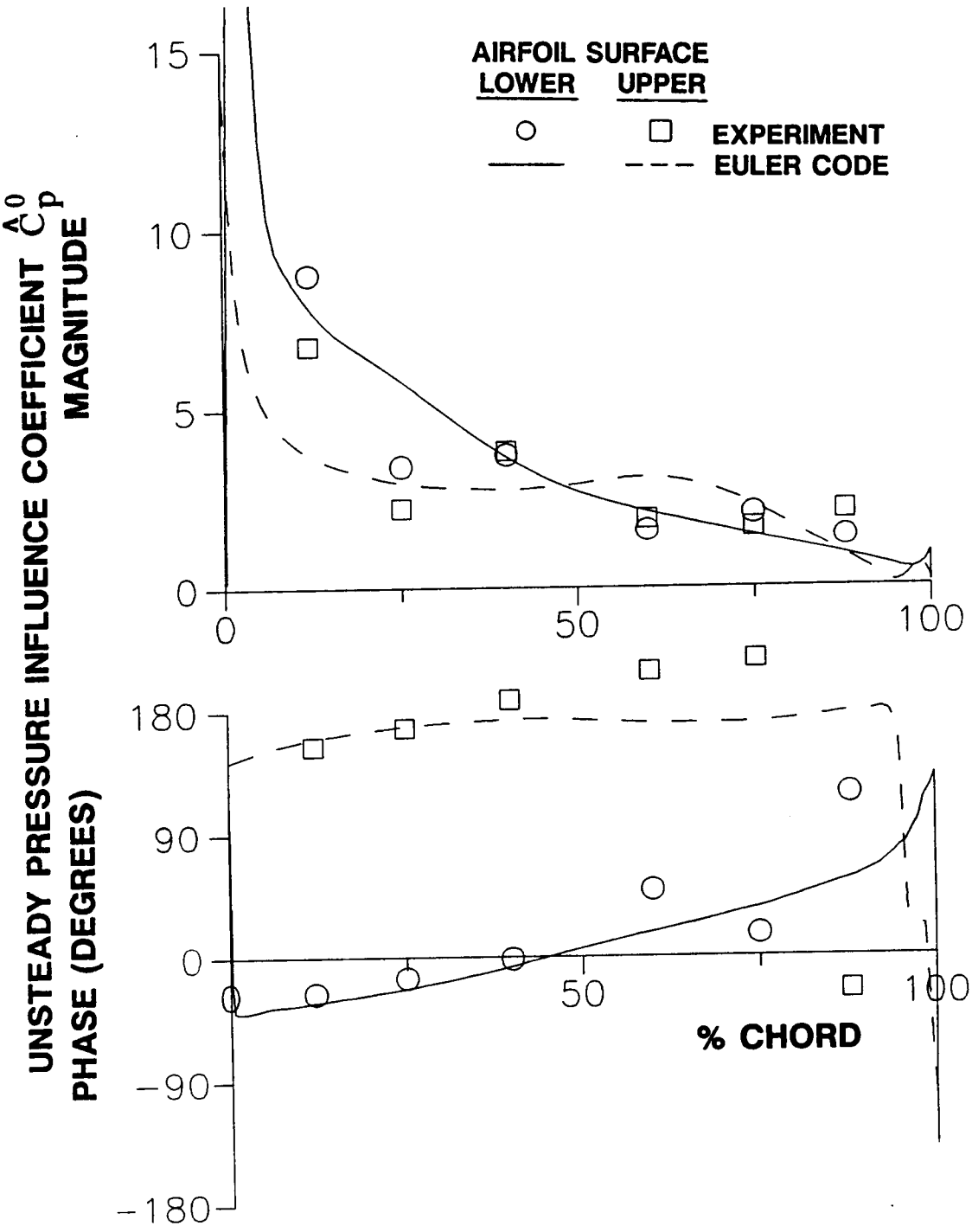

Figure 5.33 Unsteady pressure influence coefficient distribution, oscillating airfoil in relative position 0, high solidity cascade, M = 0.65, α_0 = 0 degrees, k = 0.39

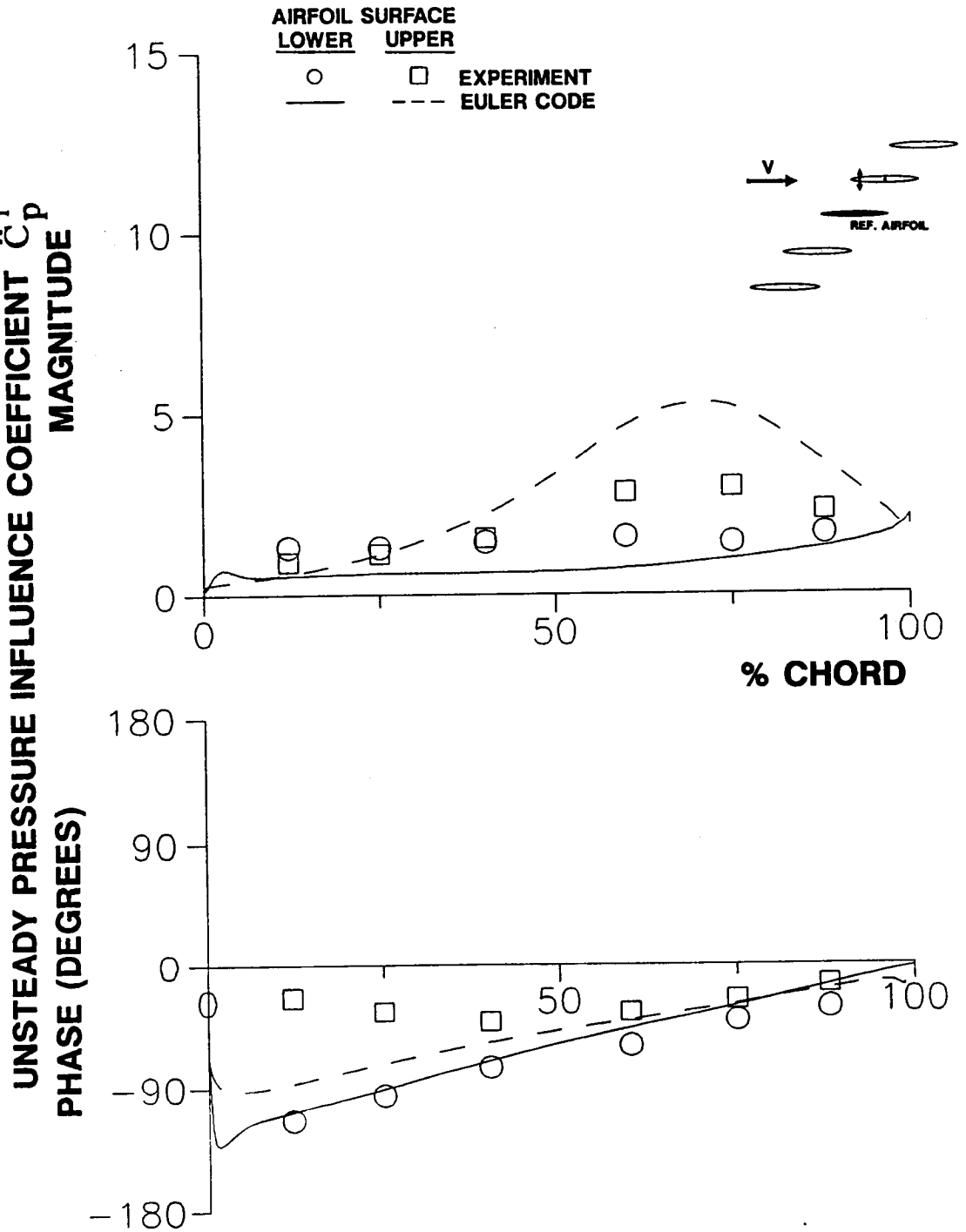

Figure 5.34 Unsteady pressure influence coefficient distribution, oscillating airfoil in relative position 1, high solidity cascade, M = 0.65, α_0 = 0 degrees, k = 0.39

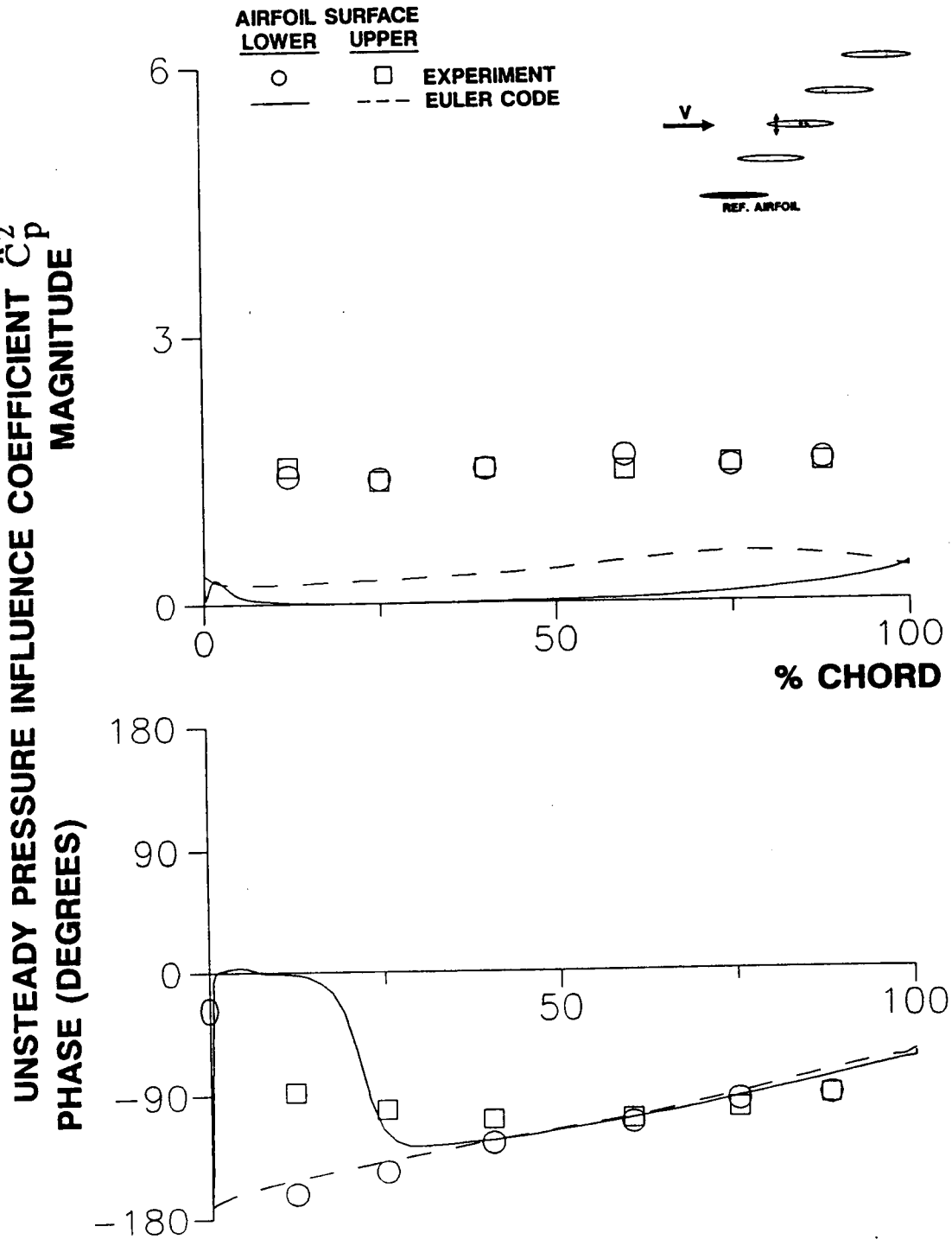

Figure 5.35 Unsteady pressure influence coefficient distribution, oscillating airfoil in relative position 2, high solidity cascade, M = 0.65, $\alpha_0 = 0$ degrees, k = 0.39

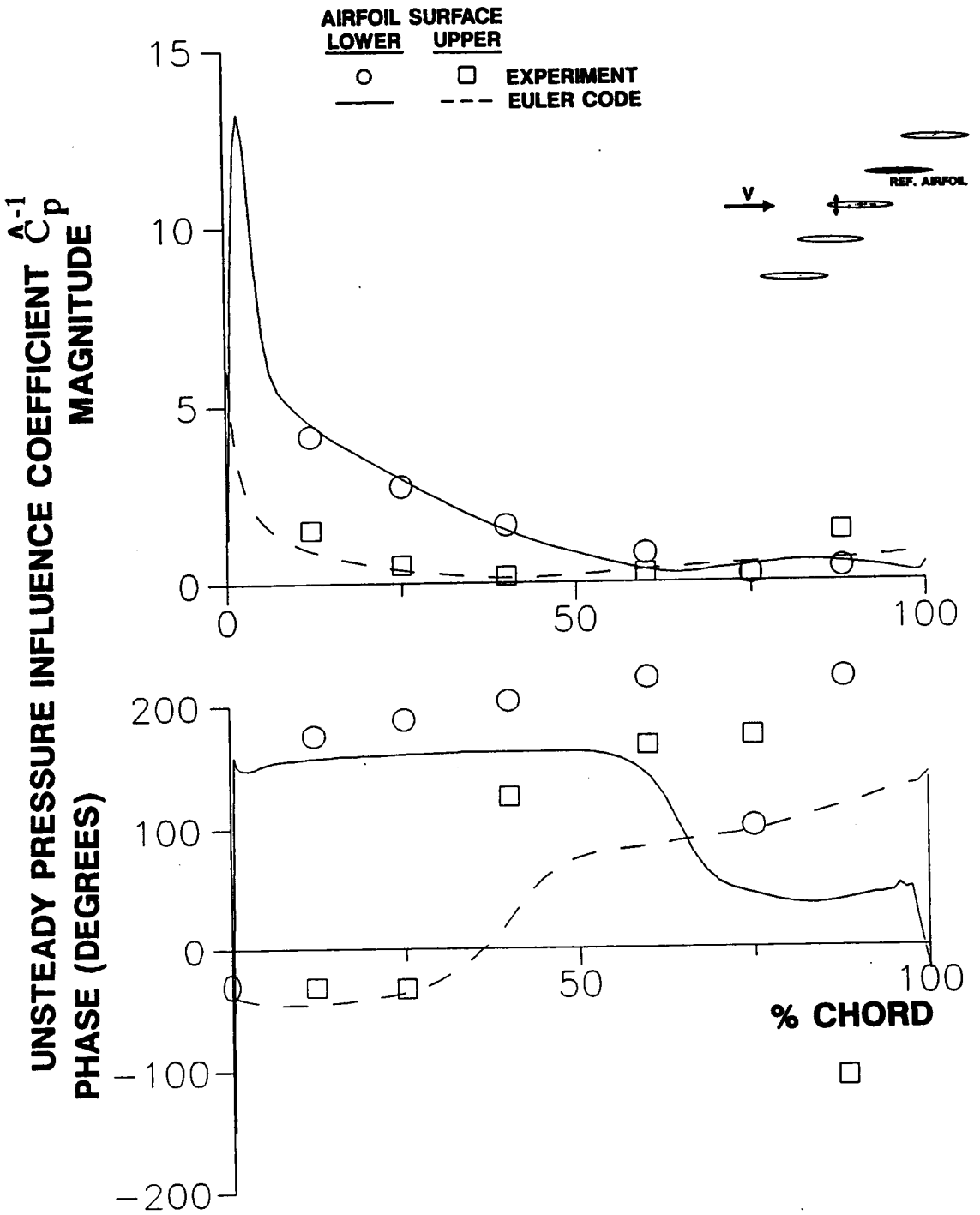

Figure 5.36 Unsteady pressure influence coefficient distribution, oscillating airfoil in relative position -1, high solidity cascade, M=0.65, α_0=0 degrees, k=0.39

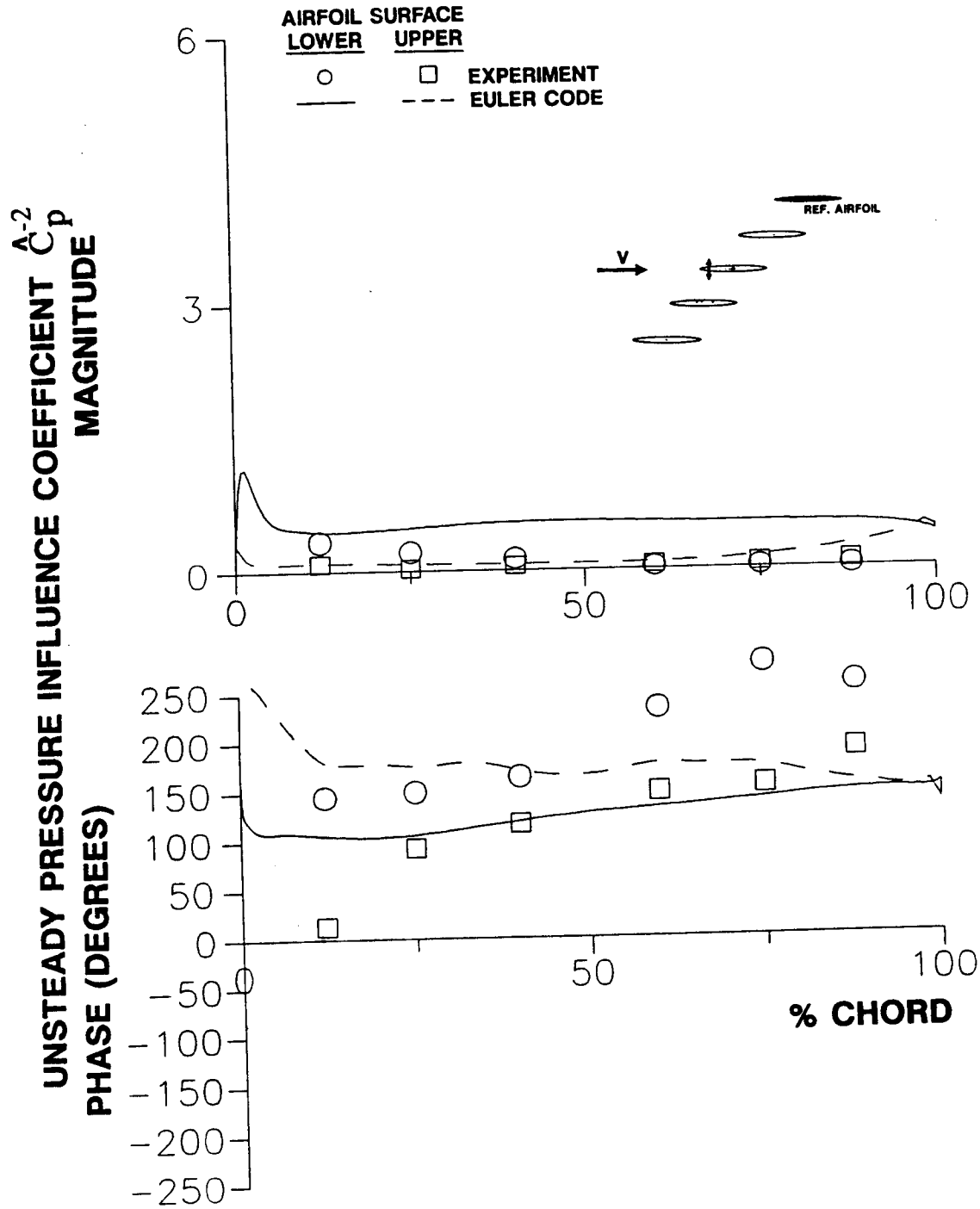

Figure 5.37 Unsteady pressure influence coefficient distribution, oscillating airfoil in relative position -2, high solidity cascade, M = 0.65, $\alpha_0 = 0$ degrees, k = 0.39

Interblade Phase Angle Results

Airfoil surface unsteady pressure coefficient distributions obtained via summation of influence coefficients predicted by the Euler code are correlated with experiment data obtained using the influence coefficient technique and also the data for all airfoils oscillating. The influence coefficients are summed over the oscillating airfoil relative positions ranging from -2 to 2, as indicated by N = 2 in the figure legends. Results for the unsteady pressure difference coefficient distributions are also presented, these plots including linearized analysis results. The low solidity cascade configuration is used with an inlet Mach number of 0.55 and a reduced frequency of 0.20. The combination of lowest inlet Mach number and lowest reduced frequency is used to minimize the upstream-traveling wave effect in the experimental influence coefficient data.

Correlation of the airfoil surface unsteady pressure coefficient distributions for in-phase oscillations is shown in Figure 5.38. The experimental influence coefficient data and the all-airfoils-oscillating data are in very good mutual agreement. The Euler code predictions for the airfoil lower surface magnitudes are in very good agreement with these data, but the predicted lower surface phases lead the data by a small amount. The predicted upper surface magnitudes are larger than the experimental data over the forward half of the airfoil but generally smaller along the aft half. The predicted upper surface phase angles are in good agreement with both data sets. The unsteady pressure difference coefficients, ΔC_p, are presented in Figure 5.39 along with linearized analysis results for a finite number of oscillating airfoils. Correlation of the Euler code predictions with the data and the linearized analysis results is generally very good. Only in the leading edge region do significant phase angle differences arise.

For β=45 degrees, Figure 5.40, the Euler code predictions for C_p correlate well with the experimental influence coefficient data, although the code predictions for the magnitudes tend to be slightly larger than the data. In comparison to the influence coefficient data, the all-airfoils-oscillating magnitude data are in good

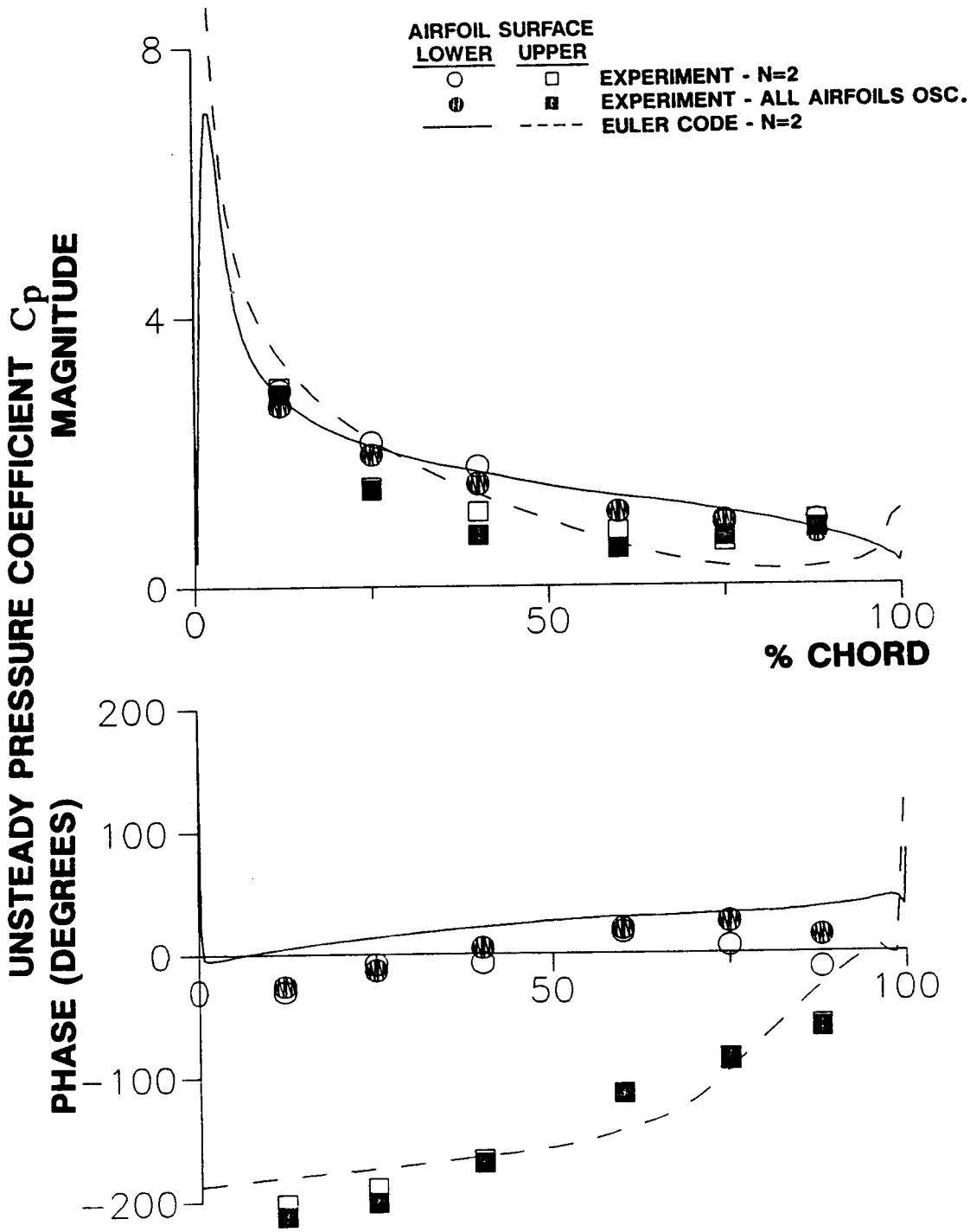

Figure 5.38 Airfoil surface unsteady pressure coefficient distributions, M=0.55, k=0.20, β=0 degrees

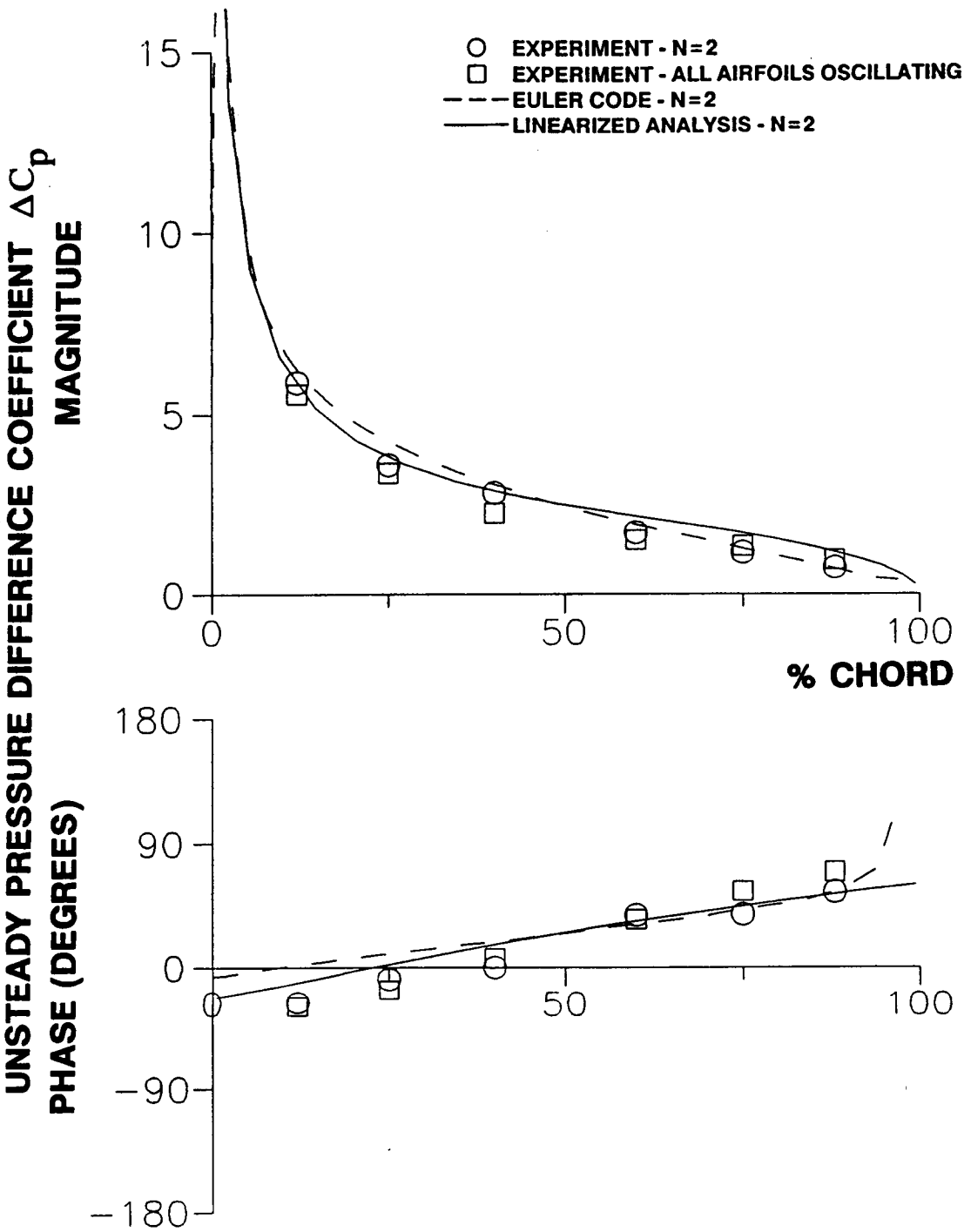

Figure 5.39 Airfoil surface unsteady pressure difference coefficient distributions, M=0.55, k=0.20, β=0 degrees

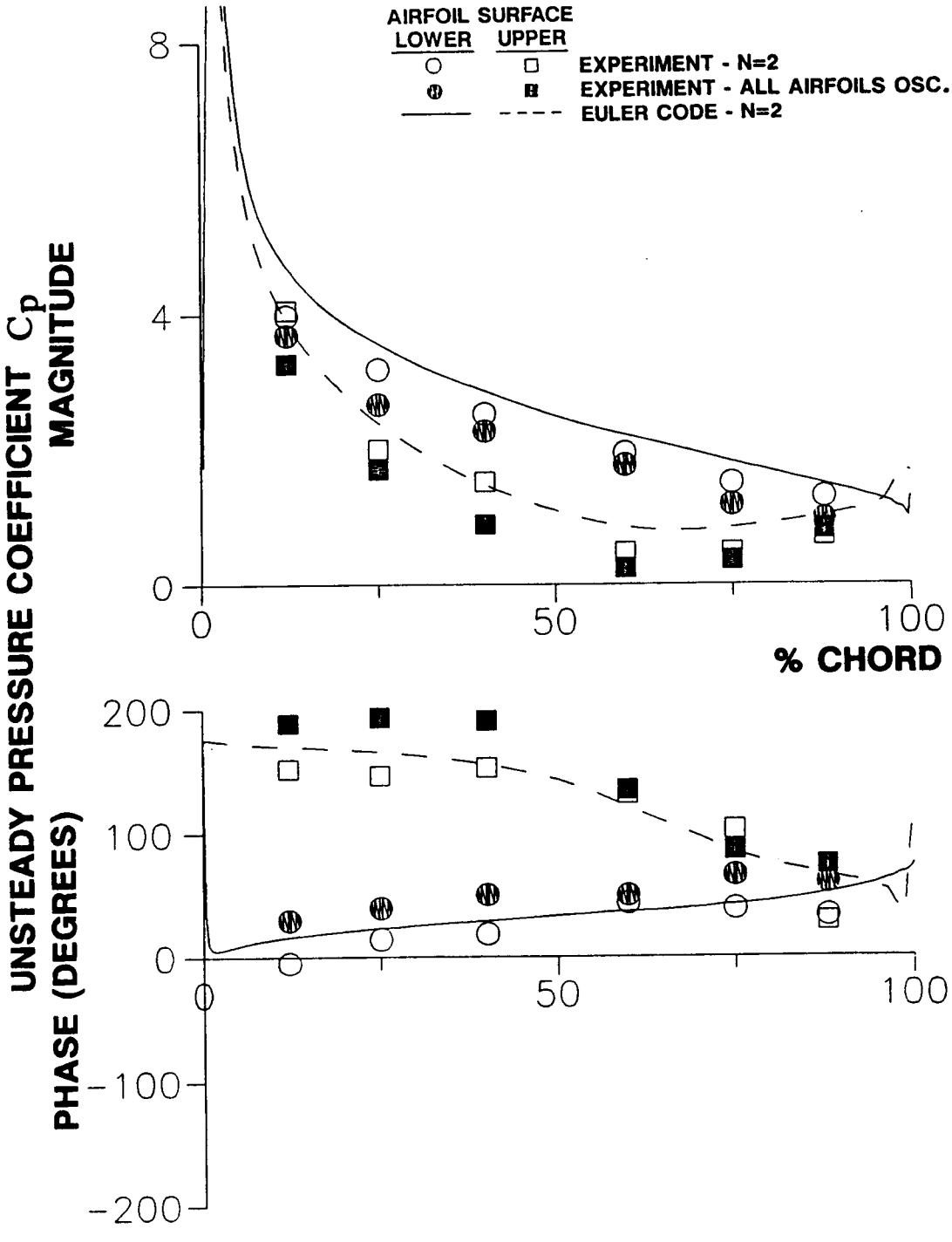

Figure 5.40 Airfoil surface unsteady pressure coefficient distributions, M=0.55, k=0.20, β=45 degrees

agreement but phase differences exist along the first 50% of chord. The Euler code predictions for ΔC_p are in good agreement with the experimental influence coefficient data, Figure 5.41. The all-airfoils-oscillating magnitude data are in good agreement with the experimental influence coefficient data, but there is an offset between the two sets of phase data. Relative to the experimental influence coefficient data, the linearized analysis predicts larger magnitudes, but the phase angles are in good agreement.

For β=-45 degrees, the two sets of experimental data and the Euler code predictions for C_p are in good agreement, Figure 5.42. However, the code tends to predict larger magnitudes than measured, particularly on the airfoil upper surface. As expected, then, the ΔC_p correlation is also good, Figure 5.43. The two sets of experimental data and the results from the linearized analysis are in particularly good agreement, while the Euler code predicts slightly larger magnitudes and slightly different phases.

Poor cascade dynamic periodicity was found for β=90 degrees, thus it is not surprising that the correlation between the data for all airfoils oscillating and the influence coefficient data is not particularly good for that value of interblade phase angle, Figure 5.44. The Euler code predicts larger magnitudes than determined using the experimental influence coefficients, but the phase angles are in very good agreement. These differences result in Euler code predictions for $|\Delta C_p|$ which are significantly greater than magnitudes determined from the experimental influence coefficients, Figure 5.45. The linearized analysis predicts even larger magnitudes. With the exception of the all-airfoils-oscillating data, the phase angle results are in good agreement, particularly near the leading edge.

The two sets of experimental data revert to good mutual agreement for β=-90 degrees, Figure 5.46. As for β=90 degrees, the Euler code predicts larger magnitudes for C_p than determined using the experimental influence coefficients, but the phase

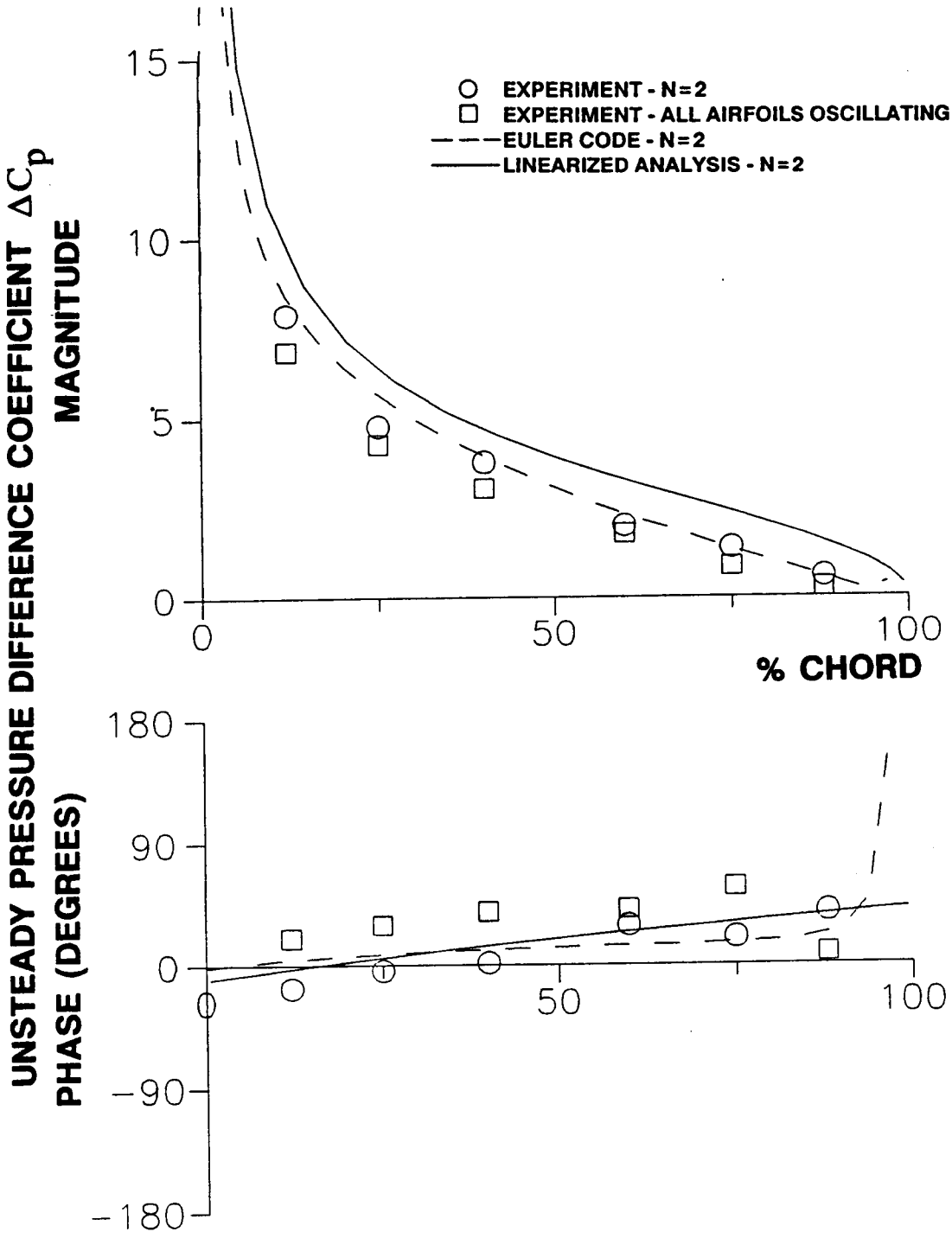

Figure 5.41 Airfoil surface unsteady pressure difference coefficient distributions, M=0.55, k=0.20, β=45 degrees

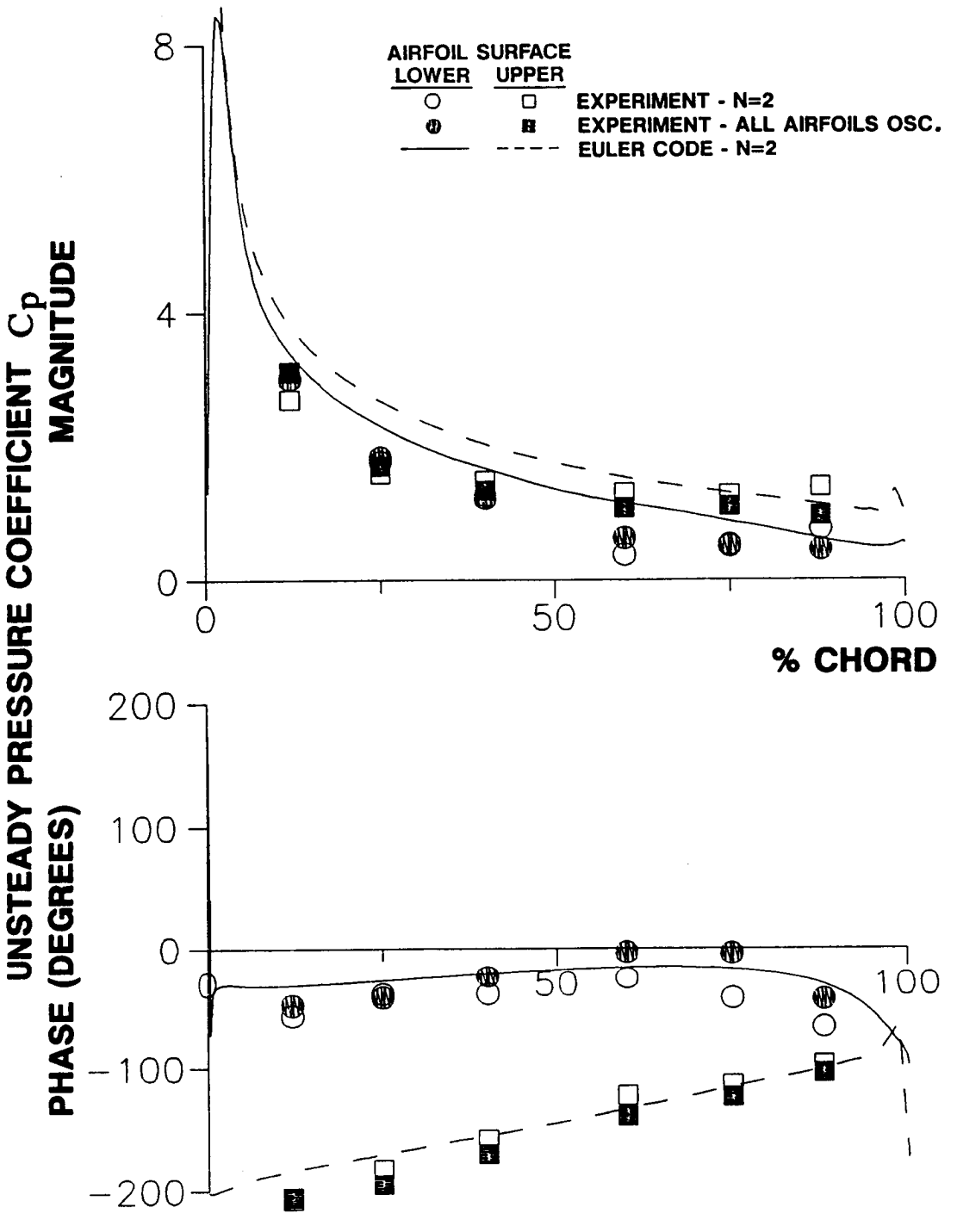

Figure 5.42 Airfoil surface unsteady pressure coefficient distributions, M=0.55, k=0.20, β=-45 degrees

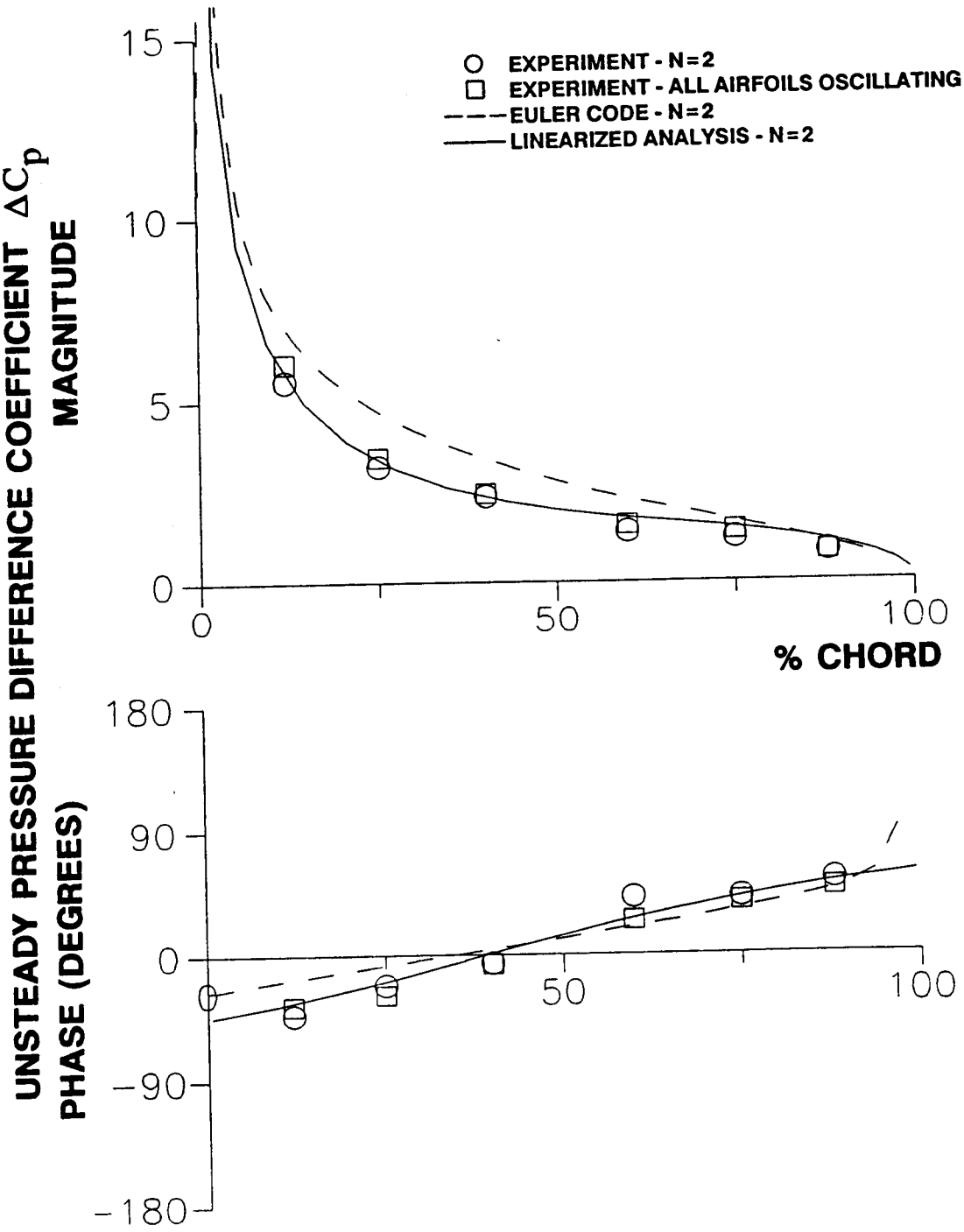

Figure 5.43 Airfoil surface unsteady pressure difference coefficient distributions, M=0.55, k=0.20, β=-45 degrees

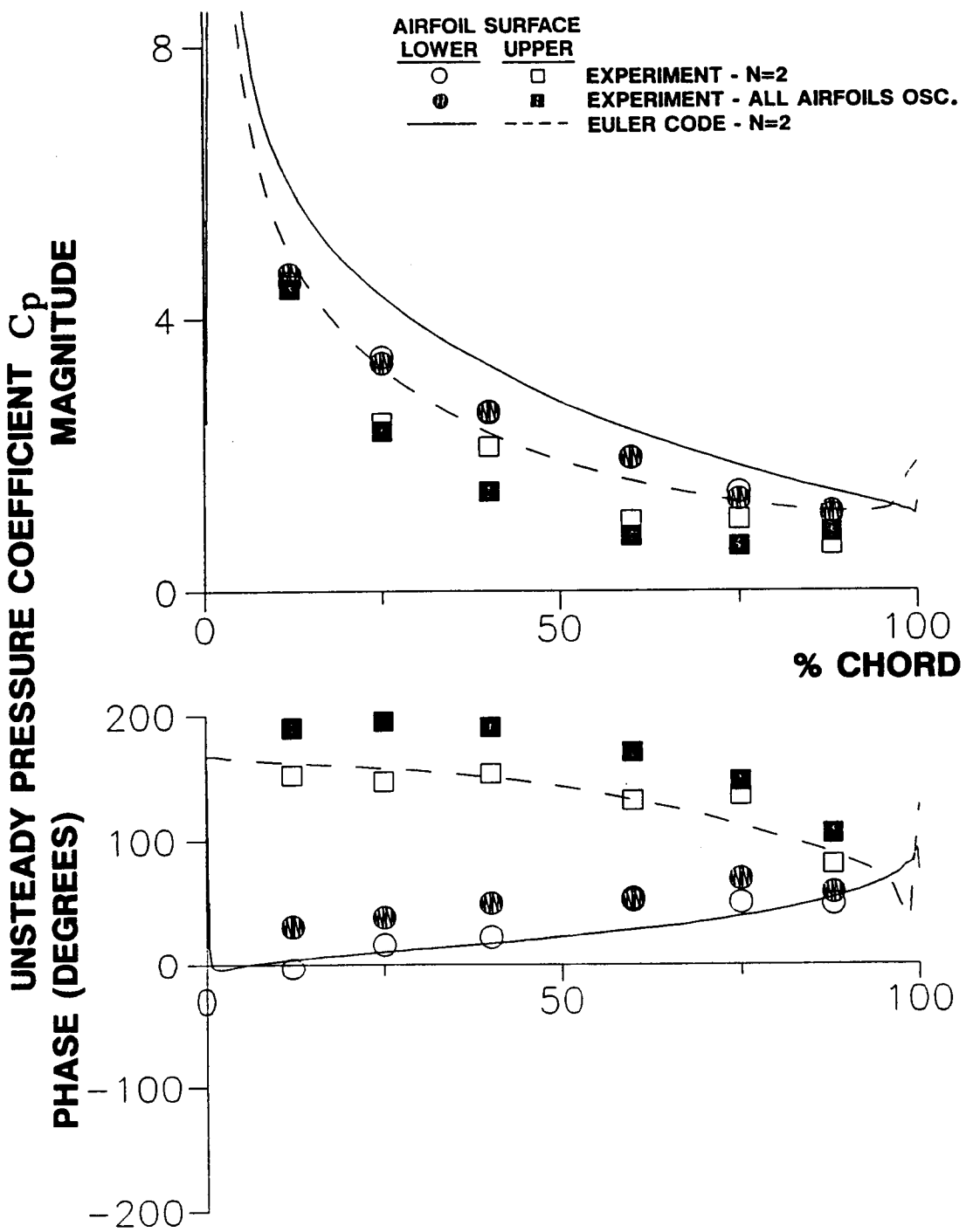

Figure 5.44 Airfoil surface unsteady pressure coefficient distributions, M=0.55, k=0.20, β=90 degrees

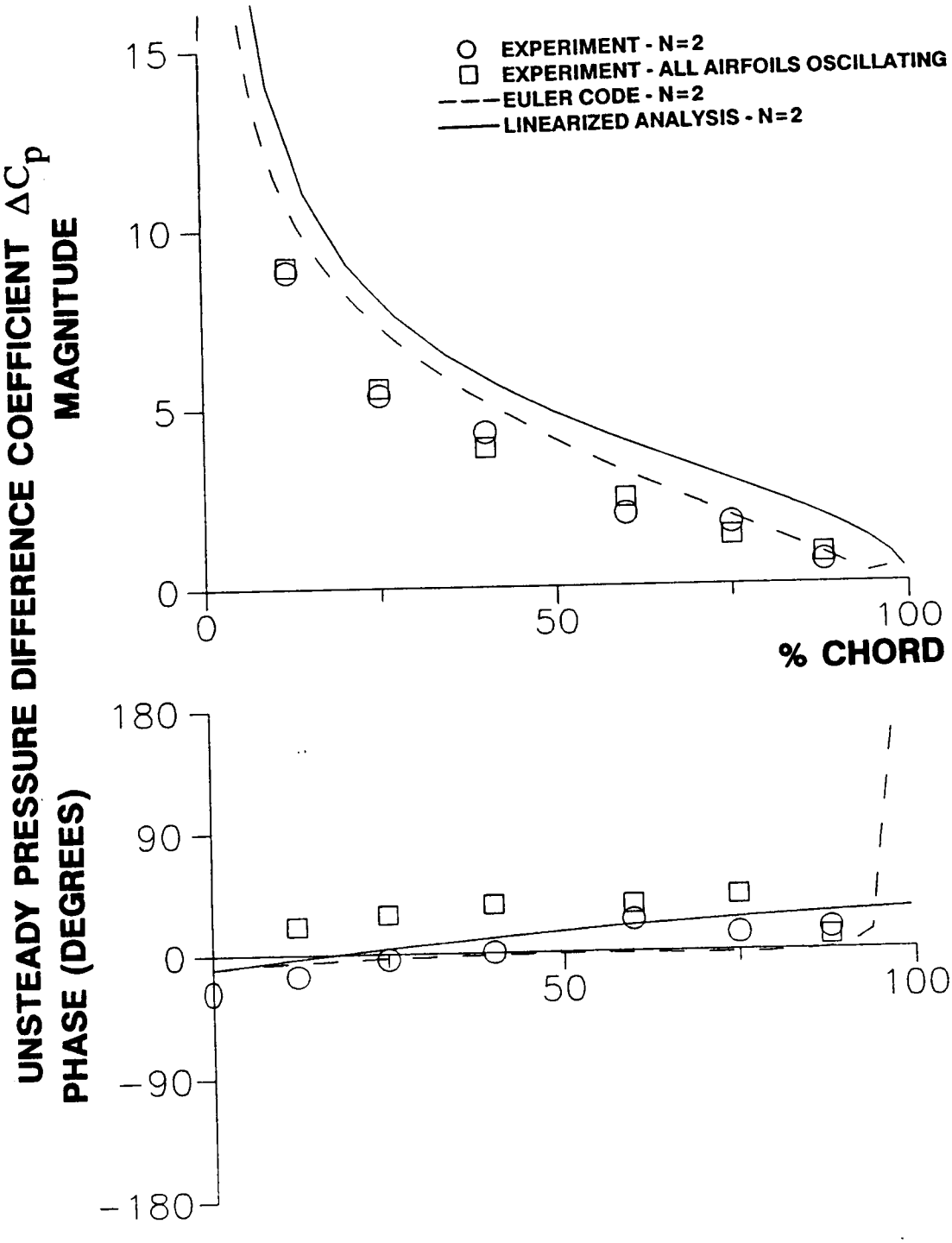

Figure 5.45 Airfoil surface unsteady pressure difference coefficient distributions, M=0.55, k=0.20, β=90 degrees

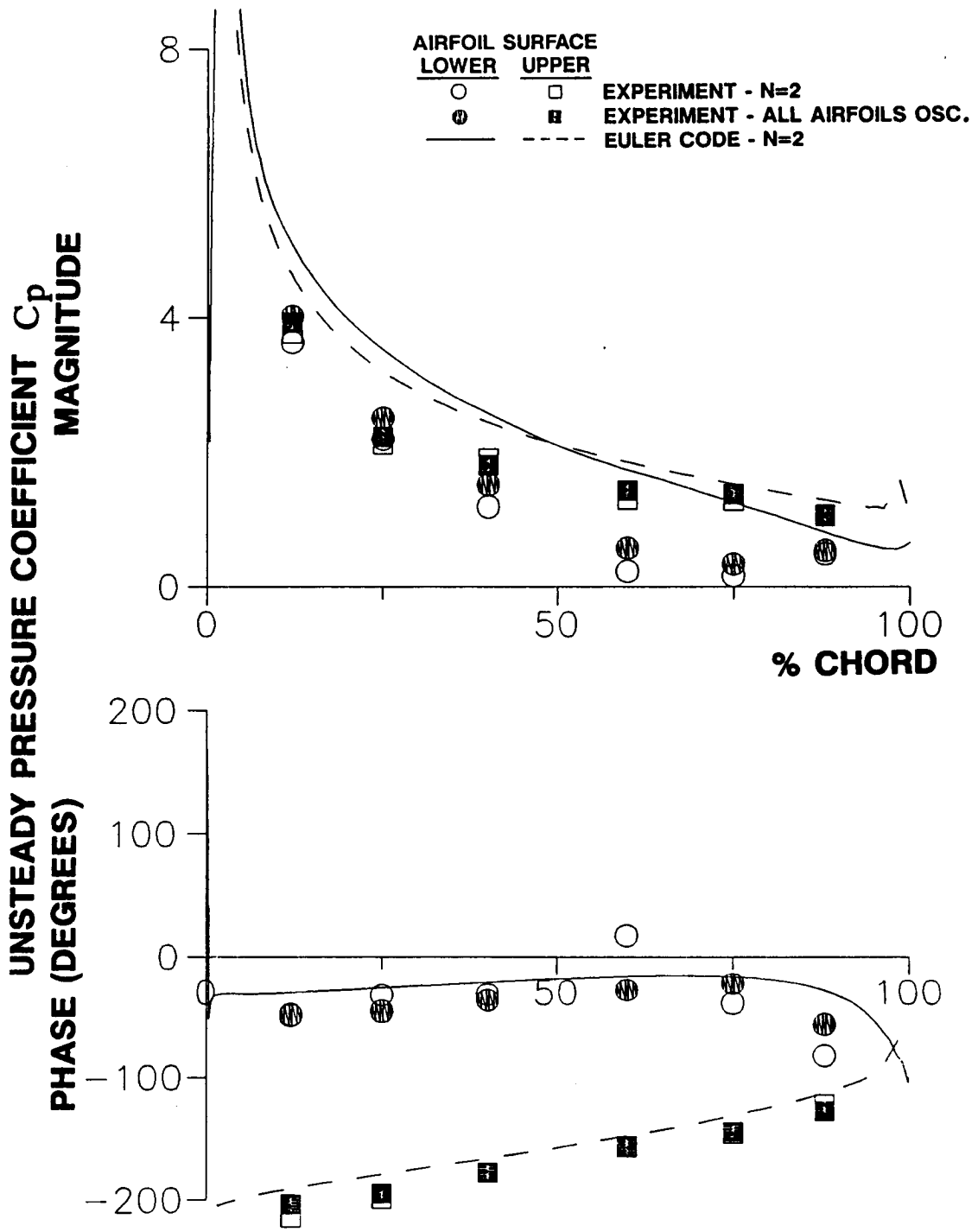

Figure 5.46 Airfoil surface unsteady pressure coefficient distributions, M=0.55, k=0.20, β=-90 degrees

angles are in very good agreement. Thus the Euler code predictions for the magnitude of ΔC_p are also larger than the data and, in this case, often larger than the linearized analysis predictions, Figure 5.47. The phase angle correlation is very good.

Out-of-phase oscillations result in differences in the C_p phase angle values as determined by the two experimental techniques, Figure 5.48. In comparison to the experimental influence coefficient data, the Euler code again predicts larger magnitude for C_p, but the phase angle values are in very good agreement. Thus the Euler code predictions for the magnitude of ΔC_p, Figure 5.49, are also larger than the experimental data, but in very good agreement with linearized analysis predictions. Except for the all-airfoils-oscillating data, the phase angle correlation is very good.

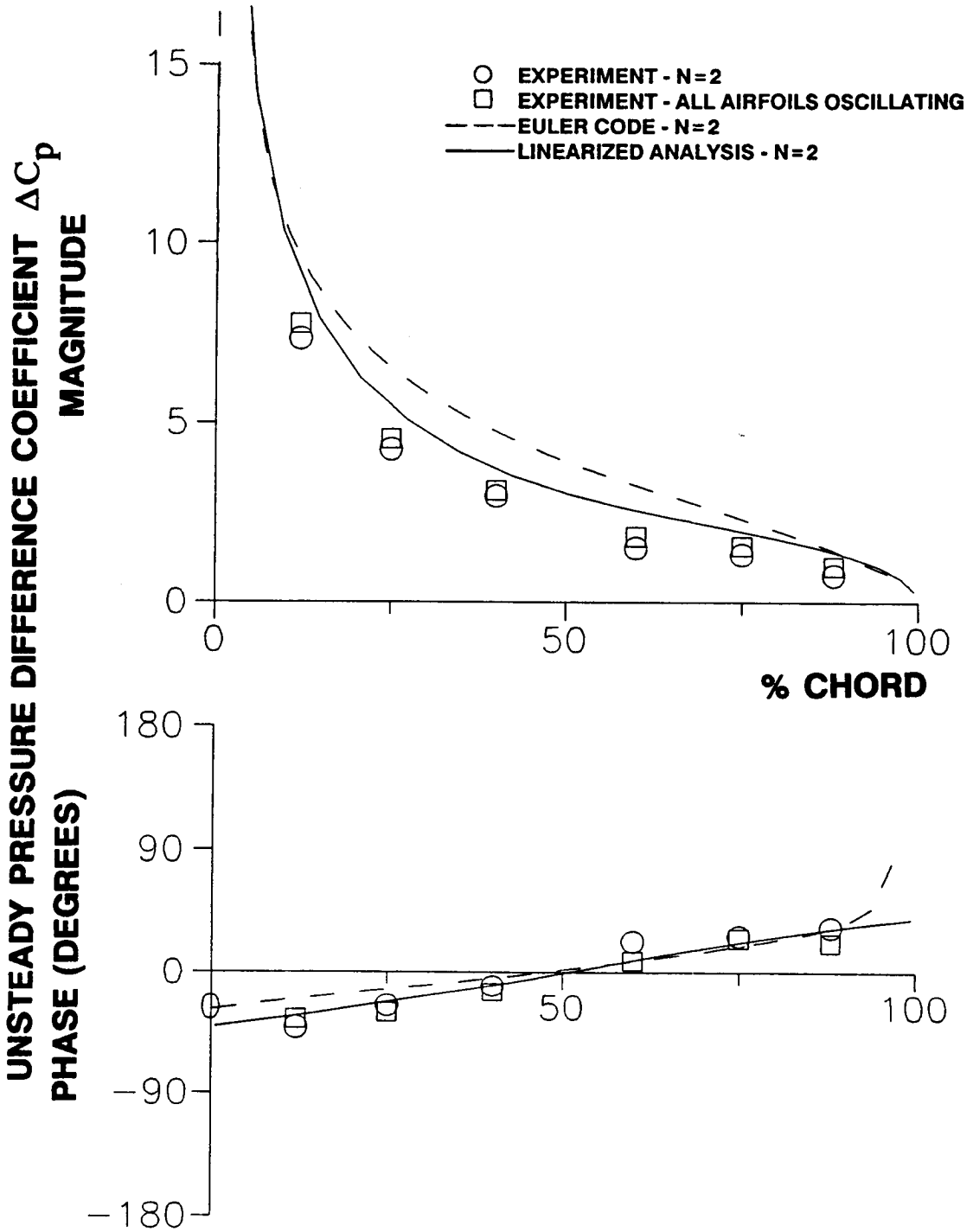

Figure 5.47 Airfoil surface unsteady pressure difference coefficient distributions, M=0.55, k=0.20, β=-90 degrees

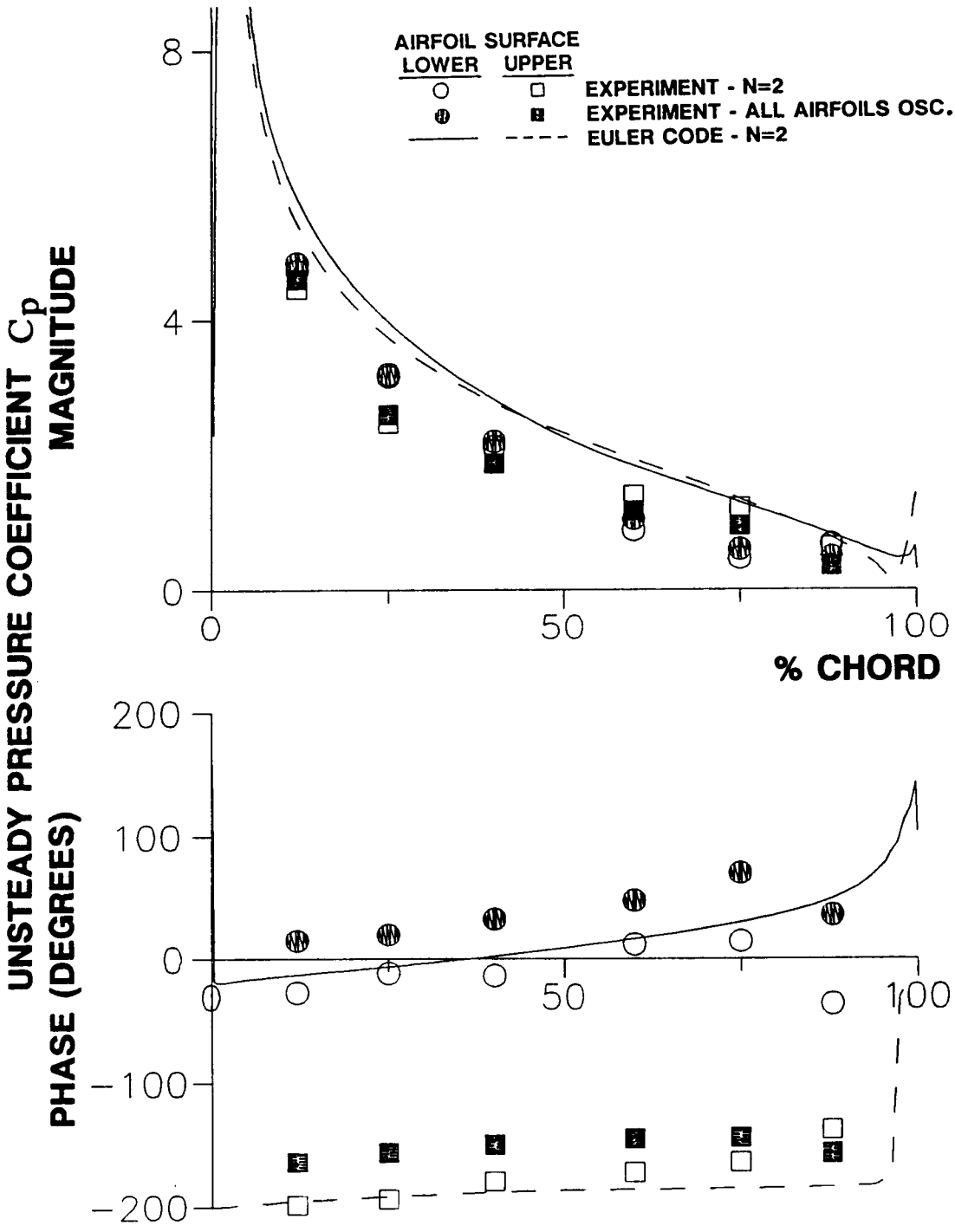

Figure 5.48 Airfoil surface unsteady pressure coefficient distributions, M = 0.55, k = 0.20, β = 180 degrees

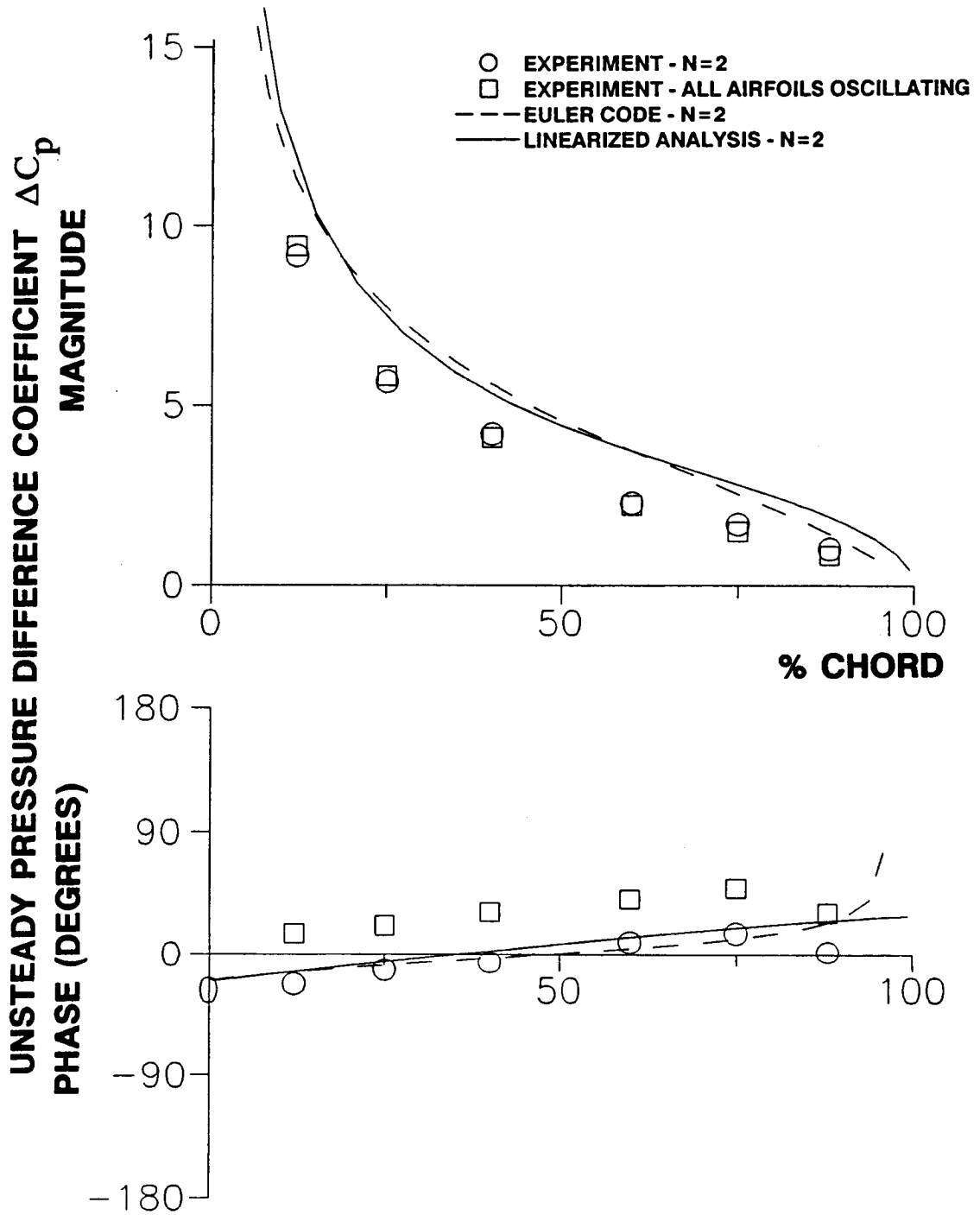

Figure 5.49 Airfoil surface unsteady pressure difference coefficient distributions, M=0.55, k=0.20, β=180 degrees

CHAPTER 6

SUMMARY, CONCLUSIONS AND RECOMMENDATIONS

Linear oscillating cascade aerodynamics have been investigated using experimental and computational methods. Two methods of determining the oscillating cascade aerodynamics have been used: (1) the conventional method in which all the airfoils oscillate simultaneously at a fixed interblade phase angle; and (2) the unsteady aerodynamic influence coefficient technique. In this technique, only one airfoil in the cascade is oscillated at a time, with the resulting airfoil surface unsteady pressure distribution measured on one dynamically instrumented reference airfoil. The unsteady aerodynamics of an equivalent cascade with all airfoils oscillating at any specified interblade phase angle are then determined through a vector summation of these data.

Steady and unsteady aerodynamic data were obtained in the NASA Lewis Transonic Oscillating Cascade Facility using a cascade of biconvex airfoils executing torsion mode oscillations at values of reduced frequency as great as 0.45. Two cascade solidities, 0.65 and 1.3, were investigated for several different mean flow conditions ranging from subsonic to transonic. Detailed steady airfoil surface pressure distributions quantified the mean flow field. Unsteady airfoil surface pressure distributions were measured using flush-mounted, miniature high-response pressure transducers, then discrete Fourier analysis techniques were used to analyze the unsteady pressure data.

It was found that, depending upon the steady and unsteady aerodynamic conditions, the wind tunnel walls may have a detrimental effect on the cascade unsteady aerodynamics. Only at interblade phase angle values where the experimental all-airfoils-oscillating data generally had good dynamic periodicity, -90 and -45 degrees, did the all-airfoils-oscillating data correlate consistently well with the experimental influence coefficient data and the linearized analysis results. It was subsequently found by application of linearized unsteady aerodynamic theory that, at those two values of interblade phase angle, pressure waves are produced which do not interfere with the cascade unsteady aerodynamics. However, at the other interblade phase angles where the correlation was not generally good, pressure waves were predicted which could interfere with the cascade unsteady aerodynamics by reflection off a wind tunnel wall back into the cascade. Whether the waves were subresonant (attenuating with distance from the cascade) or superresonant (propagating unattenuated) made no difference.

The wind tunnel walls also caused two potentially detrimental effects in the influence coefficient experiments. One relatively minor effect, the reflection of pressure disturbances off a wind tunnel wall onto the adjacent airfoil, caused spurious unsteady pressures on that airfoil. The other effect, the creation of an upstream-traveling pressure wave, often had a large effect on the unsteady pressure distributions of airfoils upstream of the oscillating airfoil.

The upstream-traveling wave phenomenon was confirmed to be a consequence of the wind tunnel walls by correlation of experimentally-determined influence coefficients with those determined by an Euler code which did not model the walls. From the experimental data, the wave amplitude was found to increase with reduced frequency and Mach number, and as a consequence, the summation of influence coefficient series for the dynamic pressure coefficient was found to be convergent

only for the lowest combination of Mach number and reduced frequency. However, the unsteady pressure difference coefficient series is generally convergent. In fact, for the low solidity cascade, good unsteady pressure difference coefficient agreement was generally found between values determined by the experimental influence coefficient technique and values predicted by the linearized analysis.

Thus to make this linear cascade a reliable facility for the experimental quantification of oscillating cascade aerodynamics, it is necessary to reduce the effects of the wind tunnel walls. It is recommended that the solid walls of the wind tunnel in the vicinity of the cascade be replaced with acoustically-treated walls designed using the technology developed to reduce aircraft gas turbine engine noise [40]. Then, to determine the effectiveness of the new walls, the experimental investigation reported herein could be repeated.

In addition, an Euler code for oscillating, cascaded airfoils was modified for implementation of the unsteady aerodynamic influence coefficient technique. The Euler code was first improved by modification of the upstream and downstream boundary conditions using a one-dimensional approximation to the Euler equations. Then the unsteady aerodynamic influence coefficient technique was implemented by further modification of the code. The resulting predictions were correlated with the experimental data and also with the linearized analysis predictions.

The Euler code boundary condition modifications were found to improve the ability of the code to predict the unsteady aerodynamics of a cascade of flat plates oscillating simultaneously. Influence coefficients predicted by the Euler code were found to be in good agreement with the experimental data. Summation of the predicted influence coefficients to obtain predicted unsteady pressure coefficients for various values of interblade phase angle were found to be in good agreement with

the experimental data and the linearized analysis results. Thus the Euler code implementation of the unsteady aerodynamic influence coefficient technique was found to be a valid method for the calculation of oscillating cascade aerodynamics.

However, the ability of the code to predict the steady state aerodynamics of the high solidity biconvex airfoil cascade at 7 degrees of incidence was not good. To be useful for a wide range of cascade geometries and flow conditions, the steady state aerodynamic predictions of this code must be improved. Two-dimensional inlet and exit boundary conditions may be useful in this respect.

LIST OF REFERENCES

1. Jeffers II, J.D. and Meece, C.E., "F100 Fan Stall Flutter Problem Review and Solution," *AIAA Journal of Aircraft,* Vol. 12, No. 4, April 1975, pp. 350-357.

2. Mehmed, O., Kaza, K.R.V., Lubomski, J.F. and Kielb, R.E., "Bending-Torsion Flutter of a Highly Swept Advanced Turboprop," *NASA TM-82975,* 1982.

3. Smith, S.N., "Discrete Frequency Sound Generation in Axial Flow Turbomachines," *Aeronautical Research Council Reports and Memoranda No. 3709,* March 1972.

4. Fleeter, S., "Fluctuating Lift and Moment Coefficients for Cascaded Airfoils in a Nonuniform Compressible Flow Field," *AIAA Journal of Aircraft,* Vol. 10, No. 2, February 1973, pp. 93-98.

5. Whitehead, D.S., "Classical Two-Dimensional Methods," *AGARD Manual on Aeroelasticity in Axial-Flow Turbomachines Volume 1 Unsteady Turbomachinery Aerodynamics, AGARDograph No. 298,* M.F. Platzer and F.O. Carta, editors, London, 1987, pp. (3-1)-(3-30).

6. Atassi, H.M. and Akai, T.J., "Aerodynamic and Aeroelastic Characteristics of Oscillating Loaded Cascades at Low Mach Number," *ASME Paper 70-GT-111,* March 1979.

7. Verdon, J.M. and Caspar, J.R., "Subsonic Flow Past an Oscillating Cascade with Finite Mean Flow Deflection," *AIAA Journal,* Vol. 18, No. 5, May 1980, pp. 540-548.

8. Whitehead, D.S., "The Calculation of Steady and Unsteady Transonic Flow in Cascades," *Cambridge University Report CUED/A-Turbo/TR118,* 1982.

9. Verdon, J.M. and Caspar, J.R., "A Linearized Unsteady Aerodynamic Analysis for Transonic Cascades," *Journal of Fluid Mechanics,* Vol. 149, December 1984, pp. 403-429.

10. Verdon, J.M. and Usab, W.J., "Application of a Linearized Unsteady Aerodynamic Analysis to Standard Cascade Configurations," *NASA CR-3940,* January 1986.

11. Chiang, H.D. and Fleeter, S., "Locally Analytical Numerical Method for Inviscid Oscillating Airfoil Aerodynamics," presented at the *SIAM 1986 National Meeting,* Boston, July 1986.

12. Hall, K.C. and Crawley, E.F., "Calculation of Unsteady Flows in Turbomachinery Using the Linearized Euler Equations," *Unsteady Aerodynamics and Aeroelasticity of Turbomachines and Propellers,* H.E. Gallus and S. Servaty, editors, Aachen Institute of Technology, Aachen, February 1988, pp. 15-38.

13. Huff, D.L., "Numerical Analysis of Flow Through Oscillating Cascade Sections," *NASA TM-101417,* 1989.

14. He, L., "An Euler Solution for Unsteady Flows Around Oscillating Blades," *ASME Paper 89-GT-279,* 1989.

15. Kao, Y.-F., "A Two-Dimensional Unsteady Analysis for Transonic and Supersonic Cascade Flows," *Ph.D. Thesis*, Purdue University, May 1989.

16. Davies, M.R.D. and Whitehead, D.S., "Unsteady Aerodynamic Measurements in a Transonic Annular Cascade," *Unsteady Aerodynamics of Turbomachines and Propellers,* Cambridge University Engineering Department, Cambridge, 1984, pp. 487-502.

17. Shaw, L.M., Boldman, D.R., Buggele, A.E. and Buffum, D.H., "Unsteady Pressure Measurements on a Biconvex Airfoil in a Transonic Oscillating Cascade," *ASME Journal of Engineering for Gas Turbines and Power*, Vol. 108, No. 1, January 1986, pp. 53-59.

18. Kobayashi, H., "Annular Cascade Study of Low Back-Pressure Supersonic Fan Blade Flutter," *ASME Paper 89-GT-297*, 1989.

19. Hanamura, Y., Tanaka, H. and Yamaguchi, K., "A Simplified Method to Measure Unsteady Forces Acting on the Vibrating Blades in Cascade," *Bulletin of the JSME,* Vol. 23, No. 180, June 1980, pp. 880-887.

20. Hanamura, Y. and Yamaguchi, K., "An Experimental Investigation on Aerodynamic Interblade Interactions of a Vibrating Cascade in Transonic Flow," *JSME International Journal,* Vol. 30, No. 270, 1987, pp. 1919-1927.

21. Hanamura, Y. and Yamaguchi, K., "An Experimental Investigation on the Flutter of the Cascade of Turbomachinery in Transonic Flow," *Journal of the Faculty of Engineering, The University of Tokyo (B),* Vol. 39, No. 3, 1988, pp. 311-338.

22. Szechenyi, E., "Fan Blade Flutter - Single Blade Instability of Blade to Blade Coupling?," *ASME Paper 85-GT-216,* 1985.

23. Bolcs, A., Fransson, T.H. and Schlafli, D., "Aerodynamic Superposition Principle in Vibrating Turbine Cascades," *AGARD-CPP-468/469,* 1989.

24. Gerolymos, G.A., "Numerical Integration of the Blade-to-Blade Surface Euler Equations in Vibrating Cascades," *AIAA Journal,* Vol. 26, No. 12, December 1988, pp. 1483-1492.

25. Boldman, D.R. and Buggele, A.E., "Wind Tunnel Tests of a Blade Subjected to Midchord Torsional Oscillation at High Subsonic Stall Flutter Conditions," *NASA TM-78998,* October 1978.

26. Capece, V.R. and Fleeter, S., "Forced Response Unsteady Aerodynamics in a Multistage Compressor," *Purdue University Report ME-TSPC-TR-87-12,* August 1987.

27. Mallon, J.R., Final Report: Installation and Testing of a Strain Isolation System on Government Furnished Blades, NASA Contract NAS3-21611, March 1983.

28. Englund, D.R., Grant, H.P. and Lanati, G.A., "Measuring Unsteady Pressure on Rotating Compressor Blades," *NASA TM-79159,* 1979.

29. Oppenheim, A.V. and Shafer, R.W., *Digital Signal Processing,* Englewood Cliffs: Prentice-Hall, 1975.

30. Bergland, G.D. and Dolan, M.T., "Fast Fourier Transform Algorithms," *Programs for Digital Signal Processing,* IEEE Digital Signal Processing Committee, editor, New York: IEEE Press, 1979.

31. Kline, S.J. and McClintock, F.A., "Describing Uncertainties in Single-Sample Experiments," *Mechanical Engineering,* January 1953, pp. 3-8.

32. Landau, L.D. and Lifshitz, E.M., *Fluid Mechanics,* 2nd edition, Oxford: Pergamon Press, 1987.

33. Sankar, N.L. and Tang, W., "Numerical Solution of Unsteady Viscous Flow Past Rotor Sections," *AIAA Paper 85-0129,* 1985.

34. Wu, J.C., "A Study of Unsteady Turbulent Flow Past Airfoils," *Ph.D. Thesis,* Georgia Institute of Technology, August 1988.

35. Janus, J.M., "The Development of a Three-Dimensional Split Flux Vector Euler Solver with Dynamic Grid Applications," *M.S. Thesis,* Mississippi State University, August 1984.

36. Sorenson, R.L., "A Computer Program to Generate Two-Dimensional Grids About Airfoils and Other Shapes by the Use of Poisson's Equation," *NASA TM-81198,* 1980.

37. Chima, R.V., "Explicit Multi-Grid Algorithm for Quasi Three-Dimensional Viscous Flow in Turbomachinery," *Journal of Propulsion and Power,* Vol. 3, No. 5, 1987, pp. 397-405.

38. Burgess, J.C., "On Digital Spectrum Analysis of Periodic Signals," *Journal of the Acoustical Society of America,* Vol. 58, No. 3, September 1975, pp. 556-567.

39. Pulliam, T.H. and Steger, J.L., "Recent Improvements in Efficiency, Accuracy, and Convergence for Implicit Approximate Factorization Algorithms," *AIAA Paper 85-0360,* January 1985.

40. Groeneweg, J.F. and Rice, E.J., "Aircraft Turbofan Noise," *Journal of Turbomachinery,* Vol. 109, January 1987, pp. 130-141.

Appendix A. Discrete Fourier Analysis Techniques

Discrete Fourier transform methods are used to analyze the time-dependent pressure signals. In particular, these pressure signals, typically periodic with a fundamental frequency equal to the airfoil oscillation frequency, are decomposed via Fourier analysis methods to determine the magnitude and phase of the dominant frequency components. Despite the widespread availability of Fourier analysis software, this is not a trivial task due to the spectral leakage phenomenon. The basic analysis of this problem and the formulation of a scheme for correction of leakage effects has been accomplished by Burgess [38]. This approach will now be outlined with continuous time signals of a single frequency considered first. These results will be extended to discrete data, then the Hanning window will be discussed as will periodic signals with higher harmonics.

A.1 Continuous Time Signals

The Fourier series coefficients (FSC) of the continuous time signal $p(t)$ over the interval $0 \le t < T$ are defined as:

$$p_n = \frac{1}{T}\int_0^T p(t)e^{-i\omega_n t}dt \qquad (A.1)$$

where ω_n, the radian frequency, is equal to $n\omega_0$, and $\omega_0 = 2\pi/T$. The integer frequency index n varies between $-\infty$ and $+\infty$. The inverse relation is

$$p(t) = \sum_{n=-\infty}^{\infty} p_n e^{i\omega_n t} \qquad (A.2)$$

for $0 \le t < T$. This gives a periodic result $p(t + lT) = p(t)$ for any integer l.

Consider a signal $p(t) = A\cos\Omega t$, $0 \le t < T$. The FSC are

$$p_n = \frac{A}{2}\left[\frac{\sin(\Omega-\omega_n)T/2}{(\Omega-\omega_n)T/2}e^{i(\Omega-\omega_n)T/2} + \frac{\sin(\Omega+\omega_n)T/2}{(\Omega+\omega_n)T/2}e^{i(\Omega+\omega_n)T/2}\right]. \qquad (A.3)$$

Figure A.1 depicts an envelope of the magnitude of p_n as expressed by Equation A.3. The presence of multiple side lobes in the spectrum, termed leakage, generally occurs despite the fact that the cosine wave under consideration has a single frequency component. As shown, spectral lines fall in the envelope with spacing ω_0. Under specific sampling conditions, there will be just two spectral lines, located at $\omega_n = \pm\Omega$, which yield the correct magnitude and phase of the cosine signal. However, this will not generally be the case, as indicated in Figure A.1. The most important feature shown is that none of the lines are at the frequency Ω. Obviously, errors generally occur in doubling the magnitude of the largest spectral line to obtain the amplitude of the cosine signal. Also, phase errors will occur. Thus the task is to correctly infer the magnitude and phase of the wave from such a spectrum.

To analyze this problem, Equation A.3 will be written in a more useful form. Let T_Ω denote the period of the wave. Then

$$\Omega T_\Omega = 2\pi. \tag{A.4}$$

Choose m to be the number of wavelengths sampled. Thus

$$m = \frac{T}{T_\Omega}. \tag{A.5}$$

Splitting m into integer and fractional parts r and s, respectively, gives

$$m = r + s. \tag{A.6}$$

Using Equations A.4 through A.6,

$$(\Omega \pm \omega_n)\frac{T}{2} = \pi(m \pm n).$$

With these results, Equation A.3 becomes

$$p_n = \frac{A}{2}\left[\frac{\sin\pi(m-n)}{\pi(m-n)}e^{i\pi m} + \frac{\sin\pi(m+n)}{\pi(m+n)}e^{-i\pi m}\right]e^{-i\pi n}. \tag{A.7}$$

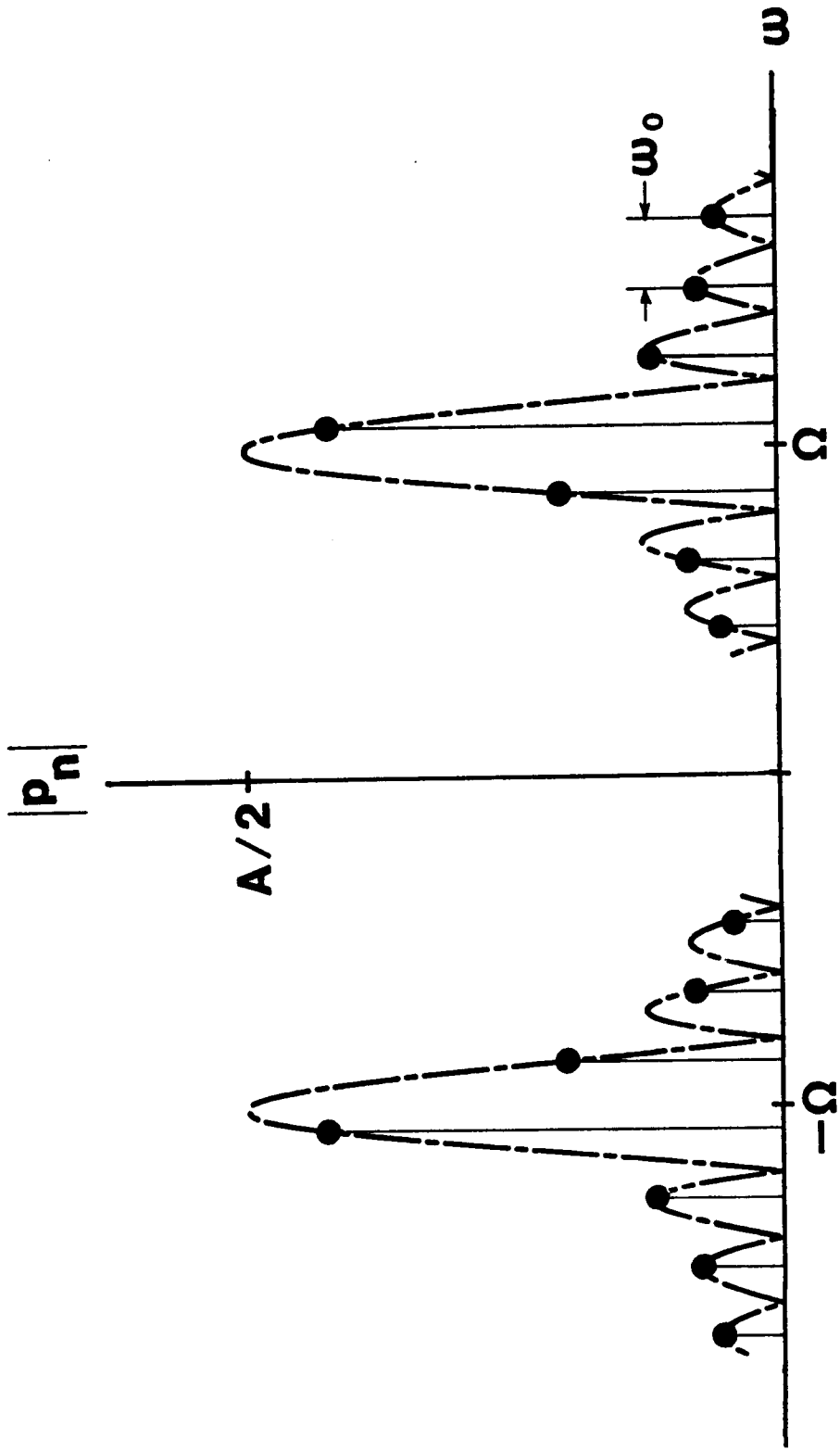

Figure A.1 Magnitude spectrum of a cosine wave

Identities such as the following are then applied to Equation A.7:

$$e^{i\pi m}\sin\pi(m-n) = e^{i\pi(s+n)}\sin\pi s .$$

This results in

$$p_n = \frac{A}{2}\left[\frac{\sin\pi s}{\pi(m-n)}e^{i\pi s} + \frac{\sin\pi s}{\pi(m+n)}e^{-i\pi s}\right]. \qquad (A.8)$$

The importance of the parameter s is revealed by Equation A.8. For example, when $s = 0$,

$$p_n = \frac{A}{2} \quad \text{for} \quad n = \pm r$$

$$= 0 \quad \text{for all} \quad n \neq \pm r .$$

Thus, in this special case, the correct magnitude and phase are recovered directly from the spectrum. This result is illustrated in Figure A.2; the absence of leakage contrasts with the example of Figure A.1, which illustrates a typical result for nonzero values of s.

Recalling that s is the fractional part of T/T_Ω, $s = 0$ thus corresponds to sampling an integer number of periods of the wave. This is shown in Figure A.3(a). Calculation of Fourier series coefficients assumes that the given signal is periodic in T; the periodic continuation of the signal of Figure A.3(a) is the continuous signal shown in part (b) of the figure.

When s is nonzero, the corresponding periodic continuation will not be continuous, as seen in Figure A.4. These discontinuities are the source of the spectral leakage shown in Figure A.1.

The correction scheme depends upon simplification of Equation A.8. For convenience, denote the first term in Equation A.8 as the direct contribution and the second term as the image contribution. Let U_d and U_i denote the magnitudes of the direct and image parts.

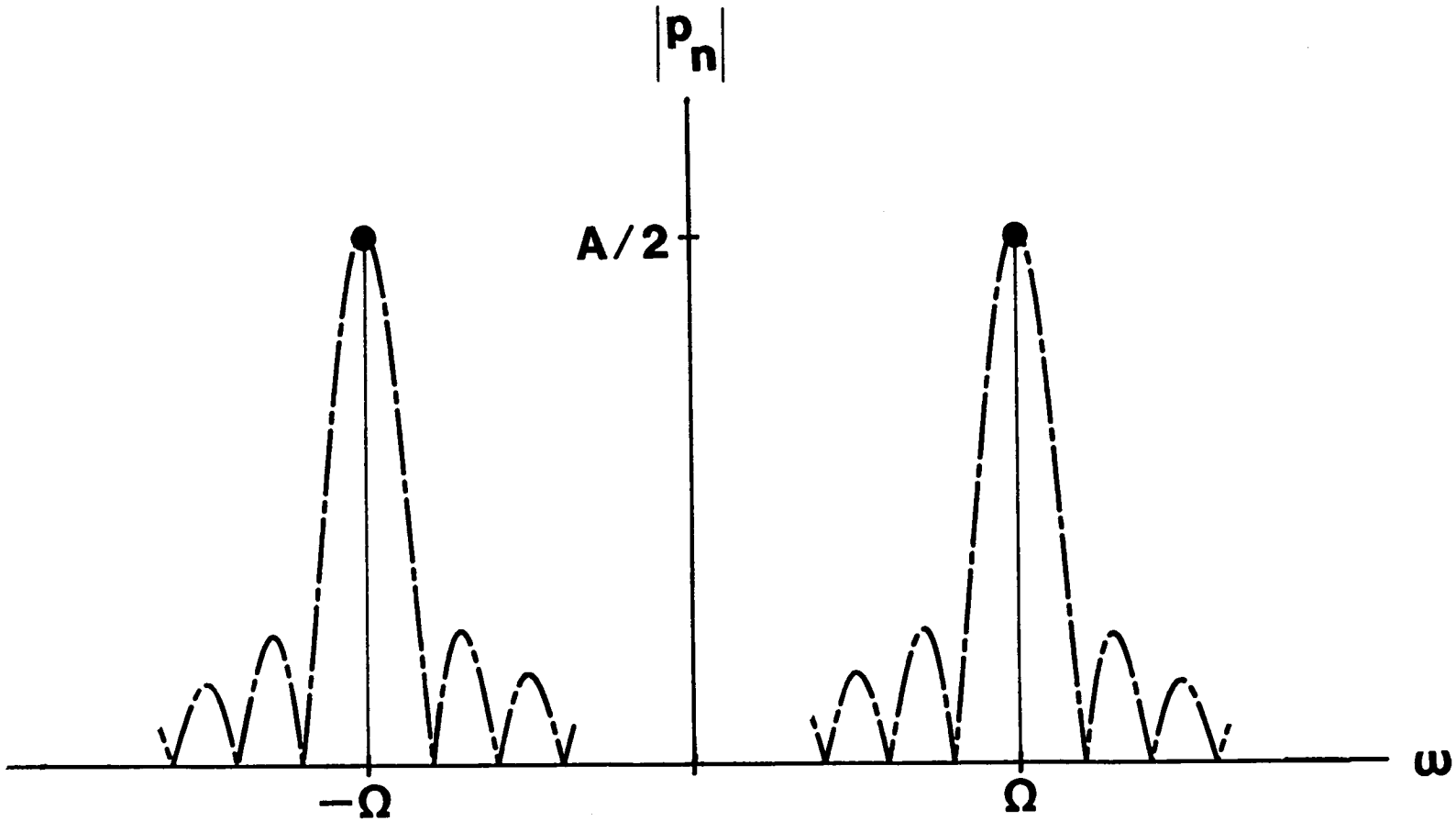

Figure A.2 Magnitude spectrum of a cosine wave, s=0

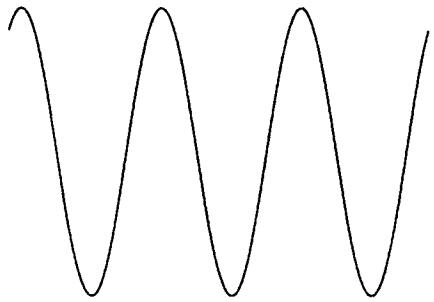

(a) Sampled signal

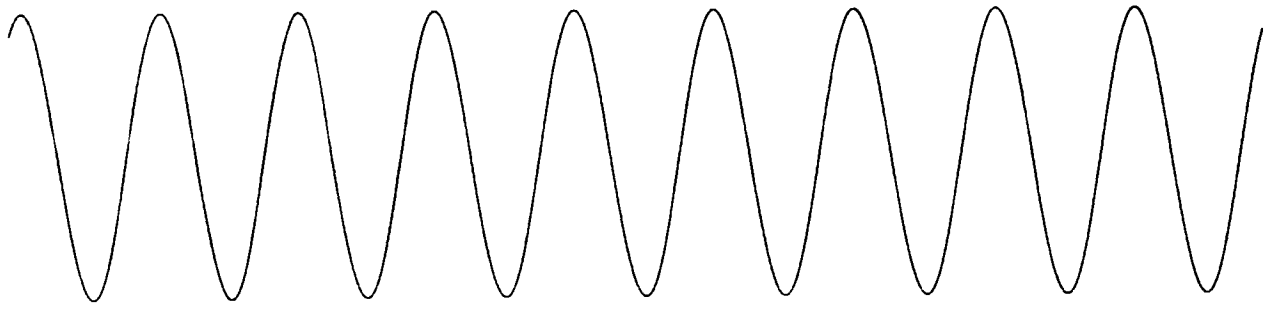

(b) Periodic continuation of sampled signal

Figure A.3 Periodic continuation of a signal with an integer number of periods

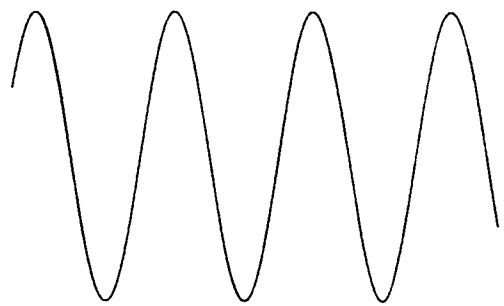

(a) Sampled signal

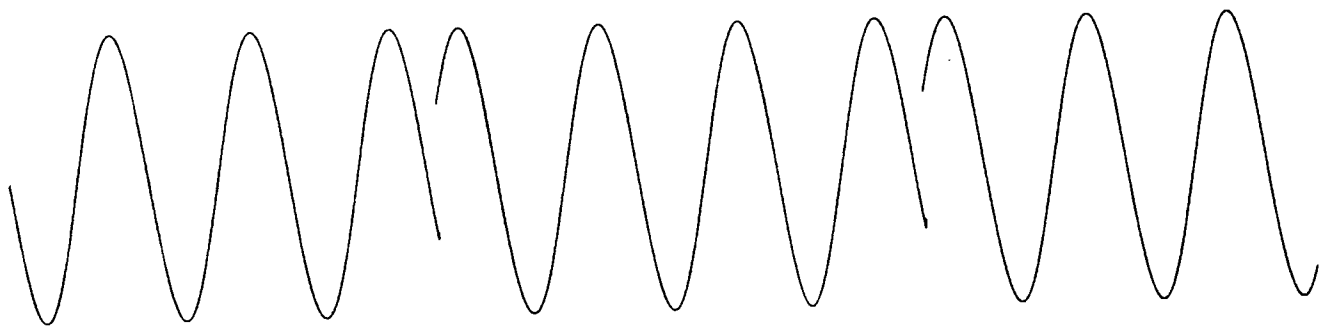

(b) Periodic continuation of sampled signal

Figure A.4 Periodic continuation of a signal with a noninteger number of periods

$$U_d = \frac{A}{2} \frac{\sin \pi s}{\pi (m-n)}$$

$$U_i = \frac{A}{2} \frac{\sin \pi s}{\pi (m+n)}$$

Their ratio is

$$\frac{U_i}{U_d} = \frac{m-n}{m+n}.$$

Attention is focused on values of $n = r$ and $n = r + 1$ which give the spectral lines bracketing Ω. When $n = r$,

$$\frac{U_i}{U_d} = \frac{s}{2r+s}.$$

For the worst case, $s = 1/2$, and

$$\frac{U_i}{U_d} = \frac{1}{4r+1}.$$

To neglect the image contribution, this ratio must be small, less than 0.01 for example. This requires $r \geq 25$ and then allows the approximation

$$p_r = \frac{A}{2} \frac{\sin \pi s}{\pi s} e^{i \pi s}. \qquad (A.9)$$

This shows that the amplitude is attenuated and a phase shift is introduced when s is nonzero. Since r is directly related to the signal observation time, specifying a minimum value for r is equivalent to requiring a minimum sampling period.

For the worst case, $s = 1/2$, Equation A.9 gives

$$p_r = \frac{A}{2} \frac{\sin \pi/2}{\pi/2} e^{i \pi/2}$$

$$= (0.6366) \frac{A}{2} e^{i \pi/2}.$$

Thus if p_r is used to estimate the amplitude and phase of the signal, the amplitude estimate may be low by as much as 36%, and the phase may be $\pi/2$ radians in error. Only when $s = 0$ will p_r directly give the desired result.

Since it is generally not possible to choose s in advance, one must find a way to estimate it from the data. Under the condition that Equation A.9 is a valid approximation, the following may be used for p_{r+1}:

$$p_{r+1} = \frac{A}{2\pi(s-1)} \sin \pi s \, e^{i\pi s}. \qquad (A.10)$$

Then

$$\frac{|p_r|}{|p_{r+1}|} = \frac{(1-s)}{s}$$

or

$$s = \frac{1}{(|p_r|/|p_{r+1}|)+1}. \qquad (A.11)$$

This calculated value of s allows Equation A.9 to be solved for A. The correct phase is the computed value for $n = r - \pi s$ radians.

In summary, when Equation A.9 is a valid approximation, Equation A.11 may be used to estimate s. Then s is used in Equation A.9 to calculate the magnitude and phase of the signal. πs is subtracted from the computed phase to get the corrected phase.

A.2 Application to Discrete Data

For a sufficient number of samples, N > 16, over a sufficient length of the signal, Burgess demonstrates Equations A.9 through A.11 are also valid for discrete Fourier series coefficients (DFSC). For the image contribution to be at most 1% of the direct contribution, the allowable values of m as a function of N are given in Table A.1.

Table A.1 Signal sampling parameters

N	m
256	$28 \leq m \leq 100$
2048	$26 \leq m \leq (N/2) - 26$

The upper limits on m arise due to the periodicity of the DSFC in N.

Calculations were performed to validate the correction scheme. A sine wave was generated with 256 equally-spaced data points and Fourier transformed, then the correction scheme was applied using the minimum value of r, 28, with the worst case value of s, 1/2. The maximum errors found to occur were 1.5 degrees in phase and 1% in magnitude.

A.3 Hanning Window

The previous results are for the case where the signal is sampled over $0 \leq t < T$ and assumed to be zero outside this interval. This amounts to implicitly windowing the data with a square window, as in Figures A.3 and A.4. To smooth the discontinuities this process may cause, Figure A.4, many other windows have been devised, such as the Hanning window. Application of a Hanning window to the data results in reduced leakage which allows more liberal sampling criteria than previously stated.

The Hanning window, expressed as

$$w(t) = \sin^2 \frac{\pi t}{T} \qquad (A.12)$$

for $0 \le t < T$, is compared with the square window in Figure A.5. The raw signal is multiplied by the Hanning window in the time domain, resulting in a signal which goes to zero at both $t = 0$ and $t = T$, thus the periodic continuation of the signal will be smooth.

The derivation of the approximate equations used for leakage correction is analogous to that for the square window. The required expressions are:

$$p_r^H = \frac{A}{4} e^{i\pi s} \left(\frac{1}{1-s^2} \right) \frac{\sin \pi s}{\pi s} \qquad (A.13)$$

and

$$p_{r+1}^H = \frac{A}{4} e^{i\pi s} \frac{1}{(1-s)(2-s)} \frac{\sin \pi s}{\pi s}. \qquad (A.14)$$

Define R as the ratio $|p_r^H| / |p_{r+1}^H|$. Then

$$R = \frac{2-s}{1+s}$$

or

$$S = \frac{2-R}{1+R}. \qquad (A.15)$$

For the magnitude of the image contribution to be at most 1% of the direct contribution, Burgess recommends $2 \le m \le (N/2) - 2$ for $N \ge 40$. This allows a much broader range of sampling conditions than the results for a square window. Calculations using 256 samples of a sine wave and $r = 2$ show the correction scheme to give less than 1% amplitude error and approximately ± 1 degree phase error.

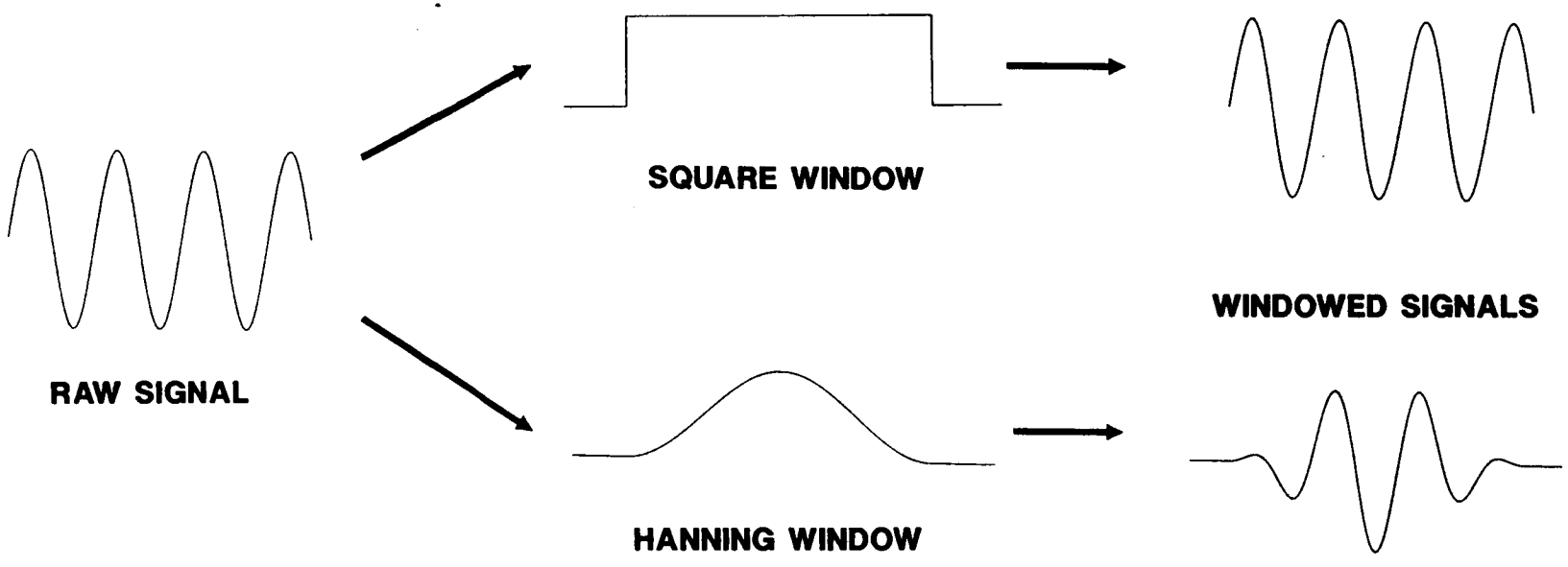

Figure A.5 Comparison of square and Hanning windows

A.4 Application to Signals with Higher Harmonics

The correction scheme will now be extended to periodic signals with frequency content at integer multiples of the fundamental frequency. This will lead to more restricted sampling criteria than before in order to keep leakage effects within the desired bounds.

Up to this point, the signal has been assumed to have one frequency component. Hence its leakage patterns were centered at $\pm\Omega$, and the resulting sampling criteria essentially restricted the leakage so that the interaction would be negligible in the neighborhood of Ω. Now, with leakage patterns at $\pm n\Omega$, the leakage extent must be more restricted for the interaction to remain negligible.

The case of equal amplitude cosine waves at frequencies $\omega_1 = \Omega$ and $\omega_2 = 2\Omega$ was analyzed. Interaction from the image frequencies $-\Omega$ and -2Ω was assumed to be negligible. Thus expressions like Equation A.9 were valid for each of the frequencies individually. Then the effect of the second harmonic on the first was deemed negligible when the ratio of the magnitude of the second to the first was less than 0.01 for the frequency line nearest Ω. With a Hanning window in effect, $5 \le m_1 \le (N-10)/2$ is a conservative requirement. m_1 is based on ω_1 so

$$m_1 = \frac{T}{T_{\omega_1}} = \frac{T}{T_\Omega}.$$

Calculations were used as before to validate the correction scheme for this case.

Appendix B. Euler Equations

The fluid is assumed to be a perfect gas with constant specific heats and viscous effects, body forces and external heat addition are neglected. The equations for the conservation of mass, momentum and energy for two-dimensional flow, the Euler equations, may be expressed in Cartesian coordinates as [39]

$$\frac{\partial \hat{Q}}{\partial t}+\frac{\partial \hat{E}}{\partial x}+\frac{\partial \hat{F}}{\partial y}=0 \tag{B.1}$$

where

$$\hat{Q}=\begin{pmatrix} \rho \\ \rho u \\ \rho v \\ e \end{pmatrix} \tag{B.2}$$

$$\hat{E}=\begin{pmatrix} \rho u \\ \rho u^2+p \\ \rho uv \\ u(e+p) \end{pmatrix} \tag{B.3}$$

and

$$\hat{F}=\begin{pmatrix} \rho v \\ \rho uv \\ \rho v^2+p \\ v(e+p) \end{pmatrix}. \tag{B.4}$$

ρ is the density, u and v are the x and y velocity components and e is the total energy per unit volume

$$e=\rho\left(c_v T+\tfrac{1}{2}(u^2+v^2)\right) \tag{B.5}$$

with temperature T and specific heat at constant volume c_v. The pressure may be expressed as

$$p=(\gamma-1)\left(e-\frac{\rho}{2}(u^2+v^2)\right). \tag{B.6}$$

All quantities in these equations are nondimensional. Lengths are divided by the airfoil chord, velocity components are divided by the inlet speed of sound, time is multiplied by the inlet speed of sound over the airfoil chord and the total energy per unit volume is divided by the product of the inlet density and the square of the speed of sound.

For a general transformation to $\xi-\eta$ coordinates, $\xi=\xi(x,y,t)$, $\eta=\eta(x,y,t)$, $\tau=t$, the Euler equations become

$$\frac{\partial Q}{\partial \tau}+\frac{\partial E}{\partial \xi}+\frac{\partial F}{\partial \eta}=0 \tag{B.7}$$

where

$$Q=J^{-1}\hat{Q} \tag{B.8}$$

$$E=J^{-1}\left(\hat{Q}\frac{\partial \xi}{\partial t}+\hat{E}\frac{\partial \xi}{\partial x}+\hat{F}\frac{\partial \xi}{\partial y}\right)=J^{-1}\begin{pmatrix}\rho u_{\xi}\\ \rho u u_{\xi}+p\frac{\partial \xi}{\partial x}\\ \rho v u_{\xi}+p\frac{\partial \xi}{\partial y}\\ u_{\xi}(e+p)-p\frac{\partial \xi}{\partial t}\end{pmatrix} \tag{B.9}$$

and

$$F=J^{-1}\left(\hat{Q}\frac{\partial \eta}{\partial t}+\hat{E}\frac{\partial \eta}{\partial x}+\hat{F}\frac{\partial \eta}{\partial y}\right)=J^{-1}\begin{pmatrix}\rho v_{\eta}\\ \rho u v_{\eta}+p\frac{\partial \eta}{\partial x}\\ \rho v v_{\eta}+p\frac{\partial \eta}{\partial y}\\ v_{\eta}(e+p)-p\frac{\partial \eta}{\partial t}\end{pmatrix}. \tag{B.10}$$

The ξ and η components of velocity are

$$u_\xi = \frac{\partial \xi}{\partial t} + u\frac{\partial \xi}{\partial x} + v\frac{\partial \xi}{\partial y}, \qquad v_\eta = \frac{\partial \eta}{\partial t} + u\frac{\partial \eta}{\partial x} + v\frac{\partial \eta}{\partial y}. \tag{B.11}$$

The transformation Jacobian is

$$J = \frac{\partial \xi}{\partial x}\frac{\partial \eta}{\partial y} - \frac{\partial \xi}{\partial y}\frac{\partial \eta}{\partial x}. \tag{B.12}$$

Applying the chain rule to the transformed spatial derivatives, Equation B.7 becomes

$$\frac{\partial Q}{\partial \tau} + A\frac{\partial Q}{\partial \xi} + B\frac{\partial Q}{\partial \eta} = 0 \tag{B.12}$$

with $A = \partial E/\partial Q$ and $B = \partial F/\partial Q$. Using Equations B.9 and B.10 and letting $K = A$ when $k = \xi$ and $K = B$ when $k = \eta$, K is expressed as

$$K = I\frac{\partial k}{\partial t} + \frac{\partial \hat{E}}{\partial \hat{Q}}\frac{\partial k}{\partial x} + \frac{\partial \hat{F}}{\partial \hat{Q}}\frac{\partial k}{\partial y} \tag{B.13}$$

where I is the identity matrix. Calculating the partial derivatives in Equation B.13 and simplifying results in

$$K = \begin{pmatrix} k_t & k_x & k_y & 0 \\ k_x\zeta^2 - u\delta & k_t + \delta - (\gamma-2)k_x u & -(\gamma-1)k_x v + k_y u & (\gamma-1)k_x \\ k_y\zeta^2 - v\delta & k_x v - (\gamma-1)k_y u & k_t + \delta - (\gamma-2)k_y v & (\gamma-1)k_y \\ \delta(-\gamma(e/\rho) + 2\zeta^2) & (\gamma(e/\rho) - \zeta^2)k_x - (\gamma-1)u\delta & (\gamma(e/\rho) - \zeta^2)k_y - (\gamma-1)v\delta & k_t + \gamma\delta \end{pmatrix} \tag{B.14}$$

where $\delta = u(\partial k/\partial x) + v(\partial k/\partial y)$, $\zeta^2 = (\gamma-1)(u^2+v^2)/2$ and $k_t = \partial k/\partial t$.

K may be expressed as the similarity transform

$$K = T_k \Lambda_k T_k^{-1}. \tag{B.15}$$

Λ_k is a diagonal matrix of the eigenvalues of K,

$$\Lambda_k = \begin{pmatrix} k_t+\delta & 0 & 0 & 0 \\ 0 & k_t+\delta & 0 & 0 \\ 0 & 0 & k_t+\delta+a|\nabla k| & 0 \\ 0 & 0 & 0 & k_t+\delta-a|\nabla k| \end{pmatrix}. \qquad \text{(B.16)}$$

$|\nabla k| = \sqrt{(\partial k/\partial x)^2+(\partial k/\partial y)^2}$ and $a = \sqrt{\gamma p/\rho}$ is the isentropic speed of sound.

The columns of T_k are right eigenvectors of K corresponding to the eigenvalues in Equation B.16 and the rows of T_k^{-1} are the corresponding left eigenvectors.

$$T_k = \begin{pmatrix} 1 & 0 & \nu & \nu \\ u & \tilde{k}_y\rho & \nu(u+\tilde{k}_x a) & \nu(u-\tilde{k}_x a) \\ v & -\tilde{k}_x\rho & \nu(v+\tilde{k}_y a) & \nu(v-\tilde{k}_y a) \\ \dfrac{\zeta^2}{\gamma-1} & \rho(\tilde{k}_y u-\tilde{k}_x v) & \nu\left(\dfrac{\zeta^2+a^2}{\gamma-1}+a\tilde{\delta}\right) & \nu\left(\dfrac{\zeta^2+a^2}{\gamma-1}-a\tilde{\delta}\right) \end{pmatrix} \qquad \text{(B.17)}$$

$$T_k^{-1} = \begin{pmatrix} 1-\zeta^2/a^2 & (\gamma-1)u/a^2 & (\gamma-1)v/a^2 & -(\gamma-1)/a^2 \\ (\tilde{k}_x v-\tilde{k}_y u)/\rho & \tilde{k}_y/\rho & -\tilde{k}_x/\rho & 0 \\ \chi(\zeta^2-a\tilde{\delta}) & \chi(\tilde{k}_x a-(\gamma-1)u) & \chi(\tilde{k}_y a-(\gamma-1)v) & \chi(\gamma-1) \\ \chi(\zeta^2+a\tilde{\delta}) & -\chi(\tilde{k}_x a+(\gamma-1)u) & -\chi(\tilde{k}_y a+(\gamma-1)v) & \chi(\gamma-1) \end{pmatrix} \qquad \text{(B.18)}$$

where $\nu = \rho/(\sqrt{2}a)$, $\chi = 1/(\sqrt{2}\rho a)$ and $\tilde{c} = c/\sqrt{k_x^2+k_y^2}$ for any c.

Expanding Equation B.12 to primitive variable form,

$$\frac{\partial Q}{\partial q}\frac{\partial q}{\partial \tau} + A\frac{\partial Q}{\partial q}\frac{\partial q}{\partial \xi} + B\frac{\partial Q}{\partial q}\frac{\partial q}{\partial \eta} = 0 \qquad \text{(B.19)}$$

with

$$\mathbf{q} = J^{-1}\begin{pmatrix} \rho \\ u \\ v \\ p \end{pmatrix}. \qquad \text{(B.20)}$$

Substituting $S^{-1} = \partial Q / \partial q$ into Equation B.19 gives

$$S^{-1}\frac{\partial q}{\partial \tau} + AS^{-1}\frac{\partial q}{\partial \xi} + BS^{-1}\frac{\partial q}{\partial \eta} = 0. \tag{B.21}$$

Multiplying by S and substituting $\tilde{A} = SAS^{-1}$ and $\tilde{B} = SBS^{-1}$,

$$\frac{\partial q}{\partial \tau} + \tilde{A}\frac{\partial q}{\partial \xi} + \tilde{B}\frac{\partial q}{\partial \eta} = 0. \tag{B.22}$$

Expressions for S^{-1} and S are

$$S^{-1} = \frac{\partial Q}{\partial q} = \begin{pmatrix} 1 & 0 & 0 & 0 \\ u & \rho & 0 & 0 \\ v & 0 & \rho & 0 \\ \frac{1}{2}(u^2+v^2) & \rho u & \rho v & 1/(\gamma-1) \end{pmatrix} \tag{B.23}$$

and

$$S = \frac{\partial q}{\partial Q} = \begin{pmatrix} 1 & 0 & 0 & 0 \\ -u/\rho & 1/\rho & 0 & 0 \\ -v/\rho & 0 & 1/\rho & 0 \\ \frac{\gamma-1}{2}(u^2+v^2) & -(\gamma-1)u & -(\gamma-1)v & (\gamma-1) \end{pmatrix}. \tag{B.24}$$

$\tilde{A}$ and $\tilde{B}$ are determined using

$$\tilde{K} = SKS^{-1} = ST_k \Lambda_k T_k^{-1} S^{-1} = R_k \Lambda_k R_k^{-1} \tag{B.25}$$

where $\tilde{K} = \tilde{A}$ when $k = \xi$ and $\tilde{K} = \tilde{B}$ when $k = \eta$. Using Equations B.18 and B.21,

$$R_k^{-1} = T_k^{-1} S^{-1} = \begin{pmatrix} 1 & 0 & 0 & -1/a^2 \\ 0 & \tilde{k}_y & -\tilde{k}_x & 0 \\ 0 & \tilde{k}_x/\sqrt{2} & \tilde{k}_y/\sqrt{2} & 1/(\sqrt{2}\rho a) \\ 0 & -\tilde{k}_x/\sqrt{2} & -\tilde{k}_y/\sqrt{2} & 1/(\sqrt{2}\rho a) \end{pmatrix} \tag{B.26}$$

and, using Equations B.17 and B.22,

$$\mathbf{R}_k = \mathbf{S}\mathbf{T}_k = \begin{pmatrix} 1 & 0 & \rho/(\sqrt{2}a) & \rho/(\sqrt{2}a) \\ 0 & \tilde{k}_y & \tilde{k}_x/\sqrt{2} & -\tilde{k}_x/\sqrt{2} \\ 0 & -\tilde{k}_x & \tilde{k}_y/\sqrt{2} & -\tilde{k}_y/\sqrt{2} \\ 0 & 0 & \rho a/\sqrt{2} & \rho a/\sqrt{2} \end{pmatrix}. \qquad \text{(B.27)}$$

Appendix C. Linearized Theory of Cascade Wave Propagation

From the linearized theory of an infinite cascade of flat plate airfoils oscillating with fixed interblade phase angle in a uniform subsonic mean flow field, reference 3, several characteristics of the resulting pressure waves which propagate away from the cascade may be determined. The approach is to assume inviscid, isentropic, two-dimensional subsonic flow through an infinite cascade of flat plate airfoils. Unsteady disturbances are assumed to be small perturbations to the steady flow field, resulting in a system of first order linear partial differential equations for the unknown perturbation quantities. When harmonic solutions which satisfy cascade periodicity are assumed, the disturbance wavelength, direction of propagation and rate of decay may be determined.

The mass conservation equation is, for the $\xi-\eta$ coordinate system of Figure C.1,

$$\frac{D\rho}{Dt}+\rho\left(\frac{\partial u}{\partial \xi}+\frac{\partial v}{\partial \eta}\right)=0. \tag{C.1}$$

The momentum equations are

$$\frac{Du}{Dt}=-\frac{1}{\rho}\frac{\partial p}{\partial \xi} \tag{C.2}$$

and

$$\frac{Dv}{Dt}=-\frac{1}{\rho}\frac{\partial p}{\partial \eta}. \tag{C.3}$$

u is the $\xi-$component of velocity, v is the $\eta-$component of velocity, ρ is the density and

$$\frac{D}{Dt}=\frac{\partial}{\partial t}+u\frac{\partial}{\partial \xi}+v\frac{\partial}{\partial \eta}. \tag{C.4}$$

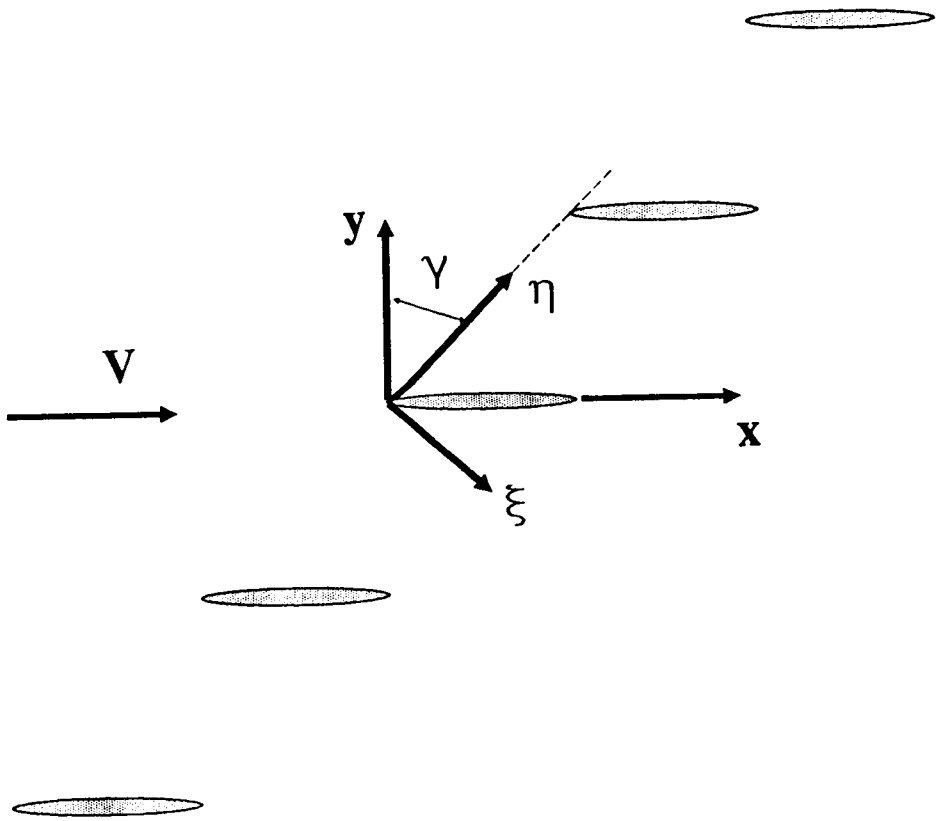

Figure C.1 Cascade coordinate system

Using the subscript 0 to denote mean values (which are constant) and 1 for the perturbations,

$$\rho = \rho_0 + \rho_1,$$

$$u = u_0 + u_1,$$

$$\ldots,$$

are substituted into the governing conservation equations. Once the equations are expanded and products of perturbations are neglected, a system of linear partial differential equations results with the perturbation quantities as the dependent variables. Conservation of mass becomes

$$\frac{D_0 \rho_1}{Dt} + \rho_0 \left(\frac{\partial u_1}{\partial \xi} + \frac{\partial v_1}{\partial \eta} \right) = 0. \tag{C.5}$$

The momentum equations become

$$\frac{D_0 u_1}{Dt} = -\frac{1}{\rho_0} \frac{\partial p_1}{\partial \xi} \tag{C.6}$$

and

$$\frac{D_0 v_1}{Dt} = -\frac{1}{\rho_0} \frac{\partial p_1}{\partial \eta} \tag{C.7}$$

with the operator

$$\frac{D_0}{Dt} = \frac{\partial}{\partial t} + u_0 \frac{\partial}{\partial \xi} + v_0 \frac{\partial}{\partial \eta}. \tag{C.8}$$

To close the system of equations, the speed of sound for isentropic flow of a calorically perfect gas, a, is introduced.

$$a^2 = \left(\frac{\partial p}{\partial \rho} \right)_s = \frac{dp}{d\rho} \tag{C.9}$$

Expanding Equations C.5 through C.7 and using C.9 to replace derivatives of ρ_1 with derivatives of p_1 gives

$$\frac{\partial \mathbf{q}}{\partial t} + \mathrm{A}\frac{\partial \mathbf{q}}{\partial \xi} + \mathrm{B}\frac{\partial \mathbf{q}}{\partial \eta} = 0 \tag{C.10}$$

where

$$\mathbf{q} = \begin{pmatrix} p_1 \\ u_1 \\ v_1 \end{pmatrix} \tag{C.11}$$

$$\mathrm{A} = \begin{pmatrix} u_0 & \rho_0 a^2 & 0 \\ 1/\rho_0 & u_0 & 0 \\ 0 & 0 & u_0 \end{pmatrix} \tag{C.12}$$

and

$$\mathrm{B} = \begin{pmatrix} v_0 & 0 & \rho_0 a^2 \\ 0 & v_0 & 0 \\ 1/\rho_0 & 0 & v_0 \end{pmatrix}. \tag{C.13}$$

For an infinite cascade of equally-spaced airfoils oscillating harmonically at a fixed interblade phase angle, the dependent variables will depend harmonically on the spatial position and the time. Thus the pressure perturbation is expressed as

$$p_1 = \overline{p}_1 e^{i(\omega t + l\xi + m\eta)} \tag{C.14}$$

where $\overline{p}_1$ is the pressure disturbance amplitude and l and m are the axial and tangential wave numbers. Analogous relations are used for u_1 and v_1.

Substituting the perturbation expressions into Equation C.10, a system of linear algebraic equations is obtained:

$$\begin{pmatrix} \omega + u_0 l + v_0 m & a^2 l \rho_0 & a^2 m \rho_0 \\ l/\rho_0 & \omega + u_0 l + v_0 m & 0 \\ m/\rho_0 & 0 & \omega + u_0 l + v_0 m \end{pmatrix} \begin{pmatrix} \overline{p}_1 \\ \overline{u}_1 \\ \overline{v}_1 \end{pmatrix} = 0. \tag{C.15}$$

To obtain a non-trivial solution to this linear system, the determinant of the coefficient matrix in Equation C.15 is set equal to 0:

$$(\omega + u_0 l + v_0 m)[(\omega + u_0 l + v_0 m)^2 - a^2(l^2 + m^2)] = 0. \qquad (C.16)$$

The two solutions to Equation C.16 encompass different physical phenomena - it is necessary to determine which solution applies to acoustic disturbances.

From the momentum equations, relations between pressure and velocity fluctuations are obtained:

$$\begin{aligned} \bar{p}_1 &= -\frac{\rho_0}{l}(\omega + u_0 l + v_0 m)\bar{u}_1 \\ &= -\frac{\rho_0}{m}(\omega + u_0 l + v_0 m)\bar{v}_1. \end{aligned} \qquad (C.17)$$

Hence for the solution of Equation C.16 obtained when $\omega + u_0 l + v_0 m = 0$, the pressure fluctuations are, from Equation C.17, zero, but the vorticity is

$$\begin{aligned} \psi_1 &= \frac{\partial v_1}{\partial \xi} - \frac{\partial u_1}{\partial \eta} \\ &= i(l\bar{v}_1 - m\bar{u}_1)e^{i(\omega t + l\xi + m\eta)}. \end{aligned} \qquad (C.18)$$

The velocity of propagation of a disturbance is simply the phase velocity, which is determined by tracking a constant disturbance phase. In this reference frame, the phase does not change with time:

$$\frac{d}{dt}(\omega t + l\xi + m\eta) = 0$$

or

$$\omega + l\frac{d\xi}{dt} + m\frac{d\eta}{dt} = 0. \qquad (C.19)$$

Combining Equation C.19 and $\omega + u_0 l + v_0 m = 0$ to eliminate ω results in

$$l\frac{d\xi}{dt} + m\frac{d\eta}{dt} = u_0 l + v_0 m. \qquad (C.20)$$

Thus the ξ and η components of velocity are equal to the mean flow velocity components u_0 and v_0. This solution corresponds to convection of vorticity by the mean flow with no associated pressure fluctuations.

For nonzero pressure disturbances, Equation C.17 implies $\omega + u_0 l + v_0 m \neq 0$. The only remaining way to satisfy Equation C.16 is

$$(\omega + u_0 l + v_0 m)^2 - a^2(l^2 + m^2) = 0. \qquad (C.21)$$

From Equations C.17, $m\bar{u}_1 = l\bar{v}_1$. Substituting this into Equation C.18, it follows that the vorticity is zero; the solution which satisfies Equation C.21 therefore corresponds to irrotational pressure perturbations.

Solving Equation C.21 for the axial wave number,

$$l = \frac{u_0(\omega + v_0 m) \pm a\sqrt{(\omega + v_0 m)^2 - (a^2 - u_0^2)m^2}}{a^2 - u_0^2} \qquad (C.22)$$

or

$$l = \frac{M_\xi((\omega/a) + M_\eta m) \pm \sqrt{((\omega/a) + M_\eta m)^2 - (1 - M_\xi^2)m^2}}{1 - M_\xi^2} \qquad (C.23)$$

where M_ξ and M_η are components of the Mach number in the ξ and η directions. The tangential wave number must satisfy cascade dynamic periodicity, which is specified by the interblade phase angle β. Hence

$$mS = \beta + 2\pi n \qquad (C.24)$$

where S is the cascade spacing and n is an integer.

The nature of acoustic wave generation depends upon the term under the radical in either of Equations C.22 and C.23. Let δ be the term under the radical in Equation C.23.

$$\delta = ((\omega/a) + M_\eta m)^2 - (1 - M_\xi^2)m^2 \qquad (C.25)$$

When $\delta = 0$, the acoustic resonance condition, only one wave is created which propagates in the circumferential direction. The sense of the direction of propagation, either $+\eta$ or $-\eta$, depends upon the tangential wave number. From Equation C.25, the tangential wave numbers at the resonances are

$$m = \frac{2kM}{C(1-M^2)}\left(M_\eta \pm \sqrt{1 - M_\xi^2}\right) \qquad (C.26)$$

where k is the reduced frequency and C is the airfoil chord. Combining Equation C.24 for $n = 0$ with Equation C.26 and solving for the resonant interblade phase angle, β_r, yields

$$\beta_r^* = \frac{2kMS}{C(1-M^2)}\left(M_\eta \pm \sqrt{1 - M_\xi^2}\right)$$

or

$$\beta_r^* = \frac{2kMS}{C(1-M^2)}\left(M\sin(\alpha_0 + \gamma) \pm \sqrt{1 - M^2\cos^2(\alpha_0 + \gamma)}\right). \qquad (C.27)$$

When $\delta > 0$, l is real and two waves propagate without decay, one going upstream and the other downstream - this behavior is termed superresonant for a subsonic mean flow field. Lastly, when $\delta < 0$, the behavior is termed subresonant and the waves decay exponentially with axial distance.

When $\delta < 0$, l is complex. Substituting $l = l^R + il^I$ in to Equation C.14 gives

$$p_1 = \overline{p}_1 e^{i(\omega t + (l^R + il^I)\xi + m\eta)}$$

$$= \overline{p}_1 e^{-l^I \xi} e^{i(\omega t + l^R \xi + m\eta)}. \qquad (C.28)$$

Thus the wave decays exponentially with distance, depending upon the imaginary part of l.

$$\frac{|p_1(\xi)|}{\overline{p}_1} = \frac{|p_1(\xi)|}{|p_1(\xi = 0)|} = e^{-|l^I \xi|} \qquad (C.29)$$

The absolute value of the exponent disallows a second solution, the non-physical case of an amplifying wave.

The axial and tangential wave numbers specify the acoustic wave propagation direction relative to ξ', η' coordinates which are parallel to the fixed ξ, η coordinate system but moving with the steady flow velocity [5]. Relative to the ξ', η' coordinates, the waves propagate at the angle

$$\theta' = \tan^{-1}\left(\frac{-m}{-l^R}\right) \qquad (C.30)$$

at the speed of sound. The wave propagation vector $\vec{V}_p$ in the fixed ξ, η coordinate system is therefore the sum of the steady flow velocity vector and the wave propagation vector relative to the moving coordinate system,

$$\vec{V}_p = (u_0 + a\cos\theta')\vec{e}_\xi + (v_0 + a\sin\theta')\vec{e}_\eta \qquad (C.31)$$

from which the direction of propagation θ in the ξ, η coordinate system is

$$\theta = \tan^{-1}\left(\frac{v_0 + a\sin\theta'}{u_0 + a\cos\theta'}\right). \qquad (C.32)$$

The disturbance wavelength is the distance a disturbance travels in one temporal period, $2\pi/\omega$. Thus

$$\lambda = \frac{2\pi}{\omega}|\vec{V}_p|. \qquad (C.33)$$

NASA
National Aeronautics and Space Administration

Report Documentation Page

1. Report No.	2. Government Accession No.	3. Recipient's Catalog No.
NASA TM-103250		

4. Title and Subtitle	5. Report Date
Aerodynamics of a Linear Oscillating Cascade	August 1990
	6. Performing Organization Code

7. Author(s)	8. Performing Organization Report No.
Daniel H. Buffum and Sanford Fleeter	E-5677
	10. Work Unit No.
	535-05-01

9. Performing Organization Name and Address	11. Contract or Grant No.
National Aeronautics and Space Administration Lewis Research Center Cleveland, Ohio 44135-3191	
	13. Type of Report and Period Covered
	Technical Memorandum

12. Sponsoring Agency Name and Address	14. Sponsoring Agency Code
National Aeronautics and Space Administration Washington, D.C. 20546-0001	

15. Supplementary Notes

Daniel H. Buffum, NASA Lewis Research Center; Sanford Fleeter, School of Mechanical Engineering, Purdue University, West Lafayette, Indiana 47907.

16. Abstract

The steady and unsteady aerodynamics of a linear oscillating cascade are investigated using experimental and computational methods. Experiments are performed to quantify the torsion mode oscillating cascade aerodynamics of the NASA Lewis Transonic Oscillating Cascade for subsonic inlet flowfields using two methods: (1) simultaneous oscillation of all the cascaded airfoils at various values of interblade phase angle, and (2) the unsteady aerodynamic influence coefficient technique. Analysis of these data and correlation with classical linearized unsteady aerodynamic analysis predictions indicate that the wind tunnel walls enclosing the cascade have, in some cases, a detrimental effect on the cascade unsteady aerodynamics. An Euler code for oscillating cascade aerodynamics is modified to incorporate improved upstream and downstream boundary conditions and also the unsteady aerodynamic influence coefficient technique. The new boundary conditions are shown to improve the unsteady aerodynamic predictions of the code, and the computational unsteady aerodynamic influence coefficient technique is shown to be a viable alternative for calculation of oscillating cascade aerodynamics.

17. Key Words (Suggested by Author(s))	18. Distribution Statement
Aerodynamics Cascade Unsteady aerodynamics Flutter	Unclassified – Unlimited Subject Category 02

19. Security Classif. (of this report)	20. Security Classif. (of this page)	21. No. of pages	22. Price*
Unclassified	Unclassified	265	A12

NASA FORM 1626 OCT 86

*For sale by the National Technical Information Service, Springfield, Virginia 22161